12-2013

# The Solid State Simulation of the Structure and Vibrational Modes of Organic, Hybrid Organometallic and Inorganic Species Using the CRYSTAL09 Code.

Steven Pellizzeri

# Abstract

An investigation of the structural and vibrational information of organic, hybrid organometallic and inorganic species was conducted using solid-state density functional theory (DFT). In this work the solid state DFT modeling was accomplished using the CRYSTAL09 code to simulate the geometries and vibrational modes of a variety of systems. These studies included: (1) the investigation of three polymorphs of vanadium phosphate, (2) three studies involving the use of 5-(4-pyridyl)tetrazole, and lastly (3) the crystal structure and simulation of α,α,α′,α′-tetrabromo-*p*-xylene. The studies involving 5-(4-pyridyl)tetrazole are comprised of (a) the comparison of a new polymorph to previously published crystallographic information of the free base 5-(4-pyridyl)tetrazole, (b) the comparison of two hydrohalide salts of 5-(4-pyridyl)tetrazole, and lastly, (c) comparing three isomorphous transition metal complexes with 5-(4-pyridyl)tetrazole as a ligand.

In the majority of these systems, with the exception of the polymorphs of vanadium phosphate, terahertz (THz) spectroscopy was used to probe the intermolecular interactions in these molecular crystals. These studies aim to increase the understanding of what effect subtle structural, compositional, or packing differences have on the vibrational normal modes, in particular in the region from 0-100 $cm^{-1}$ known as the terahertz region.

It was found that subtle differences in the structure, composition, or packing could have large and varying effects on the vibrational modes, especially in the terahertz region. In particular, there are no universal trends in the shifting of vibrational frequency; however, the nature of the normal mode has the greatest effect when comparing systems that have compositional differences.

# The Solid State Simulation of the Structure and Vibrational Modes of Organic, Hybrid Organometallic and Inorganic Species Using the CRYSTAL09 Code.

By

Steven Louis Pellizzeri

B.S. Rochester Institute of Technology, 2007

**DISSERTATION**

Submitted in partial fulfillment of the requirements for the

degree of Doctor of Philosophy in Chemistry

in the Graduate School of Syracuse University

December 2013

# Acknowledgement

I would like to thank many people for their support and encouragement throughout my time at Syracuse University.

First and foremost, I would like to thank my advisor, Dr. Jon Zubieta, for his support, time, and guidance. I am grateful to Dr. Zubieta for accommodating a theoretical physical chemist into his synthetic inorganic chemistry group.

In addition to Dr. Zubieta, I must thank Dr. Timothy Korter for all of his support helping me to navigate the wacky world of computational chemistry.

Many members of Zubieta group, past and present, have provided invaluable support to my research. I appreciate them listening to my ramblings about tables, graphs, and numbers at group meetings.

I would also like to thank my family for providing a constant source of motivation and support through these last five years.

Lastly, I especially need to thank my wonderful fiancé and soon to be wife, Tiffany Smith, for all of her support and her ability to motivate me to work hard, pushing me to be the absolute best that I can be.

# Table of Contents


**List of Abbreviations** xi

**List of Figures** xiii

**List of Tables** xx

**Chapter 1: Introduction**

1.1 Introduction 2

1.2 Chemical/Structural Diversity 4

*1.2.1 Conformational Based Polymorphism* 4

*1.2.2 Compositional Based Polymorphism* 10

*1.2.3 Packing Based Polymorphism* 14

1.3 Techniques for Determining Polymorphic Forms 17

1.4 Terahertz (THz) Spectroscopy 21

*1.4.1 Terahertz (THz) Spectroscopy* 21

*1.4.2 Applications of Terahertz Spectroscopy* 25

*1.4.2.1 Characterization of Materials* 25

*1.4.2.2 Terahertz Imaging* 27

*1.4.3 Interpretation of Terahertz Vibrations Using Modeling Techniques* 27

1.5 Density Functional Theory and Its Implementation in CRYSTAL09 28

*1.5.1 Appling Quantum Mechanics to Molecular Vibrations* 28

*1.5.2 Density Functional Theory (DFT)* 34

*1.5.3 CRYSTAL09* 39

1.6 General Research Considerations 46

1.7 References 48

**Chapter 2: A Solid-state Density Functional Theory Investigation of the Structure and Vibrational Modes of Vanadium Phosphate Polymorphs**

2.1 Introduction 64

2.2 Experimental and Theoretical Methods 69

*2.2.1 Synthesis of $VOPO_4 \cdot 2H_2O$ and $VOPO_4$* 69

*2.2.1.1 Synthesis of $VOPO_4 \cdot 2H_2O$* 69

*2.2.1.2 Synthesis of $\alpha_1$-$VOPO_4$, $\alpha_2$-$VOPO_4$, and $\beta$-$VOPO_4$* 69

*2.2.2 Theoretical Methodology of CRYSTAL09* 70

2.3 Results and Discussion 73

*2.3.1 Comparison of the Calculated and experimental Structures* 73

*2.3.2 Comparison of Theoretical and Experimental Vibrational Frequencies* 80

2.4 Conclusions 90

2.5 Acknowledgement 91

2.6 References 91

**Chapter 3: Using Terahertz Spectroscopy and Solid-state Density Functional Theory to Characterize a New Polymorph of 5-(4-pyridyl)tetrazole**

3.1 Introduction 95

3.2 Experimental and Theoretical Methods 98

*3.2.1 Experimental* 98

3.2.1.1 *Synthesis of polymorphic forms of 5-(4-pyridyl)tetrazole* 98

3.2.1.2 *Recrystallization of the α Form of 5-(4-pyridyl)tetrazole (α-4PT)* 99

3.2.1.3 *Recrystallization of the β Form of 5-(4-pyridyl)tetrazole (β-4PT)* 99

3.2.2 *X-Ray Crystallography* 99

3.2.3 *Time-domain Terahertz Spectroscopy* 100

*3.2.4 Theoretical Methodology of Crystal09* 101

3.3 Results and Discussion 103

*3.3.1 X-Ray Crystallography* 103

*3.3.1.1 X-Ray Crystallography of the α Form of 5-(4-pyridyl)tetrazole (α-4PT)* 103

*3.3.1.2 X-Ray Crystallography of the β Form of 5-(4-pyridyl)tetrazole (β -4PT)* 103

*3.3.2 Comparison of the Calculated and Experimental Structures* 105

*3.3.3 Comparison of Theoretical and Experimental Vibrational Frequencies* 112

3.4 Conclusions 120

3.5 Supporting Information 122

3.6 Acknowledgement 123

3.7 References 123

**Chapter 4: Using Solid-state Density Functional Theory and Terahertz Spectroscopy to Spectroscopically Distinguish the Various Hydrohalide Salts of 5-(4-pyridyl)tetrazole**

4.1 Introduction 127

4.2 Experimental and Theoretical Methods 130

*4.2.1 Experimental* 130

*4.2.1.1 Synthesis of Halide Salts of 5-(4-pyridyl)tetrazole* 130

*4.2.1.2 X-Ray Crystallography* 131

*4.2.2 Time-domain Terahertz Spectroscopy* 131

*4.2.3 Theoretical Methodology of Crystal09* 133

4.3 Results and Discussion 134

*4.3.1 X-Ray Crystallography* 134

*4.3.2 Comparison of the calculated and experimental structures* 135

*4.3.3 Comparison of theoretical and experimental vibrational frequencies* 140

4.4 Conclusions 148

4.5 Supporting Information 148

4.6 Acknowledgement 149

4.7 References 149

**Chapter 5: A Solid-State Density Functional Theory Investigation of the Effect of Metal Substitution (Metal = Mn, Cd, Co) on the Terahertz Spectra of Isomorphous Molecular Metal 5-(4-pyridyl)tetrazolato Complexes**

5.1 Introduction 154

5.2 Experimental and Theoretical Methods 158

*5.2.1 Experimental* 158

*5.2.1.1 Synthesis of Metal 5-(4-pyridyl)tetrazolato Complexes* 158

*5.2.1.2 X-Ray Crystallography* 158

*5.2.1.3 Time-domain Terahertz Spectroscopy* 159

*5.2.2 Theoretical Methodology of Crystal09* 160

5.3 Results and Discussion 162

*5.3.1 X-Ray Crystallography* 162

*5.3.2 Comparison of the Calculated and Experimental Structures* 162

*5.3.3 Comparison of Theoretical and Experimental Vibrational Frequencies* 169

5.4 Conclusions 175

5.5 Supporting Information 176

5.6 Acknowledgement 177

5.7 References 177

**Chapter 6: Crystal Structure and Terahertz Spectroscopy of α,α,α′,α′-Tetrabromo-*p*-xylene Modeled using Solid-State Density Functional Theory**

6.1 Introduction 182

6.2 Experimental and Theoretical Methods 184

*6.2.1 Experimental* 184

*6.2.1.1 Recrystallization of α,α,α′,α′-Tetrabromo-p-xylene.* 184

*6.2.1.2 X-Ray Crystallography* 185

*6.2.2 Time-domain Terahertz Spectroscopy* 185

*6.2.3 Theoretical Methodology of Crystal09* 186

6.3 Results and Discussion 188

*6.3.1 X-Ray Crystallography* 188

*6.3.2 Comparison of the Calculated and Experimental Structures* 188

*6.3.3 Comparison of Theoretical and Experimental Vibrational Frequencies* 193

6.4 Conclusions 197

6.5 Supporting Information 199

6.6 Acknowledgement 200

6.7 References 200

**Chapter 7: Conclusions**

7.1 Conclusions 204

**Appendix A: Chapter 3 Supporting Information** 209

**Appendix B: Chapter 4 Supporting Information** 214

**Appendix C: Chapter 5 Supporting Information** 220

**Appendix D: Chapter 6 Supporting Information** 222

# List of Abbreviations

| | |
|---|---|
| 4-PT | 5-(4-pyridyl)tetrazole |
| AO | Atomic Orbitals |
| BZ | Brillouin zone |
| CI | Configuration interaction |
| CO | Crystalline Orbital |
| CSF | Configuration state function |
| DFT | Density functional theory |
| DOS | Density of states |
| DSC | Differential scanning calorimetry |
| DTA | Differential thermal analysis |
| EM | Electromagnetic |
| FIR | Far infrared |
| GGA | Generalized gradient approximations |
| GTF | Gaussian type functions |
| GTO | Gaussian-type orbitals |
| HF | Hartree-Fock |
| IR | Infrared |
| LDA | Local density approximations |
| MPPT | Møller-Plesset perturbation theory |
| PES | Potential energy surface |
| PTFE | Polytetrafluoroethylene |
| RMSD | Root-mean-squared deviation |
| SCF | Self-consistent field |

| | |
|---|---|
| STO | Slater-type Orbitals |
| TBX | α,α,α′,α′-tetrabromo-*p*-xylene |
| TGA | Thermogravimetric analysis |
| THz | Terahertz |

# List of Figures


| | | |
|---|---|---|
| **Figure 1.1** | Schematic representation of possible packing arrangements, iii-vi, for a conformationally flexible molecule. Figure was modified from ref. 39. | 6 |
| **Figure 1.2** | Examples of conformationally flexible molecules that exhibit conformational polymorphism, with the main bond torsions are indicated with arrows. Figure was modified from ref.39. | 8 |
| **Figure 1.3** | Tautomeric polymorphic forms of 2-amino-3- hydroxy-6-phenylazopyridine Figure was modified from ref.55. | 9 |
| **Figure 1.4** | Concentration-pressure curve at 50°C for the cupric sulfate-water system. Figure was modified from ref.64. | 12 |
| **Figure 1.5** | Dissolution behavior of different forms of succinylsulfathiazole in ~0.001 N sulfuric acid solution at 20°C. The inset image is of succinylsulfathiazole. Figure was modified from ref.62. | 13 |
| **Figure 1.6** | Crystal structures of the different allotropes of carbon. (Left to right) Three-dimensional diamond and graphite (3D); two-dimensional graphene (2D); one-dimensional nanotubes (1D); and zero-dimensional buckyballs (0D).Figure was modified from ref.87. | 16 |
| **Figure 1.7** | The phase diagram of water and ice including the melting lines of metastable ices IV and XII, and extrapolated phase boundaries at low temperatures (dashed lines). Figure was modified from ref.96. | 18 |

**Figure 1.8** (1) Six possible orientations of water in Ice. (2) A pentameric fragment of an ice Ih structure. Network topologies of ice Ih (a), ice III (b), ice II (c), ice V (d), ice IV (e), ice XII (f), ice VI (g) and ice VII (h). Figure was modified from ref.96. 19

**Figure 1.9** The electromagnetic spectrum with the terahertz region shaded in blue. Figure was modified from ref.118. 22

**Figure 1.10** Two THz images of a chocolate bar. The upper image shows the variation in amplitude of the transmitted waveform allowing the embossed lettering to be visible, whereas the almonds are clearly visible due to their stronger absorption. The lower image shows the variation in transit time of the THz pulse. Here, the almonds are almost invisible, but the variation in the thickness of the sample is quite clear, allowing the embossed lettering to be easily discerned. Figure was modified from ref.127. 24

**Figure 1.11** (A) Mass m connected to a wall by a spring. The equilibrium position of the mass is x =0. (B) Masses m1 and m2 connected by a spring. 29

**Figure 1.12** (a) Potential energy curve for a classical harmonic oscillator. (b) Allowed energy levels and wavefunctions for a quantum mechanical harmonic oscillator. Figure was modified from ref. 185. 33

**Figure 1.13** The reciprocal lattice cell of 2D graphite (rhombus), the first Brillouin zone (hexagon), the irreducible part of Brillouin zone (in grey), and the coordinates of the reciprocal points according to a Pack-Monkhorst sampling, with shrinking factor A) 3 and B) 6. Figure was modified from ref.127. 41

**Figure 1.14** Generalized SCF procedure for calculating the electron density as implemented in CRYSTAL 43

**Figure 1.15** Simple scheme of the optimization process for CRYSTAL. Figure was modified from ref. 248. 45

**Figure 2.1** Polyhedral representation of the crystal structure of the α phases of vanadium phosphate ($VOPO_4$) (vanadium is shown in orange, phosphorus is shown in yellow, and oxygen is shown in red). 65

**Figure 2.2** -P-O-V-O-P- chain demonstrating the vanadium location within the octahedra for (a) $\alpha_1$-$VOPO_4$ and (b) $\alpha_2$-$VOPO_4$. 66

**Figure 2.3** Polyhedral representation of the crystal structure of the β phase of vanadium phosphate ($VOPO_4$) (vanadium is shown in orange, phosphorus in yellow, and oxygen in red). 68

**Figure 2.4** The atom labeling for the α phases of vanadium phosphate ($VOPO_4$). 77

**Figure 2.5** The atom labeling for the β phase of vanadium phosphate ($VOPO_4$). 78

**Figure 2.6** Calculated bond-length differences for each oxygen basis set compared to the structure determined through powder X-ray diffraction. Bond-length comparison for (a) $\alpha_1$-$VOPO_4$, (b) $\alpha_2$-$VOPO_4$, and (c) β-$VOPO_4$. 79

**Figure 2.7** The normalized experimental and theoretical traces for the infrared vibrational spectra of $\alpha_1$-$VOPO_4$. An empirical 11.62 $cm^{-1}$ full-width-half-maximum Lorentzian line shape has been applied to the theoretical data to aid in comparison. 82

**Figure 2.8** The normalized experimental and theoretical traces for the infrared vibrational spectra of $\alpha_2$-$VOPO_4$. An empirical 11.62 $cm^{-1}$ full-width-half-maximum Lorentzian line shape has been applied to the theoretical data to aid in comparison. 83

**Figure 2.9** The normalized experimental and theoretical traces for the infrared vibrational spectra of β-$VOPO_4$. An empirical 11.62 $cm^{-1}$ full-width-half-maximum Lorentzian line shape has been applied to the theoretical data to aid in comparison. 84

**Figure 3.1** Ball and Stick representation of the molecular cell of the α and β forms of 5-(4-pyridyl)tetrazole. (Carbon is shown in black, nitrogen is shown in light blue and hydrogen is shown in pink) 96

**Figure 3.2** Ball and stick representation of the molecular packing of the α and β forms of 5-(4-pyridyl)tetrazole displaying the differences in hydrogen bonded 5-(4-pyridyl)tetrazole chains. (Carbon is shown in black, nitrogen is shown in light blue, hydrogen is shown in pink, and hydrogen bonding shown with red dashed lines) 97

**Figure 3.3** Calculated bond-length differences for the α and β forms of 5-(4-pyridyl)tetrazole. The inset figure shows the atom labeling for the α and β forms of 5-(4-pyridyl)tetrazole. 108

**Figure 3.4** The theoretically determined Gibbs free energy per molecule for the α and β forms of 5-(4-pyridyl)tetrazole as a function of temperature at constant pressure. 111

**Figure 3.5** Normalized near-infrared vibration spectra of the α and β forms of 5-(4-pyridyl)tetrazole shown from 1800-400 $cm^{-1}$. 113

**Figure 3.6** Normalized experimental traces for the terahertz spectra of the α and β forms of 5-(4-pyridyl)tetrazole recorded at cryogenic temperature (78 K) shown from 10-95 $cm^{-1}$. 114

**Figure 3.7** The cryogenic (78K) experimental and theoretical traces for the terahertz spectra of the A) α and B) β forms of 5-(4-pyridyl)tetrazole shown from 10-95 $cm^{-1}$. An empirical 3.0 $cm^{-1}$ and 6.0 $cm^{-1}$ full-width-half-maximum Lorentzian line shape has been applied to the theoretical data of the α and β forms of 5-(4-pyridyl)tetrazole, respectively, to aid in comparison. 115

**Figure 3.8** Visualization of the vibrational normal mode corresponding to mode c. Arrows denote the direction of molecular motion. (Carbon is shown in black, nitrogen is shown in blue, and hydrogen is shown in grey) 121

**Figure 4.1** Ball and Stick representation of the molecular cell of 4-(1H-Tetrazol-5-yl)pyridinium bromide (4-PT·HBr) and 4-(1H-Tetrazol-5-yl)pyridinium chloride (4-PT·HCl). (Bromine is shown in dark red, chlorine is shown in green, carbon is shown in black, nitrogen is shown in light blue and hydrogen is shown in pink) 128

**Figure 4.2** Near-Infrared vibration spectra of 4-PT·HCl and 4-PT·HBr shown from 1600-400 $cm^{-1}$ 129

**Figure 4.3** Calculated bond-length differences for 4-(1H-Tetrazol-5-yl)pyridinium chloride (4-PT·HCl) and 4-(1H-Tetrazol-5-yl)pyridinium bromide (4-PT·HBr). The inset figure shows the atom labeling for 4-(1H-Tetrazol-5-yl)pyridinium chloride (4-PT·HCl) and 4-(1H-Tetrazol-5-yl)pyridinium bromide (4-PT·HBr). 138

**Figure 4.4** Ball and stick representation of 4-(1H-Tetrazol-5-yl)pyridinium chloride (4-PT·HCl) and 4-(1H-Tetrazol-5-yl)pyridinium bromide (4-PT·HBr) in the *ab* plane displaying the hydrogen bonded 4-(1H-Tetrazol-5-yl)pyridinium chains. (Bromine/Chlorine is shown in purple, carbon is shown in black, nitrogen is shown in light blue, hydrogen is shown in pink, and hydrogen bonding shown with red dashed lines) 139

**Figure 4.5** The experimental and theoretical traces for the terahertz spectra of 4-(1H-Tetrazol-5-yl)pyridinium chloride (4-PT·HCl). An empirical 3.0 $cm^{-1}$ full-width-half-maximum Lorentzian line shape has been applied to the theoretical data to aid in comparison. 141

**Figure 4.6** The experimental and theoretical traces for the terahertz spectra of 4-(1H-Tetrazol-5-yl)pyridinium bromide (4-PT·HBr). An empirical 3.0 $cm^{-1}$ full-width-half-maximum Lorentzian line shape has been applied to the theoretical data to aid in comparison. 142

**Figure 5.1** Ball and Stick representation of the packing structure and single molecular unit of $[M(C_6H_4N_5)_2(H_2O)_4]\cdot 2H_2O$ (M = Mn, Cd). (manganese/cadmium is shown in purple, carbon is shown in black, nitrogen is show in light blue and oxygen is shown in red) 155

**Figure 5.2** Ball and Stick representation of the packing structure and single molecular unit of $[Co(C_6H_4N_5)_2(H_2O)_4]\cdot 2H_2O$ (Co-4PT). (cobalt is shown in dark blue, carbon is shown in black, nitrogen is show in light blue and oxygen is shown in red) 156

**Figure 5.3** The atom labeling for $[M(C_6H_4N_5)_2(H_2O)_4]\cdot 2H_2O$ (M = Mn, Co, Cd ). 166

**Figure 5.4** Calculated bond-length differences for Mn-4PT, Co-4PT, and Cd-4PT 167

**Figure 5.5** The experimental and theoretical traces for the terahertz spectra of A) Mn-4PT, B) Co-4PT, and C) Cd-4PT. An empirical 3.0 $cm^{-1}$ full-width-half-maximum Lorentzian line shape has been applied to the theoretical data to aid in comparison. The 99.50 $cm^{-1}$ peak in the Co-4PT spectra was cut off to aid in visualization, the intensity peaks at ~850 $M^{-1}$ $cm^{-}$ 170

**Figure 5.6** Visualization of vibrational normal modes A) ligand scissoring along the *a* axis, B) ligand wagging along the *bc* plane, and C) pyridyl ring rotation in the *ab* plane. Arrows denote the direction of molecular motion 174

**Figure 6.1** Ball and Stick representation of the molecular packing of α,α,α′,α′-tetrabromo-*p*-xylene (TBX). (Bromine is shown in dark red, carbon is shown in black and hydrogen is shown in pink) 183

**Figure 6.2** Graphical representation of the Mulliken population analysis of α,α,α′,α′Tetrabromo-*p*-xylene. 190

**Figure 6.3** Calculated bond-length differences for α,α,α′,α′-tetrabromo-*p*-xylene (TBX). The inset figure shows the atom labeling for TBX. 192

**Figure 6.4** The experimental and theoretical traces for the terahertz spectrum of α,α,α′,α′-tetrabromo-*p*-xylene (TBX). An empirical 3.0 $cm^{-1}$ full-width-half-maximum Lorentzian line shape has been applied to the theoretical data to aid in comparison. 194

**Figure 6.5** Visualization of vibrational normal modes. Type A corresponds to modes a-c, which involve translations along the primary axes. Type B corresponds to modes d-f, which involves molecular scissoring in various planes. Type c corresponds to mode g, which involves molecular rocking in the ac plane. Arrows denote the direction of molecular motion. (Bromine is shown in red, carbon is shown in black and hydrogen is shown in grey.) 198

# List of Tables


| | | |
|---|---|---|
| **Table 2.1** | Modified atomic coordinates used for the initial structure of $\alpha_1$-$VOPO_4$. | 72 |
| **Table 2.2** | Interatomic bond lengths (Å), angles (°), and RMSD values for $\alpha_1$-$VOPO_4$. See **Figure 2.4** for atomic labels. Lowest RMSD values are shown in bold. Experimental parameters are from Ref. [25]. | 74 |
| **Table 2.3** | Interatomic bond lengths (Å), angles (°), and RMSD values for $\alpha_2$-$VOPO_4$. See **Figure 2.4** for atomic labels. Lowest RMSD values are shown in bold. Experimental parameters are from Ref. [26]. | 75 |
| **Table 2.4** | Interatomic bond lengths (Å), angles (°), and RMSD values for β-$VOPO_4$. See **Figure 2.4** for atomic labels. Lowest RMSD values are shown in bold. Experimental parameters are from Ref. [27]. | 76 |
| **Table 2.5** | Average RMSD values for interatomic bond lengths (Å), angles (°). The average does not include the values from $\alpha_1$-$VOPO_4$. The lowest average RMSD values are shown in bold. | 81 |
| **Table 2.6** | Frequency positions ($cm^{-1}$) and RMSD ($cm^{-1}$) of $\alpha_1$-$VOPO_4$ for the experimental and theoretical infrared spectra. The blanks are peaks that have no obvious correlation between experiment and theory. Lowest RMSD values are shown in bold. | 85 |
| **Table 2.7** | Frequency positions ($cm^{-1}$) and RMSD ($cm^{-1}$) of $\alpha_2$-$VOPO_4$ for the experimental and theoretical infrared spectra. The blanks are peaks that have no obvious correlation between experiment and theory. Lowest RMSD values are shown in bold. | 86 |

| | | |
|---|---|---|
| **Table 2.8** | Frequency positions ($cm^{-1}$) and RMSD ($cm^{-1}$) of β-$VOPO_4$ for the experimental and theoretical infrared spectra. The blanks are peaks that have no obvious correlation between experiment and theory. Lowest RMSD values are shown in bold. | 87 |
| **Table 2.9** | Empirical normal mode analysis for the polymorphs of vanadium phosphate. | 88 |
| **Table 3.1** | Summary of crystallographic data for the β form of 5-(4-pyridyl)tetrazole (β-4PT) | 104 |
| **Table 3.2** | Interatomic bond lengths (Å), angles (°), and RMSD values for the α form of 5-(4-pyridyl)tetrazole (α-4PT). See **Figure 3.3** for atomic labels. Experimental parameters are from 90 K crystallographic data. | 106 |
| **Table 3.3** | Interatomic bond lengths (Å), angles (°), and RMSD values for the β form of 5-(4-pyridyl)tetrazole (β-4PT). See **Figure 3.3** for atomic labels. Experimental parameters are from 90K crystallographic data. | 107 |
| **Table 3.4** | Calculated formation energies per molecule for the α (α-4PT) and β (β-4PT) forms of 5-(4-pyridyl)tetrazole, based on the geometrically optimized structures, corrected for BSSE. The values of the formation energy are derived from eq. 3.1 | 110 |
| **Table 3.5** | Frequency positions ($cm^{-1}$) and percent error for the experimental and theoretical terahertz spectra of the α form of 5-(4-pyridyl)tetrazole (α-4PT). The blanks are peaks that have no obvious correlation between the observed and theoretical spectra. Mode descriptions are described in **Table 3.7**. | 116 |

**Table 3.6** Frequency positions ($cm^{-1}$) and percent error for the experimental and theoretical terahertz spectra of the β form of 5-(4-pyridyl)tetrazole (β-4PT). The blanks are peaks that have no obvious correlation between the observed and theoretical spectra. When multiple peaks corresponded to only one peak in the experimental spectra, the weighted average was used in calculating the percent error. Mode descriptions are described in **Table 3.7**. 117

**Table 3.7** Empirical normal mode analysis of the α and β forms of 5-(4-pyridyl)tetrazole. 118

**Table 4.1** Interatomic bond lengths (Å), angles (°), and RMSD values for 4PT·HCl. See **Figure 4.3** for atomic labels. Experimental parameters are from 90 K crystallographic data. 136

**Table 4.2** Interatomic bond lengths (Å), angles (°), and RMSD values for 4PT·HBr. See **Figure 4.3** for atomic labels. Experimental parameters are from 90 K crystallographic data. 137

**Table 4.3** Frequency positions ($cm^{-1}$) and RMSD for the experimental and theoretical terahertz spectra of 4PT·HCl. The blanks are peaks that have no obvious correlation between the room temperature and cryogenic experimental spectra. When multiple peaks corresponded to only one peak in the experimental spectra, the weighted average was used in calculating the RMSD. Mode descriptions are described in **Table 4.5**. 143

**Table 4.4** Frequency positions ($cm^{-1}$) and RMSD for the experimental and theoretical terahertz spectra of 4PT·HBr. When multiple peaks corresponded to only one peak in the experimental spectra, the weighted average was used in calculating the RMSD. Mode descriptions are described in **Table 4.5**. 144

**Table 4.5** Empirical normal mode analysis of the halide salts of 5-(4-pyridyl)tetrazole. 145

**Table 5.1** Interatomic bond lengths (Å), angles (°), and RMSD values for Mn-4PT. See **Figure 5.3** for atomic labels. Experimental parameters are from Ref. [6]. 163

**Table 5.2** Interatomic bond lengths (Å), angles (°), and RMSD values for Co-4PT. See **Figure 5.3** for atomic labels. Experimental parameters are from 90K crystallographic data. 164

**Table 5.3** Interatomic bond lengths (Å), angles (°), and RMSD values for Cd-4PT. See **Figure 5.3** for atomic labels. Experimental parameters are from Ref. [6]. 165

**Table 5.4** Frequency positions ($cm^{-1}$) and RMSD for the experimental and theoretical terahertz spectra of the metal 5-(4-pyridyl)tetrazolato complexes. The blanks are peaks that have no obvious correlation between experiment and theory. Visual inspection was used to correlate experimental and theoretical vibrational modes. Mode descriptions are described in **Table 5.5**. 171

**Table 5.5** Empirical normal mode analysis of the metal 5-(4-pyridyl)tetrazolato complexes. 172

**Table 6.1** Summary of crystallographic data for α,α,α′,α′-tetrabromo-*p*-xylene. 189

**Table 6.2** Interatomic bond lengths (Å), angles (°), and RMSD values for α,α,α′,α′-tetrabromo-*p*-xylene. See **Figure 6.3** for atomic labels. Experimental parameters are from 90 K crystallographic data 191

**Table 6.3** Frequency positions ($cm^{-1}$) and RMSDs for the experimental and theoretical terahertz spectra of α,α,α′,α′-tetrabromo-*p*-xylene. The blanks are peaks that have no obvious correlation between the room temperature and cryogenic experimental spectra. When multiple peaks corresponded to only one peak in the experimental spectra, the weighted average was used in calculating the RMSD. Mode descriptions are described in **Table 6.4**. 195

**Table 6.4** Empirical normal mode analysis of the halide salts of α,α,α′,α′-tetrabromo-*p*-xylene 196

# Chapter 1

# Introduction

## 1.1 Introduction

Of the three major states of matter, only one phase has the ability to have drastic permanent changes based solely on the orientation of the molecules. Molecules in the liquid and gas phases have many degrees of freedom including translational, rotational, and vibrational motions. In contrast, the molecules in the solid phase are held relatively rigid to one another. This rigidity restricts the ability of the molecules to move and rotate freely in respect to neighboring molecules; therefore, the molecules can only possess vibrational freedom. This lack of translational and rotational freedom means that a substance can crystallize into different crystalline states, which has been termed polymorphism.

The term 'polymorphism' is derived from the Greek word 'polus' meaning many and 'morph' meaning shape.[1] In the context of chemical and material sciences, polymorphism is broadly defined as the ability for a material to crystallize in different arrangements. Essentially, the molecule can exist as two or more crystalline phase that contains different arrangements or conformations. According to John Halebaian and Walter McCrone, the safest criterion for the classification of a system as being polymorphic is that the two polymorphs are different in the crystal structure but the same in the liquid or vapor states.[2]

Known since the beginning of modern chemistry, polymorphism is a not a new concept and is often credited to Mitschelich[3] for using the term in his work on the isomorphous sulfates of iron, cobalt, nickel, magnesium, copper, zinc, and manganese. However, the concept was not a new idea at the time since Humphry Davy commented that diamond and graphite only differ in their arrangement of carbon atoms in the solid phase in 1809.[2] Looking even farther back the concept might have been first realized in 1788 when German chemist Martin Heinrich Klaproth observed that calcium carbonate crystallizes both as calcite and as aragonite.[2]

Polymorphism is an ever-present phenomenon, occurring in every area of chemistry, ranging from organic to inorganic to biological and everywhere in-between.[4] Polymorphism is not only limited to chemistry alone, even the materials in living organisms crystallize in specific polymorphic forms under selective control as observed in biological mineralization.[5,6] The often quoted statement by McCrone states that 'virtually all compounds are polymorphic and the number of polymorphs of a material depends on the amount of time and money spent researching the compound'.[7,8] This statement seems to hold true based on the ~500,000 hits on the term 'polymorphism' through SciFinder®.[9]

The importance of polymorphs stems not only from curiosity but also from the different properties that the same compound can exhibit based only on its solid-state arrangement. These differences can be found in its thermodynamic proprieties (solubility, free energy, melting point, etc.), spectroscopic properties, kinetic properties (dissolution rate, stability), or mechanical properties (hardness, compatibility, tableting, tensile strength, etc.).[1] These differing properties are of great concern for many industries particularly in pharmaceuticals;[2,10,11] however, polymorphism has consequences in the quality and manufacturing of many industrial products.[12]

In some cases the use of the wrong polymorph can have devastating effects; a prime example is found in the explosives industry where sensitivity of detonation can be polymorph dependent.[13,14] Pigment color and solubility are polymorphic dependent[15-18] as are photographic and photolithographic sensitizers.[19,20] The performance of industrial products based on natural fats and waxes[21,22] and their derived soaps,[23] and many petroleum products[24,25] can vary in usefulness based on their polymeric forms. The effects of polymorphism even extends into the processing, acceptability and deterioration of foods and confections containing fats,[26] sugars,[27-29] polysaccharides[30-32] and other components.[33,34]

Many factors can contribute to the formation of polymorphs. Generally at a given temperature and pressure only one form of a substance is thermodynamically stable and all others are metastable.[35] However, if the conversion of one or more of the metastable forms were slow, then it would be reasonable to encounter these polymorphs under normal conditions. If these conditions were then adjusted the once metastable form could become the dominate form. The generation of polymorphs is not trivial, because the free energy difference[36] is generally around a few kJ $mol^{-1}$ and the process of crystallization is affected by many physical parameters. These parameters include the nature of the solvent, cooling and stirring rates, temperature, pressure and the presence of impurities.[35]

## 1.2 Chemical/Structural Diversity

Chemical and structural diversity in the same molecule can be the result of a variety of factors. Three of these approaches are going to be highlighted in this investigation, due to their occurrence in this work. The first to be discussed are conformational differences, which are the result of different molecular configurations of the same compound. The second difference is based on composition, while this is not true polymorphism, they could be considered pseudo-polymorphs because these structures are isomorphous, but have different compositions.[12] Lastly, differences based purely on packing will be discussed. In these examples, the molecular units are identical; however, their packing in three-dimensional space is different.

### *1.2.1 Conformational Based Polymorphism*

In the field of polymorphism, differences in definition and distinction are quite common. At one time polymorphism was only regarded as a different arrangement of rigid molecules in the solid state.[37] However, this narrow definition disregards differences in the arrangements of

molecules that exist in different forms, such as isomeric, tautomeric, zwitterionic, and chiral structures, as well as conformers.[12] Differences based on these changes in conformation are quite common in systems containing flexible components due to their internal degrees of freedom, and are seen in all types of systems ranging from organic to inorganic and even biological systems. This becomes obvious when taking into consideration the drive for energy minimization, because any changes in packing will cause geometrical change and conversely any change in geometry will invite different molecular packing.[38] As illustrated in **Figure 1.1**[39] conformationally flexible molecules have a large number of packing arrangements based merely on conformation. Conformational polymorphism in biological systems will not be discussed in detail. However, there are many descriptions in the literature pertaining to the polymorphism exhibited by proteins,[40] steroids,[41-43] barbiturates,[44,45] and antihistamines.[46]

Conformational polymorphism is very common in organic systems and more increasingly observed in organometallic systems. This is due to the flexible torsions and low-energy conformers common to organic compounds via rotations about single bonds[39] or the delocalized metal-ligand bonding and variable oxidations states in organometallic systems.[47] More specifically, in the case of organometallic molecules, deformation pathway affects the molecular structure thereby changing the crystal structure, as well as producing different conformations based on different structural isomers. Ferrocene is a classic example conformational polymorphism of organometallic molecules in which one disordered room temperature and two ordered low-temperatures crystalline forms are known.[48] The crystalline forms differ only in the relative orientation of the cyclopentadienyl rings so that the phase transition mechanism requires only low-energy reorientation of the rings and a limited motion of the molecules in the crystal structure.

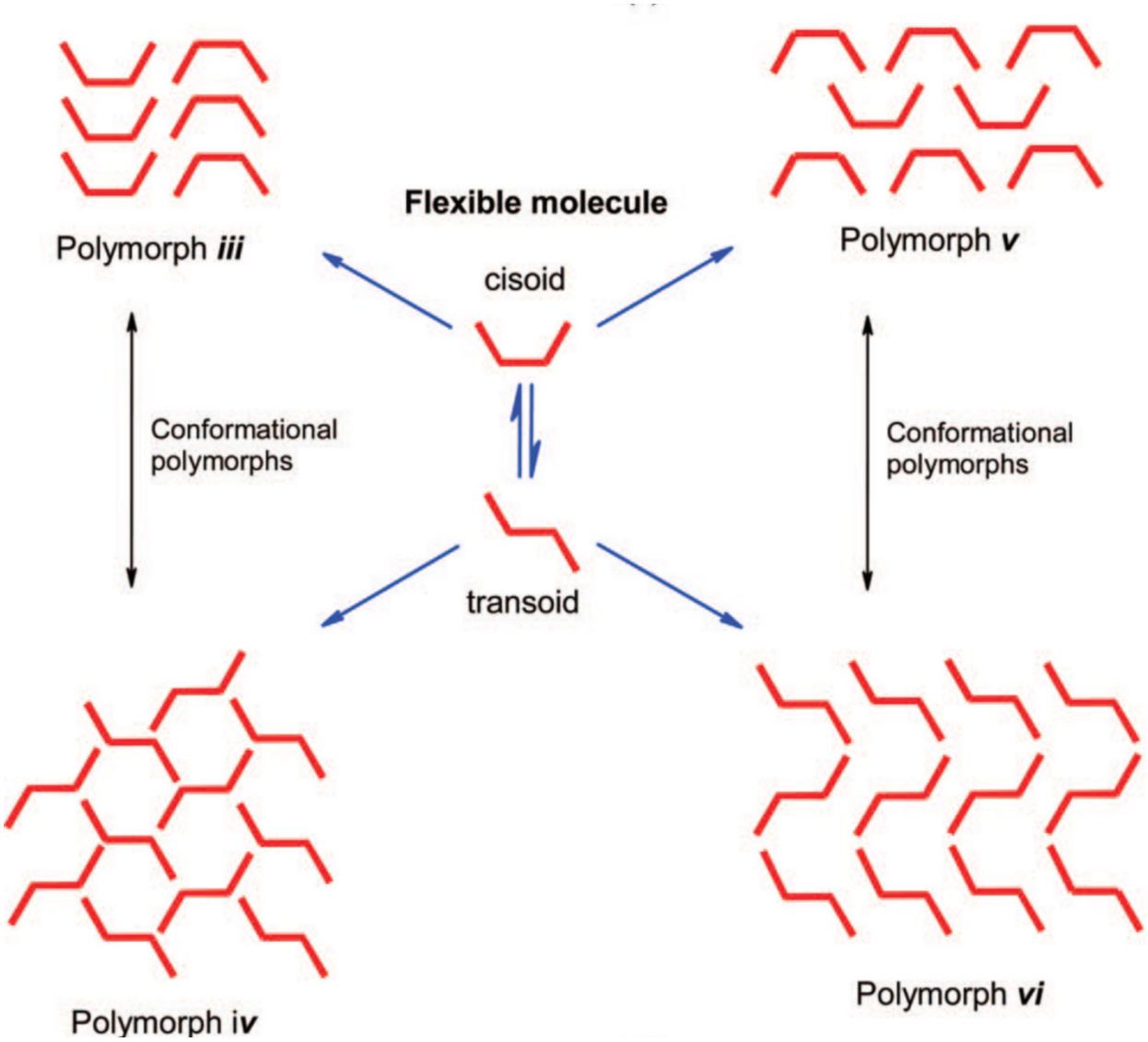


**Figure 1.1** Schematic representation of possible packing arrangements, iii-vi, for a conformationally flexible molecule. Figure was modified from ref. 39.

Classically only organic materials were thought to exhibit conformational polymorphism due to their ability to offer more complex arrangements due to the possibilities of having isomeric, tautomeric, zwitterionic, and chiral structures. In typical cases, a crystal form with a favorable conformation finds an alternative polymorph when a slightly disfavored conformation is compensated by better intramolecular interactions with neighboring molecules. Some examples of organic molecules capable of conformational polymorphism are shown in **Figure 1.2**.[39] The extent of polymorphism depends on the rigidity of the molecules. Although some floppy ring systems maintain their shape in different forms[49,50] even nominally rigid structures such as the ring systems of steroids[51] can show substantially different conformations in different polymorphs.

Another form of conformational polymorphism is the result of some compounds being able to exist in either a tautomeric or zwitterionic form. This type of polymorphism is generally allowed if you consider the simplest definition/classification of a polymorph. The two polymorphs will be different in the solid state, but identical in the liquid and vapor states.[2] Frequently in tautomerism, the two crystalline forms will differ; however they will produce identical solutions.[52,53] Tautomeric polymorphism is surprisingly rare, considering the wide spread occurrence of tautomerism in solution.[54] A well-investigated example is that of 2-amino-3- hydroxy-6-phenylazopyridine[55] as shown in **Figure 1.3**, which crystalizes as a red low temperature form (a) as well as a blue high temperature form (b).

The last type of conformational polymorphism is due to chirality. Using the same definition that supported the inclusion of tautomeric systems as polymorphs; racemates and conglomerates of rapidly interconverting chiral systems should be included as polymorphs.[56] In these systems, the conformation change is a result of a change in reflection of an asymmetrical

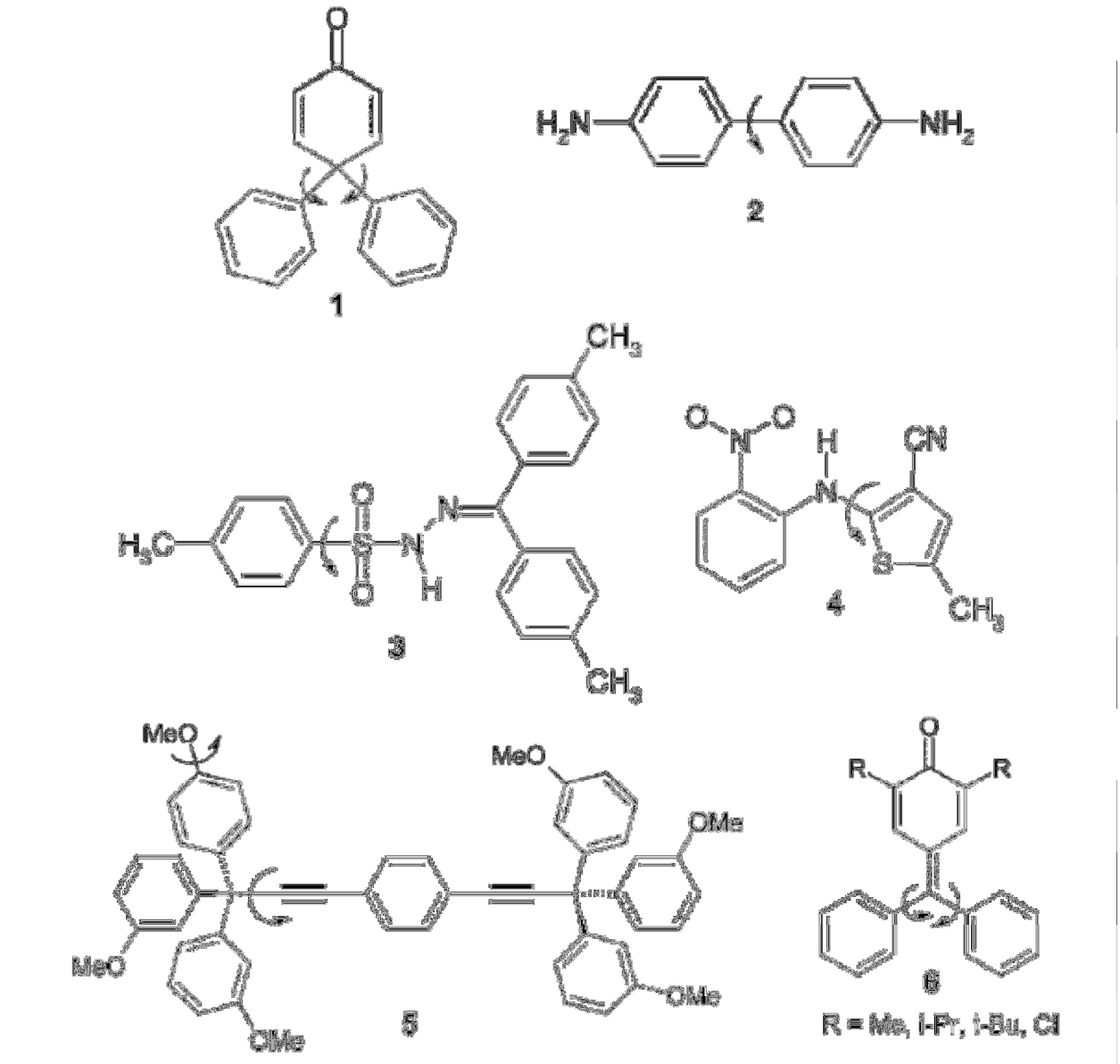


**Figure 1.2** Examples of conformationally flexible molecules that exhibit conformational polymorphism, with the main bond torsions are indicated with arrows. Figure was modified from ref.39.

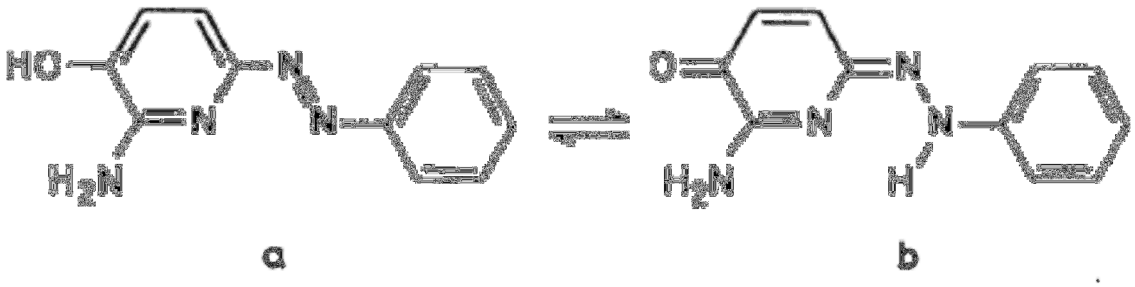


**Figure 1.3** Tautomeric polymorphic forms of 2-amino-3- hydroxy-6-phenylazopyridine
Figure was modified from ref.55.

structure across a mirror plane. Examples of this type of polymorphism where rapidly interchanging enantiomers in solution are capable of independent crystal structures are known[57,58] but uncommon.

### *1.2.2 Compositional Based Polymorphism*

Polymorphism based on composition would not be truly considered polymorphic because the compositions are different. However, their extreme similarity in structure, mostly independent on the identity of parts of their structure, could classify them as "pseudo-polymorphic". The term "pseudo-polymorphic" is becoming increasingly more common,[10,59,60] particularly due to its frequent use in the pharmaceutical industry. It is usually used in the description of hydrates or solvates compared to an anhydrous form, which cannot be considered truly polymorphic by any of the definitions of polymorphism. In this investigation, the term "pseudo-polymorphic" is being expanded to include not only hydrates or solvates, but also in the description of salts,[4] where there is no large deviation in structure. In addition, transition metal complexes, where the transition metal is different but once again, there are no large deviations in structure are also being included under this definition.

The study of the pseudo-polymorphism of solvates is a complex topic, partly due to the fact that solvates can also exhibit polymorphism.[59,61,62] This aspect of solvate pseudo-polymorphism will not be focused on in this work; instead the focus will be on the effects caused by the identity of the solvent and the number of solvent molecules present. Most solvates are prepared by crystallization of the compound in the respective solvent of solvation. In addition, multiple solvents could be used during crystallization and one or more could be incorporated into the final crystal. For example, in the crystallization process of a salt, the solvent, water, has a strong effect on how the salt crystallizes. The water weakens the attractive forces of the salt and

causes the ions to separate, and once the ions are free they gather water around them. When these hydrated ions reach a nucleation site, they crystallize into a salt hydrate, bringing some or all of the attached water into the solid composition.[63] However, the hydrated ions can combine in several ways to form different solids even when the number of water molecules is definite. The consequence is that solvates of a compound containing a different number of moles of solvent can be prepared by changing the crystallization conditions by holding the temperature constant or by maintaining the pressure constant.[10] An example of this is seen in the concentration-pressure curve at 50°C for the cupric sulfate-water system shown in **Figure 1.4**.[64]

Another aspect of the pseudo-polymorphic solvates is the identity of the solvent and the effect it has on the complex. This is apparent in the pharmaceutical industry where much attention is given to the identity of the solvent in crystalline active compounds. An example of this is can be seen in the dissolution of anhydrous, hydrated, and pentanol-solvated forms of succinylsulfathiazole as illustrated in **Figure 1.5**.[62] The dissolution of succinylsulfathiazole is dependent on the pseudo-polymorphic form. In this example, the hydrated form is ~4 times less soluble when compared to the anhydrous form, and inversely the pentanol solvate is approximately twice as soluble as the anhydrous and ~8 times as soluble as the hydrate. This shows the importance of solvent in the crystallization of various materials. In particular, the size and shape of the solvent affects how the parent molecules pack and adjusts the intramolecular interactions between them.

The pseudo-polymorphism of salts could be considered analogous to the pseudo-polymorphism of solvates. The study of the pseudo-polymorphism of salts expands into inorganic chemistry[65] where the salt component acts as charge compensating anion or cation. However, the study of pseudo-polymorphic salts is focused primarily in the pharmaceutical

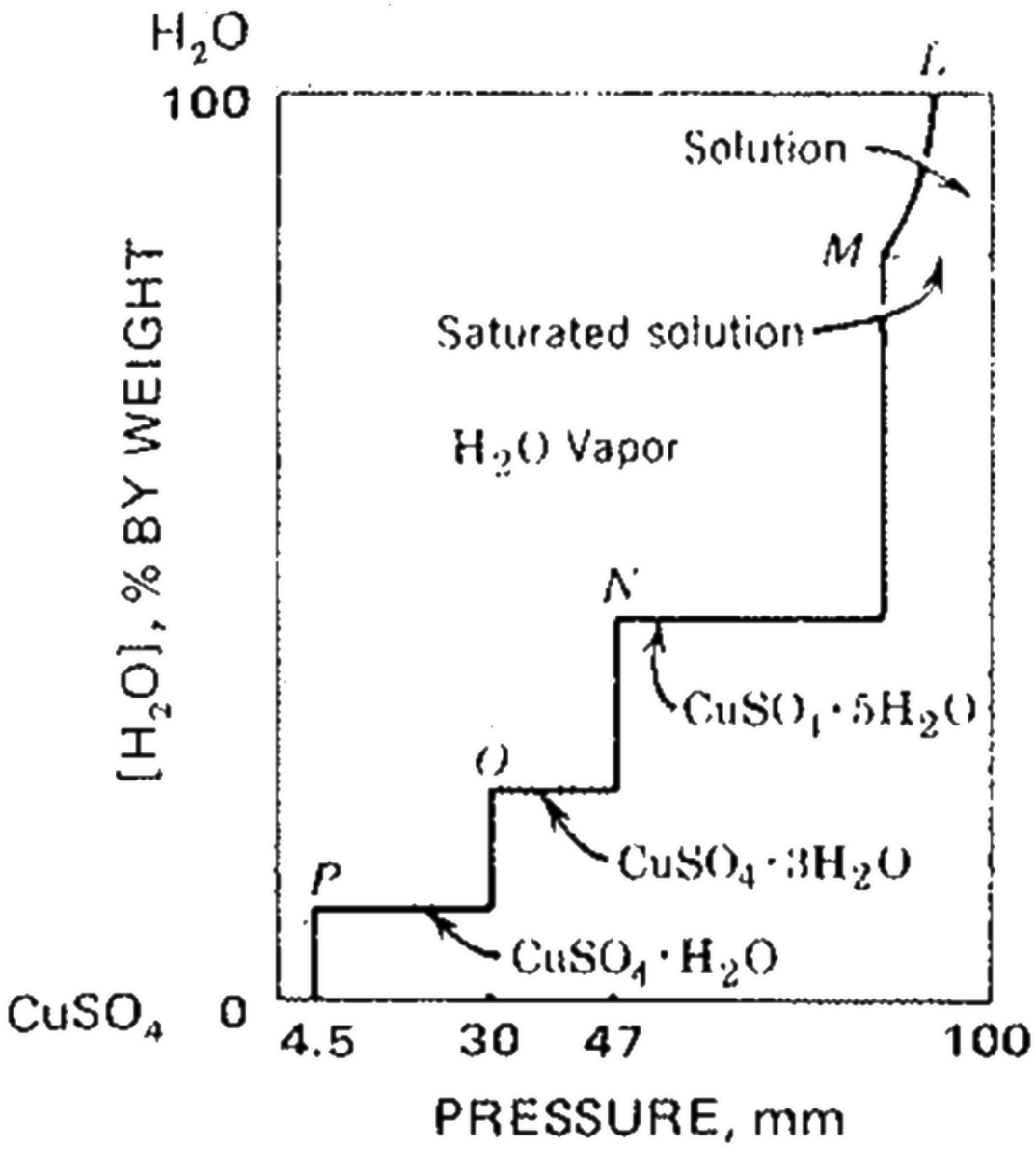


**Figure 1.4** Concentration-pressure curve at 50°C for the cupric sulfate-water system. Figure was modified from ref.64.

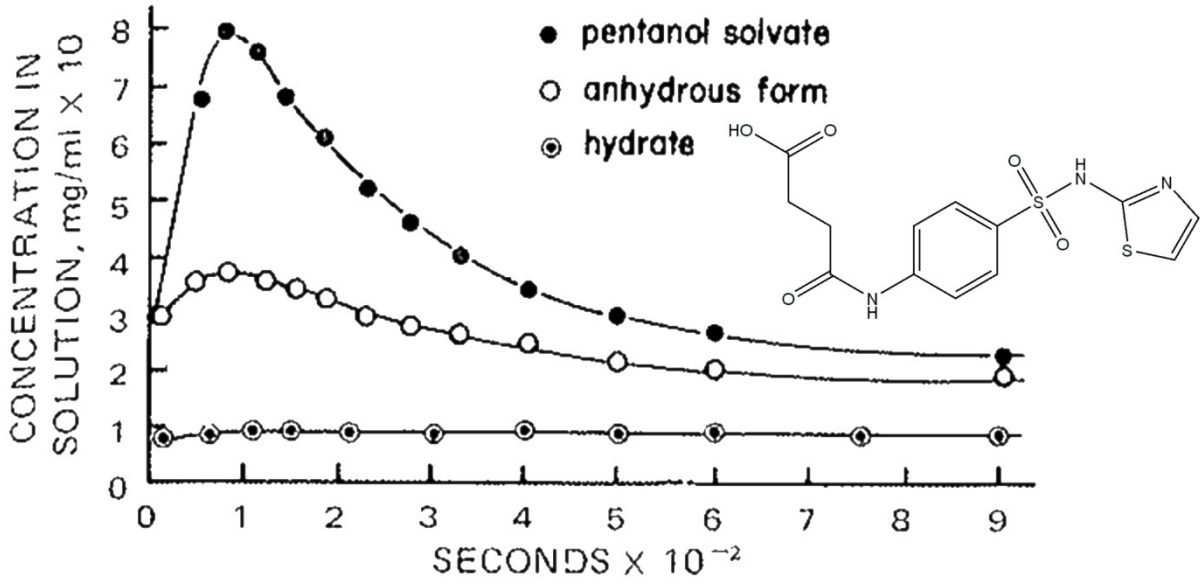


**Figure 1.5** Dissolution behavior of different forms of succinylsulfathiazole in ~0.001 N sulfuric acid solution at 20°C. The inset image is of succinylsulfathiazole. Figure was modified from ref.62.

industry, where the properties of the salts of the same compound can greatly vary. This is due to the fact that the salts of acidic and basic drugs have generally higher solubilities than their corresponding acid or base forms.[66] In addition, crystalline salts can offer useful attributes such as improved chemical stability, and higher bioavailability relative to those of the free base or acid.[67] One molecule that has had a lot of attention because of its polymorphism due to salt formation is sertaline HCl known commercially as Zoloft®. Zoloft® has a reported 28 phases ranging from polymorphs, solvates, hydrates and amorphous phases.[67,68] By adjusting the acidic salt component, the solubilities and melting points vary greatly. In one reported case sertaline HBr was crystallized and no obvious differences were observed in the packing of the two salts. However, the bromide ion caused the drug to produce sedation and dermatological problems and the doses had to be limited for toxicity reasons.[67] Therefore minor differences in the salt, producing pseudo-polymorphs, that have no effect on the geometry of the compound can have drastic differences in properties.

The last type of pseudo-polymorphism to be introduced relates to transition metal complexes. In transition metal complexes, it is easy to induce pseudo-polymorphism by replacing the transition metal in the system with another transition metal without changing the overall structure of the complex.[69] The result of these modifications can have drastic differences on their properties[70] ranging from simple changes in thermal stability[71] to changing toxicity in radiopharmaceuticals,[72] or could result in different magnetic properties.[73]

### *1.2.3 Packing Based Polymorphism*

Polymorphism based exclusively on the packing of molecules in the crystalline state is one of the oldest and most common forms of polymorphism. In this variety of polymorphism, the molecular constituents have no differences in conformation or composition, just the arrangement

in space of one molecule to another. This type of polymorphism is most commonly seen in the elements, minerals, and some simple species.

The polymorphism exhibited by elements is commonly called 'allotropism'. Most elements have this type of polymorphism.[74] However, the most commonly discussed elements that exhibit well studied allotropism are carbon,[75,76] sulfur,[77,78] boron,[79-84] and phosphorus.[85,86] These variations in packing cause the properties of each form to vary largely from one to another. The classical example of this phenomenon is seen in the polymorphs of carbon. There are five major solid forms of carbon, illustrated in **Figure 1.6**,[87] two of these allotropes have been known since ancient times, diamond and graphite; however, graphene,[88,89] fullerenes[90-92] and nanotubes[93] have been much more recently discovered.

The five major forms of carbon each vary drastically in their properties. Comparing the two most common crystalline forms of carbon, diamond and graphite, diamond is an electoral insulator, is the hardest known natural substance, has the highest known thermal conductivity and is highly durable. On the other hand, graphite is a good conductor, slippery and is not very durable.[94] Both are composed of the same element, but the physical properties are on opposite sides of the "mechanical spectrum", due only to their packing. The tetrahedral packing of carbon in diamond results in a rigid, covalent three-dimensional framework lending incredible strength, in comparison to the stacked planer sheets in graphite, consisting of only weaker van der Waal interactions. This stacking of sheets results allows the graphite to separate readily from neighboring layers, stimulating its slipperiness.

Polymorphism in minerals is another example of a long understood concept in chemistry. As previously mentioned this concept could date back to 1788 when German chemist Martin Heinrich Klaproth observed that calcium carbonate ($CaCO_3$) crystallizes both as calcite and as

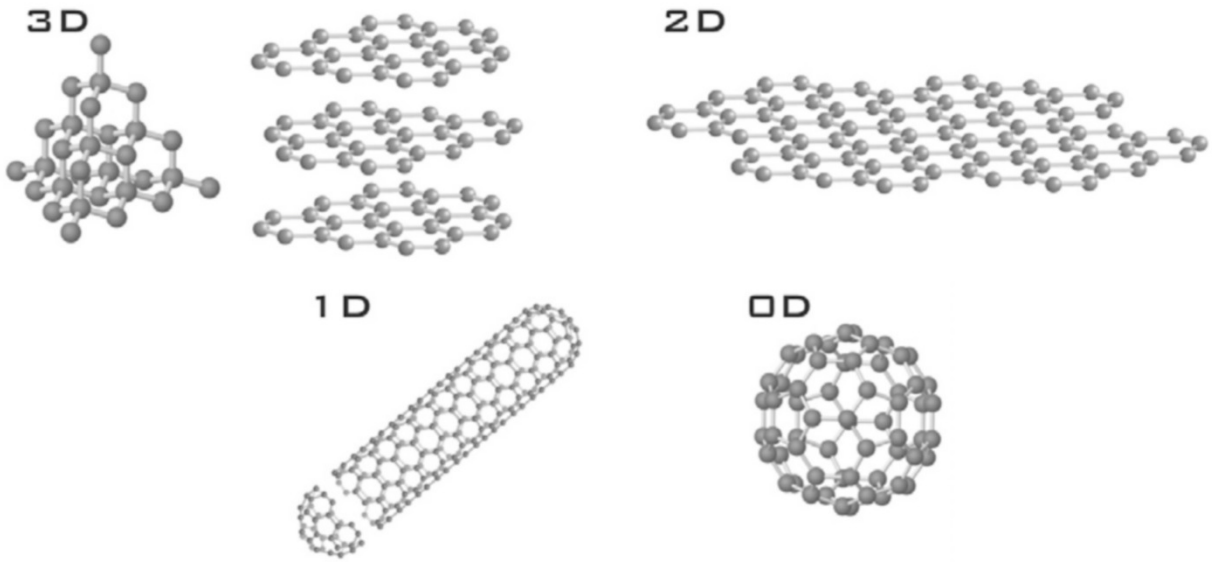


**Figure 1.6** Crystal structures of the different allotropes of carbon. (Left to right) Three-dimensional diamond and graphite (3D); two-dimensional graphene (2D); one-dimensional nanotubes (1D); and zero-dimensional buckyballs (0D).Figure was modified from ref.87.

aragonite.[2] The possible reason that this phenomenon was observed prior to the invention of most modern analytical techniques was that these polymorphs resulted in a change of space group resulting in changes in the physical structure of the crystals. Calcite crystalizes in a rhombohedral space group while aragonite crystalizes in an orthorhombic space group. Other examples of mineral polymorphism can be seen in zinc sulfide (ZnS) which crystallizes as either wurtzite (hexagonal) or sphalerite (cubic), or Titanium oxide ($TiO_2$) which crystalizes as rutile (tetragonal), brookite (orthorhombic) and anatase (tetragonal).[2,95]

The last classical example of polymorphism as a consequence of molecular packing is related to the third most common molecule in the universe, water. The solid from of water, ice, is heavily studied due to the over fifteen polymorphic forms due to differences in the packing of the water molecules. These polymorphic forms are dependent on the temperature and pressure that the ice is crystallized under, illustrated in **Figure 1.7**.[96]

The arrangement of the water molecules in each polymorph is determined by the hydrogen bonding between adjacent water molecules. The exact bonding rules state that one and only one hydrogen atom is found along each of the hydrogen bonds and that always two hydrogen atoms are covalently bonded to each of the oxygen atoms, which preserves the stoichiometry of the $H_2O$ molecules.[97] These bonding rules create "tetrahedra" comprised of the points representing hydrogens or hydrogen bonds where the central atom is the oxygen. The different packing of these tetrahedra in three-dimensional space creates the different polymorphs, as illustrated in **Figure 1.8**.[96]

## 1.3 Techniques for Determining Polymorphic Forms

Since the generation of polymorphs can be accomplished via subtle variations in synthesis and their properties can vary wildly, the identification of polymorphs has emerged as a

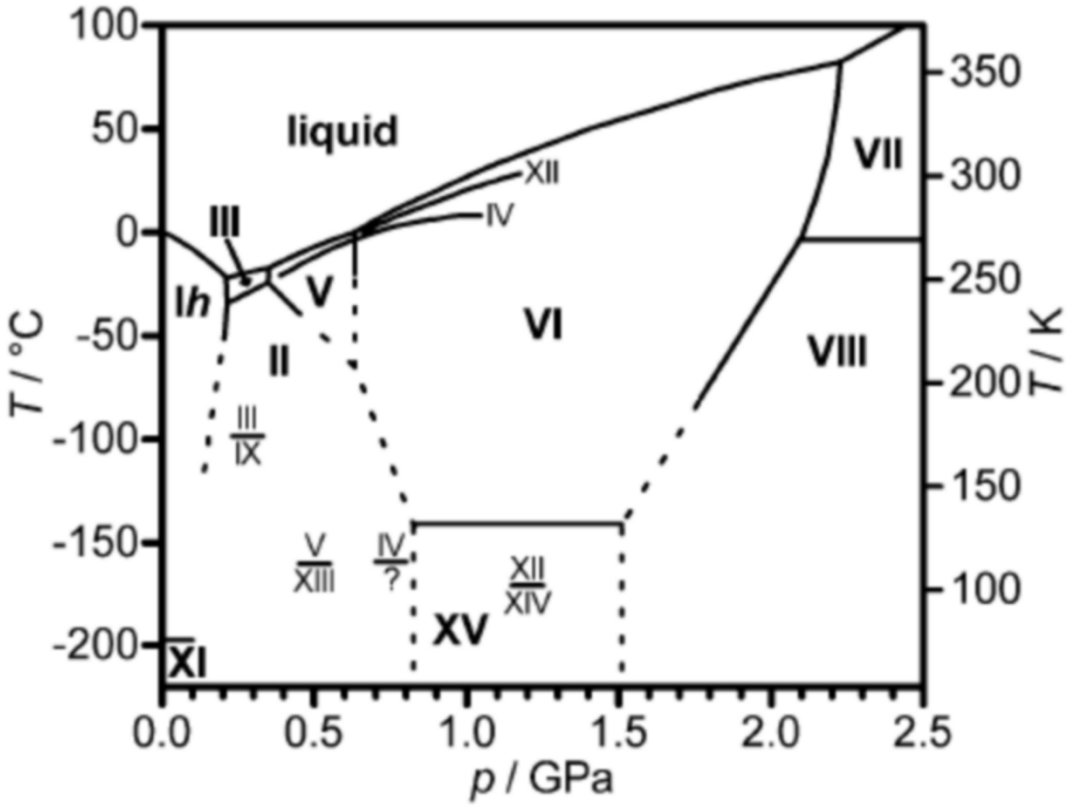


**Figure 1.7** The phase diagram of water and ice including the melting lines of metastable ices IV and XII, and extrapolated phase boundaries at low temperatures (dashed lines). Figure was modified from ref.96.

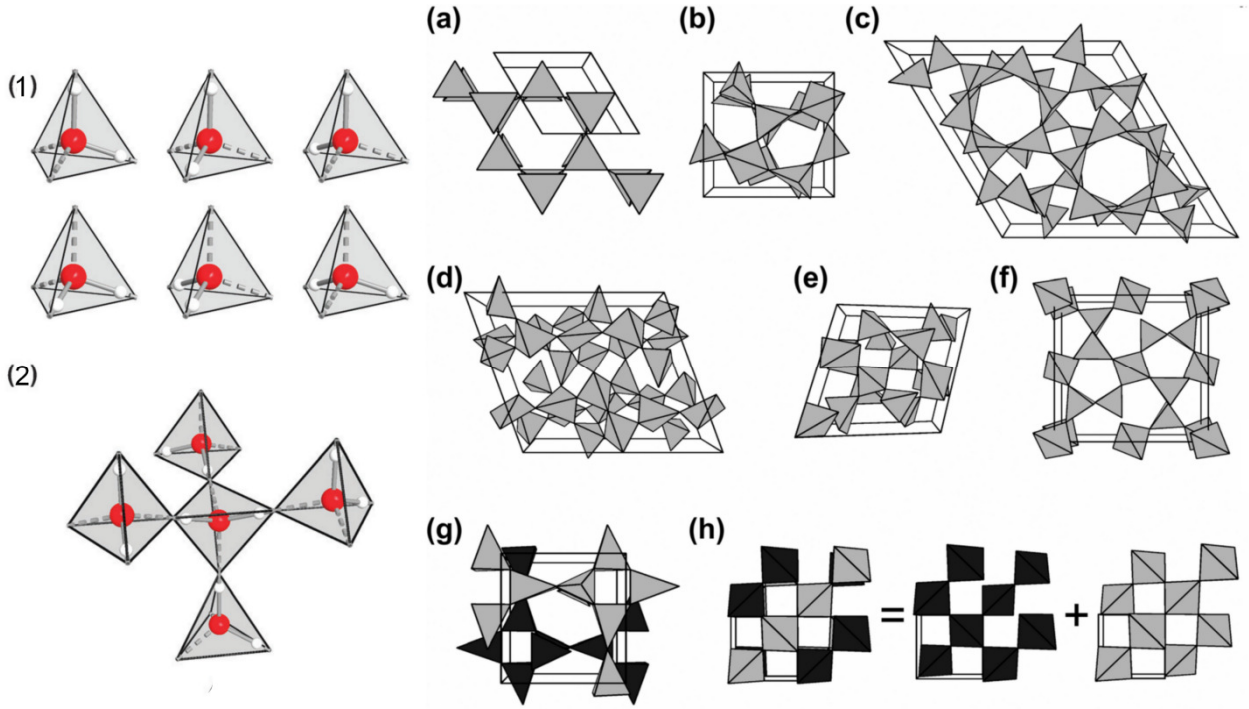


**Figure 1.8** (1) Six possible orientations of water in Ice. (2) A pentameric fragment of an ice Ih structure. Network topologies of ice Ih (a), ice III (b), ice II (c), ice V (d), ice IV (e), ice XII (f), ice VI (g) and ice VII (h). Figure was modified from ref.96.

crucial field. This is especially true in the pharmaceutical industry, where the study of polymorphism during development has become blindingly apparent. In an effort to extend the patent life of major products, the discovery of desirable polymorphs is explored in order to obtain subsidiary patents.[12]

The analytical techniques for investigating polymorphism can vary wildly depending on the properties of interest. One of the earliest and still used methods of polymorph characterization was accomplished by the use of microscopy, either by optical crystallography[98] or hot-stage microscopy[99] which tracks changes in the refractive indices and polarizability. Another major technique in use for the characterization of polymorphs include thermal techniques such as thermogravimetric analysis (TGA), differential thermal analysis (DTA), and differential scanning calorimetry (DSC). These techniques can be used to describe thermal events associated with polymorphs under controlled heating.[100,101] A more direct technique for the investigation of polymorphs can be accomplished using X-ray crystallography either as a single crystal[102-104] or as a powder.[105-107]

Single crystal X-Ray diffraction gives direct structural information about the polymorph, which allows direct investigation of molecular packing. However if single crystals cannot be obtained, the use of powder X-ray diffraction, which can give characteristic diffraction patterns unique to each polymorph can be obtained. Interestingly, new polymorphs could be obtained using either of these techniques. For example, due to the frequent use of cryogenic temperatures in single crystal X-Ray diffraction, low temperature polymorphs could be obtained or the grinding of powder samples for powder X-ray diffraction could lead to pressure induced polymorphic changes.[35]

Another technique that has found widespread use is solid-state NMR. This technique is useful for the characterization of organic compounds. However, it should not be used on its own but as a complementary technique. In addition, the small chemical shifts differences between polymorphs can be obscured by the large line widths of magic-angle spinning necessary for solid-state NMR.[4] The last technique of importance to the characterization and identification of polymorphs is the use of spectroscopy.

Traditional spectroscopic techniques have been used in the characterization of polymorphs including infrared vibrational spectroscopy[108-112] and Raman spectroscopy.[113-115] There is however a major disadvantage in the use of these techniques, in that the spectra tend to appear virtually identical[51,116] or be due to an artifact of interconversion.[112] In addition, the very low frequencies where the greatest difference between polymorphs might be expected are inaccessible using commercial instruments. One spectroscopic technique that overcomes this obstacle is terahertz (THz) spectroscopy. THz spectroscopy measures the lattice vibrations unique to molecular solids in the terahertz (THz), or far-infrared, region of the electromagnetic spectrum typically considered to range from 0.1 THz to 10 THz (3 – 333 $cm^{-1}$).

## 1.4 Terahertz (THz) Spectroscopy

### *1.4.1 Terahertz (THz) Spectroscopy*

The terahertz (THz), or far-infrared, region of the electrometric spectrum is typically considered to encompass the range from 0.1to 10 THZ (3-333 $cm^{-1}$), situated between the infrared and microwave regions,[117] illustrated in **Figure 1.9**.[118]

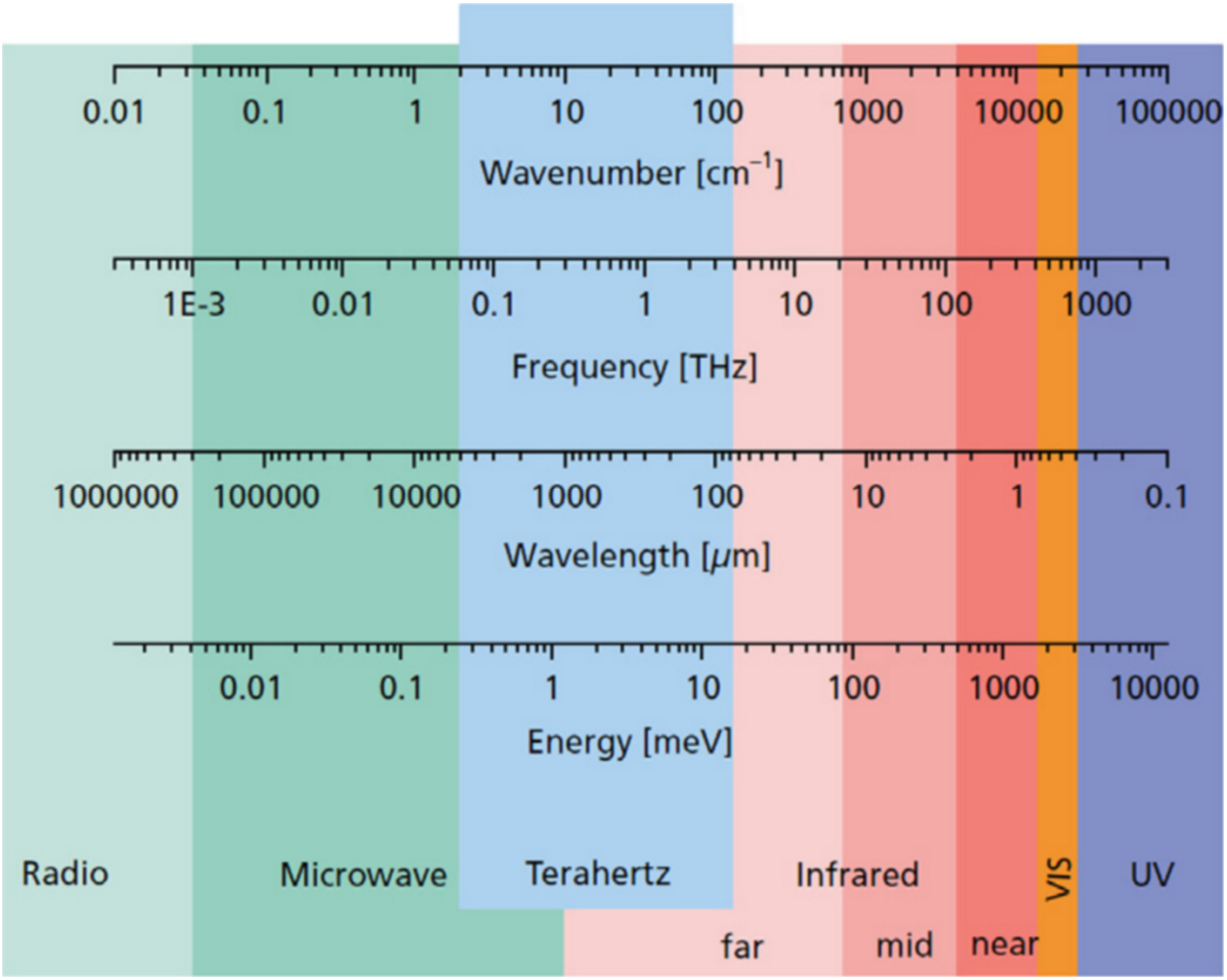


**Figure 1.9** The electromagnetic spectrum with the terahertz region shaded in blue. Figure was modified from ref.118.

The terahertz (THz) region has proven to be one of the most elusive, because THz radiation is resistant to the techniques commonly employed in creating and investigating the well-established neighboring regions of electromagnetic spectrum. THz spectroscopy was born due to efforts to generate and detect ultra-short electrical transient as they propagated down a transmission line.[119] As understood from Maxwell's equations, a time-varying electrical current would radiate an electromagnetic (EM) pulse, and it was subsequently realized that these transmission lines were generating short EM pulses. In 1988/1989, reports[120,121] were published that described these EM pulses propagating through space from a generator to a detector, which lead to envisioning their use as a far-IR light source and detector pair. This discovery was a large improvement over the far-IR light sources used in the 1960s,[122] which typically utilized arc lamp sources and bolometric detection. With these light sources, the power falls off sharply at long wavelengths and can have interference from blackbody radiation from the surrounding laboratory.[119]

Low-energy interactions caused by this region are exhibited by a large number of materials. Therefore collecting data in this region would be of great use in complementing the knowledge of material behavior obtained with far infrared (FIR) and Raman spectroscopy.[118] In particular, one of the most attractive properties of THz waves is their ability to penetrate a wide variety of materials, so they can be used to analyze content through many types of packaging materials, including paper, plastics, leather and wood.[117,123] More importantly, THz waves are non-destructive, so this allows their use in quality-control applications for industry,[124-126] (an example is shown in **Figure 1.10**)[127] and probing biological materials for identification,[128] medical diagnostics,[129] and security.[130-132] THz spectroscopy has been proven to be an effective means for measuring many important physical and chemical phenomena, such as lattice

**Figure 1.10** Two THz images of a chocolate bar. The upper image shows the variation in amplitude of the transmitted waveform allowing the embossed lettering to be visible, whereas the almonds are clearly visible due to their stronger absorption. The lower image shows the variation in transit time of the THz pulse. Here, the almonds are almost invisible, but the variation in the thickness of the sample is quite clear, allowing the embossed lettering to be easily discerned. Figure was modified from ref.127.

vibrations in crystalline materials,[133,134] relaxation dynamics of liquids and biomolecules,[135-138] and semiconductor carrier dynamics.[119,126,139]

A major field in THz spectroscopy is the investigation of the generation and detection of THz radiation for the use in THz spectroscopic systems. This subject will not be covered, due to it being outside the scope of this work. Information on this topic can be found in many review articles including the cited works in the following references: 117, 118, 119, and 127.

### *1.4.2 Applications of Terahertz Spectroscopy*

The number of applications for THz spectroscopy are growing and becoming more divergent since its initial use in the late 1980s. There are primarily two subsets that these applications fall under, either the characterization of materials or imaging.

#### *1.4.2.1 Characterization of Materials*

A large amount of work has gone into the characterization of materials in the gas, liquid, and solid phase, as well as in biomaterials and biological systems. The first demonstration of THz spectroscopy was reported in 1989 and consisted of the absorption spectrum of water vapor.[140] Other examples of gas-phase THz spectroscopy include its use to probe the tunneling-inversion in methyl halides[141] and the rotational transitions of water in flames[142,143] which would normally be impossible with standard analytical techniques. As the last example showed, the main purpose of gas-phase analysis is to probe the molecular rotational transitions in the vibrational ground state that creates the observed absorption profile. This technique is extremely sensitive; orders of magnitude more sensitive than microwave spectroscopy and has a better resolution than IR spectroscopy because of lower Doppler effects. This sensitivity was demonstrated to a detection limit as low as one part-per-trillion during the analysis of the

combustion products of cigarettes[144] and this sensitivity drew interest from a security standpoint for the identification of volatile explosive materials.[145] The drawback of this type of THz spectroscopy is that ambient water vapor absorbs THz radiation, thus increasing the signal-to-noise ratio, resulting in most research to be conducted on the condensed phase.

The research done on liquids is primarily focused on water and aqueous solutions due to biological applications. In liquids, the absorptions that would occur in the THz region are mainly dependent on the interaction and relaxation of dipoles inside the liquid, from polar liquids or induced dipoles in non-polar liquids.[146] These interactions result in vibrations that are characteristic of the collective intermolecular motions inside the liquid, allowing the probing of properties ranging from solvent reorientation dynamics[147,148] to electron solvation.[149]

Solid-state materials are also highly studied using THz spectroscopy, ranging from molecular crystals to semiconductors. THz spectroscopy is commonly used to study electronic processes and lattice modes for a variety of systems including conducting polymers,[150] insulators,[151-153] and semiconductors.[154] This is due to the carrier events being on the scale of tens to hundreds of femtoseconds leading to variations in the THz region. In addition, the phonon modes[155,156] are often found in the range of several THz to tens of THz.

In addition to these more traditional solid-state materials, molecular solids have also been heavily investigated. Most if not all molecular crystals have lattice vibrational modes in the THz region that are unique to each crystal, giving them a characteristic THz spectrum dependent on its specific intermolecular interactions.[119] There are two fields where a lot of attention has been given to the THz spectra of molecular solids, security and polymorphism. THz spectroscopy has been used to record spectral "fingerprints" of a variety of explosives, poisons, and illicit drugs,[157] which would be useful in the detection of these materials, and as an extension, the development

of compact mobile THz devices is an active area of interest.[158,159] The other heavily studied field is in the pharmaceutical industry because of the THz spectrum is sensitive to crystallinity and chirality, making it a potential method for the detection of polymorphs in drug substances.[160-162]

#### *1.4.2.2 Terahertz Imaging*

While there are many uses of THz radiation as spectroscopic technique, it has also found use as an imaging technique, commonly referred to as T-ray Imaging.[127] T-ray imaging was first used in 1995[163,164] for the imaging of plant and animal material, but since then this technique has expanded into many different fields. Due to the non-destructive nature of THz radiation, T-ray imaging has found many industrial applications such as quality control in food processing,[124,165] monitoring of water content and the detection of foreign objects, in the paper industry,[166-168] and extensively in the plastics industries,[124,169,170] to measure glass-transition temperatures and fiber orientation.

In addition to being non-destructive, many materials are transparent to THz radiation. More interestingly, many materials that are opaque at optical frequencies and provide very low contrast to x-rays, such as paper, plastic and ceramics are non-absorbing in the THz range. Based on changes in refractive index, different materials can be distinguish by THZ radition.[117] This can provide many niche applications such as full-body security screening and luggage scanners in airports.[132,159]

### *1.4.3 Interpretation of Terahertz Vibrations Using Modeling Techniques*

The fundamental physical interpretation of the THz spectra and the interaction of THz radiation is also an important area of research. It is generally understood that the THz absorption spectrum of a molecular crystal is comprised of lattice vibrations, which are the product of the

intermolecular interactions specific to the unique three-dimensional arrangement inside the crystal.[118] Unlike Near-IR spectroscopy there are no characteristic group frequencies in the THz spectra of crystalline molecular solids; therefore, the understanding of the basic vibrational motions caused by the absorption bands is quite challenging. To overcome these challenges numerical simulations are normally carried out for the modeling of THz spectra using commercial software for the implementation of density functional theory (DFT).

One requirement to accurately interpret THz spectra is the computational approach must accurately model the intermolecular forces that govern the THz region. This can be accomplished by using solid-state density functional theory. Solid-state simulations have been reported for a variety of molecular crystals; including explosives,[171-173] biological molecules,[174-177] illicit drugs,[178-180] and pharmaceutical compounds.[160-162,181] In addition, a wide range of predictive software can be used for evaluation of THz spectra with the most common being: Gaussian, CRYSTAL, CPMD, Castep, CHARMM, VASP and D3mol.[126,171,182]

## 1.5 Density Functional Theory and Its Implementation in CRYSTAL09

### *1.5.1 Appling Quantum Mechanics to Molecular Vibrations*

Vibrations in a system can often be described by applying the concept of the classical harmonic oscillator. At its simplest, the classical treatment of a harmonic oscillator is a mass connected to a wall by means of an ideal spring, **Figure 1.11A**. This concept can be extended to a two mass system as envisioned by two masses connect to a spring, **Figure 1.11B**.

As the mass oscillates about its equilibrium position, the force is said to be harmonic if the force ($F$), which is equivalent to mass ($m$) times acceleration ($a$), due to the spring is proportion to its displacement ($x$) from its equilibrium position such that it follows eq. 1.1

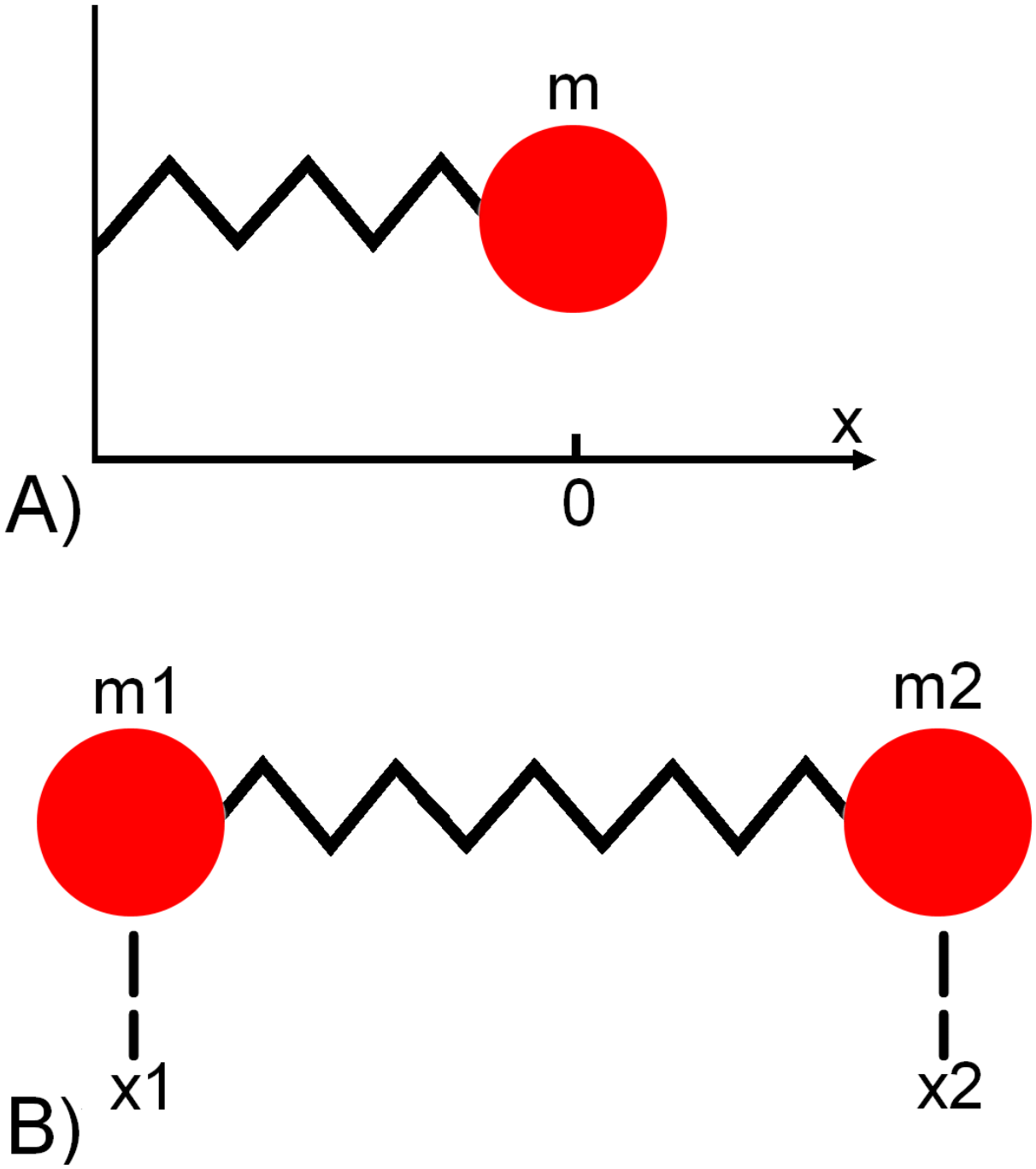


**Figure 1.11** (A) Mass m connected to a wall by a spring. The equilibrium position of the mass is x =0. (B) Masses m1 and m2 connected by a spring.

$$F = -kx \text{ or } ma + kx = 0 \qquad \text{(eq. 1.1)}$$

The value *k*, is the force constant that changes in magnitude based on the strength of the spring. Therefore, a weak spring will have a small force constant and a stiff spring will have a large force constant. This relation is known as Hooke's Law.[183] After some mathematical rearrangements the energy (*E*) as sum of the potential and kinetic energies can be expressed as eq.1.2

$$E = \frac{1}{2}kx_o^2 \qquad \text{(eq. 1.2)}$$

which is the product of the force constant times the initial value of the displacement squared. If this system is expanded to that shown in **Figure 1.11B**, there are two equations of motions, however the force equation is similar as eq. 1.1 with the following exceptions:

$$F = \mu a \quad \text{where} \quad \mu = \frac{m_1 m_2}{m_1 + m_2}$$

and

$$x = (x_2 - x_1) - l_0$$

The force is now equivalent to the reduced mass ($\mu$) times acceleration and the displacement is now the difference between the two masses $(x_1, x_2)$, subtracted by the equilibrium position of the spring $l_0$. Therefore, the fundamental vibration frequency ($v$) for a diatomic molecule is

$$v = \frac{1}{2\pi}\sqrt{\frac{k}{\mu}} \qquad \text{(eq. 1.3)}$$

The main difference between the classical model for the harmonic oscillator and the quantum mechanical model is that any energy is valid in the classical model of the harmonic oscillator, which is a stark contrast to the quantum mechanical model where the energy is quantized.

To determine the vibrational frequencies for the quantum mechanical model,[184] it is necessary to start from the time-independent Schrödinger equation HΨ=EΨ and, knowing that the potential energy is $V = \frac{1}{2} kx^2$ , this makes the classical Hamiltonian function for the harmonic oscillator equal to eq. 1.4

$$H = -\frac{h^2}{8\pi m}\frac{d^2}{dx^2} + \frac{1}{2}kx^2 \qquad \text{(eq. 1.4)}$$

Transforming the Schrödinger equation to

$$-\frac{h^2}{8\pi^2\mu}\frac{d^2\Psi}{dx^2} + \frac{1}{2}kx^2\Psi = E\Psi \qquad \text{(eq. 1.5)}$$

moreover, solving this equation shows that energy for the harmonic oscillator is quantized and is limited to

$$E_n = \left(n + \frac{1}{2}\right)hv \qquad n = 0,1,2,\ldots \qquad \text{(eq. 1.6)}$$

therefore, the vibration energy ($E_n$) is equal to the vibration quantum number ($n$) plus a half times Planck's constant times the fundamental vibrational frequency ($v$) given in eq. 1.6. In addition to the energy levels of the vibration modes, the wavefunctions for each level can also be determined given by the equation

$$\Psi_n(x) = N_n H_n\left(\alpha^{1/2}x\right)e^{-\alpha x^2/2} \qquad \text{(eq. 1.7)}$$

where

$$\alpha = \sqrt{\frac{8\pi^2 k\mu}{h^2}}$$

and

$$N_n = \frac{1}{(2^n n!)^{1/2}} \left(\frac{\alpha}{\pi}\right)^{1/4} \qquad \text{(eq. 1.8)}$$

and the $H_n(\alpha^{1/2}x)$ term is a Hermite polynomials. These wavefunctions can then be plotted to give **Figure 1.12**, which shows the difference between the classical and quantum mechanical harmonic oscillator.[185]

These equations only exactly apply to one unique oscillation between two atoms. However, in a molecular crystal there are multiple atoms oscillating. The general methodology still applies to these larger systems if they are considered to move coherently. Taking eq. 1.6 into consideration, the vibration must be associated with a large mass or a very small force constant to be located in the THz region. For the majority of molecular crystals the THz region consists of intermolecular contributions from translations and rotations, which involve weaker electrostatic and dispersive forces. The system could be considered one large mass if all of these molecules are vibrating together and the weak attractive forces between these molecules give rise to a weak force constant. In addition to intermolecular motions, intramolecular motions consisting of global distortions of the molecules, torsional motions, or flexing of ringed structures that are hindered by the intermolecular interactions are present, but are often mixed with external vibrations.

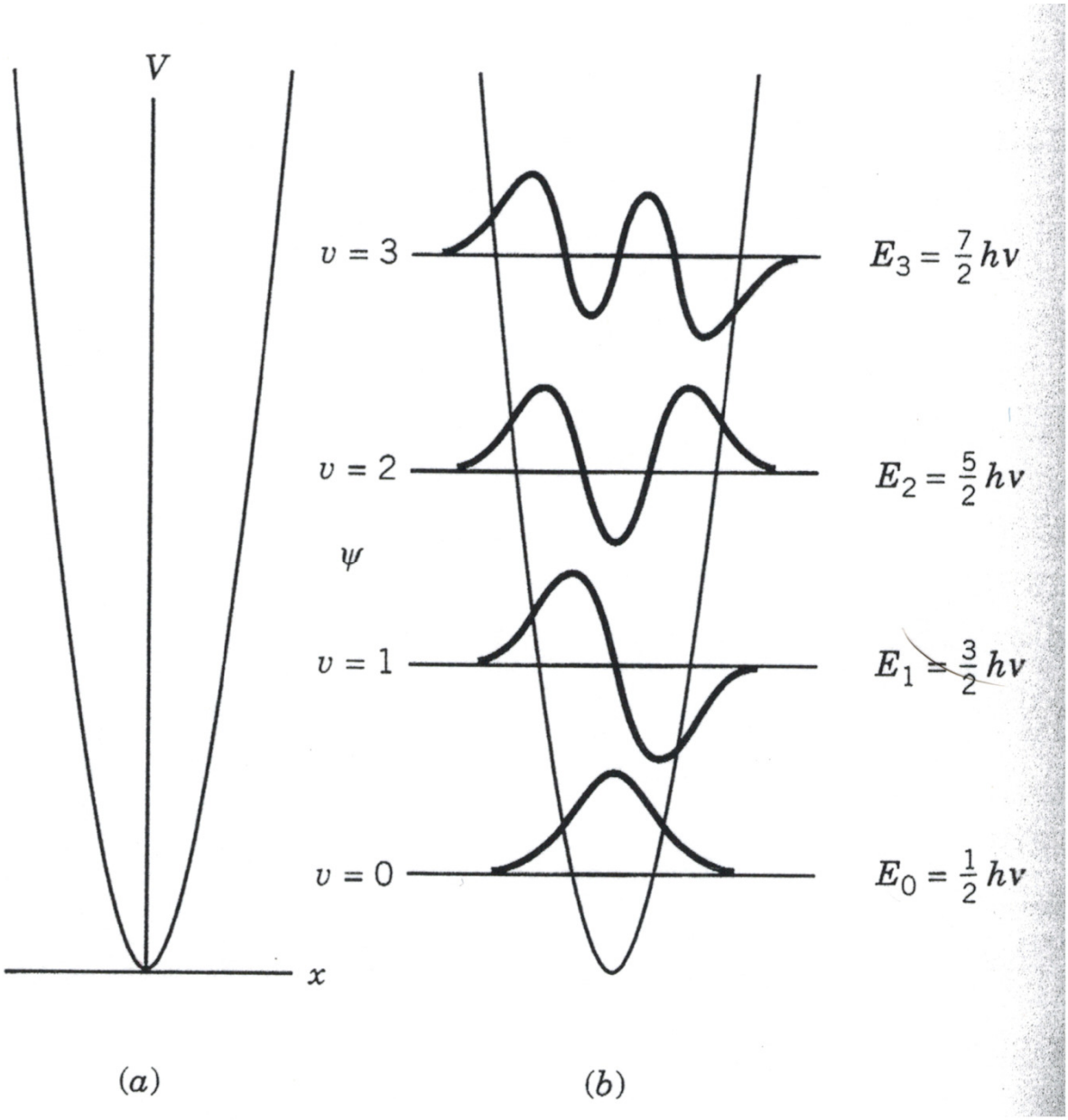


**Figure 1.12** (a) Potential energy curve for a classical harmonic oscillator. (b) Allowed energy levels and wavefunctions for a quantum mechanical harmonic oscillator. Figure was modified from ref. 185.

### *1.5.2 Density Functional Theory (DFT)*

First-principles calculations or *ab intio* calculations begin with only the fundamental physical constants needed to describe the interactions between particles.[183] With these constants and dynamic equations; the energy of a system can be calculated. To treat atomic systems whose electrons have extremely small masses, quantum mechanics must be employed. Quantum mechanics at its root is a probabilistic approach, which calculates the probability of a particle being at a certain location at a certain time, being described by a well-behaved wavefunction $\Psi$.[184] This assumption leads to the Schrödinger equation $H\Psi=E\Psi$, where the energy of system (E) is dependent of this wavefunction and a Hamiltonian (H) which depends on the system being described. Solving the Schrödinger equation for a one-electron system is not trivial but can be done. However as the system grows larger the solutions become much more problematic to obtain. Because of these problems, many methods were developed to approximate the energies for large systems, one of which is density functional theory (DFT).[186]

Many methods were developed to approximate the solutions to the wavefunction of large systems, the earliest being the Hartree-Fock method (HF), which is used to find spin-orbitals that can then be used to construct configuration state functions (CSFs). This method is still used today. There are limitations however to HF methods, primarily when large basis sets are used on molecules that contain many atoms and electrons. Therefore, an alternative method, density functional theory (DFT) was developed that instead of using CSFs, employs the concept of electron probability density.[183] A more thorough explanation of DFT can be found in references: 187-191. While the density alone cannot obtain all information such as the conventional kinetic energy expression, it does however characterize the potential energy experienced by the

electrons. In addition, the use of density in some predictive methods can be more accurate than the HF method.[192]

One reason for the popularity of DFT is that it takes into account electron correlation while being less computationally demanding than configuration interaction (CI) calculations or Møller-Plesset perturbation theory (MPPT). In addition, calculations on molecules with 100 atoms or more are done in a significantly less time than HF methods. Lastly, systems containing d-shell electrons more frequently agree with experimental results using DFT.

The concept of a density functional was the basis of early but useful approximate models developed in the late 1920s by E. Fermi and L.H. Thomas, the Thomas-Fermi method,[193-195] and the work of J.C. Slater in the 1950s, Hartree-Fock-Slater method.[196] It was not till 1964 that a formal proof was given by P. Hohenberg and W. Kohn that the ground-state energy and all other ground state properties could be determined by the electron density.[197] Later in 1965 the derivation of a one-electron equation from which the electron density could be obtained was solved by W. Kohn and L.J. Sham.[198] The energy ($E$) calculated for the system ($\rho$) can be expressed[192] as

$$E[\rho] = T[\rho] + V[\rho] + J[\rho] + E_{XC}[\rho] \qquad \text{(eq. 1.9)}$$

Where $T[\rho]$ is the kinetic energy, $V[\rho]$ is the potential energy, $J[\rho]$ is the columbic energy and $E_{XC}[\rho]$ is the exchange-correlation energy. However, the exchange-correlation energy is not known explicitly as a function of the system or its orbitals. Therefore, this value must be approximated. This approximation has been an active area of research[199-202] and since no standard computational method exists, the calculations must be compared to experimental values. To this end many functionals incorporate empirical or semi-empirical information.[203-205]

A large number of functionals have been developed and fall into three general categories: local density approximations, generalized gradient approximations, and hybrid functionals. Local density approximations (LDA) are based on the exchange energy of a uniform electron gas, which can be directly calculated, and the correlation energy of an electron gas fit to experimental measurements.[206] Generalized gradient approximations (GGA) are modified LDA functionals that accounts for the inhomogeneity of the electron density.[205] The last method discussed are hybrid functionals, which include Hartree-Fock corrections in addition to density functional correlation and exchange.[207] There are a large amount of correlation and exchange functionals available for use such as LDA functionals [P86 (Perdew 1986),[208] PZ (Perdew-Zunger),[209] VBH (von Barth-Hedin),[210] VWN (Vosko-Wilk-Nusair),[211] LDA (Dirac-Slater)[212]], GGA functionals [LYP (Lee-Yang-Parr),[213] PBE (Perdew-Burke-Ernzerhof),[214] PWGGA (Perdew-Wang 1991),[215] WL (Wilson-Levy),[216] B (Becke),[205] P (Perdew),[217] B86 (Becke 1986),[218] B95 (Becke 1995),[219] WCGGA (Wu-Cohen)[220]] and combinations of the correlation and exchange functionals, hybrid functionals [PBE0,[221] B1PW91,[222] B3PW[215,223-226]]. The functional primarily used in this study is the B3LYP[213,223] functional, which is one of the most widely used functionals for DFT calculations. The B3LYP functional is a combination of Becke's 3 parameter functional (B3) combined with the non-local correlation developed by C. Lee, W. Yang, and R.G. Parr (LYP).

Besides functionals, another important aspect of DFT calculations is the selection of a proper basis set. The choice of basis set is of fundamental importance because a real atom has an infinite number of orbitals; therefore, to accurately describe a real atom, an infinitely large basis set would be necessary. Since it is physically impossible to obtain this basis set, the number of orbitals in the basis set must be truncated, and this is where the choice of basis set is crucial. If a basis set is chosen that does not contain enough orbitals, the atom will not be accurately

described. On the other hand, if too many orbitals were included, the amount of time necessary to complete the calculation would be prohibitive for routine use. Therefore a basis set must be chosen that it large enough to meet the accuracy that is wished to be obtained, while small enough to be completed in a reasonable amount of time.

There are two primary types of basis sets, Slater-type Orbitals (STO) and Gaussian-type orbitals (GTO). Slater type orbitals are approximate atomic orbitals, which model the actual wavefunctions by fitting to numerically computed wavefunctions. For atomic calculations, the STO basis functions are centered on the atomic nucleus. However, in a polyatomic species they are centered on each atom.[183] Therefore with molecules of more than three atoms the evaluation of the two-electron integrals is impractical. The introduction of Gaussian-type orbitals (GTO) in 1950 by S.F. Boys[227] played a major role in making *ab initio* calculations feasible.[228] The central advantage of GTOs is that the product of two Gaussians at different centers is equal to a single Gaussian function centered at a point between the two atoms. Therefore two-electron integrals on three and four different centers can be reduced to integrals over two difference centers, which is much easier to calculate.[183]

The simplest type of basis set is a minimal basis set in which one function is used to represent each orbital of elementary valence theory; however, this type of basis set is not normally sufficient for chemical accuracy. To increase accuracy, the number of functions in the basis set can be increased by doubling or tripling the number of basis functions present in the minimal basis set. The downside of doing this is that the calculations become increasingly more taxing. Therefore a split-valence basis set can be used where the inner electrons are characterized by one basis function and the valence electrons are characterized by two basis functions.

There is a disadvantage in using GTOs over STOs in that GTOs do a poor job of describing the orbitals near the atomic nuclei. To overcome this problem several GTOs can be grouped together to form a contracted Gaussian function, which is a linear combination of the primitive Gaussian functions, thereby reducing the number of unknown parameters which can lead to a large time savings with nearly no loss of accuracy. There are multiple ways of contracting Gaussian basis sets; the most popular method was developed by the research group of John Pople.[229] The standard notation for these basis sets is X-YZG, where the G stands for Gaussian, the X indicates the number of primitive Gaussian functions that are used for the core orbitals; the number of values after the hyphen represent the value of zeta for the basis set. Y and Z represents the number of functions for the valence-shell orbitals where one is a linear combination of Y primitive Gaussian functions and the other is a linear combination of Z primitive Gaussian functions. For example, the 3-21G basis set is comprised of one contracted Gaussian composed of three primitives for the core electrons. In addition, it is a double-zeta basis set where the valence shell orbitals are comprised of two functions, one is a contracted Gaussian of two primitives and the other is a single primitive Gaussian Orbital.[183]

The accumulation of the above information can be used to infer many useful properties of atomic systems; however, this is not usually done from "scratch" for every calculation. This information has been adapted for use by many research groups around the world for a more broad audience. By implementing the fundamentals of quantum chemistry, density functional theory and basis sets, into a computer program, a thorough knowledge of intricate quantum mechanics is not a necessary (but useful) requirement. One such computer program that was developed for the use of predicting molecular structure and properties was CRYSTAL.

### *1.5.3 CRYSTAL09*

CRYSTAL is a general-purpose program for the study of crystalline solids, and the first that has been distributed publicly.[230] Developed by R. Dovesi, C. Pisani, C. Roetti, M. Causá, and V.R. Saunders at the University of Torino, the first version was released in 1988[231] and then rereleased six additional times as CRYSTAL92,[232] CRYSTAL95,[233] CRYSTAL98,[234] CRYSTAL03,[235] CRYSTAL06,[236] and the most recent CRYSTAL09.[237] The CRYSTAL program computes the electronic structure of periodic systems within Hartree-Fock, density functional or various hybrid approximations.

To be able to perform these calculations on crystalline solids, the infinite three-dimensional structure must be reduced to a finite number of parameters. This can be accomplished by exploiting the use of symmetry of the system, which is inherent in one form or another in the solid state. The fundamental approximation made is the expansion of the single particle wave functions ('Crystalline Orbital', CO) as a linear combination of Bloch functions (BF) defined in terms of local functions ('Atomic Orbitals', AOs) which are, in turn, linear combinations of Gaussian type functions (GTF).[230]

Exploiting the use of translational symmetry allows factorization of the eigenvalue problem in periodic systems, because the Bloch functions are a basis for irreducible representations of the translation group. Therefore, in periodic calculations the point symmetry is used to reduce the number of points needed to calculate the matrix equations. In addition, the point symmetry is used to reconstruct the Hamiltonian, which is also symmetric with respect to the point group operators of the system.

Another important aspect of *ab initio* calculations for periodic structures is integration over reciprocal space. The unit cell of a crystalline system can be defined in the reciprocal lattice

and is referred to as the Brillouin zone (BZ). The Brillouin zone is defined as all points in reciprocal space that lies closer to Γ which refers to the (0,0,0) point of the Brillouin zone. This usage of reciprocal space means any reciprocal points beyond the first Brillouin zone are redundant when evaluating the Bloch functions and integrating over the Brillouin zone is equivalent to evaluating the sum over an infinite number of translational lattice vectors. This definition is exploited in CRYSTAL during the self-consistent procedure, when determining the Fermi energy (EF), and reconstructing the one-electron density matrix. Moreover, after self-consistency is reached, calculating the density of states (DOS) and a number of observable quantities also exploit the redundancy generated using Bloch functionals. The Fermi energies are evaluated starting from the knowledge of the eigenvalues and the eigenvectors at a certain set of sampling points which in three-dimensional crystals belongs to a lattice called the Monkhorst net,[238] where only points of the Monkhorst net belonging to the irreducible part of the Brillouin Zone (BZ) are considered, illustrated in **Figure 1.13**. This net must be dense enough to sample enough of the Brillouin Zone to allow the energy to be calculated correctly. To determine the necessary number of reciprocal points needed is done normally through trial and error, by gradually increasing the number of points to find a value of the total energy that does not change with increased sampling.

Two completely different situations must also be considered, depending on whether the system is an insulator (or zero gap semiconductor), or a conductor. If the system is an insulator, all the bands are either fully occupied or vacant and the identification of EF is elementary. On the other hand if the system is a conductor an additional parameter needs to be supplied to define a Gilat net[239,240] which is analogous to the Monkhorst net, with the exception that the value of the Gilat net is generally larger resulting in a denser net. Once the sampling of reciprocal space is

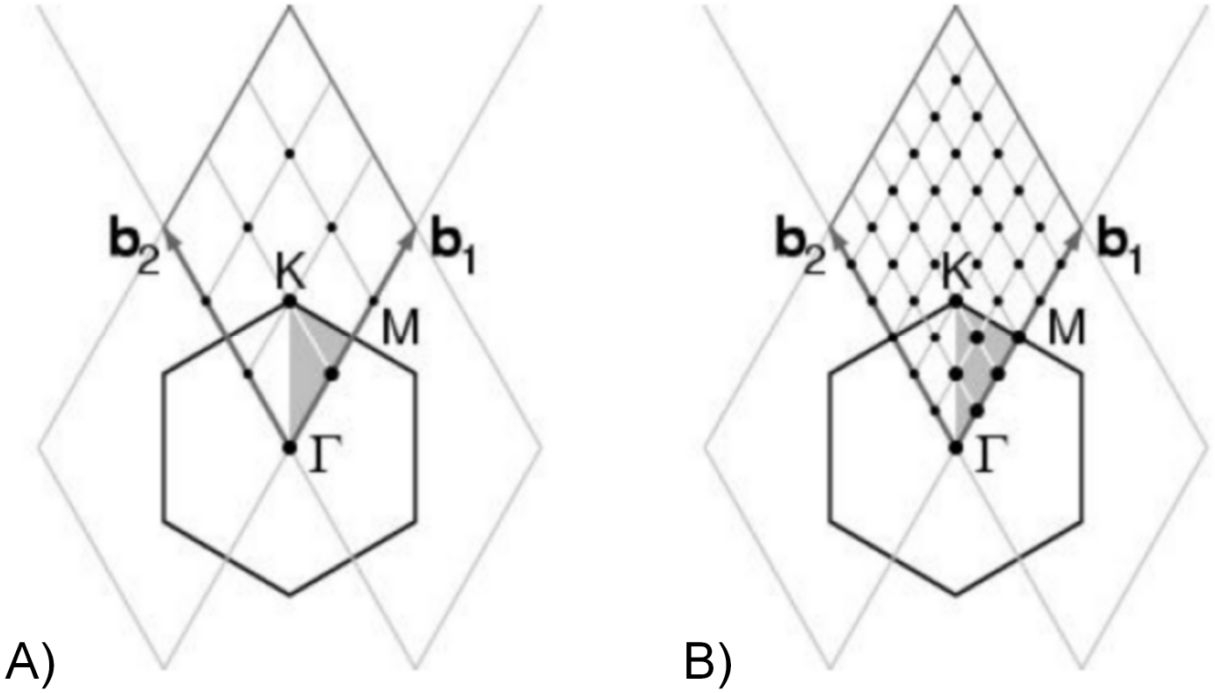


**Figure 1.13** The reciprocal lattice cell of 2D graphite (rhombus), the first Brillouin zone (hexagon), the irreducible part of Brillouin zone (in grey), and the coordinates of the reciprocal points according to a Pack-Monkhorst sampling, with shrinking factor A) 3 and B) 6. Figure was modified from ref.237.

adequate, the calculation of the electron density in real space requires an iterative procedure to simultaneously determine the appropriate set of orbitals and to satisfy the Kohn-Sham Hamiltonian, referred to as the self-consistent field (SCF).

At each point in reciprocal space ($k$) the calculation of the electron density is solved using the Roothaan-Hall equation[241,242]

$$F(k)A(k) = S(k)A(k)E(k) \qquad \text{(eq.1.10)}$$

in which $S(k)$ is the overlap matrix over the Bloch functions, $E(k)$ is the diagonal energy matrix, $A(k)$ is the expansion coefficients of the Bloch function. The Fock matrix in direct space is the summation of the one-electron and two-electron contributions in the basis set of the atomic orbitals, where the one-electron contribution is the sum of the kinetic and nuclear attraction and the two-electron term is the sum of the Coulomb and exchange contributions.[230] The iterative process for solving for the expansion coefficients is outlined in **Figure 1.14**. After choosing a basis set and geometry, an initial guess is made for the density matrix. Using this density matrix the Fock matrix is calculated and a set of expansion coefficients is then found. These expansion coefficients are then used to determine a new density matrix. This process is repeated until the new density matrix is the same or within the given tolerances of the previously calculated density matrix. This process is the basis for calculating a single point energy.

One of the most important processes in the modeling of chemical systems is the determination of the equilibrium structure. The atomic positions and lattice parameters of crystal structure must be iteratively optimized to reach the potential energy minimum on the potential energy surface (PES). To determine the location of this minimum, basic methods are employed, using first- and second- derivatives, which allow the identification and characterization of stationary points of the PES. As the atomic positions are adjusted the first derivatives of the

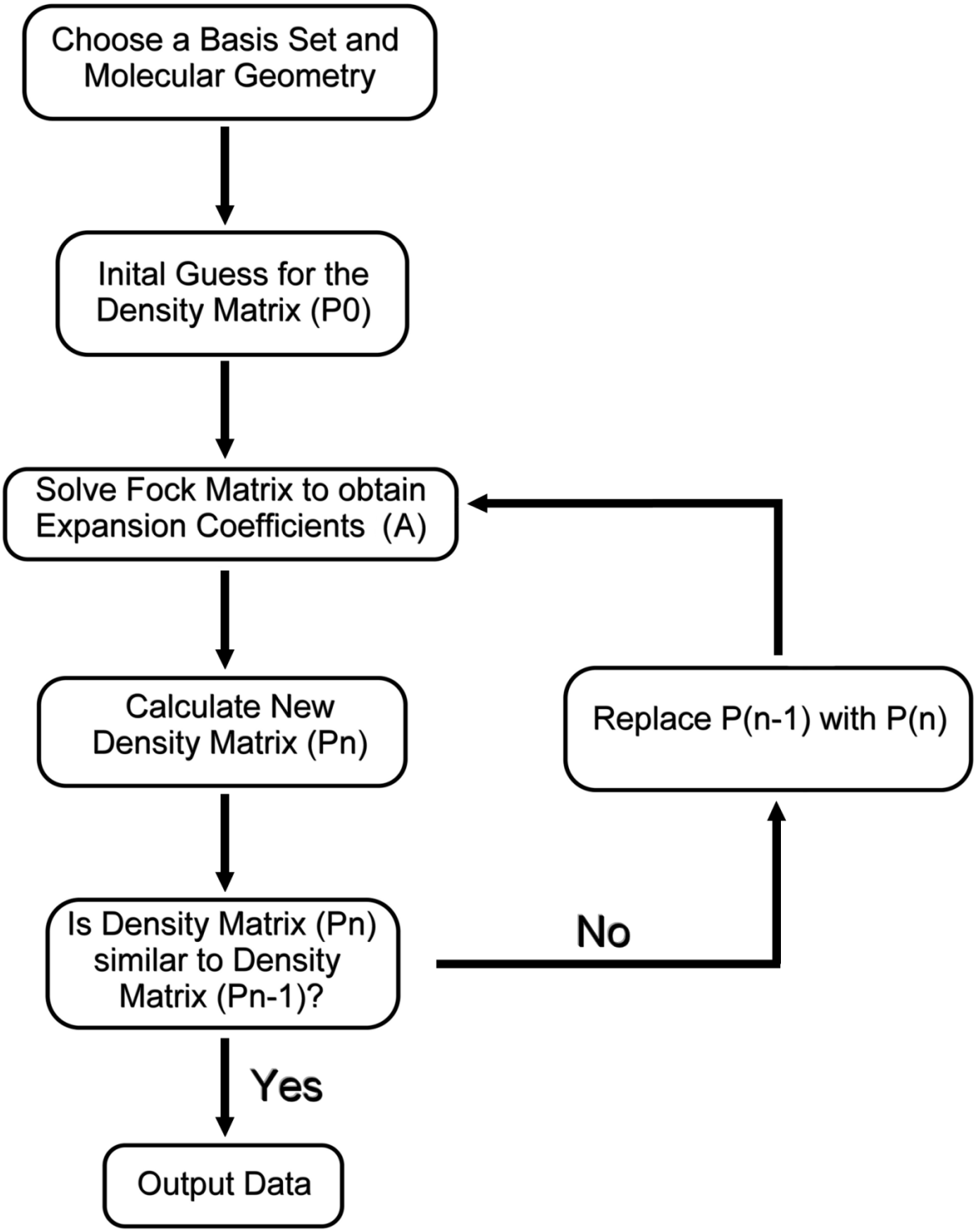


**Figure 1.14** Generalized SCF procedure for calculating the electron density as implemented in CRYSTAL

potential energy with respect to the atomic positions will reach zero (or within some specified tolerance), and the second derivatives are positive, indicating a minimum energy configuration. CRYSTAL utilizes gradient-based algorithms to analytically calculate the necessary derivatives needed to optimize the structure.[243] To accomplish this a quasi-Newtonian optimization scheme is implemented, where in the gradients are evaluated each time the energy is computed and the second derivative matrix (Hessian matrix) is updated by using a Broyden-Fletcher-Goldfarb-Shanno scheme.[244-248] A simple flowchart for the optimization process of the geometry is shown in **Figure 1.15**.[249]

With the geometry optimized, the most useful property in relation to this work is the determination of vibrational frequencies. While the goal of this work is to obtain vibrational frequencies, the importance of an accurate geometry optimization is crucial. This is due to vibrational frequencies only being meaningful if the crystalline structure is at a stationary point on the potential energy surface. The vibrational frequencies are determined in CRYSTAL by first analytically determining the energy first derivatives with respect to the atomic positions and then calculating the second derivatives numerically at a point where all the first derivatives are zero.[250-252] Due to the infinite nature of crystalline systems, the atomic positions are not followed in real space, but in reciprocal space. The frequencies are only calculated at the special point Γ (0,0,0) allowing the frequencies to be evaluated in the same manner as for molecules. This means that in the determination for the first-derivatives, each atom is displaced along each of the three Cartesian coordinates in the Brillouin zone, and the energy derivatives are evaluated. Vibrational frequencies can then be computed from the force constants obtained from diagonalization of the energy derivatives.

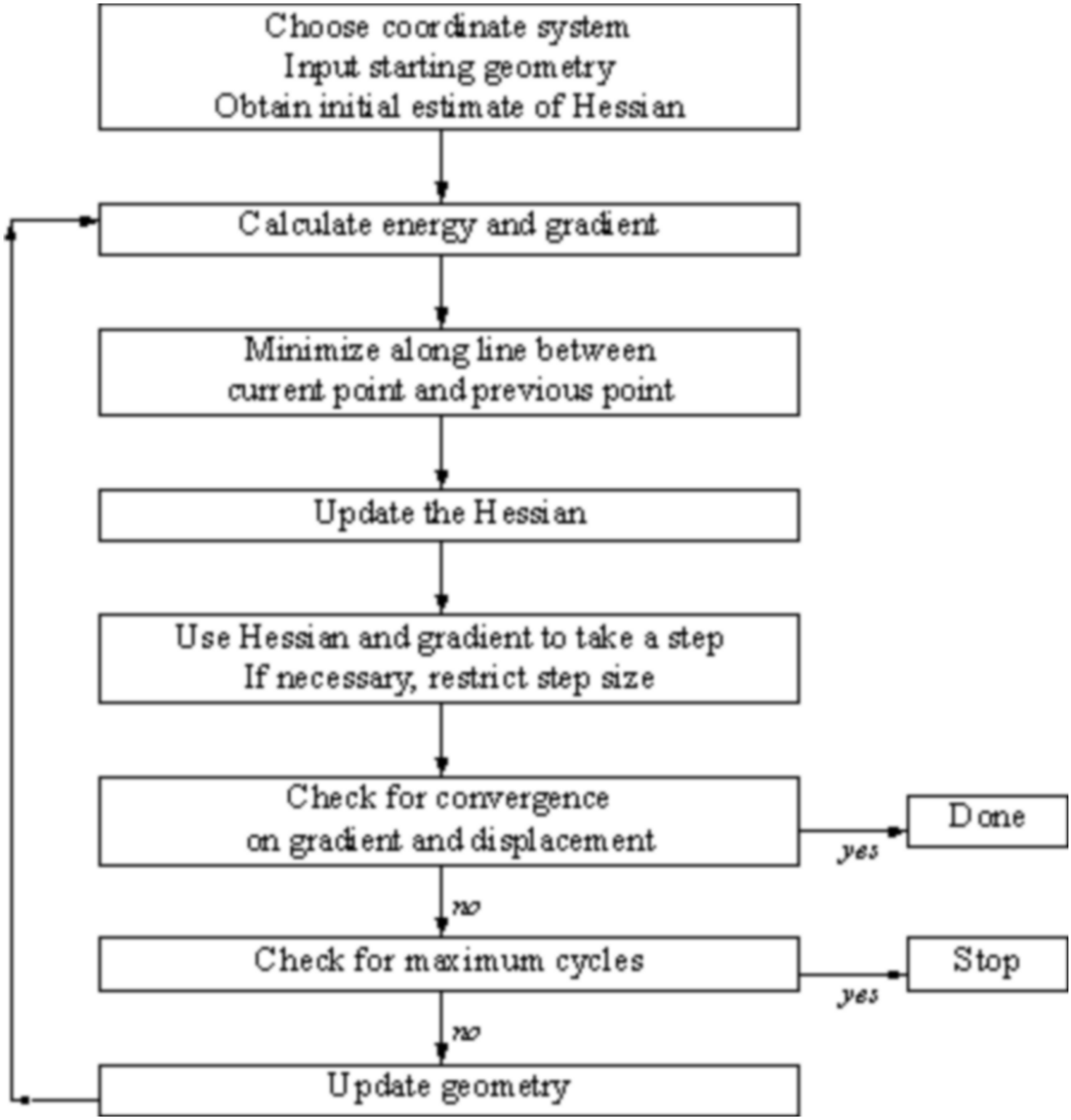


**Figure 1.15** Simple scheme of the optimization process for CRYSTAL. Figure was modified from ref. 249.

As an extension of the locations of the vibrational harmonic frequencies, the intensities of the vibrations with respect to one another are also important. The default method of calculating the intensities of the vibrations in the current version of CRYSTAL (CRYSTAL09) is accomplished using the Berry phase approach.[230] The Berry phase approach consists of evaluating the Born charges, which are the derivative of the dipole moment with respect to the atomic displacements, as polarization differences between the central and the distorted geometries.[252]

## 1.6 General Research Considerations

The work presented in this thesis is not focused on one particular set of substances. However, the technique used to characterize each substance is the same. The general theme centers on the analysis of the vibrational spectra of a variety of organic, hybrid organometallic and inorganic species modeled using solid-state density functional theory (DFT). The solid-state DFT method used in this study was implemented in CRYSTAL09, which has shown much potential for it use in the characterization of crystalline solids.

The systems investigated in the work range from purely inorganic to purely organic. Each contained a set of substances that could be considered as polymorphic to one another, either in a traditional sense or as pseudo-polymorphs. The first to be investigated was the purely inorganic vanadium phosphate system consisting of three conformational polymorphs of $VOPO_4$, which were all derived by different methods of dehydrating $VOPO_4 \bullet 2H_2O$. The next substance investigated included three different sets of complexes based on the 5-monosubstituted tetrazole, 5-(4-pyridyl)tetrazole. The last substance studied was α,α,α′,α′-Tetrabromo-p-xylene, which exhibited unique packing due to the system being held together primarily by electrostatic interactions.

The studies involving 5-(4-pyridyl)tetrazole were comprised of the comparison of a new polymorph based purely on packing to previously published crystallographic information of the free acid 5-(4-pyridyl)tetrazole. The next study was the comparison of two hydrohalide salts of 5-(4-pyridyl)tetrazole, which could be considered pseudo-polymorphs due to the only difference being the identity of the anion. The last set of compounds compared where three isomorphous transition metal complexes with 5-(4-pyridyl)tetrazole as a ligand, which could also be considered pseudo-polymorphic, where the polymorphism is based on composition.

The vibrational technique used to characterized most of these systems, with the exception of the polymorphs of vanadium phosphate, was terahertz (THz) spectroscopy. THz spectroscopy was used to probe the intermolecular interactions in these molecular crystals, which are unique to this region. It was found that subtle differences in the structure, composition, or packing could have large and varying effects on the vibrational modes, especially in the terahertz region. However, no universal trends in the vibrational frequency could be determined. Nevertheless, it was determined that the nature of the normal mode has the greatest effect when comparing systems that have compositional differences.

Through the investigation of these systems, a variety of structure types have been able to be modeled using solid-state DFT and in particular using CRYSTAL09. However, a great deal of work could still be done because most systems have polymorphic forms based on how hard one looks for them. The methods demonstrated in this work, could be used as a starting point for the investigation of organic, hybrid organometallic and inorganic species. This is especially true for transition-metal complexes, which are plagued by unfilled *d* orbitals and different spin configurations, which if not accounted for properly would result in an unobtainable solution or be inaccurate.

## 1.7 References


[1] R. Purohit and P. Venugopalan, *Resonance*, **2009**, *14*, 882.

[2] J. Haleblian and W. McCrone, *J. Pharm. Sci.*, **1969**, *58*, 911.

[3] E. Mitscherlich, *Ann. Chim. Physics.*, **1822**, *19*, 350.

[4] R. K. Harris, *Analyst*, **2006**, *131*, 351.

[5] L. Addadi and S. Weiner, Angew. *Chem. Int. Ed. Engl.*, **1992**, *31*, 153.

[6] K. Sato, *J. Phys. D: Appl. Phys.*, **1993**, *26*, B77.

[7] W.C. McCrone in D. Fox, M.M. Labes, and A. Weissberger (Eds.), Physics and Chemistry of the Organic Solid State, Interscience, New York, **1963**, p 725.

[8] J. Bernstein, *J. Phys. D: Appl. Phys.*, **1993**, *26*, B66.

[9] SciFinder; Chemical Abstracts Service: Columbus, https://scifinder.cas.org (accessed July 9, 2013).

[10] J. Haleblian, *J. Pharm. Sci.*, **1975**, *68*, 1269.

[11] A. Burger in D.D. Bremer and P. Speiser (Eds.), Topics in Pharmaceutical Sciences, Elsevier, Amsterdam, **1983**, p 347.

[12] T. L. Threlfall, *Analyst.*, **1995**, *120*, 2435.

[13] R.J. Karpowicz, S.T. Sergio, T.B. Brill, *Ind. Eng. Chem. Prod. Res. Dev.*, **1983**, *22*, 363.

[14] J.A. Kohlbeck, *Microscope*, **1982**, *30*, 249.

[15] M.C. Etter, R.B. Kress, J. Berstein, D.C. Cash, *J. Am. Chem. Soc.*, **1984**, *106*, 6921.

[16] D.N. Kendall, *Anal. Chem.*, **1952**, *24*, 382.

[17] G. Susich, *Anal. Chem.*, **1950**, *22*, 425.

[18] A. Whitaker, *J. Soc. Dyers Colour*, **1992**, *108*, 282.

[19] D.L. Morel, E.L. Stogyrn, A.K. Ghosh, T. Feng, P.E.Purwin, R.F. Shaw, C. Fishman, G.R. Bird, A.P. Piechowski, *J. Phys. Chem.: Solids State Phys.*, **1984**, *88*, 923.

[20] M.C. Etter, R.B. Kress, J. Berstein and D.J. Cash, *J. Am. Chem. Soc.*, **1984**, *106*, 6921.

[21] D. Small (Ed.), The Physical Chemistry of Lipids, Plenum, New York, **1986**.

[22] N. Garti and K. Sato (Eds.), Crystallization and Polymorphism of Fats and Fatty Acids, Marcel Dekker, New York, **1988**.

[23] S. Gupta, *J. Am. Oil Chem. Soc.*, **1991**, *94*, 450.

[24] S. P. Srivastara, J. Handoo, K.M. Agrawal, G.C. Joshi, *J. Phys. Chem. Solids*, **1993**, *54*, 639.

[25] G. Ungar, *J. Phys. Chem.*, **1983**, *87*, 689.

[26] L. deMan, C.F. Shen, J.F. deMan, *J. Am. Oil Chem. Soc.*, **1991**, *68*, 70.

[27] M. Saltmarsh and T.P. Labuza, *J. Food Sci.*, **1980**, *45*, 1231.

[28] Y. Roos and M. Karel, *Int. J. Food Sci. Technol.*, **1991**, *26*, 55.

[29] T.M. Herrington and A.C. Branfield, *J. Food Technol.*, **1984**, *19*, 427.

[30] R.L. Wille and E.S. Lutton, *J. Am. Oil Chem. Soc.*, **1966**, *43*, 491.

[31] A. Imberty, A. Buleon, T. Vihn, S. Perez, *Starch/Staerke*, **1991**, *43*, 375.

[32] B.J.D. Le Révérend, P.J. Fryer, S. Coles, S. Bakalis, *J. Am. Oil Chem. Soc.*, **2010**, *87*, 239.

[33] H. Bothe and H.K. Cammenga, *J. Therm. Anal.*, **1979**, *16*, 267.

[34] J. Pirttimäki, E. Laine, J. Ketolainen, P. Parrien, *Int. J. Pharm.*, **1993**, *95*, 93.

[35] M. Caira, *Top. Curr. Chem.*, **1998**, *198*, 163.

[36] J.D. Dunitz in G.R. Desiraju (Ed.), The crystal as a supramolecular entity: perspectives in supramolecular chemistry, vol. 2, Wiley, New York, **1996**, p 2.

[37] N.H. Hartshorne and A. Stuart, Crystals and the Polarizing Microscope, Edward Arnold, London, 4th edn., **1970**, p 20.

[38] S.M. Reutzel and M.C. Etter, *J. Phys. Org. Chem.*, **1992**, *5*, 44.

[39] A. Nangia, *Acc. Chem. Res.*, **2008**, *41*, 595.

[40] A.P. Jackson, A. Maxwell, D.B. Wigley, *J. Mol. Biol.*, **1991**, *217*, 15.

[41] M. Kuhnert-Brandstätter, E. Junger, A. Kofler, *Mikrochem. J.*, **1965**, *9*, 105.

[42] M. Kuhnert-Brandstätter and H. Grimme, *Sci. Pharm.*, **1967**, *35*, 287.

[43] M. Kuhnert-Brandstätter and H. Grimme, *Mikrochim. Acta*, **1968**, 115.

[44] M. Brandstätter, *Z. Physik. Chem.*, **1942**, *A191*, 227.

[45] M. Kuhnert-Brandstätter and M. Aepkers, *Mikrochim. Acta*, **1962**,1055.

[46] M. Kuhnert-Brandstätter, R. Hofmann, M. Senn, *Mikrochem. J.*, **1963**, *7*, 357.

[47] D. Braga and F. Grepioni, *Chem. Soc. Rev.*, **2000**, *29*, 229.

[48] J. Dunitz, *Acta Crystallogr. Sect. B*, **1995**, *51*, 619.

[49] W.L. Duax, *J. Chem. Ed.*, **1988**, *65*, 502.

[50] A.J. Blake, R.O. Gould, M.A. Halerow, M. Schroender, *Acta Cryst. Sect. B*, **1993**, *49*, 773.

[51] R.A. Fletton, R.K. Harris, A.M. Kenwright, R.W. Lancaster, K.J. Packer, N. Sheppard, *Spectrochim. Acta. Part A*, **1987**, *43*, 1111.

[52] M.A. Garcia, C. Lopez, R.M. Claramunt, A. Kenz, M. Pierrot, J. Elguero, *Helv. Chim. Acta*, **2002**, *85*, 2763.

[53] M. Bauer, R.K. Harris, R.C. Rao, D.C. Apperley, C.A. Rodger, *J. Chem. Soc. Perkin Trans.2*, **1998**, *3*, 475.

[54] J. Elguero, C. Marzin, A.R. Katritzki, P. Linda, The Tautomerism of Heterocycles, Academic Press, London, **1966**.

[55] G.R. Desiraju, *J. Chem. Soc. Perkin Trans. 2*, **1983**, *7*, 1025.

[56] J.D. Dunitz, *Pure Appl. Chem.*, **1991**, *63*, 177.

[57] Okada, T. Takebayashi, M. Mashimoto, S. Kasiga, S. Sato, C. Tamura, *J. Chem. Soc., Chem. Commun.*, **1983**, *14*, 784.

[58] K.R. Wilson and R.E. Pincock, *Can. J. Chem.*, **1977**, *55*, 889.

[59] M. Kuhnert-Brandstätter and P. Gasser, *Microchem. J.*, **1971**, *16*, 419.

[60] R. David and D. Giron, Handbook of Powder Technology, **1994**, 9, 193.

[61] J. Haleblain, R. Koda, J. Biles, *J. Pharm. Sci.*, **1971**, *60*, 1485.

[62] E. Shefter and T. Higuchi, *J. Pharm. Sci.*, **1963**, *52*, 781.

[63] A. Holden and P. Singer, Crystals and Crystal Growing, Doubleday, Garden City, NY, **1961**, p. 67.

[64] F. Daniels and R. Alberty, Physical Chemistry, Wiley, New York, 2nd edn., **1961**, p 256.

[65] W. Ouellette, A.V. Prosvirin, V. Chieffo, K.R. Dunbar, B. Hudson, J. Zubieta, *Inorg. Chem.*, **2006**, *45*, 9346.

[66] A.T.M. Serajuddin, *Adv. Drug Deliver. Rev.*, **2007**, *59*, 603.

[67] J. F. Remenar, J. M. MacPhee, B.K. Larson, V. A. Tyagi, J. H. Ho, D. A. McIlroy, M. B. Hickey, P. B. Shaw, O. Almarsoon, *Org. Process Res. Dev.*, **2003**, *7*, 990.

[68] O.Almarsson, M.B. Hickey, M.L. Peterson, S.L. Morissette, S. Soukasne, C. McNulty, M. Tawa, J.M. MacPhee, J. F. Remenar, *Cryst. Growth Des.*, **2003**, *3*, 927.

[69] J.C. MacDonald, T.M. Luo, G.T.R. Palmore, *Cryst. Growth Des.*, **2004**, *4*, 1203.

[70] W. Ouellette, S. Jones, J. Zubieta, *CrystEngComm*, **2011**, *13*, 4457.

[71] T.M. Smith, D. Symester, K. Perrin, J. Vargas, M. Tichenor, C.J. O'Connor, J. Zubieta, *Inorg. Chim. Acta*, **2013**, *402*, 46.

[72] M. Bartholomä, J. Valliant, K.P. Maresca, J. Babich, J. Zubieta, *Chem. Commun.*, **2009**, *5*, 493.

[73] W. Ouellette, A.V. Prosvirin, J. Valeich, K.R. Dunbar, J. Zubieta, *Inorg. Chem.*, **2007**, *46*, 9067.

[74] C.N. Singman, *J. Chem. Educ.*, **1984**, *61*, 137.

[75] W.P. Hoffman in S. Yip (Ed.), Material Science of Carbon, Springer, Netherlands, **2005**, p 2923.

[76] J. Donohue, The Structure of the Elements, John Wiley and Sons INC., New York, **1974**, p 1.

[77] B. Meyer. *Chem. Rev.*, **1964**, *15*, 845.

[78] B. Meyer. *Chem. Rev.*, **1976**, *76*, 367.

[79] A.W. Laubengayer, D.T. Hurd, A.E. Newkirk, J.L. Hoard, *J. Amer. Chem. Soc.*, **1943**, *65*, 1924.

[80] B.F. Decker and J.S. Kasper, *Acta Cryst.*, **1959**, *12*, 503.

[81] St. V. Naray-Szabo' and C.W. Tobias, *J. Amer. Chem. Soc.*, **1949**, *71*, 1882.

[82] J.L. Hoard, R.E. Hughes, D.E. Sands, *J. Amer. Chem. Soc.*, **1958**, *80*, 4507.

[83] L. Gorski, *Phys. Staus. Solidi.*, **1963**, *3*, K316.

[84] C.P. Talley, S. LaPlaca, B. Post, *Acta Cryst.*, **1960**, *13*, 271.

[85] J.F. Cannon, *J. Phys. Chem. Ref. Data*, **1974**, *3*, 781.

[86] H. Jung, *Centralblatt Min. Geol.*, **1926**, *A*, 107.

[87] M.L. Katsnelson, *Mater. Today*, **2007**, *10*, 20.

[88] K.S. Novoselov, A.K. Geim, S.V. Morozov, D. Jiang, Y. Zhang, S.V. Dubonos, I.V. Grigorieva, A.A. Firsov, *Science*, **2004**, *306*, 666.

[89] K.S. Novoselov, D. Jiang, F. Schedin, T.J. Booth, V.V. Khotkevich, S.V. Morozov, A.K. Geim, *Proc. Natl. Acad. Sci. USA*, **2005**, *102*, 10451.

[90] R.F. Curl, *Rev. Mod. Phys.*, **1997**, *69*, 691.

[91] H. Kroto, *Rev. Mod. Phys.*, **1997**, *69*, 703.

[92] R.E. Smalley, *Rev. Mod. Phys.*, **1997**, *69*, 723.

[93] D. Iijima, *Nature*, **1991**, *354*, 56.

[94] D.F. Shrier, P. Atkins, T. Overton, J. Rourke, M. Weller, F. Armstrong, Inorganic Chemistry 4th edition, W.H. Freeman and Company,New York, **2006**, p. 319.

[95] CRC, Handbook of Chemistry and Physics, 94th Ed., **2013**, editor W.M. Haynes, On-line Edition p. 4-145

[96] C.G. Salzmann, P.G. Radaelli, B. Slater, J.L. Finney, *Phys. Chem. Chem. Phys.*, **2011**, *13*, 18468.

[97] J.D. Bernal and R.H. Fowler, *J. Chem. Phys.*, **1933**, *1*, 515.

[98] J.A. Biles, *J. Pharm. Sci.*, **1962**, *51*, 601.

[99] W.C. McCrone, Hot Stage Microscopy, Mettler Tech. Bull., No. 3003, **1968**.

[100] D. Giron, *Thermochim. Acta*, **1995**, *248*, 1.

[101] D. Giron, *J. Therm. Anal. Calorim.*, **2001**, *64*, 37.

[102] A. Gavezzotti and G. Filippini, *J. Am. Chem. Soc.*, **1995**, *117*, 12299.

[103] D. Braga, S.L. Giaffreda, F. Grepioni, A. Pettersen, L. Maini, M. Curzi, M. Polito, *Dalton Trans.*, **2006**, *10*, 1249.

[104] H. G. Brittain, *Spectroscopy*, **2000**, *15*, 34.

[105] M. Tremayn, *Phil. Trans. R. Soc. Lond. A*, **2004**, *362*, 2691.

[106] U. W. Schönenberger, J. R. Günter, H.R. Oswald, *J. Solid State Chem.*, **1971**, *3*,190.

[107] K.D.M. Harrs and E.Y. Cheung, *Org. Process Res. Dev.*, **2003**, *7*, 970.

[108] W.Z. Ostwald, *Phys. Chem.*, **1897**, *22*, 306.

[109] R.J. Mesley, *Spectrochim. Acta*, **1966**, *22*, 889.

[110] B. Cleverly and P.P. Williams, *Tetrahedron*, **1959**, *7*, 277.

[111] D.N. Kendall, *Anal. Chem.*, **1953**, *25*, 382.

[112] A. Burger and A. Lettenbuchler, *Pharmazie*, **1993**, *48*, 262.

[113] J. Answar, S.E Tarling, P.J. Barnes, *J. Pharm. Sci.*, **1989**, *78*, 337.

[114] G.A. Neville, H.D. Beckstead, H.F. Shurvell, *J. Pharm. Sci.,* **1992**, *81*, 1141.

[115] C.M. Deeley, R.A. Spragg, T.L. Threfall, *Spectrochim. Acta., Part A*, **1991**, *47*, 1217.

[116] M. Kuhnert-Brandstätter and I. Moser, *Mikrochim. Acta.*, **1981**, *I.*, 421.

[117] B. Ferguson and X. Zhang, *Nat. Mater.*, **2002**, *1*, 26.

[118] J. El Haddad, B. Bousquet, L. Canioni, P. Mounaix, *Trends Anal. Chem.*, **2013**, *44*, 98.

[119] M.C. Beard, G.M. Turner, C.A. Schmuttenmaer, *J. Phys. Chem. B*, **2002**, *106*, 7146.

[120] D.H. Auston and M.C. Nuss, *IEEE J. Quantum Electron.*, **1988**, *QE-24*, 184.

[121] D. Krokel, D. Grischkowsky, M.B. Ketchen, *Appl. Phys. Lett.*, **1989**, *54*, 1046.

[122] W.G. Rothschild and K.D. Moeller, *Phys. Today*, **1970**, *23*, 44.

[123] S.I. Dexheimer,Terahertz Spectroscopy: Principles and Applications, Taylor Francis Group, New York, **2008**.

[124] C. Jansen, S. Wietzke, O. Peters, M. Scheller, N. Vieweg, M. Salhi, N. Krumbholz, C. Jördens, T. Hochrein, M. Koch, *Appl. Opt.*, **2010**, *49*, E48.

[125] R.K. May, S. Zhong, I. Warr, L.F. Gladden, Y. Shen, J.A. Zeitler, *J. Pharm. Sci.*, **2010**, *100*, 1535.

[126] P.U. Jepsen, D.G. Cooke, M. Koch, *Laser Photonics Rev.*, **2011**, *5*, 124.

[127] D.M. Mittleman, M. Gupta, R. Neelamani, R.G. Baraniuk, J.V. Rudd, M. Koch, *Appl. Phys. B*, **1999**, *68*, 1085.

[128] E.P.J. Parrott, Y. Sun, E. Pickwell-Macpherson, *J. Mol. Struct.*, **2011**, *1006*, 66.

[129] Y. Watanabe, K. Kawase, T. Ikari, *Appl. Phys. Lett.*, **2003**, *83*, 800.

[130] M.H. Arbab, D.P. Winebrenner, E.I. Thorsos, A. Chen, *Appl. Phys. Lett.*, **2010**, *97*, 181903/1.

[131] C.T. Konek, B.P. Mason, J.P. Hooper, C.A. Stoltz, J. Wilkinson, *Chem. Phys. Lett.*, **2010**, *489*, 48.

[132] A.W.M. Lee, Q. Qin, S. Kumar, B.S. Williams, Q. Hu, J.L. Reno, *Appl. Phys. Lett.*, **2006**, *89*, 141125/1.

[133] D.F. Plusquellic, K. Siegrist, E.J. Heilweil, O. Esenturk, *ChemPhysChem*, **2007**, *8*, 2412.

[134] P.F. Taday, Philos. Trans. *R. Soc. London, Ser. A*, **2004**, *362*, 351.

[135] T. Arikawa, M. Nagai, K. Tanaka, *Chem. Phys. Lett.*, **2008**, *457*, 12.

[136] U. Møller, D.G. Cooke, K. Tanaka, P.U. Jepsen, *J. Opt. Soc. Am. B*, **2009**, *26*, A113.

[137] S. Funkner, G. Niehues, D.A. Schmidt, M. Heyden, G. Schwaab, K.M. Callahan, D.J. Tobias, M. Havenith, *J. Am. Chem. Soc.*, **2011**, *134*, 1030.

[138] G. Niehues, M. Heyden, D.A. Schmidt, M. Havenith, *Faraday Discuss.*, **2011**, *150*, 193.

[139] C.A. Schmuttenmaer, *Chem. Rev.*, **2004**, *104*, 1759.

[140] M. Exter, C. Fattinger, D. Grischkowsky, *Opt. Lett.*, **1989**, *14*, 1128.

[141] H. Harde, R.A. Cheville, D. Grischkowsky, *J. Opt. Soc. Am. B: Opt. Phys.*, **1997**, *14*, 3282.

[142] R.A. Cheville, and D. Grischkowsky, *Opt. Lett.*, **1998**, *23*, 531.

[143] R.A. Cheville, and D. Grischkowsky. *J. Opt. Soc. Am. B: Opt. Phys.*, **1999**, *16*, 317.

[144] D. Bigourd, A. Cuisset, F. Hindle, S. Matton, E. Fertein, R. Bocquet, G. Mouret, *Opt. Lett.*, **2006**, *31*, 2356.

[145] R.J. Foltynowicz, R.E. Allman, E. Zuckerman, *Chem. Phys. Lett.*, **2006**, *431*, 34.

[146] J.E. Pedersen, S.R. Keiding, *IEEE J. Quant. Electron.*, **1992**, *28*, 2518.

[147] G. Haran, W.D. Sun, K. Wynne, R.M. Hochstrasser, *Chem.Phys. Lett.*, **1997**, *274*, 365.

[148] R. McElroy and K. Wynne, *Phys. Rev. Lett.*, **1997**, *79*, 3078.

[149] E. Knoesel, M. Bonn, J. Shan, T.F. Heinz, *Phys. Rev. Lett.*, **2001**, *86*, 340.

[150] T.I Jeon, D. Grischkowsky, A.K. Mukherjee, R. Menon, *Appl. Phys. Lett.*, **2000**, *77*, 2452.

[151] D. Grischkowsky, S. Keiding, M. Vanexter, C.J. Fattinger, *Opt. Soc. Am. B: Opt. Phys.*, **1990**, *7*, 2006.

[152] C., Zhang, K.S. Lee, X.C. Zhang, X. Wei, Y.R. Shen, *Appl. Phys. Lett.*, **2001**, *79*, 491.

[153] M. Li, J. Fortin, J.Y. Kim, G. Fox, F. Chu, T. Davenport, T.M. Lu, X.C. Zhang, *IEEE J. Sel. Top. Quantum Electron.*, **2001**, *7*, 624.

[154] D. Grischkowsky and S. Keiding, *Appl. Phys. Lett.*, **1990**, *57*, 1055.

[155] G.C. Cho, P.Y. Han, X.C. Zhang, H.J. Bakker, *Opt. Lett.*, **2000**, *25*, 1609.

[156] M. Schall, P.U. Jepsen, *Appl. Phys. Lett.*, **2000**, *77*, 2801.

[157] M.C. Kemp, *IEEE Trans. THz Sci. Technol.*, **2011**, *1*, 282.

[158] I.R.L. Duling and D. Zimdars, *Laser Focus World*, 2007, *43*, 63.

[159] D. Zimdars, J. White, G. Stuk, G. Sucha, G. Fichter, S.L. Williamson, *Int. J. High Speed Electron. Syst.*, **2007**, *17*, 271.

[160] M.D. King, W.D. Buchanan, T.M. Korter, *Anal. Chem.*, **2011**, *83*, 3786.

[161] F. Pascale, C.M. Zicovich-Wilson, F.L. Gejo, B. Civalleri, R. Orlando, R.J. Dovesi, *Comput. Chem.*, **2004**, *25*, 888.

[162] M.D. King, W.D. Buchanan, T.M. Korter, *J. Pharm. Sci.*, **2011**, *100*, 1116.

[163] B.B. Hu, and M.C. Nuss, *Opt. Lett.*, **1995**, *20*, 1716.

[164] R. Lipkin, *Sci. News*, **1995**, *148*, 136.

[165] C. Joerdens, M. Koch, *Opt. Eng.*, **2008**, *47*, 037003/1.

[166] D. Banerjee, W. von Spiegel, M.D. Thomson, S. Schabel, H.G. Roskos, *Opt. Express*, **2008**, *16*, 9060.

[167] M. Reid and R. Fedosejevs, *Appl. Opt.*, **2006**, *45*, 2766.

[168] P. Mousavi, F. Haran, D. Jez, F. Santosa, S. Dodge John, *Appl. Opt.*, **2009**, *48*, 6541.

[169] S. Wietzke, C. Jansen, T. Jung, M. Reuter, B. Baudrit, M. Bastian, S. Chatterjee, M. Koch, *Opt. Express*, **2009**, *17*, 19006.

[170] N. Krumbholz, T. Hochrein, N. Vieweg, I. Radovanovic, I. Pupeza, M. Schubert, K. Kretschmer, M. Koch, *Polym. Eng. Sci.*, **2010**, *51*, 109.

[171] D.G. Allis and T.M. Korter, *ChemPhysChem*, **2006**, *7*, 2398.

[172] E.M. Witko and T.M. Korter, *J. Phys. Chem. A*, **2011**, *115*, 10052.

[173] D.G. Allis, J.A. Zeitler, P.F. Taday, T.M. Korter, *Chem. Phys. Lett.*, **2008**, *463*, 84.

[174] M.D. King, W. Ouellette, T.M. Korter, *J. Phys. Chem. A*, **2011**, *115*, 9467.

[175] M.D. King, P.M. Hakey, T.M. Korter, *J. Phys. Chem. A*, **2010**, *114*, 2945.

[176] M.D. King and T.M. Korter, *J. Phys. Chem. A*, **2011**, *115*, 14391.

[177] A.G. Markelz, A. Roitberg, E.J. Heilweil, *Chem. Phys. Lett.*, **2000**, *320*, 42.

[178] P.M. Hakey, D.G. Allis, M.R. Hudson, W. Ouellette, T.M. Korter, *ChemPhysChem*, **2009**, *10*, 2434.

[179] P.M. Hakey, M.R. Hudson, D.G. Allis, W. Ouellette, T.M. Korter, *J. Phys. Chem. A*, **2009**, *113*, 13013.

[180] P.M. Hakey, D.G. Allis, M.R. Hudson, T.M. Korter, *IEEE Sens. J.*, **2010**, *10*, 478.

[181] M.D. King, W.D. Buchanan, T.M. Korter, *Phys. Chem. Chem. Phys.*, **2011**, *13*, 4250.

[182] R. Fu, Z. Li, B.-B. Jin, C.-H. Zhang, H. Dai, Y.-H. Xue, *J. Chen, Spectrosc. Spectral Anal.*, **2010**, *30*, 2023.

[183] P. Atkins, R. Friedman, Molecular Quantum Mechanics 4th edition, Oxford University Press Inc., New York, **2005**.

[184] J.L. McHale, Molecular Spectroscopy, Pearson Education, New Jersey, **1999**.

[185] R.J. Silbey, R.A. Alberty, M.G. Bawendi, Physical Chemistry 4th edition, John Wiley & Sons, Inc., New York, **2005**.

[186] D.S. Sholl, J.A. Steckel, Density Functional Theory: A Practical Introduction, Wiley, **2009**.

[187] S. Borman, *Chem. Eng. News*, **1990**, *68*, 22.

[188] T. Ziegler, *Chem. Rev.*, **1991**, *91*, 651

[189] W. Kohn, *Rev. Mod. Phys.*, **1999**, *71*, 1253

[190] M.K. Harbola and A. Banerjee, *J. Theor. Comput. Chem.*, **2003**, *2*, 301

[191] T. Nakajima, T. Tsuneda, H. Nakano, K. Hirao, *J. Theor. Comput. Chem.*, **2002**, *1*, 109

[192] D.B. Cook, Handbook of Computional Quantum Chemistry, Dover, New York, **2005**.

[193] L.H. Thomas, *Proc. Cambridge Phil. Soc.*, **1927**, *33*, 542.

[194] E. Fermi, *Rend. Lincei*, **1927**, *6*, 602.

[195] E. Fermi, *Z. Phys.*, **1928**, *48*, 73.

[196] J.C. Slater, *Phys. Rev.*, **1951**, *81*, 385.

[197] P. Hohenberg and W. Kohn, *Phys. Rev.*, **1964**, *864*, B136.

[198] W. Kohn and L.J. Sham, *Phys. Rev.*, **1965**, *1133*, A140.

[199] S. Kurth, J.P. Perdew, P. Blaha, *Int. J. Quantum Chem.*, **1999**, *75*, 889.

[200] J.P. Perdew, S. Kurth, A. Zupan, P. Blaha, *Phys. Rev. Lett.*, **1999**, *82*, 2544.

[201] J. Sun, M. Marsman, G.I. Csonka, A. Ruzsinszky, P. Hao, Y.S Kim, G. Kresse, J.P. Perdew, *Phys. Rev. B: Condens. Matter*, **2011**, *84*, 035117/1.

[202] J. Tao, J.P. Perdew, V.N. Staroverov, G.E. Scuseria, *Phys. Rev. Lett.*, **2003**, *91*, 146401/1.

[203] M. Ernzerhof, and G.E. Scuseria, *J. Chem. Phys.*, **1999**, *110*, 5029.

[204] J.P. Perdew, K. Burke, M. Ernzerhof, *Phys. Rev. Lett.*, **1996**, *77*, 3865.

[205] A.D. Becke, *J. Chem. Phys.*, **1988**, *88*, 1053.

[206] G. Ortiz and P. Ballone, *Phys. Rev. B: Condens. Matter*, **1994**, *50*, 1391.

[207] B.J. Lynch and D.G. Truhlar, *J. Phys. Chem.*, **2003**, *107*, 8996.

[208] J. P. Perdew, *Phys. Rev. B*, **1986**, *33*, 8822.

[209] J. P. Perdew and A. Zunger, *Phys. Rev. B*, **1981**, *23*, 5048.

[210] U. von Barth and L. Hedin, *J. Phys. C: Solid State Phys.*, **1972**, *5*, 1629.

[211] S.H. Vosko, L. Wilk, M. Nusair, *Can. J. Phys.*, **1980**, *58*, 1200.

[212] P.A.M. Dirac, *Proc. Cambridge Phil. Soc.,* **1930**, *26*, 376.

[213] C. Lee, W. Yang, R.G. Parr, *Phys. Rev. B*, **1988**, *37*, 785.

[214] J. P. Perdew, K. Burke, and M. Ernzerhof, *Phys. Rev. Lett.*, **1996**, *77*, 3865.

[215] J.P. Perdew and Y. Wang, *Phys. Rev. B*, **1992**, *45*, 13244.

[216] L.C. Wilson and M. Levy, *Phys. Rev. B*, **1990**, *41*, 12930.

[217] J.P. Perdew, *Phys. Lett. A*, **1992**, *165*, 79.

[218] A.D. Becke, *J. Chem. Phys.*, **1986**, *85*, 7184.

[219] A.D. Becke, *Can. J. Chem.*, **1996**, *74*, 995.

[220] Z. Wu and R.E. Cohen, *Phys. Rev. B*, **2006**, *73*, Art. n. 235116.

[221] C. Adamo and V. Barone. *J. Chem. Phys.*, **1999**, *110*, 6158.

[222] J.P. Perdew, J.A. Chevary, S.H. Vosko, K.A. Jackson, M.R. Pederson, D.J. Singh, C. Fiolhais, *Phys. Rev. B*, **1992**, *46*, 6671.

[223] A.D. Becke, *J. Chem. Phys.*, **1993**, *98*, 5648.

[224] J.P. Perdew, Electronic Structure of Solids 1991, Akademie Verlag, Berlin, **1991**.

[225] J.P. Perdew and Y. Wang, *Phys. Rev. B*, **1986**, *33*, 8800.

[226] J.P. Perdew and Y. Wang, *Phys. Rev. B*, **1989**, *40*, 3399.

[227] S.F. Boys, *Proc. R. Soc. (London)*, **1950**, *A200*, 542.

[228] A.F. Jalbout, F. Nazari, L. Turker, *J. Mol. Struct. THEOCHEM*, **2004**, *671*, 1.

[229] D.J. Hehre, L. Radom, P.v.R. Schleyer, and J.A. Pople, Ab initio molecular orbital theory, Wiley, New York, **1986**.

[230] R. Dovesi, V.R. Saunders, C. Roetti, R. Orlando, C. M. Zicovich-Wilson, F. Pascale, B. Civalleri, K. Doll, N.M. Harrison, I.J. Bush, Ph. D'Arco, M. Llunell, CRYSTAL09 User's Manual, University of Torino, Torino, **2009.**

[231] R. Dovesi, C. Pisani, C. Roetti, M. Caus`a, and V.R. Saunders. CRYSTAL88, An ab initio all-electron LCAO-Hartree-Fock program for periodic systems. QCPE Pgm N.577. Quantum Chemistry Program Exchange, Indiana University, Bloomington, Indiana, **1989**.

[232] R. Dovesi, C. Roetti, and V.R. Saunders. CRYSTAL92 User's Manual. Universitá di Torino and SERC Daresbury Laboratory, **1992**.

[233] R. Dovesi, V.R. Saunders, C. Roetti, M. Caus`a, N. M. Harrison, R. Orlando, and E. Aprá. CRYSTAL95 User's Manual. Universitá di Torino, **1996**.

[234] V.R. Saunders, R. Dovesi, C. Roetti, M. Causá, N. M. Harrison, R. Orlando, and C.M. Zicovich-Wilson. CRYSTAL98 User's Manual. Universitá di Torino, Torino, **1998**.

[235] V.R. Saunders, R. Dovesi, C. Roetti, R. Orlando, C.M. Zicovich-Wilson, N. M. Harrison, K. Doll, B. Civalleri, I. Bush, Ph. D'Arco, and M. Llunell. CRYSTAL03 User's Manual. Universitá di Torino, Torino, **2003**.

[236] R. Dovesi, V.R. Saunders, C. Roetti, R. Orlando, C.M. Zicovich-Wilson, F. Pascale, B. Civalleri, K. Doll, N.M. Harrison, I.J. Bush, Ph. D'Arco, and M. Llunell. CRYSTAL06 User's Manual. Universitá di Torino, Torino, **2006**.

[237] R Dovesi, V. R. Saunders, R. Roetti, R. Orlando, C.M. Zicovich-Wilson, F. Pascale, B. Civalleri, K. Doll, N. M. Harrison, I. J. Bush, P. D'Arco, M. Llunell, CRYSTAL09 User's Manual. University of Torino: Torino, **2009**.

[238] H.J. Monkhorst and J.D. Pack, *Phys. Rev.*, **1976**, *13*, 5188.

[239] G. Gilat, *J. Comp. Phys.,* **1972**, *10*, 432.

[240] G. Gilat and L.J. Raubenheimer, *Phys. Rev.*, **1966**, *144*, 390.

[241] C.C.J. Roothaan, *Rev. Mod. Phy.*, **1951**, *23*, 69.

[242] G.G. Hall, *Proc. R. Soc. Lond. A*, **1951**, *205*, 541.

[243] B. Civalleria, Ph. D'Arcob, R. Orlando, V.R. Saunders, R. Dovesia, *Chem. Phys. Lett.*, **2001**, *34*, 131.

[244] C.G. Broyden, *IMA J. Appl. Math.*, **1970**, *6*, 76.

[245] C.G. Broyden, *IMA J. Appl. Math.*, **1970**, *6*, 222.

[246] R. Fletcher, *Comput. J*, **1970**, *13*, 317.

[247] D. Goldfarb, *Math. Comput.*, **1970**, *24*, 23.

[248] D.F. Shanno, *Math. Comput.,* **1970**, *24*, 647.

[249] B. Civalleri and C. Roetti. CRYSTAL Tutorial Project. http://www.theochem.unito.it/crystal_tuto/mssc2008_cd/tutorials/index.html (accessed July 30, 2013).

[250] F. Pascale, C.M. Zicovich-Wilson, F. Lopez Gejo, B. Civalleri, R. Orlando and R. Dovesi, *J. Comput. Chem.,* **2004**, *25*, 888.

[251] C.M. Zicovich-Wilson, F. Pascale, C. Roetti, V.R. Saunders, R. Orlando and R. Dovesi, *J. Comput. Chem.*, **2004**, *25*, 1873.

[252] C.M. Zicovich-Wilson, F. J. Torres, F. Pascale, L. Valenzano, R. Orlando and R. Dovesi, *J. Comput. Chem.*, **2008**, *29*, 2268.

# Chapter 2

# A Solid-state Density Functional Theory Investigation of the Structure and Vibrational Modes of Vanadium Phosphate Polymorphs

The material contained within this chapter is published in *Journal of Molecular Structure* (Pellizzeri, S.; Korter, T.M.; Zubieta, J. *J. Mol. Struct.* **2011**, *1003*, 21-30). This article has been reproduced with permission from Elsevier.

## 2.1 Introduction

Vanadium phosphates have been experimentally studied for decades and used commercially for their selective catalysis of n-butane to maleic anhydride since the mid-1960s.[1] These materials have more recently also found use as cathode materials in Li ion rechargeable batteries because of their ability to electrochemically intercalate and deintercalate Li.[2] The majority of modern investigations of vanadium phosphates have focused on their physical properties, while correlations of the structural and vibrational characteristics of these materials remain relatively unexplored.

In the broad field of vanadium phosphates, $VOPO_4$ could be considered the simplest of the vanadium(V) phosphate materials. However, it is structurally complex due to the existence of seven distinct crystal phases, $\alpha_1$, $\alpha_2$, $\beta$, $\varepsilon$, $\delta$, $\gamma$, and $\omega$.[2] Our understanding about these phases is somewhat limited because these polymorphs are difficult to synthesize as single crystals, necessitating the use of powder diffraction methods to determine structure. In this study, the three oldest known phases $\alpha_1$, $\alpha_2$, and $\beta$ are compared using mid-infrared vibrational spectroscopy coupled with solid-state density functional theory (DFT) calculations to show the differences in the vibrational modes caused by the subtle structural differences in each phase.

The $\alpha_1$, $\alpha_2$, and $\beta$ crystal phases of $VOPO_4$ have structures consisting of vanadium octahedra and phosphate tetrahedral units with small structural differences between phases. The $\alpha$ phases both contain a layered structure of vanadium octahedra and phosphate tetrahedra linked through extremely long V-O bonds (~2.5– 2.8 Å) as seen in **Figure 2.1**. The only structural difference between the two $\alpha$ phases is the location of the vanadium within its octahedron: in the $\alpha_1$ phase the vanadium is located on the same side of the equatorial plane as the phosphorus while in the $\alpha_2$ the vanadium is on the opposite side, as shown in **Figure 2.2**.[3]

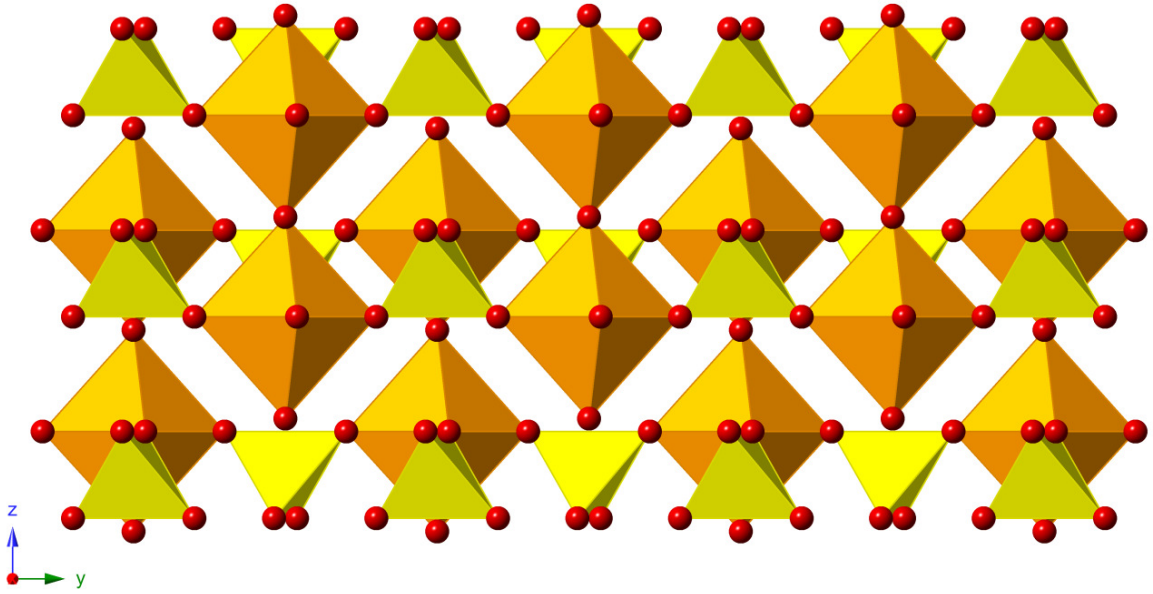


**Figure 2.1** Polyhedral representation of the crystal structure of the α phases of vanadium phosphate ($VOPO_4$) (vanadium is shown in orange, phosphorus is shown in yellow, and oxygen is shown in red).

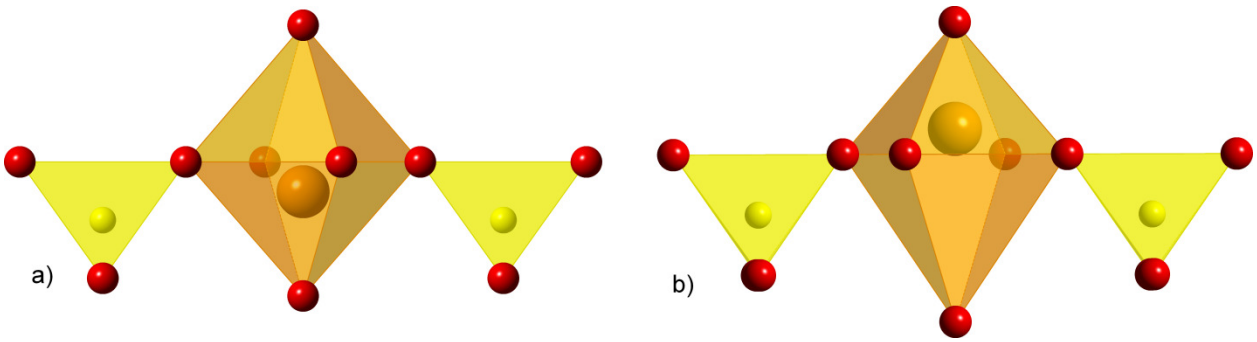


**Figure 2.2** -P-O-V-O-P- chain demonstrating the vanadium location within the octahedra for (a) $\alpha_1$-$VOPO_4$ and (b) $\alpha_2$-$VOPO_4$.

The α phases can also allow water molecules to be reversibly intercalated between these layers leading to hydrates such as $VOPO_4 \cdot H_2O$ and $VOPO_4 \cdot 2H_2O$.[4] The β phase differs from the α phases in that, instead of the layers being held together by long V=O···V interactions, it is comprised of a 3D network held together by the P-O-V interactions in all directions, as illustrated in **Figure 2.3**.

To study the various crystal phases of $VOPO_4$, the vibrational modes were simulated using solid-state DFT as implemented in CRYSTAL09. The CRYSTAL code has been used previously to simulate many inorganic systems to determine their structural, electronic and magnetic properties[5–7] and the vibrational spectra of organic systems.[8–10] Solid-state DFT methods utilize periodic boundary conditions which are required to accurately simulate vibrational motions that are perturbed by crystal packing forces and perhaps equally important, to couple external lattice motions to the internal ‘‘molecular’’ motions of the asymmetric repeat unit of the vanadium phosphate phases, which can be of great significance.

Due to the variation in space group symmetries of the $VOPO_4$ crystal phases, differences can be seen in the number and location of the vibrational modes. The aim of this research is to use FT-IR coupled with the simulated frequency and intensity of the vibrational modes to show the ability of solid-state DFT to determine and predict the subtle spectral differences and similarities between the $\alpha_1$, $\alpha_2$, and β crystal phases of $VOPO_4$.

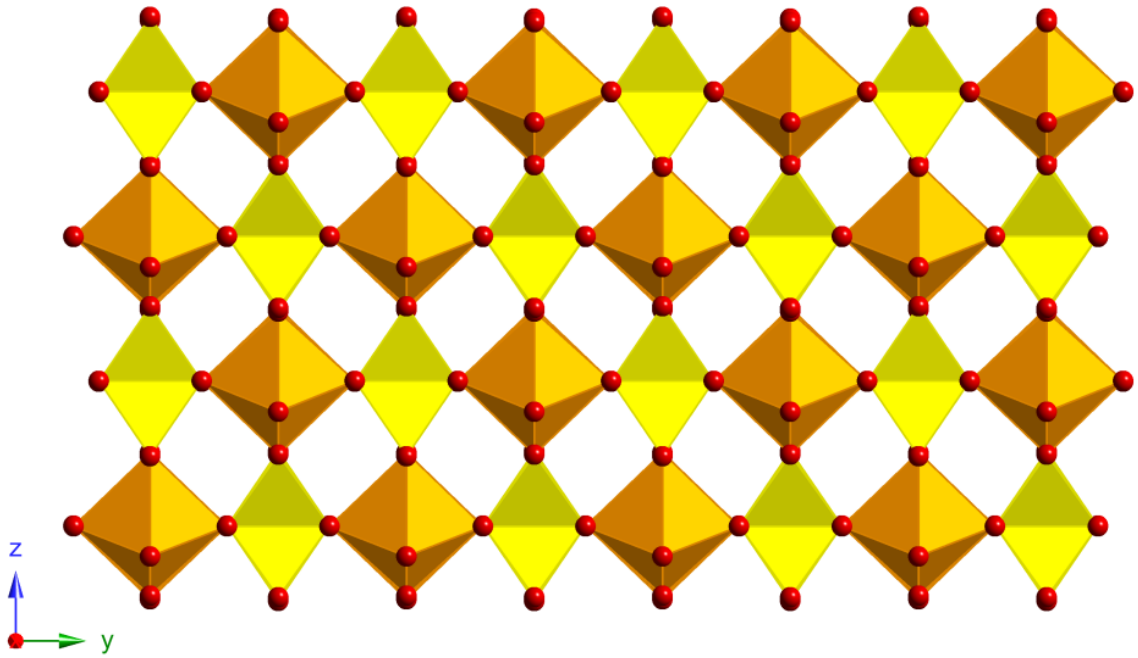


**Figure 2.3** Polyhedral representation of the crystal structure of the β phase of vanadium phosphate ($VOPO_4$) (vanadium is shown in orange, phosphorus in yellow, and oxygen in red).

## 2.2 Experimental and Theoretical Methods

### *2.2.1 Synthesis of $VOPO_4 \cdot 2H_2O$ and $VOPO_4$*

Vanadium(V) oxide (98%), phosphoric acid (85 wt.% in H2O), and molybdenum trioxide (99.5%) were purchased from Aldrich and used without further purification. Water was distilled above 3.0 MΩ in-house using a Barnstead Model 525 Biopure Distilled Water Center. The various phases of $VOPO_4$ were prepared on a TA Q500 series thermogravimetric analysis (TGA) instrument under flowing nitrogen on a platinum TGA pan. The infrared spectra were obtained on a Thermo Nicolet IR200 FT-IR using the KBr pellet method and a spectral resolution of 4 $cm^{-1}$ over the range of 4000–400 $cm^{-1}$. The KBr was dried prior to usage.

#### *2.2.1.1 Synthesis of $VOPO_4 \cdot 2H_2O$*

$VOPO_4 \cdot 2H_2O$ was prepared according to literature procedures by refluxing a mixture of $V_2O_5$ (0.5 g), 85% $H_3PO_4$ (4.46 g), and $H_2O$ (12 mL) at 403 K for 16 h.[4] The yellow product was filtered, washed with acetone, and kept under ambient conditions. Infrared spectroscopy was used to confirm the product identity.[11]

#### *2.2.1.2 Synthesis of $\alpha_1$-$VOPO_4$, $\alpha_2$-$VOPO_4$, and $\beta$-$VOPO_4$*

The procedure used to produce the phases of $VOPO_4$ is similar to that previously reported;[4] however, the procedure was modified as follows. The initial hydrate was finely ground prior to the TGA cycle and after the initial run was removed from the TGA and ground again prior to the final TGA cycle. This is done to ensure a thorough conversion of the hydrate to the intended phase. Thus, $\alpha_1$-$VOPO_4$ was prepared by heating approximately 5 mg of $VOPO_4 \cdot 2H_2O$ to 673 K at 5 K/min and held at this temperature for 30 min. $\alpha_2$-$VOPO_4$ was prepared by first

grinding together $VOPO_4 \cdot 2H_2O$ and 1% by weight of $MoO_3$ and allowing this mixture to sit overnight under ambient conditions. Subsequently, approximately 5 mg of this mixture was heated to 973K at 5 K/min and held at this temperature for 30 min. β-$VOPO_4$ was prepared by heating approximately 5 mg of $VOPO_4 \cdot 2H_2O$ to 973 K at 20 K/min and holding at this temperature for 30 min. The infrared spectra were obtained immediately after the second cycle was completed to reduce the chance of rehydration to the dihydrate phase.

### *2.2.2 Theoretical Methodology of CRYSTAL09*

Geometry optimizations, harmonic frequencies, and infrared (IR) intensity calculations were performed using the CRYSTAL09 program.[12,13] All calculations were performed using the PBE0[14] hybrid density functional. The basis set chosen for vanadium was the V_86-411d31G basis set[15] and for phosphorus the P_85-21d1G [16] basis set. Due to the limited number of basis sets that have been optimized for use in CRYSTAL09 for large atoms, the vanadium and phosphorous basis sets that were used for these calculations were those with the largest number of orbital descriptions and those most recently published. Five different oxygen basis sets were used to compare basis sets optimized for use in CRYSTAL versus standard Pople basis sets. The Pople basis set used was the 6-31G(d,p) Gaussian-type basis set[17,18] obtained from the EMSL Basis Set Exchange.[19,20] The basis sets that were optimized for use with CRYSTAL were O_6-31d1,[21] O_8-411d1_2005,[22] O_8-411d1_2006,[23] and O_8-411d11G.[24]

The positions of the atoms contained within the unit cell were optimized within the constraints of the literature lattice parameters and space group symmetry. The experimental coordinates were used as starting positions for the simulation of the $\alpha_1$, $\alpha_2$, and β crystal phases of $VOPO_4$.[25–27] It should be noted that since the atomic coordinates for $\alpha_1$-$VOPO_4$ have yet to be obtained experimentally, the structure is assumed to be the isomorphous with α-$VOSO_4$ as

suggested by Tachez et al.[3] Using the atomic coordinates from α-$VOSO_4$ as a starting point, the atomic positions were adjusted to give bond length values corresponding to the longest bond length and edge–edge distances given by Tachez et al.[3] The atomic positions used are listed in **Table 2.1**.

From the optimized structures, the bond lengths and bond angles were determined and compared with the experimental crystallographic results. After optimizing the structures, harmonic- limit normal-mode analyses on the $VOPO_4$ phases were conducted. Frequencies were determined by a mass-weighted numerical evaluation of the Hessian matrix[28] and infrared intensities were calculated through the Berry phase approach.[13] The Berry phase approach consists of evaluating the Born charges, based on the derivative of the dipole moment with respect to the atomic displacements, as polarization differs between the equilibrium and the normal-mode displaced geometries; the polarization difference is then equal to the time-integrated transient macroscopic current that flows through the insulating sample during the vibrations.[13]

Several of the convergence parameters were changed to optimize the accuracy and computational time of the calculations. The convergence criteria were modified to set the root mean square of the maximum gradient (TOLDEG) and the maximum displacement (TOLDEX) to be 0.00001 and 0.00004 angstroms, respectively. To improve the numerical accuracy of the calculations the truncation criteria for bielectronic integrals (TOLINTEG) was set to 8 8 8 8 16 and the DFT integration was set to XLGRID (75,974) (see Refs. [12,13] for details). Total energy convergence (TOLDEE) was set to DE < $1 \times 10^{-8}$ Hartree for the geometry optimizations, and DE < $1 \times 10^{-11}$ Hartree for frequency analyses. To assist in a timely convergence, the ‘‘Fock/KS matrix mixing’’ (FMIXING) was increased from the default value of zero to 50 for all

**Table 2.1** Modified atomic coordinates used for the initial structure of $\alpha_1$-$VOPO_4$.

| Space Group | P4/n | | |
|---|---|---|---|
| Unit Cell Dimensions | a= 6.20, c= 4.11 | | |
| Atom | x | y | z |
| V | 0 | 0.5 | 0.6052 |
| P | 0 | 0 | 0.5 |
| O1 | 0 | 0.5 | 0.22 |
| O2 | 0.7 | 0.462 | 0.715 |

three systems. The eigenvalue level shifter was also activated with the level shifter set to a value that corresponds to a shift of 0.5 Hartree, and the state was locked, confining it to an insulating state (see Refs. [12,13] for details). Determination of the optimum sampling of reciprocal space was performed by comparing the total energy of the converged system to the k-point count using the keyword SHRINK. The optimum SHRINK values for the $VOPO_4$ phases were determined to be SHRINK = 8 which corresponds to 260 points in the Brillouin zone.

## 2.3 Results and discussion

### *2.3.1 Comparison of the Calculated and Experimental Structures*

The calculated and X-ray experimental bond lengths, bond angles, and the root-mean-squared deviation (RMSD) values are shown in **Tables 2.2–2.4** (see **Figures 2.4 and 2.5** for the labeling scheme) for each of the phases of $VOPO_4$, and the results are visualized in **Figure 2.6**.

Each of the phases behaved differently with the five oxygen basis sets investigated, demonstrating the importance of basis set choice on the accuracy of a simulation when considering subtle structural variations.

For the $\alpha_1$ phase, the basis set that most accurately represented the bond lengths was 6-31G(d,p), while the worst was O_8-411d11G. The basis set that best represented the bond angles for the $\alpha_1$ phase was 6-31G(d,p), and the one that most poorly predicted the angles was O_6-31d1. However, since there are no definitive atomic coordinates to use as an experimental comparison, it is difficult to truly compare the bond lengths and angles for this phase because of the limitation of comparing them to those of $\alpha$-$VOSO_4$. For the $\alpha_2$ phase, the basis set that provided the most accurate representation of the bond lengths and angles was O_8-411d1_2006,

**Table 2.2** Interatomic bond lengths (Å), angles (°), and RMSD values for $\alpha_1$-$VOPO_4$. See **Figure 2.4** for atomic labels. Lowest RMSD values are shown in bold. Experimental parameters are from Ref. [25].

| Bond, Å | Experiment | 6-31G(d-p) | 6-31d1 | 8-411d1_2005 | 8-411d1_2006 | 8-411d11G |
|---|---|---|---|---|---|---|
| **V-O1a** | 1.5832 | 1.5670 | 1.5538 | 1.5612 | 1.5649 | 1.5536 |
| **V-O1b** | 2.5268 | 2.5430 | 2.5560 | 2.5488 | 2.5451 | 2.5564 |
| **V-O2** | 1.9284 | 1.9016 | 1.8875 | 1.8840 | 1.8814 | 1.8855 |
| **P-O2** | 1.5408 | 1.5539 | 1.5395 | 1.5435 | 1.5446 | 1.5405 |
| | **RMSD** | **0.01881** | 0.02912 | 0.02714 | 0.02689 | 0.02997 |

| Angle, ° | Experiment | 6-31G(d-p) | 6-31d1 | 8-411d1_2005 | 8-411d1_2006 | 8-411d11G |
|---|---|---|---|---|---|---|
| **O1a-V-O2** | 103.534 | 101.407 | 101.108 | 101.800 | 101.824 | 101.923 |
| **O1b-V-O2** | 76.466 | 78.593 | 78.892 | 78.200 | 78.176 | 78.077 |
| **O1a-V-O1b** | 180.000 | 180.000 | 180.000 | 180.000 | 180.000 | 180.000 |
| **O2a-V-O2a** | 86.861 | 87.758 | 87.873 | 87.603 | 87.594 | 87.554 |
| **O2a-V-O2b** | 152.933 | 157.186 | 157.784 | 156.400 | 156.351 | 156.154 |
| **O2a-P-O2a** | 110.009 | 110.171 | 110.532 | 109.255 | 109.337 | 109.240 |
| **O2a-P-O2b** | 109.203 | 109.123 | 108.943 | 109.579 | 109.538 | 109.587 |
| **V-O2-P** | 128.562 | 130.560 | 132.693 | 132.564 | 132.712 | 132.628 |
| **V-O1-V** | 180.000 | 180.000 | 180.000 | 180.000 | 180.000 | 180.000 |
| | **RMSD** | **1.8846** | 2.4434 | 1.9807 | 1.9960 | 1.9240 |

**Table 2.3** Interatomic bond lengths (Å), angles (°), and RMSD values for $\alpha_2$-$VOPO_4$. See **Figure 2.4** for atomic labels. Lowest RMSD values are shown in bold. Experimental parameters are from Ref. [26].

| Bond, Å | Experiment | 6-31G(d,p) | 6-31d1 | 8-411d1_2005 | 8-411d1_2006 | 8-411d11G |
|---|---|---|---|---|---|---|
| **V-O1a** | 1.5781 | 1.5667 | 1.5532 | 1.5621 | 1.5659 | 1.5548 |
| **V-O1b** | 2.8559 | 2.8673 | 2.8808 | 2.8719 | 2.8681 | 2.8792 |
| **V-O2** | 1.8581 | 1.8855 | 1.8716 | 1.8687 | 1.8648 | 1.8693 |
| **P-O2** | 1.5424 | 1.5468 | 1.5323 | 1.5369 | 1.5377 | 1.5346 |
| | **RMSD** | 0.01605 | 0.01952 | 0.01279 | **0.00955** | 0.01783 |

| Angle, ° | Experiment | 6-31G(d,p) | 6-31d1 | 8-411d1_2005 | 8-411d1_2006 | 8-411d11G |
|---|---|---|---|---|---|---|
| **O1a-V-O2** | 101.675 | 101.980 | 102.032 | 101.509 | 101.464 | 101.359 |
| **O1b-V-O2** | 78.325 | 78.020 | 77.968 | 78.491 | 78.536 | 78.641 |
| **O1a-V-O1b** | 180.000 | 180.000 | 180.000 | 180.000 | 180.000 | 180.000 |
| **O2a-V-O2a** | 87.653 | 87.531 | 87.509 | 87.719 | 87.736 | 87.777 |
| **O2a-V-O2b** | 156.650 | 156.041 | 155.936 | 156.982 | 157.072 | 157.282 |
| **O2a-P-O2a** | 109.282 | 109.433 | 109.671 | 109.192 | 109.068 | 109.222 |
| **O2a-P-O2b** | 109.566 | 109.490 | 109.372 | 109.611 | 109.673 | 109.595 |
| **V-O2-P** | 147.237 | 144.443 | 147.005 | 146.385 | 146.723 | 146.291 |
| **V-O1-V** | 180.000 | 180.000 | 180.000 | 180.000 | 180.000 | 180.000 |
| | **RMSD** | 0.9665 | 0.3380 | 0.3172 | **0.2572** | 0.4101 |

**Table 2.4** Interatomic bond lengths (Å), angles (°), and RMSD values for β-$VOPO_4$. See **Figure 2.4** for atomic labels. Lowest RMSD values are shown in bold. Experimental parameters are from Ref. [27].

| Bond, Å | Experiment | 6-31G(d,p) | 6-31d1 | 8-411d1_2005 | 8-411d1_2006 | 8-411d11G |
|---|---|---|---|---|---|---|
| **V-O1** | 1.8863 | 1.8863 | 1.8806 | 1.8822 | 1.8799 | 1.8843 |
| **V-O2** | 1.8533 | 1.8536 | 1.8383 | 1.8404 | 1.8385 | 1.8388 |
| **V-O3** | 1.9021 | 1.9248 | 1.9072 | 1.8985 | 1.8944 | 1.9000 |
| **V-O4a** | 1.5649 | 1.5634 | 1.5500 | 1.5580 | 1.5632 | 1.5514 |
| **V-O4b** | 2.5915 | 2.5486 | 2.5750 | 2.5900 | 2.5839 | 2.5973 |
| **P-O1** | 1.5275 | 1.5412 | 1.5275 | 1.5343 | 1.5361 | 1.5318 |
| **P-O2** | 1.5388 | 1.5619 | 1.5494 | 1.5525 | 1.5539 | 1.5505 |
| **P-O3** | 1.5174 | 1.5382 | 1.5263 | 1.5330 | 1.5350 | 1.5300 |
| | **RMSD** | 0.02095 | 0.01101 | **0.00951** | 0.01113 | 0.00967 |

| Angle, ° | Experiment | 6-31G(d,p) | 6-31d1 | 8-411d1_2005 | 8-411d1_2006 | 8-411d11G |
|---|---|---|---|---|---|---|
| **O1-V-O1** | 154.340 | 153.082 | 155.016 | 154.019 | 154.234 | 154.090 |
| **O1-V-O2** | 88.292 | 88.036 | 88.559 | 87.897 | 87.846 | 87.920 |
| **O1-V-O3** | 87.498 | 87.626 | 87.139 | 87.589 | 87.643 | 87.517 |
| **O1-V-O4a** | 102.814 | 103.452 | 102.468 | 102.985 | 102.880 | 102.949 |
| **O1-V-O4b** | 77.170 | 76.551 | 77.508 | 77.011 | 77.119 | 77.046 |
| **O2-V-O3** | 160.948 | 161.280 | 159.971 | 159.818 | 159.666 | 159.541 |
| **O2-V-O4a** | 100.550 | 100.286 | 100.202 | 100.997 | 100.902 | 101.072 |
| **O2-V-O4b** | 82.454 | 83.740 | 82.956 | 81.413 | 81.245 | 81.268 |
| **O3-V-O4a** | 98.502 | 98.434 | 99.827 | 99.185 | 99.432 | 99.386 |
| **O3-V-O4b** | 78.494 | 77.540 | 77.015 | 78.406 | 78.420 | 78.273 |
| **O4a-V-O4b** | 176.997 | 175.974 | 176.842 | 177.590 | 177.853 | 177.659 |
| **O1-P-O1** | 107.554 | 106.766 | 107.959 | 107.513 | 107.521 | 107.480 |
| **O1-P-O2** | 108.965 | 109.251 | 109.066 | 109.200 | 109.212 | 109.168 |
| **O1-P-O3** | 110.290 | 109.971 | 109.976 | 109.566 | 109.503 | 109.565 |
| **O2-P-O3** | 110.704 | 111.511 | 110.742 | 111.701 | 111.791 | 111.794 |
| **V-O1-P** | 138.458 | 137.463 | 139.013 | 138.145 | 138.158 | 138.213 |
| **V-O2-P** | 138.387 | 136.130 | 137.252 | 137.189 | 137.064 | 137.196 |
| **V-O3-P** | 154.153 | 153.560 | 154.744 | 153.272 | 153.257 | 153.272 |
| **V-O4-V** | 137.713 | 140.972 | 140.046 | 138.435 | 138.565 | 138.393 |
| | **RMSD** | 1.1416 | 0.8537 | **0.6535** | 0.7364 | 0.7123 |

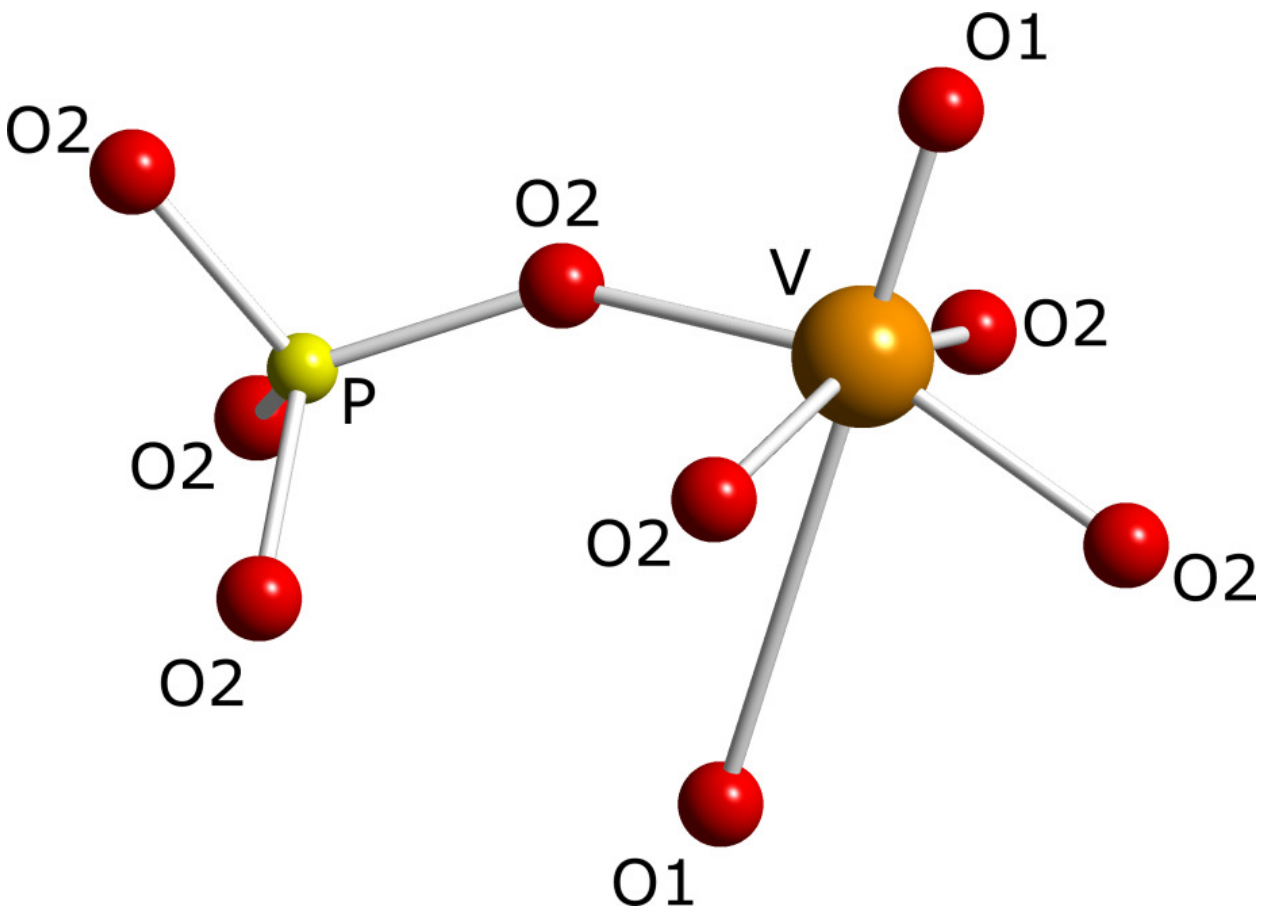


**Figure 2.4** The atom labeling for the α phases of vanadium phosphate ($VOPO_4$).

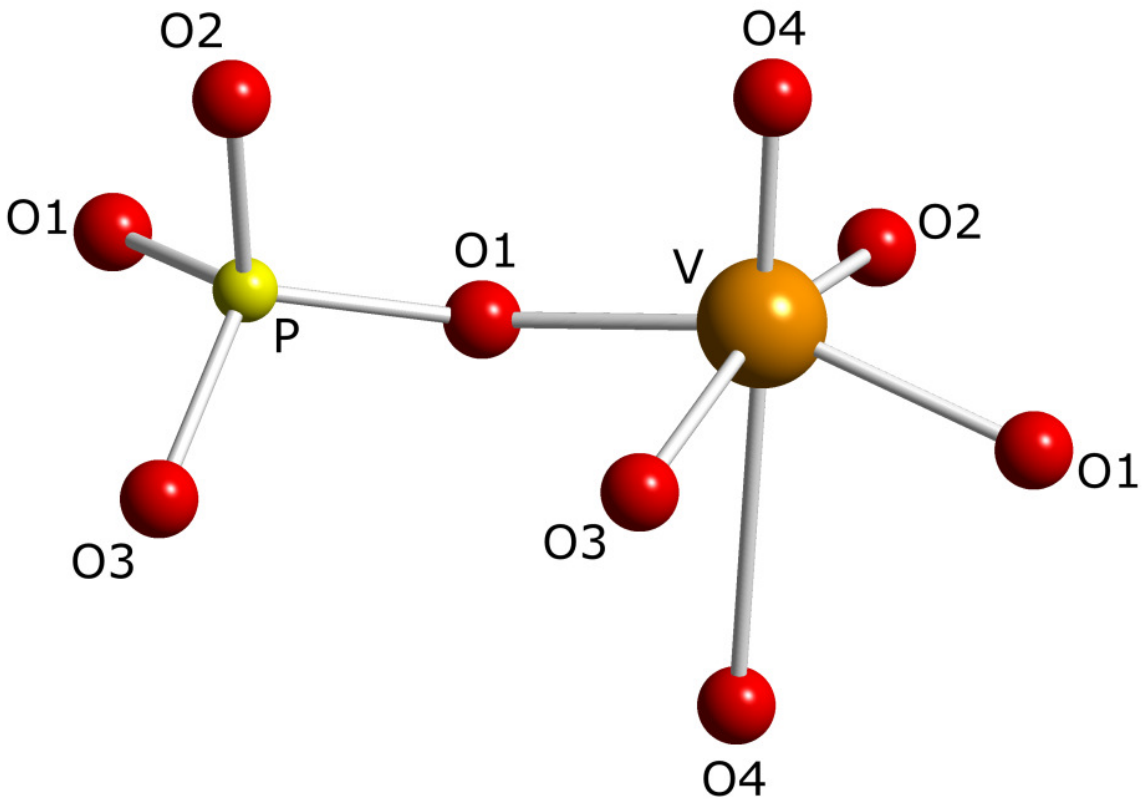


**Figure 2.5** The atom labeling for the β phase of vanadium phosphate ($VOPO_4$).

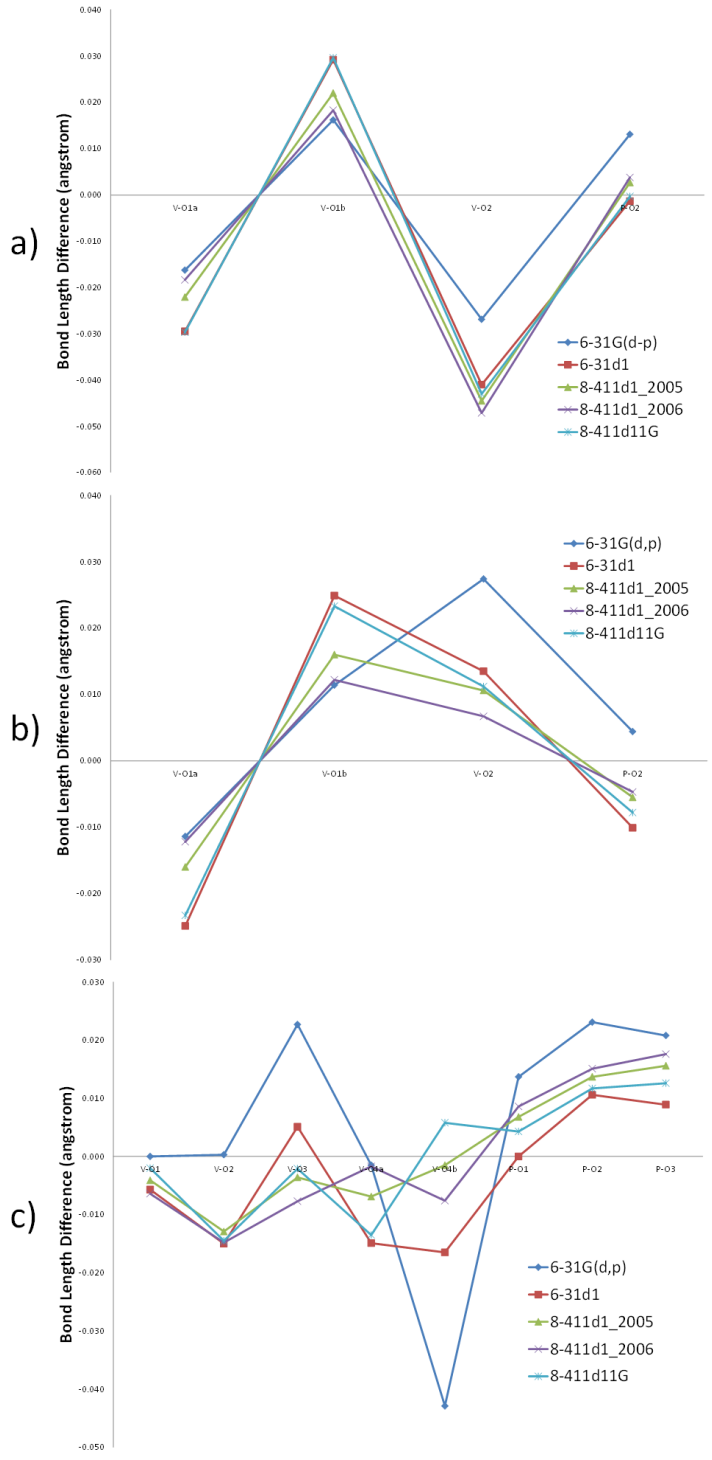


**Figure 2.6** Calculated bond-length differences for each oxygen basis set compared to the structure determined through powder X-ray diffraction. Bond-length comparison for (a) $\alpha_1$-$VOPO_4$, (b) $\alpha_2$-$VOPO_4$, and (c) $\beta$-$VOPO_4$.

while the worst performing basis sets representing the bond lengths and angles were O_6-31d1 and 6-31G(d,p), respectively. For the β phase, the basis set that most accurately represented the bond lengths and angles was O_8-411d1_2005. The basis set that worst represented the bond lengths and angles for the β phase was 6-31G(d,p). **Table 2.5** shows the average RMSD values for the bond lengths and angles for each of the explored basis sets of oxygen. Overall, the basis set that most adequately modeled the crystalline structures of the various polymorphs of $VOPO_4$ was O_8-411d1_2006.

As demonstrated, the necessity to evaluate multiple basis sets is apparent in the use of CRYSTAL09 because a small numerical difference in the description of the molecular orbitals greatly affects the accuracy of the simulations. Basis set choice can change the numerical results drastically from material to material even in instances where the only change may be in the structural morphology of the same material.

### *2.3.2 Comparison of Theoretical and Experimental Vibrational Frequencies*

The experimental and calculated infrared spectra are shown in **Figures 2.7-2.9**, and the results are summarized in **Tables 2.6–2.8** for each of the phases of $VOPO_4$. Analysis of the vibrational modes is shown in **Table 2.9**. Once again, the various polymorphs exhibited sensitivity to the different oxygen basis sets.

For the $\alpha_1$ phase the basis set that provided the most accurate representation of the infrared spectrum was O_8-411d1_2005, while the worst was 6-31G(d,p). For the $\alpha_2$ phase, two basis sets most precisely duplicated the infrared spectrum, 6-31G(d,p) and O_8-411d1_2005, while the worst was O_6-31d1. For the β phase, the basis set that provided the closest for the infrared spectrum was 6-31G(d,p), while the worst was O_6-31d1. The agreements between

**Table 2.5** Average RMSD values for interatomic bond lengths (Å), angles (°). The average does not include the values from $\alpha_1$-$VOPO_4$. The lowest average RMSD values are shown in bold.

| Bond | 6-31G(d,p) | 6-31d1 | 8-411d1_2005 | 8-411d1_2006 | 8-411d11G |
|---|---|---|---|---|---|
| $\alpha_1$ | 0.01881 | 0.02912 | 0.02714 | 0.02689 | 0.02997 |
| $\alpha_2$ | 0.01605 | 0.01952 | 0.01279 | 0.00955 | 0.01783 |
| $\beta$ | 0.02095 | 0.01101 | 0.00951 | 0.01113 | 0.00967 |
| **Average** | 0.01860 | 0.01988 | 0.01648 | **0.01586** | 0.01916 |

| Angle | 6-31G(d,p) | 6-31d1 | 8-411d1_2005 | 8-411d1_2006 | 8-411d11G |
|---|---|---|---|---|---|
| $\alpha_1$ | 1.8846 | 2.4434 | 1.9807 | 1.9960 | 1.9240 |
| $\alpha_2$ | 0.9665 | 0.3380 | 0.3172 | 0.2572 | 0.4101 |
| $\beta$ | 1.1416 | 0.8537 | 0.6535 | 0.7364 | 0.7123 |
| **Average** | 1.3309 | 1.2117 | **0.9838** | 0.9965 | 1.0155 |

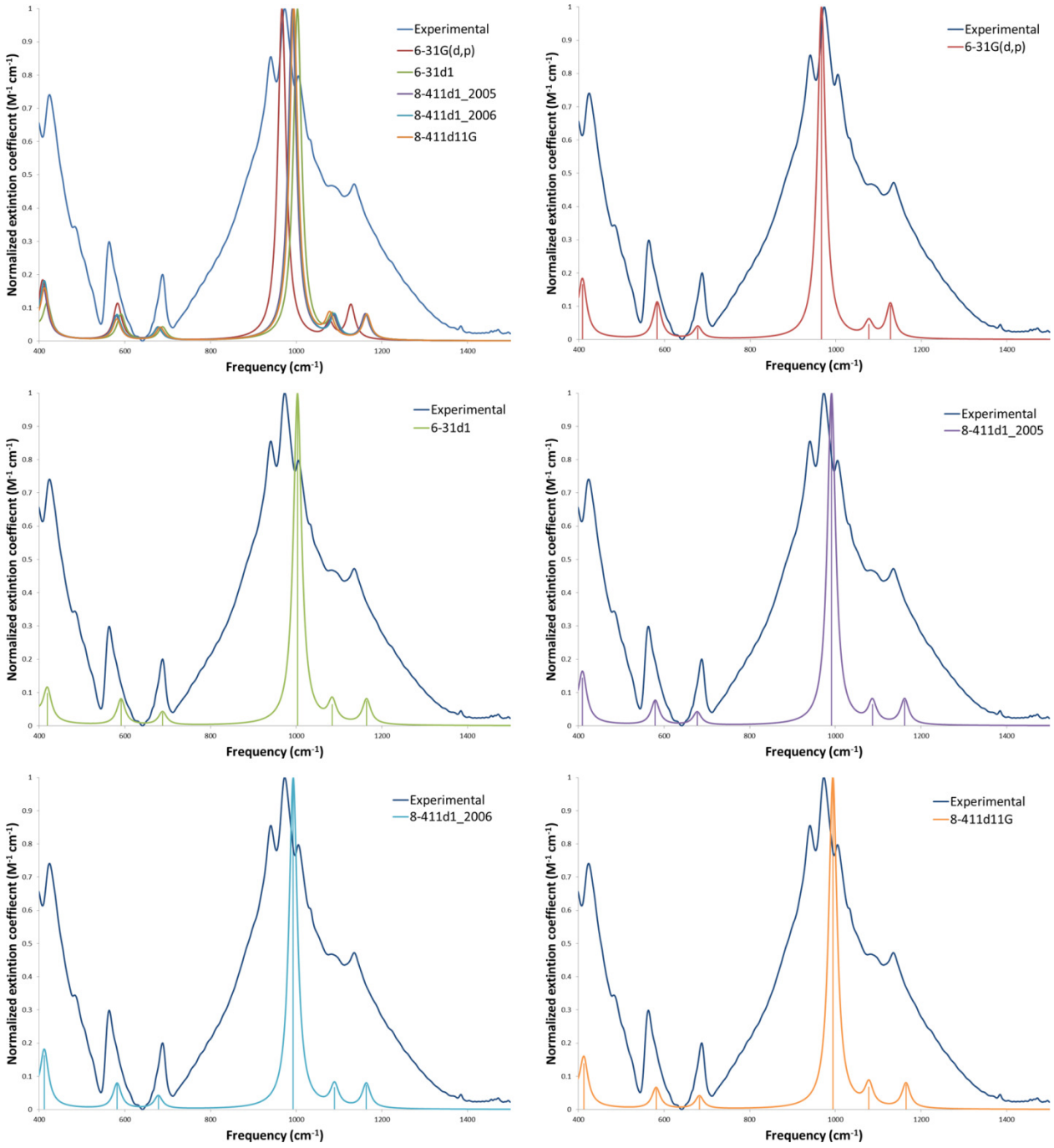


**Figure 2.7** The normalized experimental and theoretical traces for the infrared vibrational spectra of $\alpha_1$-$VOPO_4$. An empirical 11.62 $cm^{-1}$ full-width-half-maximum Lorentzian line shape has been applied to the theoretical data to aid in comparison.

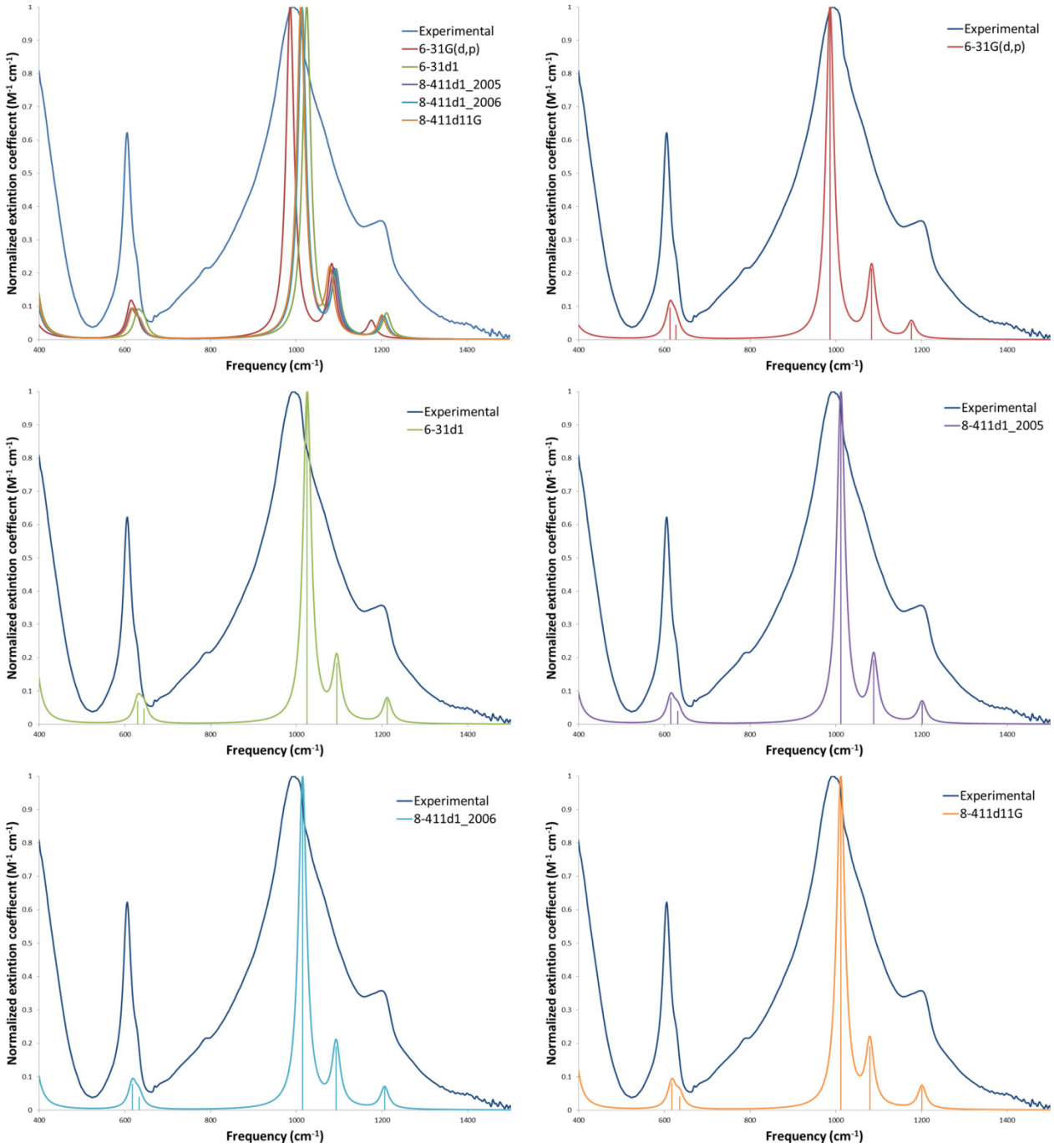


**Figure 2.8** The normalized experimental and theoretical traces for the infrared vibrational spectra of $\alpha_2$-$VOPO_4$. An empirical 11.62 $cm^{-1}$ full-width-half-maximum Lorentzian line shape has been applied to the theoretical data to aid in comparison.

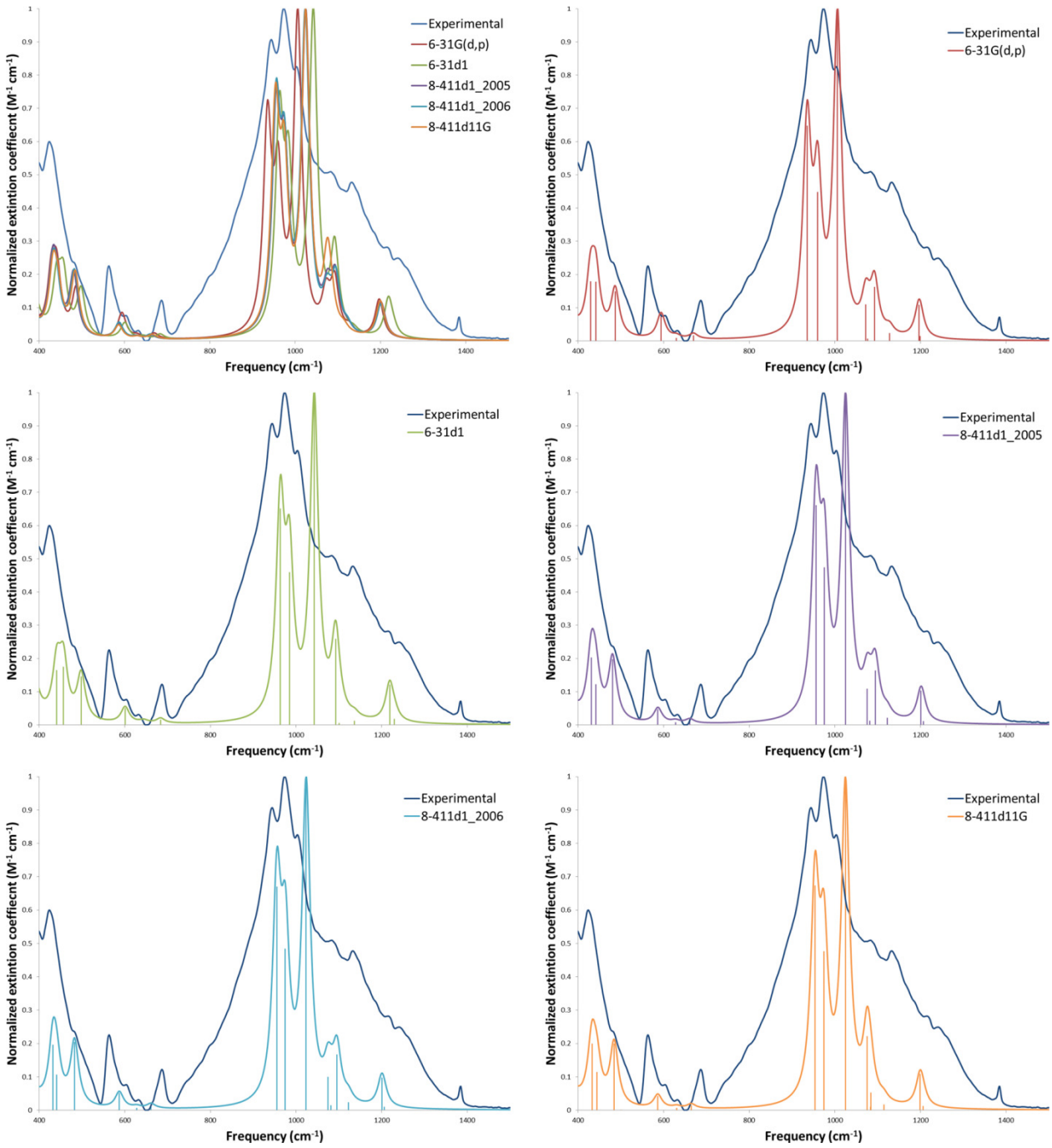


**Figure 2.9** The normalized experimental and theoretical traces for the infrared vibrational spectra of β-$VOPO_4$. An empirical 11.62 $cm^{-1}$ full-width-half-maximum Lorentzian line shape has been applied to the theoretical data to aid in comparison.

**Table 2.6** Frequency positions ($cm^{-1}$) and RMSD ($cm^{-1}$) of $\alpha_1$-$VOPO_4$ for the experimental and theoretical infrared spectra. The blanks are peaks that have no obvious correlation between experiment and theory. Lowest RMSD values are shown in bold.

| **Experiment** | **6-31G(d,p)** | **6-31d1** | **8-411d1_2005** | **8-411d1_2006** | **8-411d11G** |
|---|---|---|---|---|---|
| 424.3 | 408.8 | 418.5 | 408.8 | 410.8 | 412.7 |
| 563.1 | 582.4 | 590.1 | 578.5 | 582.4 | 580.5 |
| 688.5 | 676.9 | 688.5 | 676.9 | 678.8 | 682.7 |
| 941.1 | ---- | ---- | ---- | ---- | ---- |
| 971.9 | ---- | ---- | ---- | ---- | ---- |
| 1004.7 | 966.2 | 1002.8 | 991.2 | 993.2 | 993.2 |
| 1083.8 | 1078.0 | 1083.8 | 1085.7 | 1089.6 | 1078.0 |
| 1135.9 | 1128.2 | 1164.8 | 1161.0 | 1162.9 | 1164.8 |
| **RMSD** | 21.6 | 17.9 | **16.9** | 17.6 | 17.2 |

**Table 2.7** Frequency positions ($cm^{-1}$) and RMSD ($cm^{-1}$) of $\alpha_2$-$VOPO_4$ for the experimental and theoretical infrared spectra. The blanks are peaks that have no obvious correlation between experiment and theory. Lowest RMSD values are shown in bold.

| Experiment | 6-31G(d,p) | 6-31d1 | 8-411d1_2005 | 8-411d1_2006 | 8-411d11G |
|---|---|---|---|---|---|
| 605.5 | 615.2 | 632.5 | 615.2 | 619.0 | 619.0 |
| 624.8 | 624.8 | 640.6 | 628.7 | 628.7 | 632.5 |
| 991.2 | 985.4 | 1025.9 | 1012.4 | 1014.4 | 1010.5 |
| ---- | 1083.8 | 1093.4 | 1087.7 | 1091.5 | 1078.0 |
| 1197.6 | 1176.4 | 1211.1 | 1201.4 | 1205.3 | 1201.4 |
| **RMSD** | **12.0** | 24.3 | **12.0** | 14.1 | 12.5 |

**Table 2.8** Frequency positions ($cm^{-1}$) and RMSD ($cm^{-1}$) of β-$VOPO_4$ for the experimental and theoretical infrared spectra. The blanks are peaks that have no obvious correlation between experiment and theory. Lowest RMSD values are shown in bold.

| Experiment | 6-31G(d,p) | 6-31d1 | 8-411d1_2005 | 8-411d1_2006 | 8-411d11G |
|---|---|---|---|---|---|
| 424.3 | 435.8 | 443.5 | 433.9 | 433.9 | 433.9 |
| 482.1 | 486.0 | 497.5 | 480.2 | 482.1 | 484.0 |
| 563.1 | --- | --- | --- | --- | --- |
| 603.6 | 594.0 | 599.8 | 586.3 | 586.3 | 586.3 |
| 632.5 | 626.8 | 642.2 | 626.8 | 626.8 | 628.7 |
| 686.5 | 669.2 | 682.7 | 659.5 | 661.5 | 663.4 |
| 944.9 | 935.3 | 964.2 | 956.5 | 956.5 | 954.6 |
| 973.9 | 958.4 | 983.5 | 971.9 | 971.9 | 971.9 |
| 1002.8 | 1006.7 | 1043.3 | 1024.0 | 1024.0 | 1024.0 |
| 1083.8 | 1082.8 | 1091.5 | 1084.8 | 1084.8 | 1076.1 |
| 1132.0 | 1124.3 | 1133.9 | 1120.4 | 1120.4 | 1112.7 |
| 1214.9 | 1197.6 | 1218.8 | 1201.4 | 1201.4 | 1199.5 |
| **RMSD** | **10.8** | 16.3 | 13.7 | 13.3 | 14.0 |

**Table 2.9** Empirical normal mode analysis for the polymorphs of vanadium phosphate.

| $\alpha_1$-VOPO4 | Normal Mode |
|---|---|
| 424.3 | $\delta_{P-O} + \delta_{V-O}$ |
| 563.1 | $\delta_{P-O}$ |
| 688.5 | $\delta_{P-O}$ |
| 1004.7 | $v_{P-O}^{as}$ |
| 1083.8 | $v_{V-O}$ |
| 1135.9 | $v_{P-O}^{as}$ |

| $\alpha_2$-VOPO4 | Normal Mode |
|---|---|
| 605.5 | $\delta_{P-O}$ |
| 624.8 | $\delta_{P-O}$ |
| 991.2 | $v_{P-O}^{as}$ |
| 1087.0 | $v_{V-O}$ |
| 1197.6 | $v_{P-O}^{as}$ |

| β-VOPO4 | Normal Mode |
|---|---|
| 424.3 | $\delta_{P-O} + \delta_{V-O}$ |
| 482.1 | $\delta_{P-O} + \delta_{V-O}$ |
| 563.1 | $\delta_{P-O} + \delta_{V-O}$ |
| 603.6 | $\delta_{P-O} + v_{V-O}^{as}$ |
| 632.5 | $\delta_{P-O}$ |
| 686.5 | $\delta_{P-O} + v_{V-O}$ |
| 944.9 | $v_{P-O}^{as}$ |
| 973.9 | $v_{P-O}^{as}$ |
| 1002.8 | $v_{P-O}^{as}$ |
| 1083.8 | $v_{P-O} + v_{V-O}$ |
| 1132.0 | $v_{V-O}^{as}$ |
| 1214.9 | $v_{P-O}^{as}$ |

theory and experiment were all good based on the low RMSD values, but the best overall performer was the O_8-411d1_2005 basis set.

Each phase has a different number of peaks in the range between 400 and 1500 $cm^{-1}$. When an empirically-determined Lorentzian line shape with a full width at half-maximum of 11.62 $cm^{-1}$ is added to the theoretical line spectra, the low intensity peaks and the strong peaks coalesce to give a representation that can be easily compared to the experimental IR spectra shown in **Figures 2.7–2.9**. This allows correlations between theory and experiment to be readily made.

From the experimental spectrum for the $\alpha_1$ phase, eight peaks are observed, while in the theoretical only six are obtained. Two peaks that are apparent in the experimental spectrum and not in the theoretical spectrum occur at 941.1 $cm^{-1}$ and 971.9 $cm^{-1}$. These two peaks can be explained as a possible consequence of the sample not being fully dehydrated prior to the spectrum being recorded or the conversion of the $\alpha_1$ phase back to the starting dihydrate. The higher frequency peak is the result of the 1004.7 $cm^{-1}$ peak shifting to 971.9 $cm^{-1}$, and the peak at 941.1 $cm^{-1}$ corresponds to a major peak in the hydrated form $VOPO_4 \cdot 2H2O$ as suggested in previous literature.[29,30]

In the experimental spectrum for the $\alpha_2$ phase, four peaks are observed, while in the simulation, five are obtained. The theoretical spectrum places a peak at ~1086 $cm^{-1}$, which is not observed in the experimental spectrum. This is most likely due to the peak being hidden within the bandwidth of the observed 991 $cm^{-1}$ peak.

From the experimental spectrum for the β phase, 13 peaks are observed, while in the theoretical spectrum only 12 were predicted. In all of the spectra, one peak is missing as they all lack a feature to be correlated with the 563.1 $cm^{-1}$ experimental absorption. This 563.1 $cm^{-1}$ peak

most likely originates from $VOPO_4 \cdot 2H_2O$ contamination which has been reported to contain a 569 $cm^{-1}$ vibration.[30] It should be noted that in the 6-31G(d,p), O_8- 411d1_2005, and O_8-411d1_2006 basis set spectra the peak at 1083 $cm^{-1}$ is split into two separate peaks, so for comparison to the experimental results, the two peaks are averaged and are reported in **Table 2.8**.

## 2.4 Conclusions

The solid-state simulation of the crystalline structures and vibrational frequencies of three phases of $VOPO_4$ have been performed using several different basis sets describing the electron density associated with the oxygen atoms. This was done to illustrate that small differences in the molecular orbital descriptions have dramatic effects on the accuracy of computational investigations.

For the three phases of vanadium phosphate, there was a trend in the best performing basis set through each of the numerical comparisons: bond length, angle, and IR frequencies. The basis set that overall preformed the best was O_8-411d1_2005, while the worst overall performer was O_8-31d1. The $\alpha_1$ phase had the highest discrepancies between the theoretical and experimental values. This is most likely due to the suspect literature values for the atomic positions of the atoms within the unit cell, requiring bond length and angle correlations based on those of a structure modified from $\alpha$-$VOSO_4$ and not $\alpha_1$-$VOPO_4$. However, the experimentally obtained IR spectrum of $\alpha_1$-$VOPO_4$ can be directly compared to that of the theoretical spectrum suggesting that the theoretical structure and modified experimental structure are in good agreement. Based on the consistencies for the $\alpha_2$ and $\beta$ phases, the basis set that best represents the experimental bond lengths and angles also represents the best correlation with the infrared spectrum. Therefore, it can be concluded that the atomic positions obtained from the

O_8- 411d1_2005 basis set are closer to the actual positions then those assumed by the current literature for $\alpha_1$-$VOPO_4$. However, without experimental verification from the solution of the powder diffraction data for the $\alpha_1$-$VOPO_4$, this cannot be corroborated.

While there appears to be a large deviation between the $\alpha_1$ and $\alpha_2$ phases, based primarily on the position of the vanadium within the octahedral unit, the differences between the $\alpha_1$ and $\beta$ phase are much more subtle. The infrared spectra are very similar with the majority of the most intense peaks located at similar frequencies. The bond lengths were also very similar in each case. These structural similarities could be the possible explanation for why the facile transformation of the $\alpha_1$ phase into the $\beta$ phase, while the $\alpha_2$ phase does not transform to $\beta$.[3]

## 2.5 Acknowledgment

This research was supported in part by a grant from the National Science Foundation CHE0907787.

## 2.6 References

[1] S.H. Sookraj and D. Engelbert, *Catal. Today*, **1999**, *49*, 161.

[2] B.M. Azmi, T. Ishihara, H. Nishiguchi, Y. Takita, *Electrochim. Acta*, **2002**, *48*, 165.

[3] M. Tachez, F. Theobald, E. Bordes, *J. Solid State Chem.*, **1981,** *40*, 280.

[4] G. Ladwig, *Z. Anorg. Allg. Chem.*, **1965**, *338*, 266.

[5] R. Dovesi, F.F. Fava, C. Roettia, V.R. Saunders, *Faraday Discuss.*, **1997**, *106*, 173.

[6] I. Moreira, R. Dovesi, C. Roetti, V.R. Saunders, R. Orlando, *Phys. Rev. B*, **2000**, *60*, 7816.

[7] M. Catti and G. Sandrone, *Faraday Discuss.*, **1997**, *106*, 189.

[8] R. Dovesi, M. Causà, R. Orlando, C. Roetti, V.R. Saunders, *J. Chem. Phys.*, **1990**, *92*, 7402.

[9] P.M. Hakey, D.G. Allis, M.R. Hudson, W. Ouellette, T.M. Korter, *ChemPhysChem*, **2009**,*10*, 2434.

[10] J. Wilkinson, C.T. Konek, J.S. Moran, E.M. Witko, T.M. Korter, *Chem. Phys. Lett.*, **2009**, *478*, 172.

[11] C. R'Kha, M.T. Vandenborre, J. Livage, R. Prost, E. Huard, *J. Solid State Chem.*, **1986**, *63*, 202.

[12] R. Dovesi, R. Orlando, B. Civalleri, R. Roetti, V.R. Saunders, C.M. Zicovich-Wilson, *Z. Kristallogr.*, **2005**, *220*, 571.

[13] R. Dovesi, V.R. Saunders, R. Roetti, R. Orlando, C.M. Zicovich-Wilson, F. Pascale, B. Civalleri, K. Doll, N.M. Harrison, I.J. Bush, P. D'Arco, M. Llunell, CRYSTAL09 User's Manual, University of Torino, Torino, **2009**.

[14] C. Adamo and V. Barone, *J. Chem. Phys.*, **1999**, *110*, 6158.

[15] E. Ruiz, M. Llunell, P. Alemany, *J. Solid State Chem.*, **2003**, *176*, 400.

[16] C.M. Zicovich-Wilson, A. Bert, C. Roetti, R. Dovesi, V.R. Saunders, *J. Chem. Phys.*, **2002**, *116*, 1120.

[17] G.A. Petersson, A. Bennett, T.G. Tensfeldt, M.A. Al-Laham, W.A. Shirley, J. Mantzaris, *J. Chem. Phys.*, **1988**, *89*, 2193.

[18] G.A. Petersson and M.A. Al-Laham, *J. Chem. Phys.*, **1991**, *94*, 608.

[19] D. Feller, *J. Comput. Chem.*, **1996**, *17*, 1571.

[20] K.L. Schuchardt, B.T. Didier, T. Elsethagen, L. Sun, V. Gurumoorthi, J. Chase, J. Li, T.L. Windus, Basis set exchange: a community database for computational sciences, *J. Chem. Inf. Model.*, **2007**, *47*, 1045.

[21] C. Gatti, V.R. Saunders, C. Roetti, *J. Chem. Phys.*, **1994**, *101*, 10686.

[22] F. Corà, *Mol. Phys.*, **2005**, *103*, 2483.

[23] T. Bredow, K. Jug, R.A. Evarestov, *Phys. Status Solidi B*, **2006**, *243*, R10.

[24] L. Valenzano, F.J. Torres, K. Doll, F. Pascale, C.M. Zicovich-Wilson, R. Dovesi, *Z. Phys. Chem.*, **2006**, *220*, 893.

[25] J.M. Longo and R.J. Arnott, *J. Solid State Chem.*, **1970**, *1*, 394.

[26] B. Jordan and C. Calvo, *Can. J. Chem.*, **1973**, *51*, 2621.

[27] R. Gopal and C. Calvo, *J. Solid State Chem.*, **1972**, *5*, 432.

[28] F. Pascale, C.M. Zicovich-Wilson, F.L. Gejo, B. Civalleri, R. Orlando, R. Dovesi, *J. Comput. Chem.*, **2004**, *25*, 888.

[29] R.N. Bhargave and R.A. Condrate, *Appl. Spectrosc.*, **1977**, *31*, 230.

[30] $VOPO_4 \cdot 2H_2O$ infrared spectral peaks: 569.8620 (m), 680.7488 (m), 950.7341(s), 991.2319(w), 1087.655 (s).

# Chapter 3

## Using Terahertz Spectroscopy and Solid-State Density Functional Theory to Characterize a New Polymorph of 5-(4-pyridyl)tetrazole

## 3.1 Introduction

Polymorphism at its simplest definition is a phenomenon associated with different packing arrangements of the same molecule in the solid state. Polymorphism can occur in every area of chemistry ranging from organic to inorganic compounds as well as synthetic and natural polymers.1 In many compounds, polymorphs can arise in a variety of ways,2 for example re-crystallization at different temperatures3,4 or using different solvents.5 The uniqueness of polymorphs does not limit itself to structure alone, but the physical properties can vary drastically as well. For example, different polymorphs can have large differences in solubility, melting point or drug reactivity; this makes identification of polymorphs a major concern for many implementations especially in the pharmaceutical industry.[6-8]

In this study a new form of 5-(4-pyridyl)tetrazole (β) has been discovered and compared to the previously determined structure (α).[9] 5-(4-Pyridyl)tetrazole (4PT) belongs to a class of nitrogen containing heterocycles that have the highest nitrogen content and has primarily found its use as a bridging ligand in the synthesis of metal-organic frameworks.[10] The two distinct forms of 5-(4-pyridyl)tetrazole differ primarily in their packing, with the α form crystallizing in the monoclinic space group Cc and the β form crystallizing in the monoclinic space group $P2_1/n$. The comparison of the two different unit cells is shown in **Figure 3.1**. α-4PT consists of one distinct zigzagging hydrogen bonded strand running co-directionally with adjacent chains, primarily along the *c* axis. Unlike α-4PT, β-4PT consists of two distinct zigzagging hydrogen bonded strands running antiparallel along the *c* axis, as shown in **Figure 3.2**.

Terahertz (THz) spectroscopy was utilized in this study because it has been previously used to investigate polymorphs of molecular crystals where the terahertz absorption is caused by lattice vibrations unique to three-dimensional ordered solids.[11-13] Unlike near-IR vibrational

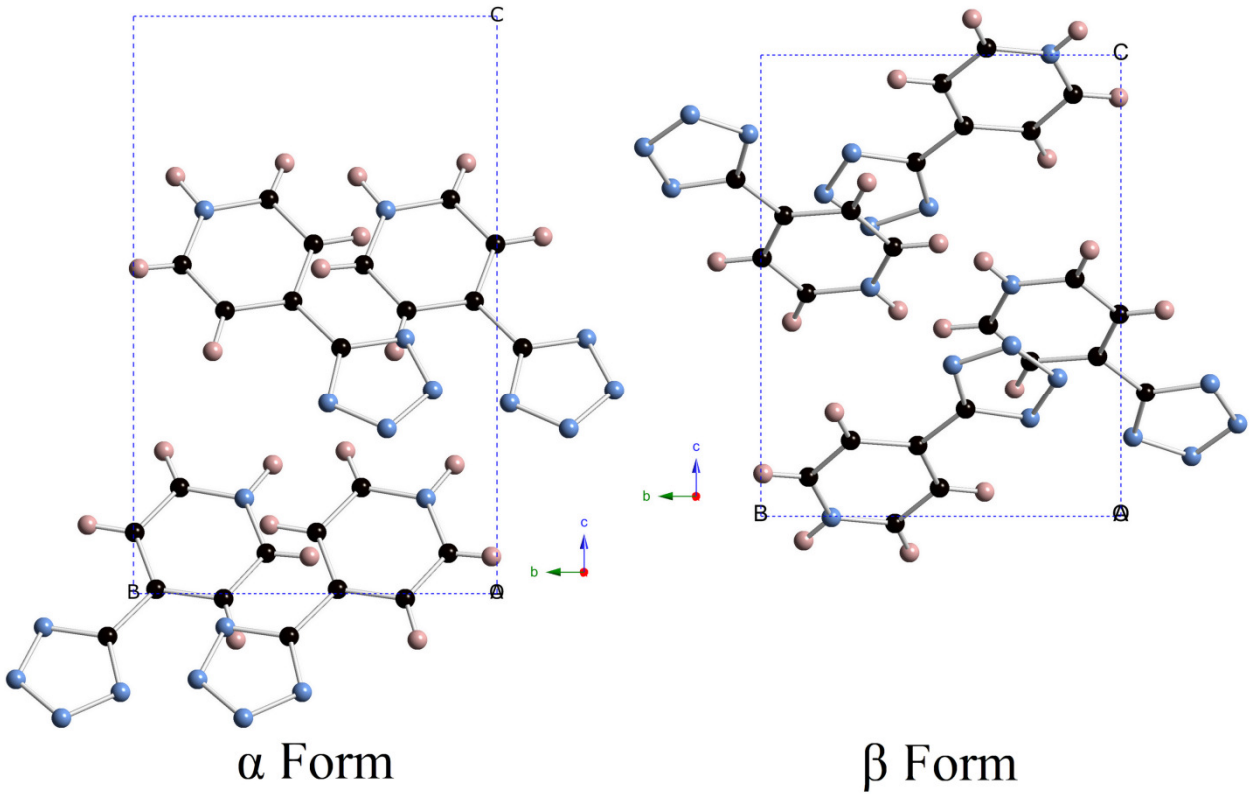


**Figure 3.1** Ball and Stick representation of the molecular cell of the α and β forms of 5-(4-pyridyl)tetrazole. (Carbon is shown in black, nitrogen is shown in light blue and hydrogen is shown in pink)

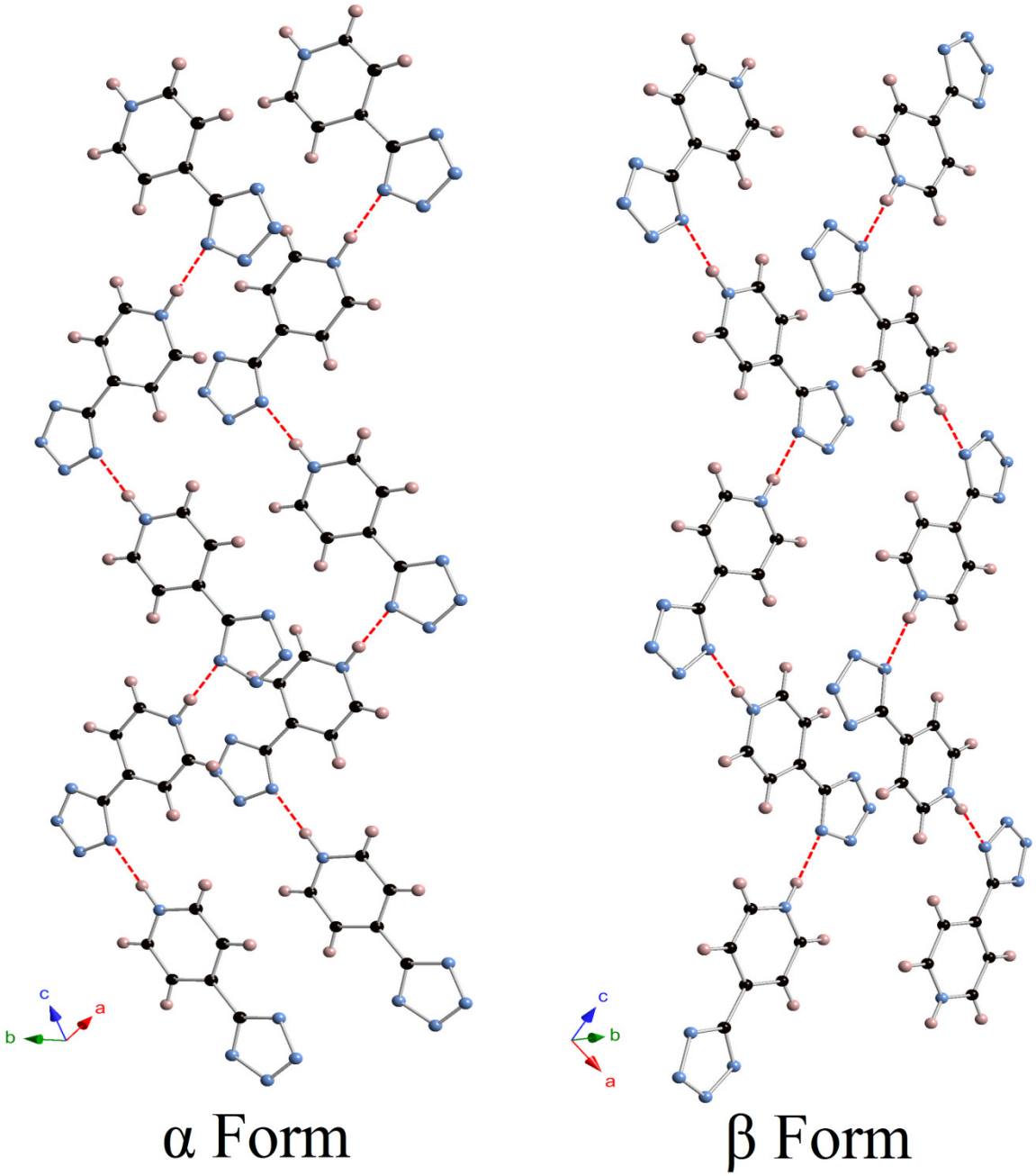


**Figure 3.2** Ball and stick representation of the molecular packing of the α and β forms of 5-(4-pyridyl)tetrazole displaying the differences in hydrogen bonded 5-(4-pyridyl)tetrazole chains. (Carbon is shown in black, nitrogen is shown in light blue, hydrogen is shown in pink, and hydrogen bonding shown with red dashed lines)

spectroscopy, there are no characteristic group frequencies in the THz region; therefore, to determine what vibrations lead to these intermolecular absorptions has fallen on computational approaches, primarily solid-state density functional theory (DFT).[14-16]

The solid-state DFT approach that was used in this study is implemented in CRYSTAL09. We have previously used CRYSTAL09 with great success in the simulations of similar compounds including hydrohalide salts of 5-(4-pyridyl)tetrazole[17] and isomorphous metal complexes with 5-(4-pyridyl)tetrazole.[18] In this study, CRYSTAL09 was used to replicate the geometric parameters of the previously known and newly discovered polymorphs of 5-(4-pyridyl)tetrazole. Furthermore, CRYSTAL09 was used to determine the vibrationally active modes in the THz region and to evaluate the normal modes that are the result of these absorptions.

## 3.2 Experimental and Theoretical Methods

### *3.2.1 Experimental*

#### *3.2.1.1 Synthesis of Polymorphic Forms of 5-(4-pyridyl)tetrazole*

All reagents were purchased from their respective vendors and used without further purification. Water was distilled above 3.0 MΩ in-house using a Barnstead Model 525 Biopure Distilled Water Center. Crude 5-(4-pyridyl)tetrazole was prepared using previously published methods.[19] The infrared spectra were obtained on a Thermo Nicolet IR200 FT-IR using the KBr pellet method and a spectral resolution of 2 $cm^{-1}$ over the range of 4000-400 $cm^{-1}$. The KBr was dried prior to usage

#### *3.2.1.2 Recrystallization of the α Form of 5-(4-pyridyl)tetrazole (α-4PT)*

To obtain the α form of 5-(4-pyridyl)tetrazole, the crude 5-(4-pyridyl)tetrazole was allowed to crystallize by slow evaporation from ethanol.[10] α-4PT was confirmed using single-crystal X-ray diffraction.

#### *3.2.1.3 Recrystallization of the β Form of 5-(4-pyridyl)tetrazole (β-4PT)*

The β form was obtained by placing crude 5-(4-pyridyl)tetrazole (0.1 g, 0.68 mmol) and water (10 mL, 556 mmol) into a 23 ml poly(tetrafluoroethylene) lined stainless steel container. The pH was adjusted with NaOH to a pH of ~6 using pHydrion vivid 1-11® pH paper. The stainless steel container was heated at 80°C for 24 hrs. under autogenous pressure. Colorless rods were obtained suitable for X-Ray Diffraction were isolated. IR (KBr pellet, $cm^{-1}$): 3434(br), 3100(w), 2528(br), 2103(w), 2016(w), 1631(s), 1529(m), 1440(m), 1387(m), 1290(w), 1200(w), 1143(w), 1040(m), 992(w), 846(m), 752(m), 527(m), 459(s).

### *3.2.2 X-Ray Crystallography*

Crystallographic data for α-4PT was collected on a Bruker-AXS SMART-CCD diffractometer using graphite-monochromated Mo Kα radiation ($\lambda$ = 0.71073 Å).[20] Crystallographic data for β-4PT was collected on a Bruker KAPPA APEX DUO diffractometer using Mo-$K_\alpha$ radiation ($\lambda$ = 0.71073Å) containing an APEX II CCD system.[21] All data collections were taken at low temperature (90K). The data was corrected for Lorentz and polarization[22] effects, and adsorption corrections were made using *SADABS*.[23] Structures were solved by direct methods. Refinements for each structure were carried out using the SHELXTL[24] crystallographic software. Following assignment of all non-hydrogen atoms, the

models were refined against $F^2$ first using isotropic and then using anisotropic thermal displacement parameters. The hydrogen atoms were introduced in calculated positions and then refined isotropically. Neutral atom scattering coefficients along with anomalous dispersion corrections were taken from the *International Tables*, Vol. C.

### *3.2.3 Time-domain Terahertz Spectroscopy*

The experimental terahertz spectra of the compounds were acquired using a pulsed time-domain THz spectrometer based on an amplified femtosecond Ti:Sapphire laser system operating in the near-infrared region. For the generation and detection of THz radiation, the instrument utilized optical rectification[24,25] and free space electro-optic sampling,[26,27] respectively. A detailed description of the spectrometer along with the experimental setup has been provided elsewhere.[28-30]

The 5-(4-pyridyl)tetrazole polymorphs were used without further purification and were mixed with a spectroscopic grade powdered polytetrafluoroethylene (PTFE) matrix. The sample and the matrix were then mechanically pulverized using a stainless-steel ball mill (Dentsply Rinn 3110-3A), allowing a homogeneous distribution of the sample through the matrix, thereby reducing the particle size, and minimizing radiation scattering.[30,31] The mixture was then pressed into a pellet at 2000 psi using a hydraulic press (ICL E-Z Press 12). The resulting sample pellet had a total mass of approximately 0.55 g, thickness of ~2.0 mm, and a diameter of 13.0 mm. The final sample pellets contained 0.67% w/w α-4PT and 0.73% w/w β-4PT. The blank (reference) pellet was prepared with pure PTFE in a similar manner.

The sample and blank pellets were both held under vacuum in a variable-temperature cryostat and held at temperatures of 293 K (room temperature) and 78 K (liquid-nitrogen temperature).

Each individual spectrum of the sample (or the blank pellet) consisted of an average of 36 THz-waveform scans over a time window of ~30 ps. These waveforms were then symmetrically zero-padded to a total of 6000 data points, and subsequently were Fourier-transformed (utilizing a Hanning window function) into the frequency-domain. Elimination of any THz absorption by the PTFE matrix was accomplished by taking a ratio of the transformed spectrum of a PTFE blank versus the transformed spectrum of a sample pellet. To improve the final signal-to-noise ratio, four blank/sample sets were collected and averaged, over a range of 10 to 95 $cm^{-1}$ with a spectral resolution of approximately 1.0 $cm^{-1}$, yielding the THz spectra reported here.

### *3.2.4 Theoretical Methodology of CRYSTAL09*

Geometry optimizations, harmonic frequencies, and intensity calculations were performed using the CRYSTAL09 program.[32,33] All calculations were performed using a spin restricted B3LYP[34] hybrid density functional. The basis set used for all atoms was a Gaussian type triple valence basis set with polarization (pob_TZVP).[35]

The positions of the atoms contained within the unit cell were optimized within the constraints of the literature lattice parameters and space group symmetry. From the optimized structures, the bond lengths and bond angles were determined and compared with the experimental crystallographic results. After optimizing the structures, harmonic-limit normal-mode analyses on the polymorphs were conducted. Frequencies were determined by diagonalization of the mass-weighted Hessian matrix to obtain eigenvalues which were then converted into frequencies and eigenvectors.[33] The hessian matrix in CRYSTAL is obtained by the numerical differentiation of the analytical gradient of the energy with respect to the atomic position. [36] Lastly, the intensities were calculated through the Berry phase approach.[33] To facilitate comparison of the theoretical spectra with experiment, a Lorentzian line shape (based

upon the average experimentally measured line width determined from simple least squares fitting) was convoluted with the simulated absorptions. This resulted in an empirical 3.0 $cm^{-1}$ and 6.0 $cm^{-1}$ full-width-half-maximum Lorentzian line shape being applied to the theoretical data of the α and β forms of 5-(4-pyridyl)tetrazole, respectively.

Several of the convergence parameters were changed to optimize the accuracy and computational time of the calculations. The convergence criteria were modified to set the root mean square of the maximum gradient (TOLDEG) and the maximum displacement (TOLDEX) to be $1 \times 10^{-5}$ and $4 \times 10^{-5}$ angstroms, respectively. To improve the numerical accuracy of the calculations the truncation criteria for bielectronic integrals (TOLINTEG) was set to 8 8 8 8 16 and the DFT integration was set to XLGRID (75,974). (See Ref. [32,33] for details). Total energy convergence (TOLDEE) was set to $\Delta E < 1 \times 10^{-8}$ Hartree for the geometry optimizations and $\Delta E < 1 \times 10^{-11}$ Hartree for frequency analyses. To assist in a timely convergence, the "Fock/KS matrix mixing" (FMIXING) was increased from the default value of zero to 50 for all systems. The eigenvalue level shifter was also activated with the level shifter set to a value that corresponds to a shift of 0.5 Hartree, and the state was locked, confining it to an insulating state. Determination of the optimum sampling of reciprocal space was determined by comparing the total energy of the converged system to the k-point count using the keyword SHRINK. The optimum SHRINK value was determined to be SHRINK = 6 6 which corresponds to 80 points in the irreducible part of the Brillouin Zone and 80 points in the Gilat Net.

## 3.3 Results and Discussion

### *3.3.1 X-Ray Crystallography*

Images of the crystal structures were generated using CrystalMaker®.[37] ORTEP plots of α-4PT and β-4PT are available as supplemental materials and are displayed in **Figure A-3** and **Figure A-4**.

#### *3.3.1.1 X-Ray Crystallography of the α Form of 5-(4-pyridyl)tetrazole (α-4PT)*

In order to accurately compare the experimentally collected data to the theoretical data, it was necessary to use unit cell parameters and atomic positions from a crystal structure that has been determined near the same temperature at which the THz spectroscopy has been performed. The previously published crystal structure for α-4PT was determined at 298K; therefore, it was necessary to collect a crystal structure at 90K, to be able to more accurately represent the THz spectrum collected at 78K. The structure was found to be isostructural with the published room temperature collection; however, the unit cell parameters are contracted slightly as expected. α-4PT crystalized in the Cc space group with unit cell dimensions of $a$ = 7.0093(8) Å, $b$ = 7.4477(8) Å, $c$ = 11.8983(13) Å, α = γ = 90.0°, and β = 95.230(2).

#### *3.3.1.2 X-Ray Crystallography of the β Form of 5-(4-pyridyl)tetrazole (β-4PT)*

The molecular structure of β-4PT crystallizes in the monoclinic space group $P2_1/n$. Crystallographic details for β-4PT are provided in **Table 3.1**.

**Table 3.1** Summary of crystallographic data for the β form of 5-(4-pyridyl)tetrazole (β-4PT)

| | β-4PT |
|---|---|
| Empirical Formula | C6 H5 N5 |
| Formula Weight | 147.15 |
| Crystal System | Monoclinic |
| Space Group | $P2_1/n$ |
| *a (Å)* | 8.9109(10) |
| *b (Å)* | 7.4034(8) |
| *c (Å)* | 9.5135(10) |
| *α (°)* | 90 |
| *β(°)* | 92.662(2) |
| *γ(°)* | 90 |
| *V(Å$^3$)* | 626.94(12) |
| *Z* | 4 |
| $D_{calc}$*(g cm$^{-3}$)* | 1.559 |
| *μ (mm$^{-1}$)* | 0.109 |
| *T (K)* | 90(2) |
| Wavelength | 0.71073 |
| $R_1$[a] | 0.0346 |
| $wR_2$[b] | 0.0878 |

[a] $R1 = \Sigma||F_o| - |F_c||/\Sigma|F_o|$. [b] $wR2 = \{\Sigma[w(F_o^2 - F_c^2)^2]/\Sigma[w(F_o^2)^2]\}^{1/2}$

### *3.3.2 Comparison of the Calculated and Experimental Structures*

The calculated and experimental bond lengths, bond angles, and the root-mean-squared deviation (RMSD) values are shown in **Table 3.2** and **Table 3.3** for α-4PT and β-4PT, respectively, and the results are visualized in **Figure 3.3**. The bond lengths were modeled for both complexes with a very reasonable amount of accuracy, replicating each of the bonds, within ±0.016Å for the α and β forms of 5-(4-pyridyl)tetrazole. The only significant deviations were found in the nitrogen-nitrogen distances of the tetrazolate ring, which were overestimated in both polymorphs by a similar amount.

The angles were also modeled with a fair degree of accuracy, as shown by the low RMSDs. The calculated RMSDs for the α-4PT and β-4PT complexes were 0.5926° and 0.6406°, respectively. It is important to note that in these systems four torsion angles were included which correspond to the torsion angles between th**e pyridyl** and tetrazolate rings. This torsion angle differs by ~3 degrees between the two polymorphs, which is reproduced by the theoretical model. The α-4PT polymorph has smaller torsion angles than the β-4PT polymorph, resulting in an arrangement that is closer to a planar conformation. This suggests that there might be more overlap of the π orbitals between the two ring systems in the α polymorph.

To evaluate the energy difference between the two polymorphs additional single-molecule calculations were performed on the molecular components of the crystals. In order to accomplish this, a molecule was isolated from the optimized bulk crystal and studied using the same theoretical methods used for the periodic solid. In addition, estimations of basis set superposition error (BSSE) were approximated using the counterpoise method.[38] For periodic boundary condition simulations, a spatial cutoff must be defined for inclusion of neighboring basis functions in the counterpoise calculation; in this work, 300 atoms within 5.0 Å of the

**Table 3.2** Interatomic bond lengths (Å), angles (°), and RMSD values for the α form of 5-(4-pyridyl)tetrazole (α-4PT). See **Figure 3.3** for atomic labels. Experimental parameters are from 90K crystallographic data.

| Bond, Å | Experimental | Theoretical |
|---|---|---|
| **N1-C1** | 1.3482 | 1.3463 |
| **N1-C5** | 1.3479 | 1.3429 |
| **N2-N3** | 1.3434 | 1.3592 |
| **N2-C6** | 1.3456 | 1.3417 |
| **N3-N4** | 1.3251 | 1.3404 |
| **N4-N5** | 1.3437 | 1.3571 |
| **N5-C6** | 1.3311 | 1.3412 |
| **C1-C2** | 1.3698 | 1.3731 |
| **C2-C3** | 1.4069 | 1.3959 |
| **C3-C4** | 1.3923 | 1.3949 |
| **C3-C6** | 1.4625 | 1.4561 |
| **C4-C5** | 1.3781 | 1.3690 |
| | **RMSD** | 0.00945 |

| Angle, ° | Experimental | Theoretical |
|---|---|---|
| **C1-N1-C5** | 121.421 | 121.676 |
| **N3-N2-C6** | 104.501 | 105.345 |
| **N2-N3-N4** | 109.201 | 108.654 |
| **N3-N4-N5** | 109.665 | 109.140 |
| **N4-N5-C6** | 104.632 | 105.170 |
| **N1-C1-C2** | 120.208 | 119.965 |
| **C1-C2-C3** | 119.995 | 119.847 |
| **C2-C3-C4** | 118.192 | 118.384 |
| **C2-C3-C6** | 122.942 | 122.648 |
| **C4-C3-C6** | 118.866 | 118.968 |
| **C3-C4-C5** | 119.707 | 119.726 |
| **N1-C5-C4** | 120.473 | 120.395 |
| **N2-C6-N5** | 111.998 | 111.686 |
| **N2-C6-C3** | 125.707 | 125.963 |
| **N5-C6-C3** | 122.284 | 122.350 |
| **C2-C3-C6-N2** | 2.478 | 0.929 |
| **C2-C3-C6-N5** | -178.841 | -178.603 |
| **C4-C3-C6-N2** | -177.589 | -179.025 |
| **C4-C3-C6-N5** | 1.091 | 1.443 |
| | **RMSD** | 0.5926 |

**Table 3.3** Interatomic bond lengths (Å), angles (°), and RMSD values for the β form of 5-(4-pyridyl)tetrazole (β-4PT). See **Figure 3.3** for atomic labels. Experimental parameters are from 90K crystallographic data.

| Bond, Å | Experimental | Theoretical |
|---|---|---|
| **N1-C1** | 1.3446 | 1.3459 |
| **N1-C5** | 1.3406 | 1.3423 |
| **N2-N3** | 1.3471 | 1.3609 |
| **N2-C6** | 1.3411 | 1.3417 |
| **N3-N4** | 1.3261 | 1.3404 |
| **N4-N5** | 1.3432 | 1.3576 |
| **N5-C6** | 1.3427 | 1.3407 |
| **C1-C2** | 1.3728 | 1.3730 |
| **C2-C3** | 1.4011 | 1.3969 |
| **C3-C4** | 1.3960 | 1.3940 |
| **C3-C6** | 1.4649 | 1.4561 |
| **C4-C5** | 1.3755 | 1.3698 |
| | **RMSD** | 0.00787 |

| Angle, ° | Experimental | Theoretical |
|---|---|---|
| **C1-N1-C5** | 121.711 | 121.804 |
| **N3-N2-C6** | 104.893 | 105.265 |
| **N2-N3-N4** | 109.214 | 108.617 |
| **N3-N4-N5** | 109.535 | 109.204 |
| **N4-N5-C6** | 104.844 | 105.098 |
| **N1-C1-C2** | 120.247 | 120.024 |
| **C1-C2-C3** | 119.636 | 119.640 |
| **C2-C3-C4** | 118.428 | 118.554 |
| **C2-C3-C6** | 122.783 | 122.614 |
| **C4-C3-C6** | 118.777 | 118.821 |
| **C3-C4-C5** | 119.528 | 119.701 |
| **N1-C5-C4** | 120.450 | 120.274 |
| **N2-C6-N5** | 111.514 | 111.815 |
| **N2-C6-C3** | 126.128 | 126.033 |
| **N5-C6-C3** | 122.356 | 122.151 |
| **C2-C3-C6-N2** | 5.401 | 5.846 |
| **C2-C3-C6-N5** | -174.041 | -175.416 |
| **C4-C3-C6-N2** | -175.898 | -173.748 |
| **C4-C3-C6-N5** | 4.661 | 4.992 |
| | **RMSD** | 0.6406 |

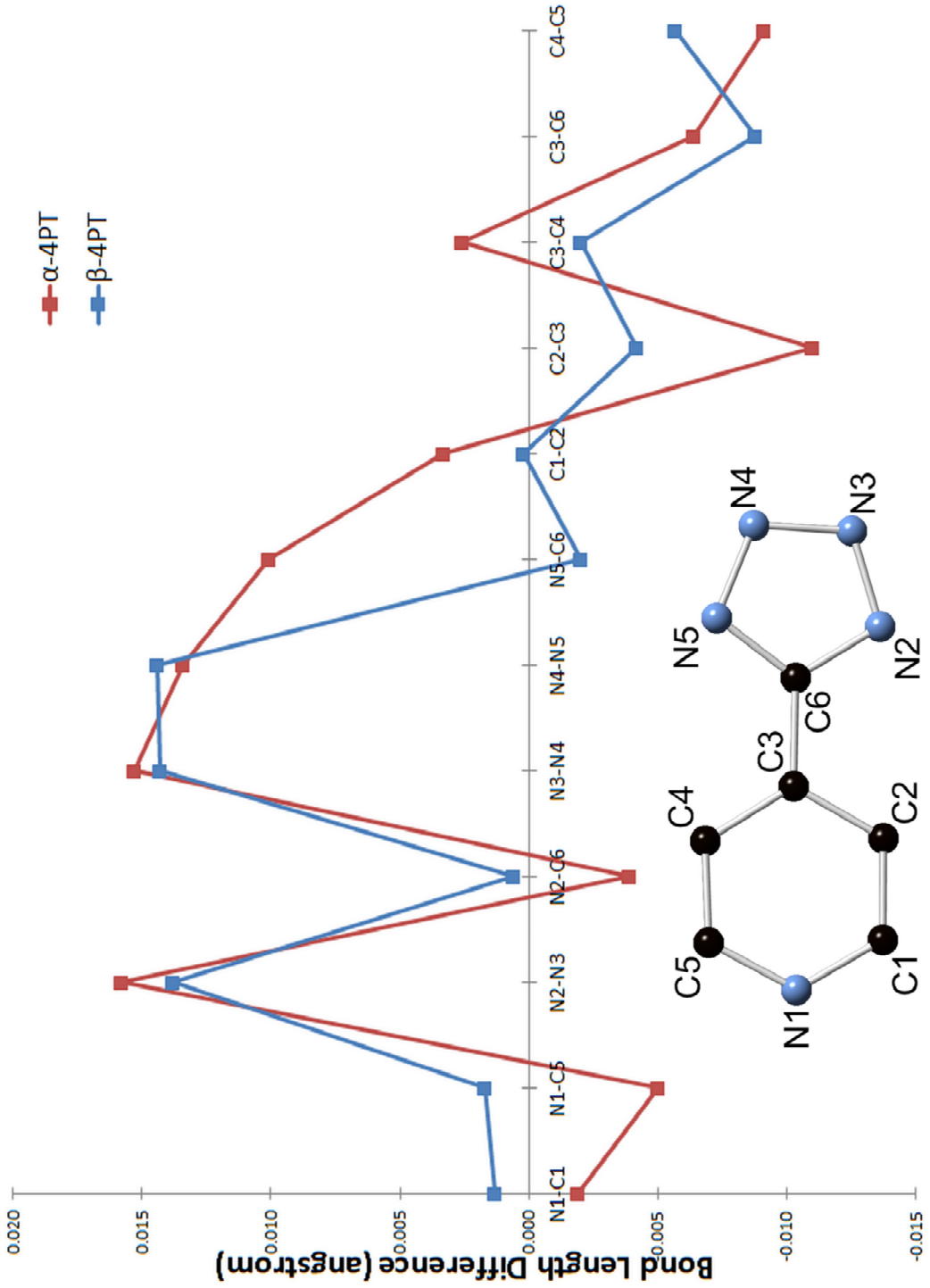


**Figure 3.3** Calculated bond-length differences for the α and β forms of 5-(4-pyridyl)tetrazole. The inset figure shows the atom labeling for the α and β forms of 5-(4-pyridyl)tetrazole.

molecule being evaluated were used to gauge BSSE effects. Once the isolated molecule energies were determined, eq.1 was used to determine the energy of formation per molecule for the solid crystal, where $E^{Form}$ denotes the energy of formation, $E_{bulk}$ represents the energy of the bulk solid, $E_{mol}$ is the energy of the isolated molecule and Z is the number of molecules in the unit cell.

$$E^{Form}\ per\ molecule = \frac{E_{bulk} - Z * E_{mol}}{Z} \qquad \text{(eq. 3.1)}$$

The values for the formation energy are summarized in **Table 3.4**. It was discovered that the energy associated with the formation of α-4PT is greater by ~0.25 kJ/mol, meaning that this form of 5-(4-pyridyl)tetrazole is the energetically more stable polymorph.

This small difference in formation energy inspired the investigation of the thermodynamic parameters to determine what effect the temperature had on the Gibbs free energy of these two systems.[36,39] The Gibbs free energy per molecule in the unit cell was determined according to eq. 3.2, where El is the electronic energy, E0 is the zero-point energy, ET is the thermal contribution to the vibrational energy, PV is pressure * volume, TS is the temperature * entropy, and lastly Z is the number of molecules in the unit cell.

$$G = \frac{El + E0 + ET + PV - TS}{Z} \qquad \text{(eq. 3.2)}$$

The Gibbs free energy was determine at a constant pressure of 1 atm and was calculated at temperatures ranging from 10K to 400 K, and the results are summarized in **Figure 3.4**. While the exact phase transition temperature cannot be determined without a much more thorough investigation, a clear trend can be seen. The α form is much more stable at low temperatures, but

**Table 3.4** Calculated formation energies per molecule for the α (α-4PT) and β (β-4PT) forms of 5-(4-pyridyl)tetrazole, based on the geometrically optimized structures. The values of the formation energy are derived from eq. 1.

| | $E_{bulk}$ (Eh) | $E_{mol}$ (Eh) | $E^{Form}$ per Molecule (Eh) | $E^{Form}$ per Molecule (kJ/mol) |
|---|---|---|---|---|
| **α-4PT** | -1010.373832 | **-505.133134** | -0.053782 | -141.20553 |
| **β-4PT** | -2020.744686 | -505.132483 | -0.053689 | -140.95945 |
| | | Absolute Difference | 9.3729E-05 | 0.246086 |

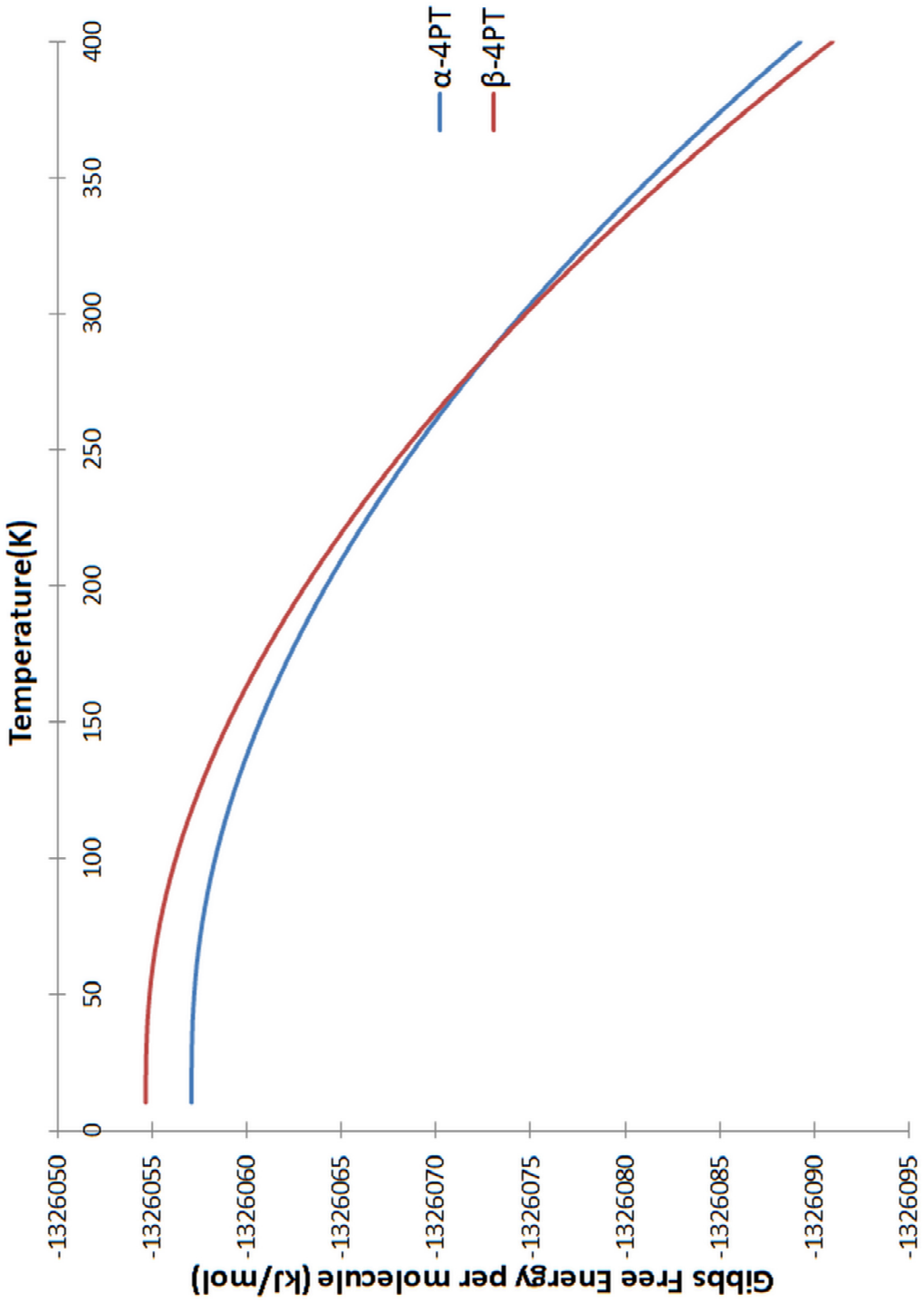


**Figure 3.4** The theoretically determined Gibbs free energy per molecule for the α and β forms of 5-(4-pyridyl)tetrazole as a function of temperature at constant pressure.

as temperature is increased, the β form is the more thermodynamically stable polymorph. This trend is supported by the experimental conditions necessary to obtain the β form, indicated by the temperature needed for the recrystallization of β-4PT.

### *3.3.3 Comparison of Theoretical and Experimental Vibrational Frequencies*

As anticipated, the near-infrared (IR) spectra of the two polymorphs are nearly indistinguishable, as illustrated in **Figure 3.5**, therefore the use of THz spectroscopy could prove useful in distinguishing these two polymorphs. The normalized THz spectrum for each polymorph recorded at cryogenic temperatures (78K) are illustrated in **Figure 3.6**, and it can be seen that while there are no major differences, the changes in the spectra are much clearer than those observed in the near-IR spectra. The experimental spectra collected at cryogenic (78K) temperatures along with the calculated terahertz spectra are compared in **Figure 3.7** and are summarized in **Table 3.5** and **Table 3.6**. The comparison of the room temperature terahertz spectra and theoretically predicated spectra of the α and β forms of 5-(4-pyridyl)tetrazole are shown in **Figure A-3**. Empirical analysis of the vibrational modes observed using J-ICE[40] is summarized in **Table 3.7**. While there is a combination of intramolecular and intermolecular motions, only the major motion is listed.

The theoretically determined terahertz spectrum reproduces a close match to the experimentally determined spectrum for both polymorphs. The predicted intensities of the theoretically determined spectra were found to be reasonably similar to the experimental terahertz spectra, the predicted intensities were found to be underestimated for α-4PT by ~18%, while the intensities was greatly overestimated by ~50% for β-4PT. There were no drastic differences in the spectra of the polymorphs, with each of the experimental spectra only

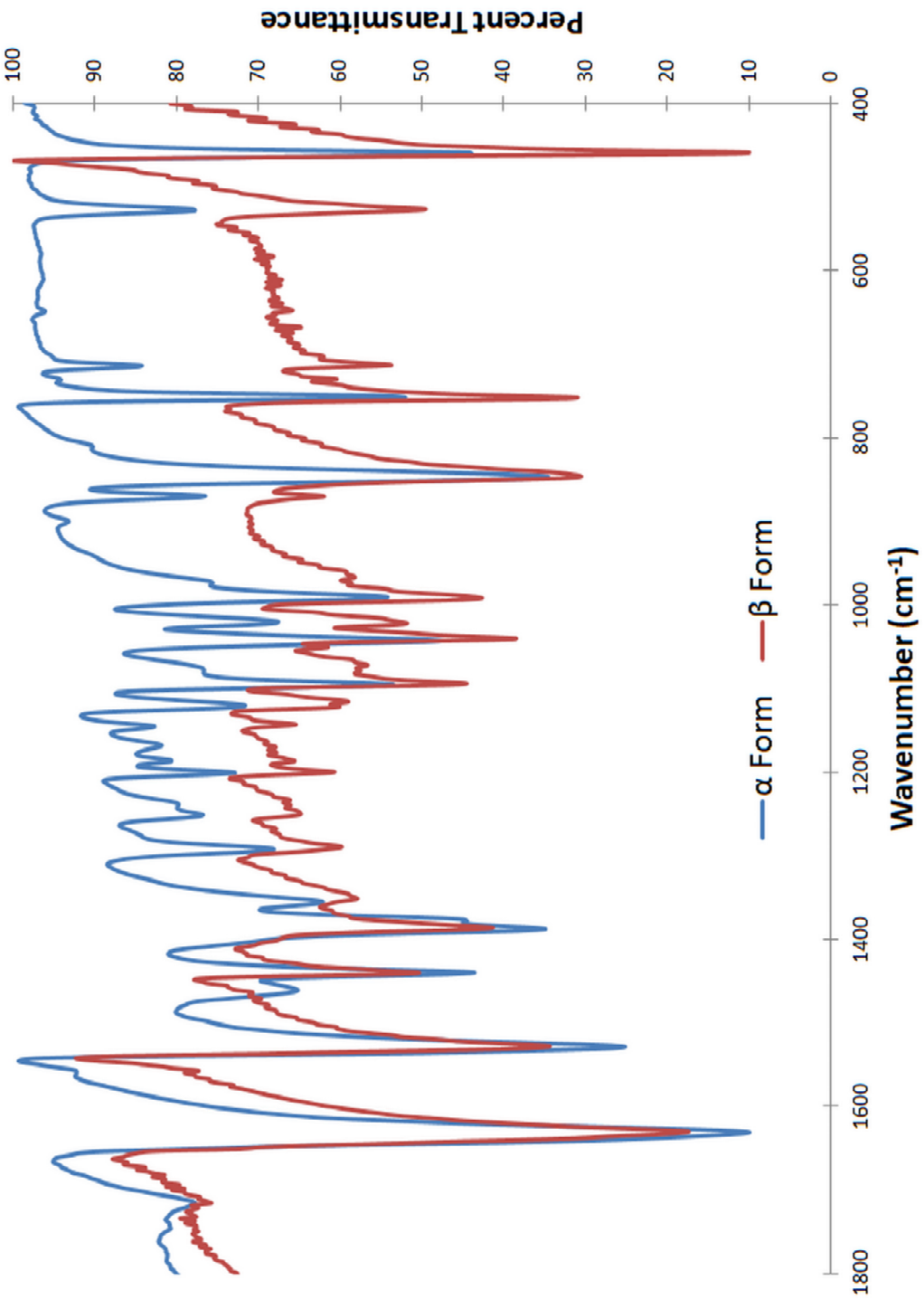


**Figure 3.5** Normalized near-infrared vibration spectra of the α and β forms of 5-(4-pyridyl)tetrazole shown from 1800-400 $cm^{-1}$.

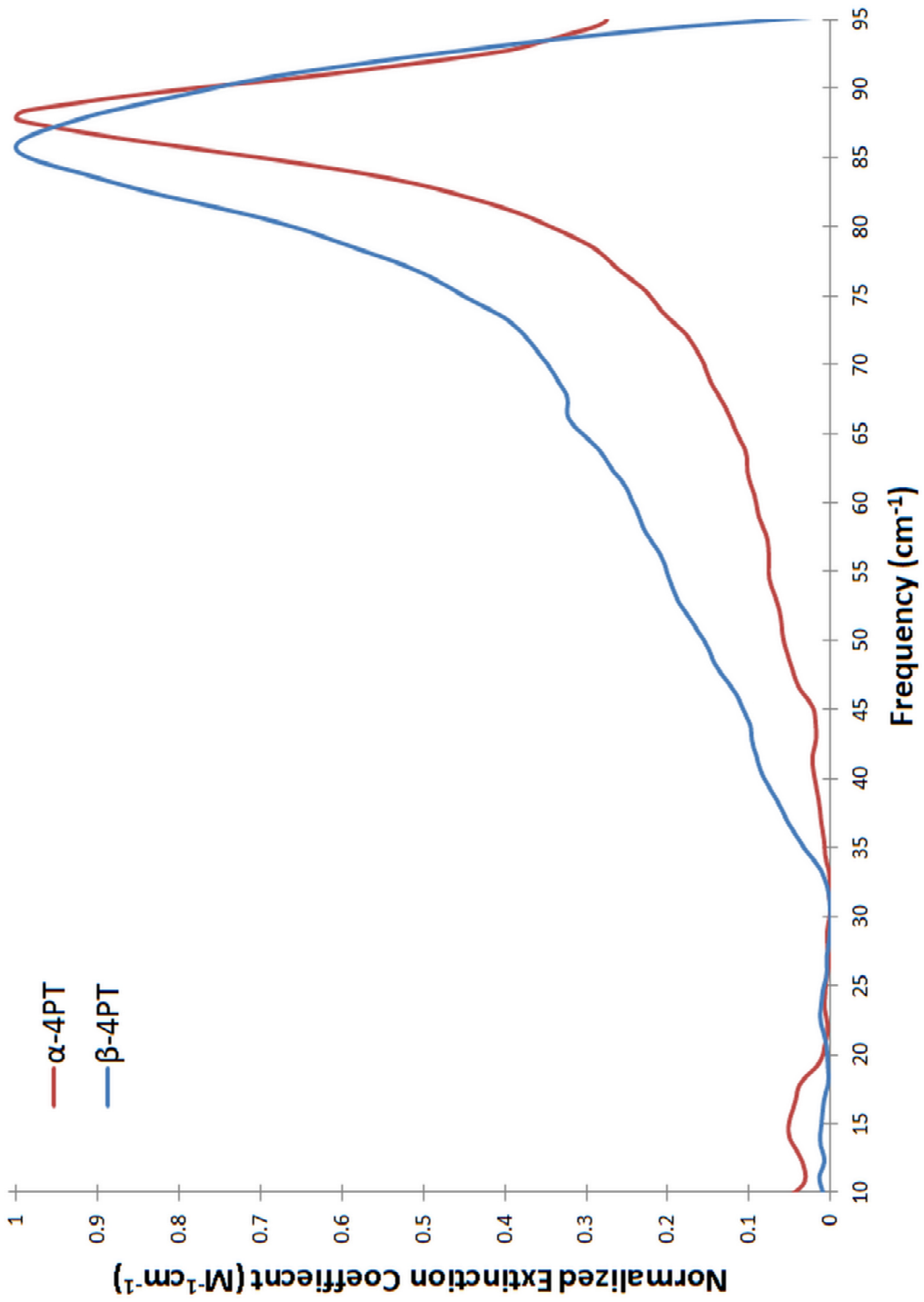


**Figure 3.6** Normalized experimental traces for the terahertz spectra of the α and β forms of 5-(4-pyridyl)tetrazole recorded at cryogenic temperature (78K) shown from 10-95 $cm^{-1}$.

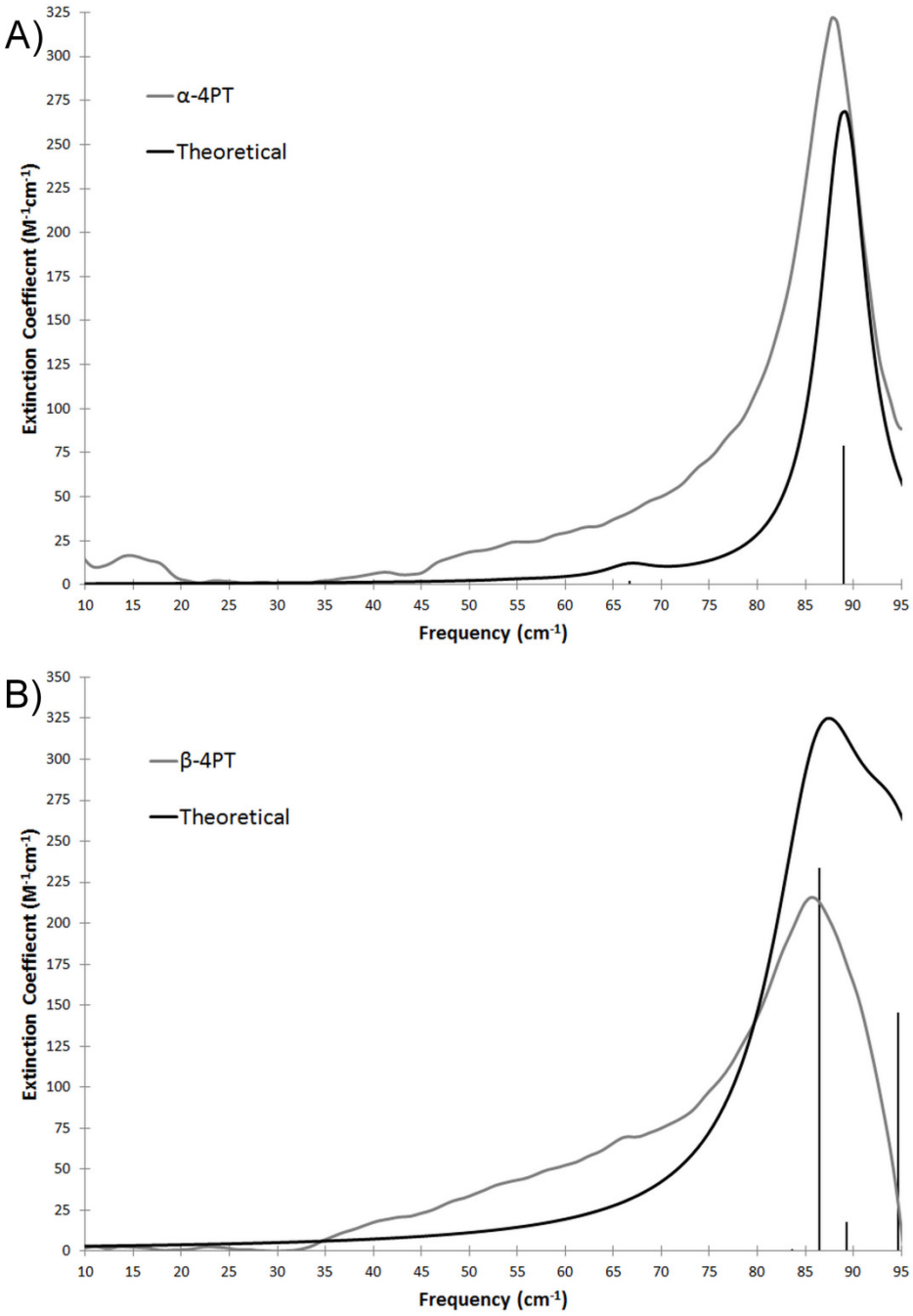


**Figure 3.7** The cryogenic (78K) experimental and theoretical traces for the terahertz spectra of the A) α and B) β forms of 5-(4-pyridyl)tetrazole shown from 10-95 $cm^{-1}$. An empirical 3.0 $cm^{-1}$ and 6.0 $cm^{-1}$ full-width-half-maximum Lorentzian line shape has been applied to the theoretical data of the α and β forms of 5-(4-pyridyl)tetrazole, respectively, to aid in comparison.

**Table 3.5** Frequency positions ($cm^{-1}$) and percent error for the experimental and theoretical terahertz spectra of the α form of 5-(4-pyridyl)tetrazole (α-4PT). The blanks are peaks that have no obvious correlation between the observed and theoretical spectra. Mode descriptions are described in **Table 3.7**.

| Mode | Exp. (78K) | Exp. (293K) | Theoretical | Intensity (ε) |
|---|---|---|---|---|
| a | --- | --- | 55.00 | 0.07 |
| b | --- | --- | 66.69 | 1.42 |
| c | 87.97 | 83.45 | 89.03 | 57.85 |
| | | **Percent Error** | 1.28% | |

**Table 3.6** Frequency positions ($cm^{-1}$) and percent error for the experimental and theoretical terahertz spectra of the β form of 5-(4-pyridyl)tetrazole (β-4PT). The blanks are peaks that have no obvious correlation between the observed and theoretical spectra. When multiple peaks corresponded to only one peak in the experimental spectra, the weighted average was used in calculating the percent error. Mode descriptions are described in **Table 3.7**.

| Mode | Exp. (78K) | Exp. (293K) | Theoretical | Intensity (ε) |
|---|---|---|---|---|
| d | | | 83.66 | 0.63 |
| c | 85.72 | 84.05 | 86.47 | 104.24 |
| d | | | 89.27 | 7.85 |
| d | --- | --- | 94.64 | 64.94 |
| e | --- | --- | 99.31 | 7.81 |
| | | **Percent Error** | 1.08% | |

**Table 3.7** Empirical normal mode analysis of the α and β forms of 5-(4-pyridyl)tetrazole.

| Mode | Description |
|---|---|
| a | Translation along *b* |
| b | Molecular Rocking in *bc* plane |
| c | Molecular Rotation along *a* |
| d | Molecular Rotation + Twisting in *ac* plane |
| e | Pyridyl ring twisting along *a* |

terahertz spectra, the predicted intensities were found to be underestimated for α-4PT by ~18%, while the intensities was greatly overestimated by ~50% for β-4PT. There were no drastic differences in the spectra of the polymorphs, with each of the experimental spectra only displaying one peak in the measured frequency range, however a shift of ~2 $cm^{-1}$ in the frequency locations from the α to β forms of 5-(4-pyridyl)tetrazole was observed. In addition to the shift in the peak location the only other difference is the observed bandwidth of the major peak, which is almost twice as large in the β form compared to the α form. This increased bandwidth could be explained by the conditions under which the collection was performed. As previously demonstrated the alpha form is the more favorable polymorph at the lower temperatures used to collect the spectra, therefore during the processing of the sample for collection there might have been some interconversion of the β form to the α form of 5-(4-pyridyl)tetrazole leading to increased inhomogeneous broadening due to higher crystalline disorder. This inference could be supported by the abnormal decrease in bandwidth at room temperature for the β form, which is slightly less than that measured at cryogenic temperatures. This is likely due to less interconversion due to the β form being as thermodynamically stable as the α form.

The theoretical frequencies that made up these spectra were much more complex. The theoretically determined frequencies for the α form show an agreeable correlation with the experimentally determined spectrum measured at 78K, overestimating the peak by 1.20%, as seen in **Figure 3.7A**. There were three peaks found in the theoretical frequency, the most intense peak at 89.03$cm^{-1}$ could be correlated to the experimentally observed peak. The asymmetric shape of the peak in the experimental spectra suggests that there is a secondary component to this vibration. This can be corroborated by the theoretical vibrational modes, which suggest that the

minor peaks whose intensities were ~2% of the intensity of the major peak could account for the broadening of the observed peak.

The theoretically determined frequencies for the β form shows a slightly better correlation with the experimentally determined spectrum measured at 78K, only overestimating the peak by 1.08%, as shown in **Figure 3.7B**. There were five peaks found in the theoretical determined frequency modes. Of those five peaks, it was determined that three of them encompassed the observed peak, centering at ~86.47cm$^{-1}$. The remaining two peaks most likely correlate to a peak/peaks that lie just outside of the measured range for this investigation.

Comparing the two theoretically determined spectra, the difference in the major peak location has produced a similar shift to that found in the experimental spectra. Furthermore, the difference was very similar and in the same order as found experimentally. This reproduction of the frequency differences indicated that the difference observed in the experimental spectra was indeed due to the changes in packing for each polymorph and not due to experimental variance.

The empirical visualization of the modes showed that there were five different motions exhibited by the two polymorphs. However, there was only one common motion in both forms and that is illustrated in **Figure 3.8**. This motion relates primarily to a whole molecule rotation along the *a* axis. The rest of the motions were all intramolecular motions with the exception of the intermolecular mode e, found in the β form at 99.31 cm$^{-1}$. This mode produced a twisting motion of the pyridyl ring around a mostly motionless tetrazolate ring.

## 3.4 Conclusions

The crystal structure of a new polymorph of 5-(4-pyridyl)tetrazole (β-4PT) was determined using single crystal X-ray diffraction. In addition, the solid-state simulation of the geometric and vibrational properties was performed using the CRYSTAL code. The crystal

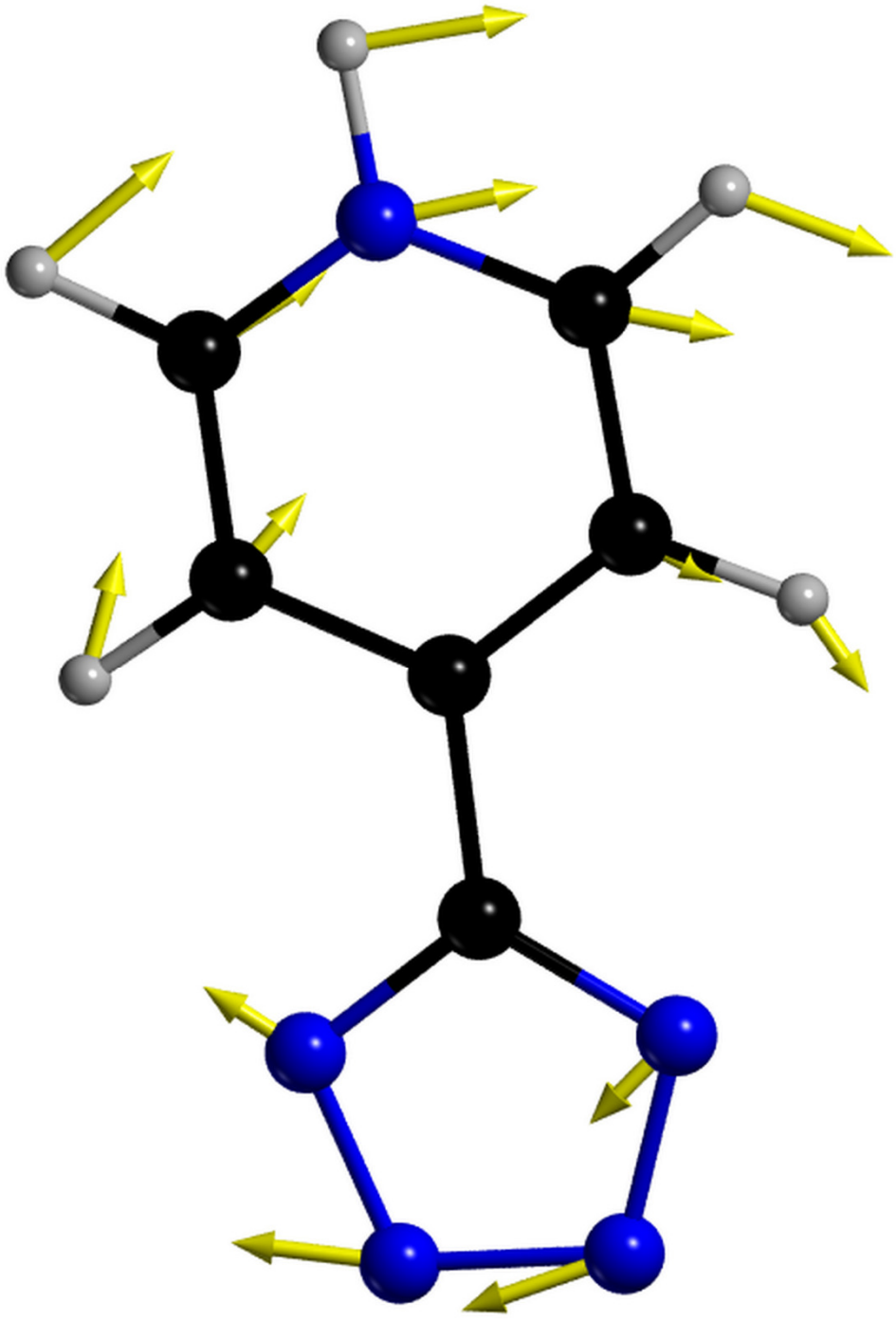

**Figure 3.8** Visualization of the vibrational normal mode corresponding to mode c. Arrows denote the direction of molecular motion. (Carbon is shown in black, nitrogen is shown in blue, and hydrogen is shown in grey)

structure revealed that the packing of adjacent hydrogen-bonded chains of β-4PT alternated in direction in comparison to the previously known form of 5-(4-pyridyl)tetrazole (α-4PT), where the adjacent hydrogen-bonded chains ran parallel to one another. Since these two systems only had packing differences with no changes in the molecular structure, they made a prime candidate for characterization by terahertz spectroscopy due to its ability to probe lattice vibrations unique to molecular crystals.

By comparing these two systems, we have shown that the compounds have nearly identical near-IR vibrations spectra, but also similar THz spectra. The primary difference was an apparent redshift in the peak location from the α to β phases of ~ 2cm$^{-1}$. It was also determined that the principal peak in each spectrum was the result of whole molecule rotation along the principal axis *a*. In addition, the energies of formation were compared, and it was found that the α form is more stable by ~.25 kJ/mol. This small difference in energy and the observed trend in the Gibbs free energy suggests that at elevated temperatures either form can be obtained, resulting in the discovery of the new polymorph of 5-(4-pyridyl)tetrazole.

### 3.5 Supporting Information

The supporting information contains an ORTEP view of the asymmetric unit of α-4PT, showing the partial atom-labeling schemes and 50% thermal ellipsoids (**Figure A-1**). In addition, the supporting information contains an ORTEP view of the asymmetric unit of β-4PT, showing the partial atom-labeling schemes and 50% thermal ellipsoids (**Figure A-2**). The supporting information also contains the room temperature terahertz spectra compared to the theoretically predicated spectra of the α and β forms of 5-(4-pyridyl)tetrazole are shown in **Figure A-3**. In addition, the normalized near-Infrared vibration spectral overlay of the α and β forms of 5-(4-pyridyl)tetrazole shown from 4000-400 cm$^{-1}$ (**Figure A-4**) is included.

Additional material available from the Cambridge Crystallographic Data Centre, CCDC No. CCDC 960961-960962, comprises the final atomic coordinates for all atoms, thermal parameters, and a complete listing of bond distances and angles. Copies of this information may be obtained free of charge on application to The Director, 12 Union Road, Cambridge, CB2 2EZ, UK, fax: +44 1223 336 033, e-mail: data_request@ccdc.cam.ac.uk or http://www.ccdc.cam.ac.uk.

### 3.6 Acknowledgment

This work was supported in part by a grant from the National Science Foundation (CHE0907787). Funding for this work was also provided by a grant from the National Science Foundation CAREER Program (CHE-0847405).

### 3.7 References

[1] R. Harris, *Analyst.,* **2006**, *131*, 351.

[2] K. Sato, *J. Phys. D Appl. Phys*., **1993**, *26,* B77.

[3] S. Pellizzeri, T.M. Korter, J. Zubieta, *J. Mol. Struct.,* **2011**, *1003*, 21.

[4] K. Sato, N. Yoshimoto, M. Suzuki, M. Kobayashi, F. Kaneko, *J. Phys. Chem.,* **1990**, *94*, 3180.

[5] K. Sato, K. Suzuki, M. Okada, N. Garti, *J. Cryst. Growth,* **1985**, *72*, 699.

[6] T. L. Threlfall, *Analyst*, **1995**, *120*, 2435.

[7] J. Haleblian and W. McCrone, *J. Pharm. Sci.*, **1969**, *58*, 911.

[8] J. Haleblian, *J. Pharm. Sci.*, **1975**, *68*, 1269.

[9] Q. Xu and J. Xu, *Acta Cryst.,* **2011**, *E67*, o43

[10] W. Ouellette, S. Jones, J. Zubieta, *CrystEngComm*, **2011**, *13*, 4457.

[11] S. P. Delaney, E. M. Witko, T.M. Smith, T.M. Korter, *J. Phys. Chem. A*, **2012**, *116*, 8051.

[12] S. P. Delaney, D. Pan, M. Galella, S.X. Yin, T.M. Korter, *Cryst. Growth Des.*, **2012**, *12*, 5017.

[13] M.D. King, W.D. Buchanan, T.M. Korter, *J. Pharm. Sci.,* **2011**, *100*, 1116**.**

[14] K. Siegrist, C.R. Bucher, I. Mandelbaum, A R. Hight Walker, R. Balu, S.K. Gregurick, D.F. Plusquellic, *J. Am. Chem. Soc.*, **2006**, *128*, 5764.

[15] R. Li, J.A. Zeitler, D. Tomerini, E.P.J. Parrott, L.F. Gladden, G.M. Day, *Phys. Chem. Chem. Phys.*, **2010**, *12*, 5329.

[16] K.C. Oppenheim, T.M. Korter, J.S. Melinger, D. Grischowsky, *J. Phys. Chem. A.,* **2010**, *114,* 12513.

[17] S. Pellizzeri, S.P. Delaney, T.M. Korter, J. Zubieta, *J. Mol. Struct*., **2013**, http://dx.doi.org/10.1016/j.molstruc.2013.07.017

[18] S. Pellizzeri, E.M. Witco, T.M. Korter, J. Zubieta, *J. Mol. Struct.*, **2013**, *1048,* 214.

[19] H. Detert and D. Schollmeier, *Synthesis,* **1999**, 999.

[20] Bruker-AXS smart Software, version 5.630, Siemens Analytical X-ray Instruments, Inc., Madison, WI, 1994.

[21] APEX II, Data Collection Software, version 2011.8-0 Bruker AXS Inc.: Madison, WI, **2005-2011**.

[22] SAINT Plus, Date Reduction Software, version, 6.45A Bruker AXS Inc.: Madison, WI, **1997-2002**.

[23] G. M. Sheldrick, SADABS University of Göttingen: Göttingen, Germany, **1996**.

[24] SHELXTL PC, version 6.12 Bruker AXS Inc.: Madison, WI, **2002**.

[25] A. Nahata, A.S. Weling, T.F. Heinz, *Appl. Phys. Lett.,* **1996**, *69*, 2321.

[26] A. Rice, Y. Jin, X.F. Ma, X.C. Zhang, D. Bliss, J. Larkin, M. Alexander, *Appl. Phys. Lett.,* **1994**, *64*, 1324.

[27] Q. Wu, M. Litz, X.C. Zhang, *Appl. Phys. Lett.,* **1996**, *68*, 2924.

[28] P.M. Hakey, D.G. Allis, M.R. Hudson, W. Ouellette, T.M. Korter, *ChemPhysChem,* **2009**, *10*, 2434.

[29] P.M Hakey, M.R. Hudson, D.G. Allis, W. Ouellette, T.M. Korter, *J. Phys. Chem. A,* **2009**, *113*, 13013.

[30] J.R. Holden and C.W. Dickinson, *J. Phys. Chem.,* **1975**, *79*, 249.

[31] T.M Lowry and F.C. Hemmings, *J. Soc. Chem. Ind., London,* **1920**, *39*, 101.

[32] R. Dovesi, R. Orlando, B. Civalleri, R. Roetti, V.R. Saunders, C.M. Zicovich-Wilson, *Z. Kristallogr.,* **2005**, *220*, 571.

[33] R Dovesi, V. R. Saunders, R. Roetti, R. Orlando, C.M. Zicovich-Wilson, F. Pascale, B. Civalleri, K. Doll, N. M. Harrison, I. J. Bush, P. D'Arco, M. Llunell, CRYSTAL09 User's Manual. University of Torino: Torino, 2009.

[34] A. D. Becke, *J. Chem. Phys.*, **1993**, *98*, 5648.

[35] M. F. Peintinger, D. V. Oliveira, T. Bredow, *J. Comput. Chem.,* **2013**, *34*,451.

[36] F. Pascale, C.M. Zicovich-Wilson, F.L. Gejo, B. Civalleri, R. Orlando, R. Dovesi, *J. Comput. Chem.*, **2004**, *25,* 888.

[37] CrystalMaker® : a crystal and molecular structures program. CrystalMaker Software Ltd., Oxford, England (www.crystalmaker.com).

[38] S.F. Boys and F. Bernardi, *Mol. Phys.*, **1970**, *19*, 553.

[39] P. Canepa, R.M. Hanson, P. Ugliengo, M. Alfredsson, *J. Appl. Cryst*., **2011**, *44*, 225.

# Chapter 4

## Using Solid-state Density Functional Theory and Terahertz Spectroscopy to Spectroscopically Distinguish the Various Hydrohalide Salts of 5-(4-pyridyl)tetrazole

The material contained within this chapter is published in *Journal of Molecular Structure* (Pellizzeri, S.; Delaney, S. P.; Korter, T.M.; Zubieta, J. *J. Mol. Struct.* **2013**, *1050*, 27-34). This article has been reproduced with permission from Elsevier.

## 4.1 Introduction

Stable nitrogen containing heterocycles play important roles in many diverse fields of chemistry. Examples of nitrogen containing heterocycle with the highest nitrogen content are the tetrazole derived compounds. Tetrazoles play an important role in coordination chemistry, as ligands with multiple binding modes to metal centers,[1] in material science as a special explosive,[2,3] and in medical chemistry, where they find a role as a surrogate for carboxyl and amide groups.[4,5] Tetrazoles can also be easily substituted, in particular the 5-monosubsituted tetrazoles are interesting because this substitution can increase their ability to coordinate to multiple metal centers to form a more complex material.[6] Furthermore, substitution can expand their use in medical chemistry due to their ionization at physiological pH values, rendering these compounds nearly 10 times more lipophilic than similar carboxylates.[7] This study looks at one particular 5-monosubsituted tetrazole, 5-(4-pyridyl)tetrazole, which can exist as either the zwitterionic free acid[8] or as two distinct hydrohalide salts 4-(1H-Tetrazol-5-yl)pyridinium chloride (4-PT·HCl)[9] and 4-(1H-Tetrazol-5-yl)pyridinium bromide (4-PT·HBr),[10] illustrated in **Figure 4.1.**

The importance of identifying halide salts is more than a curiosity, due to the fact that in pharmaceuticals much time and effort is put into salt formation. Salt formation is the most common and effective method of increasing solubility and dissolution rates of acidic and basic drugs.[11] Crystalline salts can also increase the chemical stability and can have higher bioavailability relative to the free base or acid of the active compound. Finally, salts and other crystal forms (e.g. hydrates, solvates, and cocrystals) of a drug substance are considered distinct chemical entities with their own patentable chemical and biological profiles.[12,13] In the case of the isostructural halide salts of 5-(4-pyridyl)tetrazole, **Figure 4.2** shows that near-infrared

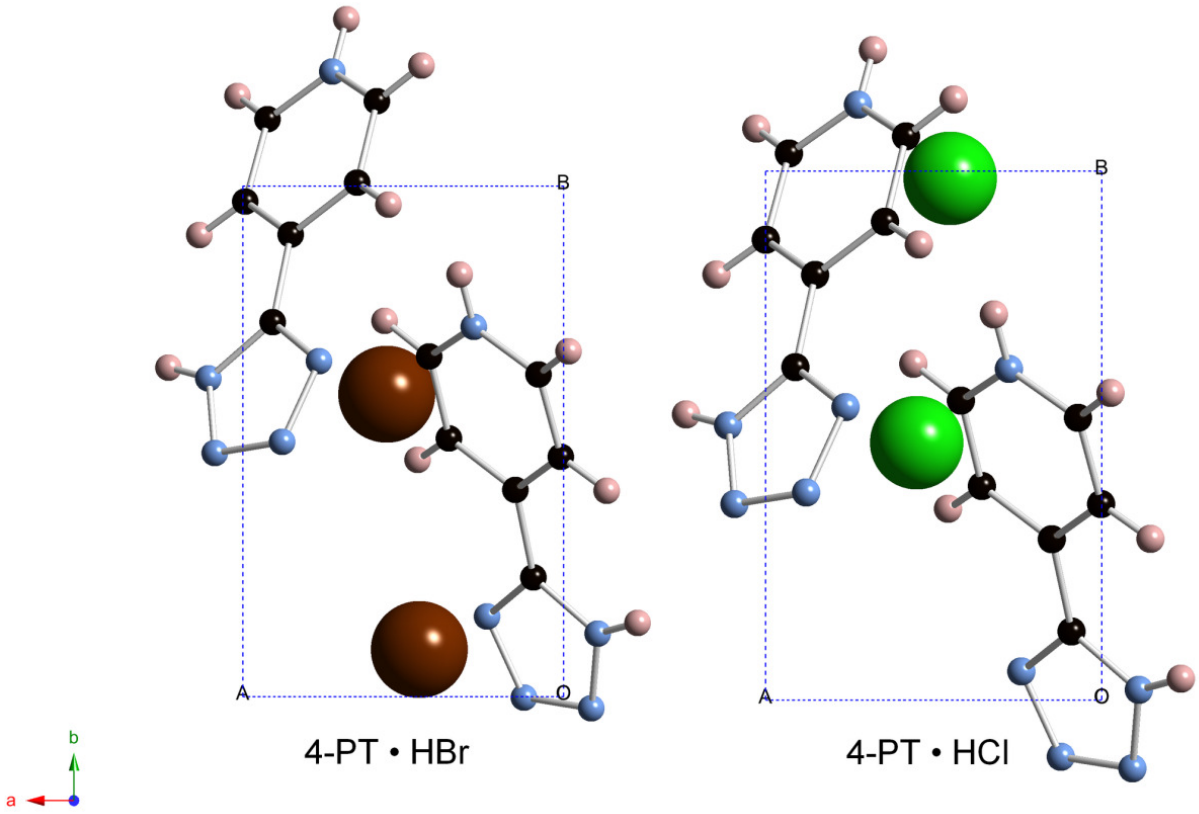


**Figure 4.1** Ball and Stick representation of the molecular cell of 4-(1H-Tetrazol-5-yl)pyridinium bromide (4-PT·HBr) and 4-(1H-Tetrazol-5-yl)pyridinium chloride (4-PT·HCl). (Bromine is shown in dark red, chlorine is shown in green, carbon is shown in black, nitrogen is shown in light blue and hydrogen is shown in pink)

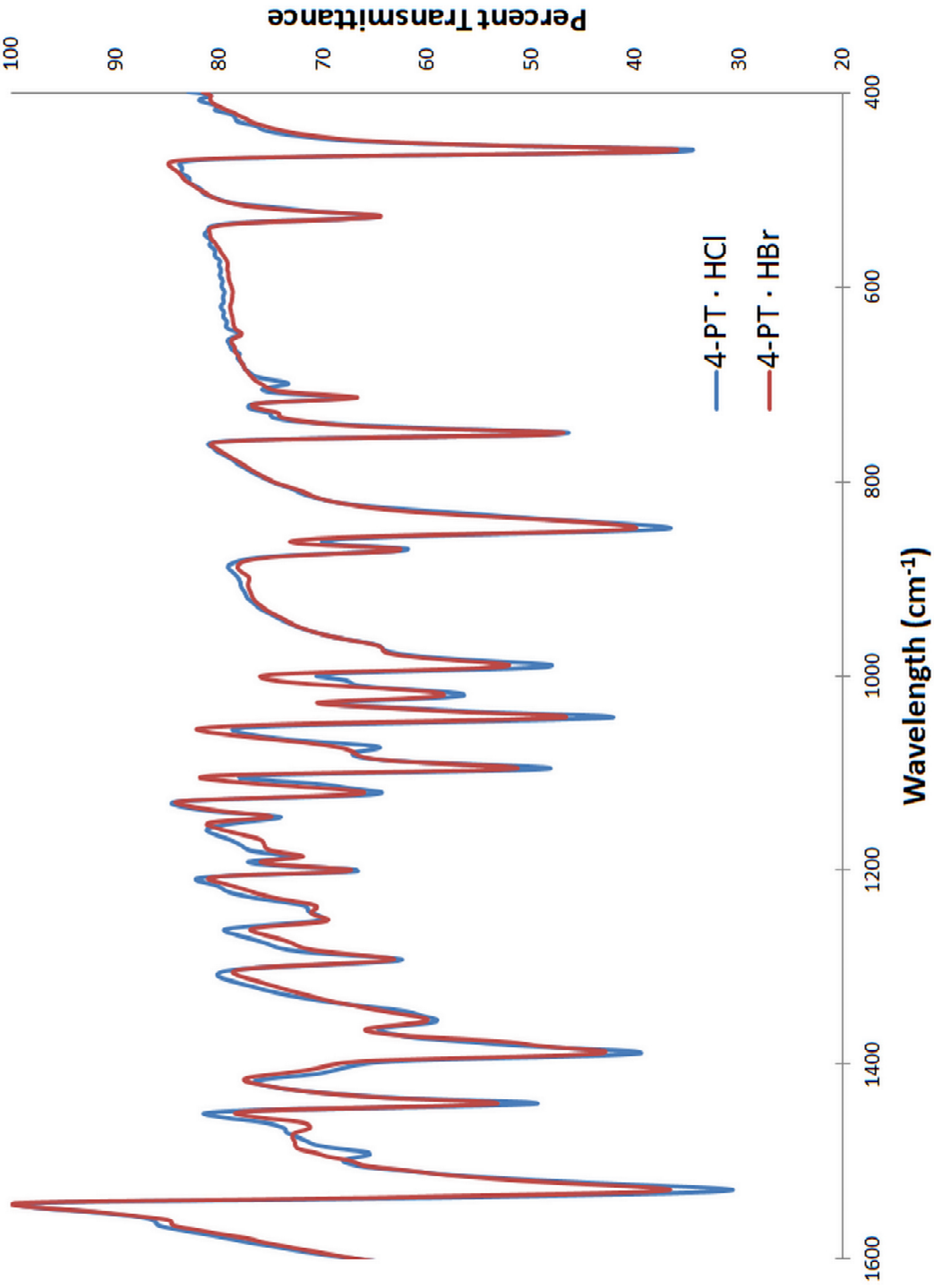


**Figure 4.2** Near-Infrared vibration spectra of 4-PT·HCl and 4-PT·HBr shown from 1600-400 $cm^{-1}$.

spectroscopy only shows subtle vibrational changes. Therefore, a spectroscopy technique that probes low energy molecular motion would prove useful.

Terahertz (THz) spectroscopy was utilized in this study because it has been previously used to investigate polymorphs of molecular crystals where the terahertz absorption is caused by lattice vibrations unique to three-dimensional ordered solids.[14-16] Unlike near-IR vibrational spectroscopy, there are no characteristic group frequencies in the THz region; therefore, computational approaches, primarily solid-state density functional theory (DFT).[17-19]

The solid-state DFT approach that was used in this study is implemented in CRYSTAL09. The CRYSTAL program has been previously used to simulate many inorganic systems to determine their structural, electronic, magnetic and vibrational properties,[20-23] as well as the vibrational spectra of organic systems.[24-26] In this study, CRYSTAL09 was used to replicate the geometric parameters of the halide salts of 5-(4-pyridyl)tetrazole as well as to determine the vibrationally active modes in the THz region and to evaluate the normal modes that are the result of these absorptions. Due to the isostructural nature of these complexes any differences that are observed in the terahertz spectra can be almost directly related to the anion rather than to symmetry or packing differences.

## 4.2 Experimental and Theoretical Methods

### *4.2.1 Experimental*

#### *4.2.1.1 Synthesis of Halide Salts of 5-(4-pyridyl)tetrazole*

All reagents were purchased from their respective vendors and used without further purification. Water was distilled above 3.0 MΩ in-house using a Barnstead Model 525 Biopure Distilled Water Center. 5-(4-pyridyl)tetrazole was prepared using previously published

methods.[27] To obtain the hydrochloride salt of 5-(4-pyridyl)tetrazole, the crude 5-(4-pyridyl)tetrazole was acidified with a water/HCl solution to a pH of about 2, then allowed to crystallize by slow evaporation. The hydrobromide salt was obtained using literature methods.[10] All halide salts of 5-(4-pyridyl)tetrazole were confirmed using single-crystal X-ray diffraction. The infrared spectra were obtained on a Thermo Nicolet IR200 FT-IR using the KBr pellet method and a spectral resolution of 2 $cm^{-1}$ over the range of 4000-400 $cm^{-1}$. The KBr was dried prior to usage

#### *4.2.1.2 X-Ray Crystallography*

Crystallographic data for all compounds were collected on a Bruker KAPPA APEX DUO diffractometer using Mo-$K_\alpha$ radiation ($\lambda$ = 0.71073 Å) containing a APEX II CCD system.[28] All data collections were taken at low temperature (90 K). The data were corrected for Lorentz and polarization[29] effects, and adsorption corrections were made using *SADABS*.[30] Structures were solved by direct methods. Refinements for each structure were carried out using the SHELXTL[31] crystallographic software. Following assignment of all non-hydrogen atoms, the models were refined against $F^2$ first using isotropic and then using anisotropic thermal displacement parameters. The hydrogen atoms were introduced in calculated positions and then refined isotropically. Neutral atom scattering coefficients along with anomalous dispersion corrections were taken from the *International Tables*, Vol. C.

### *4.2.2 Time-domain terahertz spectroscopy*

The experimental terahertz spectra of the compounds were acquired using a pulsed time-domain THz spectrometer based on an amplified femtosecond Ti:Sapphire laser system operating in the near-infrared region. For the generation and detection of THz radiation, the

instrument utilized optical rectification[32,33] and free space electro-optic sampling,[34,35] respectively. A detailed description of the spectrometer along with the experimental setup has been provided elsewhere.[25,36,37]

The 5-(4-pyridyl)tetrazole halide salts were used without further purification and were mixed with a spectroscopic grade powdered polytetrafluoroethylene (PTFE) matrix. The sample and the matrix were then mechanically pulverized using a stainless-steel ball mill (Dentsply Rinn 3110-3A), allowing a homogeneous distribution of the sample through the matrix, thereby reducing the particle size, and minimizing radiation scattering.[37,38] The mixture was then pressed into a pellet at 2000 psi using a hydraulic press (ICL E-Z Press 12). The resulting sample pellet had a total mass of approximately 0.55 g, thickness of ~2.0 mm, diameter of 13.0 mm. The final sample pellets contained 1.57% w/w 4-PT·HBr and 0.57% w/w 4-PT·HCl. The blank (reference) pellet was prepared with pure PTFE in a similar manner.

The sample and blank pellets were both held under vacuum in a variable-temperature cryostat and held at tempera.tures of 293 K (room temperature) and 78 K (liquid-nitrogen temperature).

Each individual spectrum of the sample (or the blank pellet) consisted of an average of 36 THz-waveform scans over a time window of ~30 ps. These waveforms were then symmetrically zero-padded to a total of 6000 data points, and subsequently were Fourier-transformed (utilizing a Hanning window function) into the frequency-domain. Elimination of any THz absorption by the PTFE matrix was accomplished by taking a ratio of the transformed spectrum of a PTFE blank versus the transformed spectrum of a sample pellet. To improve the final signal-to-noise ratio, four blank/sample sets were collected and averaged, over a range of 10 to 100 $cm^{-1}$ with a spectral resolution of approximately 1.0 $cm^{-1}$, yielding the THz spectra reported here.

### *4.2.3 Theoretical Methodology of CRYSTAL09*

Geometry optimizations, harmonic frequencies, and intensity calculations were performed using the CRYSTAL09 program.[39,40] All calculations were performed using a spin restricted B3LYP[41] hybrid density functional. The basis set chosen for all the atoms was a Gaussian type triple valence basis set with polarization (pob_TZVP).[42]

The positions of the atoms contained within the unit cell were optimized within the constraints of the literature lattice parameters and space group symmetry. From the optimized structures, the bond lengths and bond angles were determined and compared with the experimental crystallographic results. After optimizing the structures, harmonic-limit normal-mode analyses on the organometallic complexes were conducted. Frequencies were determined by a mass-weighted numerical evaluation of the Hessian matrix[43] and intensities were calculated through the Berry phase approach.[40]

Several of the convergence parameters were changed to optimize the accuracy and computational time of the calculations. The convergence criteria were modified to set the root mean square of the maximum gradient (TOLDEG) and the maximum displacement (TOLDEX) to be $1 \times 10^{-5}$ and $4 \times 10^{-5}$ angstroms, respectively. To improve the numerical accuracy of the calculations the truncation criteria for bielectronic integrals (TOLINTEG) was set to 8 8 8 8 16 and the DFT integration was set to XLGRID (75,974). (See Ref. [39,40] for details). Total energy convergence (TOLDEE) was set to $\Delta E < 1 \times 10^{-8}$ Hartree for the geometry optimizations and $\Delta E < 1 \times 10^{-11}$ Hartree for frequency analyses. To assist in a timely convergence, the "Fock/KS matrix mixing" (FMIXING) was increased from the default value of zero to 50 for all systems. The eigenvalue level shifter was also activated with the level shifter set to a value that corresponds to a shift of 0.5 Hartree, and the state was locked, confining it to an insulating state.

Determination of the optimum sampling of reciprocal space was determined by comparing the total energy of the converged system to the k-point count using the keyword SHRINK. The optimum SHRINK value was determined to be SHRINK = 7 7 which corresponds to 100 points in the irreducible part of the Brillouin Zone and 100 points in the Gilat Net.

## 4.3 Results and Discussion

### *4.3.1 X-Ray Crystallography*

In order to accurately compare the experimentally collected data to the theoretical data, it is necessary to use unit cell parameters and atomic positions from a crystal structure that has been determined near the same temperature at which the THz spectroscopy has been performed. The previously published crystal structures for 4PT·HCl and 4PT·HBr were determined at 298 K, therefore, it was necessary to collect crystal structures at 90K, to be able to more accurately represent the THz spectrum collected at 78K. Both structures were found to be isostructural with the published room temperature collections; however, the unit cell parameters are contracted slightly as expected. 4PT·HCl crystalized in the $P2_1$ space group with unit cell dimensions of $a$ = 4.8308(6) Å, $b$ = 7.5921(9) Å, $c$ = 10.6871(12) Å, α = γ = 90.0°, and β = 91.954(10) °. 4PT·HBr crystalized in the $P2_1$ space group with unit cell dimensions of $a$ = 4.8374(6) Å,$b$ = 7.6897(10) Å, $c$ = 11.0160(15) Å, α = γ = 90.0°, and β = 91.427(2) °. Both crystallize in similar morphologies with the 4PT·HBr being slightly expanded in the b and c axis due to the larger size of the bromide ion in comparison to the chloride ion.

### *4.3.2 Comparison of the Calculated and Experimental Structures*

The calculated and experimental bond lengths, bond angles, and the root-mean-squared deviation (RMSD) values are shown in **Table 4.1** and **Table 4.2** for 4PT·HCl and 4PT·HBr, respectively for each complex, and the results are visualized in **Figure 4.3**. The halogen nitrogen-distance was included since these complexes are held together through hydrogen bonding from the protonated pyridal nitrogen to the halogen anion, as well as from the protonated tetrazole nitrogen to the halogen anion, as illustrated in **Figure 4.4**. The halogen-nitrogen distance was used and not the hydrogen-halogen distance, because the hydrogen atoms in the experimental structure are positioned at calculated positions leading to uncertainty in their position, which is not the case for the nitrogen atoms.

The bond lengths were modeled for both complexes with a very reasonable amount of accuracy, replicating each of the bonds, with the exception of X-N1(X = Cl or Br), within ±0.025 Å for 4PT·HCl and 4PT·HBr. The X-N1 bond was overestimated in both cases by a reasonable amount, +0.051 Å for 4PT·HCl and +0.085 Å for 4PT·HBr; however, the X-N2 bond was very closely replicated in the theoretical structure. This discrepancy suggests that the halogen anion is extending along the hydrogen bonded chain as shown in **Figure 4.4** to increase the angle between X-H-N2 to get the bond angle closer to the ideal 180° for hydrogen bonding, Cl(Br)-H-N2 increases from 158.8(2)°(159.3(2)°) in the experimental structure to 170.29°(171.98°) in the theoretical structure. This would be consistent with the already nearly ideal angle between X-H-N1, which for the chloride(bromide) does not deviate much from 177.0(2)°(177.9(2)°) in the experimental structure to 178.0°(180.0°) in the theoretical structure. Therefore, there is a competition between the inherent packing forces and ideal hydrogen bonding in the crystallographic structure; however, in the theoretically derived structure the drive

**Table 4.1** Interatomic bond lengths (Å), angles (°), and RMSD values for 4PT·HCl. See **Figure 4.3** for atomic labels. Experimental parameters are from 90 K crystallographic data.

| Bond, Å | Experimental | 4PT·HCL |
|---|---|---|
| **Cl-N1** | 3.0739 | 3.1245 |
| **Cl-N2** | 3.0381 | 3.0489 |
| **N1-C1** | 1.3435 | 1.3426 |
| **N1-C5** | 1.3460 | 1.3446 |
| **N2-N3** | 1.3354 | 1.3587 |
| **N2-C6** | 1.3281 | 1.3407 |
| **N3-N4** | 1.3203 | 1.3177 |
| **N4-N5** | 1.3666 | 1.3706 |
| **N5-C6** | 1.3242 | 1.3258 |
| **C1-C2** | 1.3775 | 1.3734 |
| **C2-C3** | 1.3917 | 1.3934 |
| **C3-C4** | 1.3891 | 1.3936 |
| **C3-C6** | 1.4676 | 1.4574 |
| **C4-C5** | 1.3628 | 1.3716 |
| | **RMSD** | 0.01610 |

| Angle, ° | Experimental | 4PT·HCL |
|---|---|---|
| **N1-Cl-N2** | 90.249 | 88.89 |
| **C1-N1-C5** | 122.400 | 122.623 |
| **N3-N2-C6** | 109.566 | 108.628 |
| **N2-N3-N4** | 106.134 | 106.196 |
| **N3-N4-N5** | 109.805 | 110.192 |
| **N4-N5-C6** | 105.855 | 106.062 |
| **N1-C1-C2** | 119.703 | 119.950 |
| **C1-C2-C3** | 119.162 | 118.943 |
| **C2-C3-C4** | 119.232 | 119.535 |
| **C2-C3-C6** | 122.075 | 122.126 |
| **C4-C3-C6** | 118.693 | 118.339 |
| **C3-C4-C5** | 119.837 | 119.394 |
| **N1-C5-C4** | 119.644 | 119.533 |
| **N2-C6-N5** | 108.640 | 108.921 |
| **N2-C6-C3** | 127.156 | 126.387 |
| **N5-C6-C3** | 124.173 | 124.691 |
| **C2-C3-C6-N2** | -3.690 | -1.824 |
| **C2-C3-C6-N5** | 174.016 | 177.707 |
| **C4-C3-C6-N2** | 176.276 | 177.801 |
| **C4-C3-C6-N5** | -6.018 | -2.669 |
| | **RMSD** | 1.3247 |

**Table 4.2** Interatomic bond lengths (Å), angles (°), and RMSD values for 4PT·HBr. See **Figure 4.3** for atomic labels. Experimental parameters are from 90 K crystallographic data.

| Bond, Å | Experimental | 4PT·HBr |
|---|---|---|
| **Br-N1** | 3.2108 | 3.2953 |
| **Br-N2** | 3.1906 | 3.1908 |
| **N1-C1** | 1.3438 | 1.3427 |
| **N1-C5** | 1.3500 | 1.3449 |
| **N2-N3** | 1.3321 | 1.3579 |
| **N2-C6** | 1.3409 | 1.3408 |
| **N3-N4** | 1.3099 | 1.3176 |
| **N4-N5** | 1.3502 | 1.3713 |
| **N5-C6** | 1.3271 | 1.3257 |
| **C1-C2** | 1.3764 | 1.3733 |
| **C2-C3** | 1.3899 | 1.3931 |
| **C3-C4** | 1.3998 | 1.3941 |
| **C3-C6** | 1.4583 | 1.4582 |
| **C4-C5** | 1.3708 | 1.3712 |
| | **RMSD** | 0.02448 |

| Angle, ° | Experimental | 4PT·HBr |
|---|---|---|
| **N1-Br-N2** | 86.907 | 85.708 |
| **C1-N1-C5** | 122.219 | 122.809 |
| **N3-N2-C6** | 109.349 | 108.837 |
| **N2-N3-N4** | 105.897 | 106.052 |
| **N3-N4-N5** | 110.980 | 110.247 |
| **N4-N5-C6** | 105.781 | 106.082 |
| **N1-C1-C2** | 120.064 | 119.873 |
| **C1-C2-C3** | 119.222 | 118.905 |
| **C2-C3-C4** | 119.325 | 119.595 |
| **C2-C3-C6** | 122.507 | 122.077 |
| **C4-C3-C6** | 118.157 | 118.327 |
| **C3-C4-C5** | 119.396 | 119.436 |
| **N1-C5-C4** | 119.765 | 119.362 |
| **N2-C6-N5** | 107.992 | 108.778 |
| **N2-C6-C3** | 126.463 | 126.353 |
| **N5-C6-C3** | 125.520 | 124.866 |
| **C2-C3-C6-N2** | -5.229 | -2.448 |
| **C2-C3-C6-N5** | 172.710 | 176.785 |
| **C4-C3-C6-N2** | 175.979 | 177.848 |
| **C4-C3-C6-N5** | -6.082 | -2.919 |
| | **RMSD** | 1.4523 |

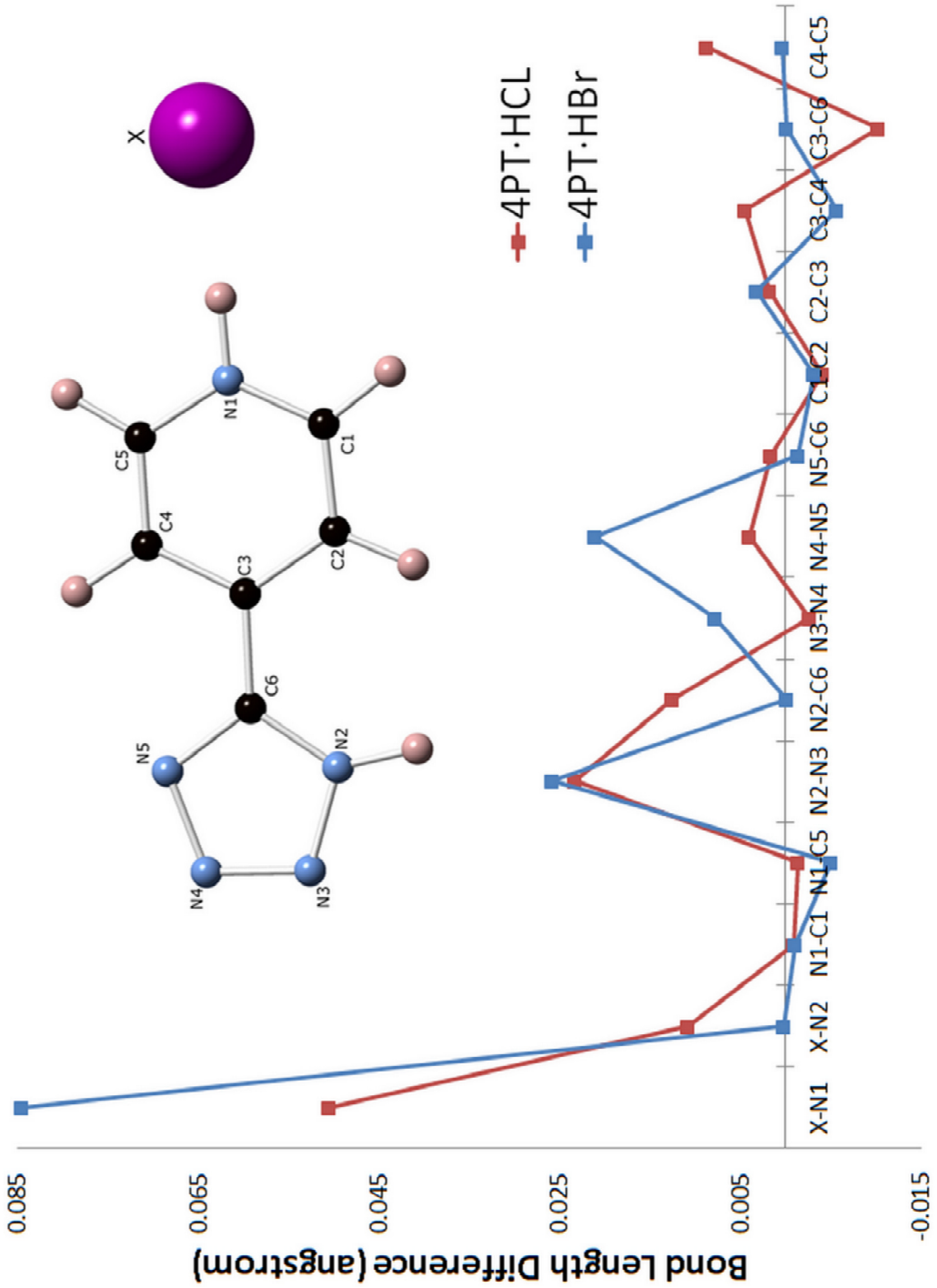


**Figure 4.3** Calculated bond-length differences for 4-(1H-Tetrazol-5-yl)pyridinium chloride (4-PT·HCl) and 4-(1H-Tetrazol-5-yl)pyridinium bromide (4-PT·HBr). The inset figure shows the atom labeling for 4-(1H-Tetrazol-5-yl)pyridinium chloride (4-PT·HCl) and 4-(1H-Tetrazol-5-yl)pyridinium bromide (4-PT·HBr).

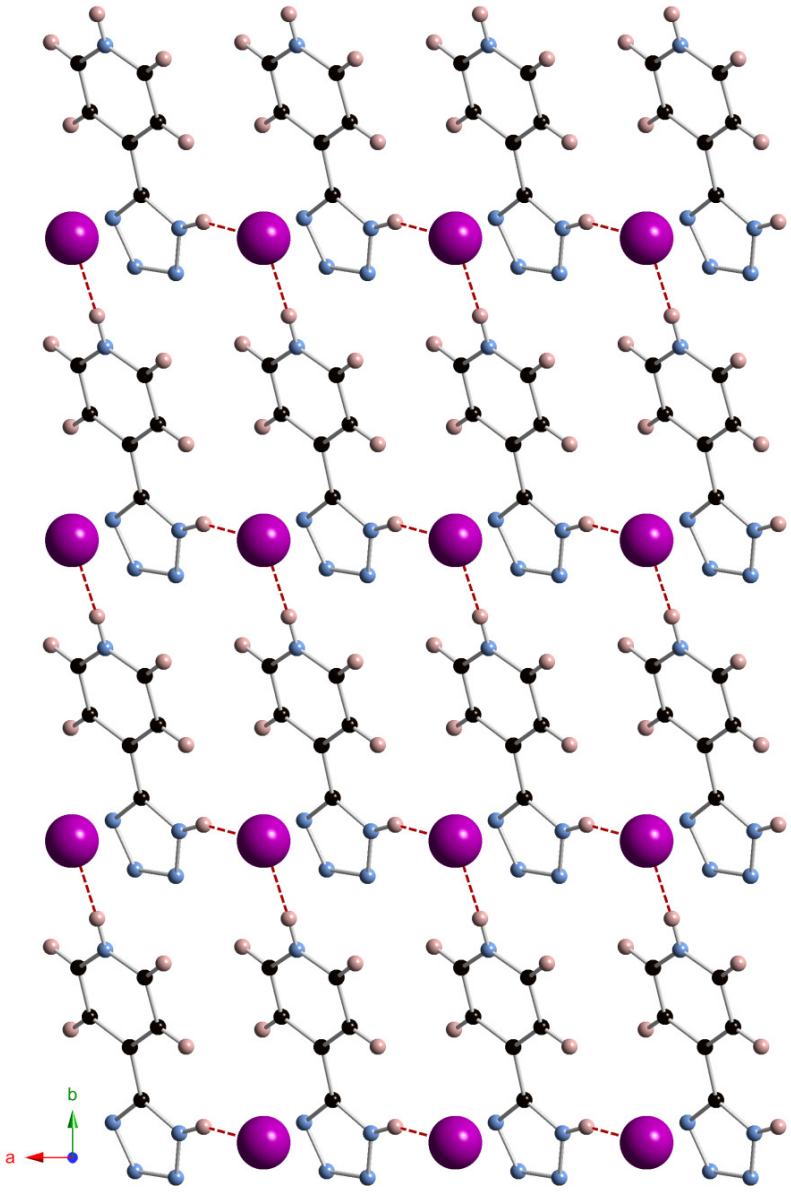


**Figure 4.4** Ball and stick representation of 4-(1H-Tetrazol-5-yl)pyridinium chloride (4-PT·HCl) and 4-(1H-Tetrazol-5-yl)pyridinium bromide (4-PT·HBr) in the *ab* plane displaying the hydrogen bonded 4-(1H-Tetrazol-5-yl)pyridinium chains. (Bromine/Chlorine is shown in purple, carbon is shown in black, nitrogen is shown in light blue, hydrogen is shown in pink, and hydrogen bonding shown with red dashed lines)

for ideal hydrogen bonding angles distorts the location of the halogen ion.

The angles were also modeled with a fair degree of accuracy, as shown by the low RMSDs. The calculated RMSDs for the 4PT·HCl and 4PT·HBr complexes were 1.3247 and 1.1577 respectively. It is important to note that in these systems, the tetrazolate ring is canted by ~6°, which is significant, because it shows that the pyridyl ring and the tetrazolate ring can move independently. Therefore, they are not locked in a planar conformation by delocalization of the π bonds over the entire molecule.

### *4.3.3 Comparison of Theoretical and Experimental Vibrational Frequencies*

The experimental and calculated terahertz spectra are shown in **Figure 4.5** and **Figure 4.6** and are summarized in **Table 4.3** and **Table 4.4**. Empirical analysis of the vibrational modes observed using J-ICE[44] are shown in **Table 4.5**. Where there is a combination of intramolecular and intermolecular motions, only the major motion is listed.

Overall, the fits of the theoretically determined terahertz spectra match well to the experimentally determined spectra. In addition to the fit, the intensities of the theoretically determined spectra are reasonably similar as seen in 4PT·HCl or slightly over estimated as with the 4PT·HBr.

The 4PT·HCl spectra at 78K and 298K both display five peaks. It can be assumed that at the higher temperature the peak at 68.59 $cm^{-1}$ in the low temperature spectrum is within the bandwidth of the high temperature peak at 74.54 $cm^{-1}$. It is also reasonable to assume that the peak at 98.07 $cm^{-1}$ in the high temperature spectrum corresponds to a peak that is outside the collection range. The theoretically determined frequencies show an agreeable correlation with the experimentally determined spectrum determined at 78K producing an RMSD of 8.518. It was

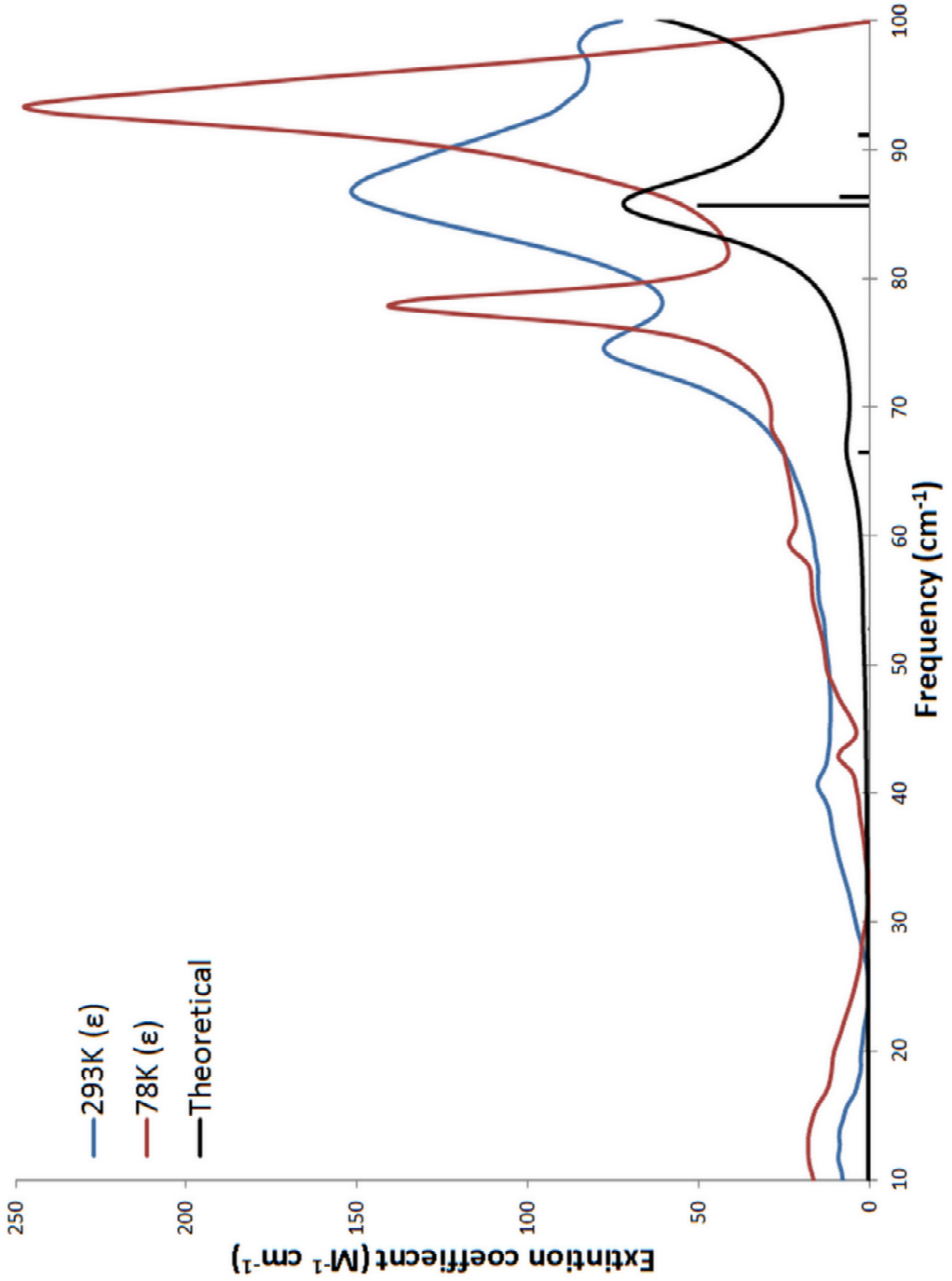


**Figure 4.5** The experimental and theoretical traces for the terahertz spectra of 4-(1H-Tetrazol-5-yl)pyridinium chloride (4-PT·HCl). An empirical 3.0 $cm^{-1}$ full-width-half-maximum Lorentzian line shape has been applied to the theoretical data to aid in comparison.

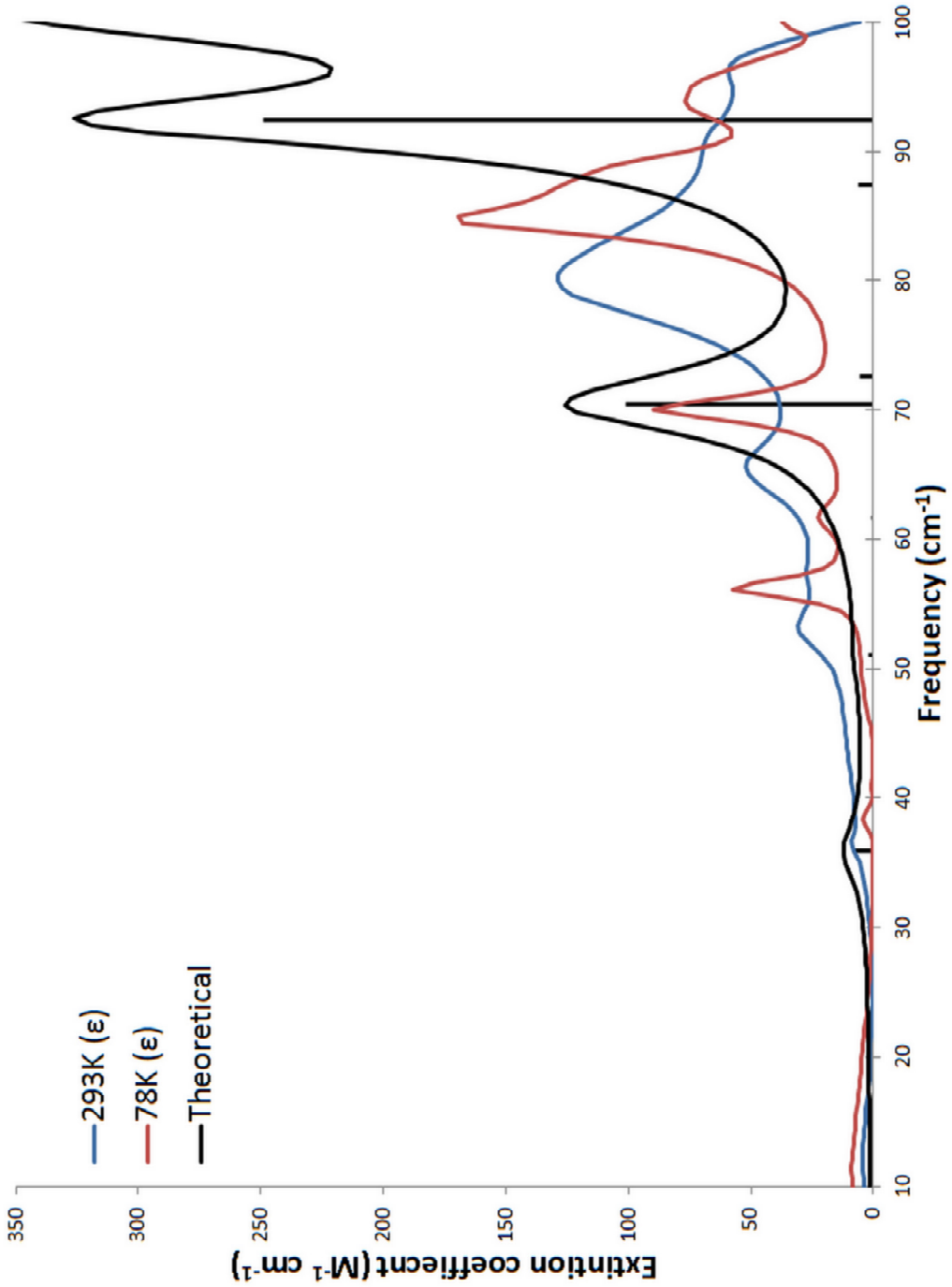


**Figure 4.6** The experimental and theoretical traces for the terahertz spectra of 4-(1H-Tetrazol-5-yl)pyridinium bromide (4-PT·HBr). An empirical 3.0 $cm^{-1}$ full-width-half-maximum Lorentzian line shape has been applied to the theoretical data to aid in comparison.

**Table 4.3** Frequency positions ($cm^{-1}$) and RMSD for the experimental and theoretical terahertz spectra of 4PT·HCl. The blanks are peaks that have no obvious correlation between the room temperature and cryogenic experimental spectra. When multiple peaks corresponded to only one peak in the experimental spectra, the weighted average was used in calculating the RMSD. Mode descriptions are described in **Table 4.5**.

| Mode | Exp. (78K) | Exp. (293K) | Theoretical | Intensity (ε) |
|---|---|---|---|---|
| a | 42.89 | 40.65 | 52.71 | 0.07 |
| b | 59.46 | 56.21 | 66.53 | 0.79 |
| c | 68.59 | --- | 71.98 | 0.03 |
| d | 77.89 | 74.54 | 85.60 | 12.15 |
| e | | | 86.29 | 2.14 |
| f | 93.27 | 86.72 | 91.14 | 0.81 |
| g | | | 105.49 | 50.63 |
| h | --- | 98.07 | 111.42 | 8.75 |
| | | **RMSD** | 8.518 | |

**Table 4.4** Frequency positions ($cm^{-1}$) and RMSD for the experimental and theoretical terahertz spectra of 4PT·HBr. When multiple peaks corresponded to only one peak in the experimental spectra, the weighted average was used in calculating the RMSD. Mode descriptions are described in **Table 4.5**.

| Mode | Exp. (78K) | Exp. (293K) | Theoretical | Intensity (ε) |
|---|---|---|---|---|
| a | 38.31 | 36.51 | 35.91 | 2.03 |
| b | 56.18 | 53.22 | 51.07 | 0.42 |
| c | 61.70 | 57.54 | 61.62 | 0.14 |
| d | 70.03 | 65.59 | 70.43 | 24.32 |
| e | | | 72.54 | 1.28 |
| f | 84.70 | 80.15 | 87.46 | 1.55 |
| g | 87.86 | | 92.39 | 59.97 |
| h | 93.65 | 90.85 | 99.75 | 27.47 |
| i | 95.40 | | 101.54 | 17.83 |
| j | | | 101.63 | 19.33 |
| | | **RMSD** | 4.120 | |

**Table 4.5** Empirical normal mode analysis of the halide salts of 5-(4-pyridyl)tetrazole.

| Mode | Description |
|---|---|
| a | Translation along *b* |
| b | Molecular rotation along *ac* plane |
| c | Translation along *a* |
| d | Internal torsion along H-X-H (X= Cl,Br) |
| e | Molecular rotation along *ab* plane |
| f | Bending between pyridyl and tetrazole ring |
| g | Molecular rotation along *b* |
| h | Translation along *c* |
| i | Molecular rotation along *bc* plane |
| j | Molecular rotation along *ac* plane |

found that two peaks in the experimental spectra were comprised of two peaks in the theoretically determined spectrum. These included the experimentally observed peak at 77.89 $cm^{-1}$ being a combination of the peaks found at 85.60 $cm^{-1}$ and 86.29 $cm^{-1}$ where the former was the major component. It was also determined that the peak at 93.27 $cm^{-1}$ was comprised of the peaks at 91.14 $cm^{-1}$ and 105.49 $cm^{-1}$ where the latter was the major component. It is interesting to note that the position of the peaks in the theoretical spectra overestimate the experimental positions by approximately 10%. If the frequency positions are scaled to 90% of the original values, then the RMSD reduces from 8.518 to 2.761, which is a significant improvement in the model of the terahertz spectrum. (Frequency positions and the visualizations are available as supplementary material in **Table B-1** and **Figure B-2**, respectively.)

The 4PT·HBr spectrum at 78K shows eight peaks, while the spectrum at 293K shows seven. The difference in the number of peaks primarily comes from the better resolution of the peaks at cryogenic temperatures; furthermore, it is safe to assume that the peak at 96.19 $cm^{-1}$ in the high temperature spectrum corresponds to a peak in the cryogenic spectrum that is outside the collection range. The theoretically determined frequencies show an excellent correlation with the experimentally determined spectrum at 78K producing an RMSD of 4.120. It was found that two peaks in the experimental spectra were comprised of two peaks in the theoretically determined spectrum. These included the experimental peak at 70.03 $cm^{-1}$ being a combination of the peaks found at 70.43 $cm^{-1}$ and 72.54 $cm^{-1}$ where the former was the major component. It was also determined that the peak at 95.40 $cm^{-1}$ was comprised of the peaks at 101.54 $cm^{-1}$ and 101.63 $cm^{-1}$ where the latter was the major component. Unlike the 4PT·HCl spectra there is no universal shift in the positions of the theoretically derived frequency positions; however, the intensities are much larger than those determined experimentally.

The empirical visualization of the modes showed that changing the ion resulted in no significant changes in the mode descriptions only changes in the mode locations, consistent with a mass effect of increasing the mass, decreasing the vibration energy. This is apparent especially in the lower energy vibrations, such as the mode identified primarily as a translation along *b,* and more interestingly in the assigned internal torsion along the H-X-H, which is assigned to the peak at 77.89 $cm^{-1}$ and 70.03 for the 4PT·HCl and 4PT·HBr models, respectively.

Approximating the difference in the vibrational frequencies using eq. 4.1 (*f* = force constant of bond, μ = reduced mass), derived from Hooke's Law, shows that the difference in the vibrational frequency between these modes is related purely by the force constant and the reduced mass, illustrated in eq. 4.2.

$$\bar{\nu} = \frac{1}{2\pi c}\sqrt{\frac{f}{\mu}} \qquad \text{(eq. 4.1)}$$

$$\frac{\bar{\nu}_{H-Cl}}{\bar{\nu}_{H-Br}} = \sqrt{\frac{f_{H-Cl}}{\mu_{H-Cl}} * \frac{\mu_{H-Br}}{f_{H-Br}}} \qquad \text{(eq. 4.2)}$$

The approximated value for this vibrational difference is 1.175, while the difference for the corresponding experimental positions was found to be 1.112. This ~1.4% difference is attributed to the actual frequency being not purely attributed to the internal torsion along the H-X-H, and that furthermore, the approximated value does not take into effect any environmental influences. However, this close approximation helps to identify the major attributing factor for the shifting to lower frequencies in the 4PT·HBr model, as primarily due to the increased mass of the bromide compared to the chloride anion.

## 4.4 Conclusions

The solid-state simulation of the geometric and vibrational properties of the halide salts of 5-(4-pyridyl)tetrazole was performed to determine the effect of the anionic substitution on the low energy terahertz vibrations. CRYSTAL09 was used with great effect in the reproduction of the structure and vibrational frequencies of 4-(1H-Tetrazol-5-yl)pyridinium chloride and 4-(1H-Tetrazol-5-yl)pyridinium bromide allowing a clear assignment of the molecular motions associated with these vibrations.

By comparing the two systems, we have shown that compounds which have nearly identical near-IR vibrations spectra have a more drastic differences in the THz region. The internal torsion was used as a comparison model due to the major motion involving primarily a halogen-hydrogen interaction. This vibrational difference in this mode showed that mass substitution has a similar effect in the terahertz region as it does in the near-infrared, in that there is red-shift in the frequency position.

## 4.5 Supporting Information

The supporting information consists of a near-infrared vibration spectral overlay of 4-PT·HCl and 4-PT·HBr shown from 4000-400 $cm^{-1}$ (**Figure B-1**). In addition, Frequency positions ($cm^{-1}$) and RMSD for the experimental and scaled theoretical terahertz spectra of 4PT·HCl where the frequency positions have been reduced to be 90% of the original value is provided (**Table B-1**) and visualized (**Figure B-2**). The supporting information also contains an ORTEP view of the asymmetric unit of α-4PT and β-4PT, showing the partial atom-labeling schemes and 50% thermal ellipsoids, **Figure B-3** and **Figure B-4**.

Additional material available from the Cambridge Crystallographic Data Centre, CCDC No. CCDC 945536-945537, comprises the final atomic coordinates for all atoms, thermal parameters, and a complete listing of bond distances and angles. Copies of this information may be obtained free of charge on application to The Director, 12 Union Road, Cambridge, CB2 2EZ, UK, fax: +44 1223 336 033, e-mail: data_request@ccdc.cam.ac.uk or http://www.ccdc.cam.ac.uk.

## 4.6 Acknowledgment

This work was supported in part by a grant from the National Science Foundation (CHE0907787). Funding for this work was also provided by a grant from the National Science Foundation CAREER Program (CHE-0847405).

## 4.7 References

[1] R.N. Butler, in: A.R. Katrizky, C.W. Rees, E.F.V. Scriven (Eds.) Comprehensive Heterocyclic Chemistry, vol. 4, Pergamon, Oxford, UK, 1996.

[2] V.A. Ostrovskii, M.S. Pevzner, T.P. Kofmna, M.B. Shcherbinin, I.V. Tselinskii, *Targets Heterocycl. Syst.,* **1999,** *3*, 467.

[3] M. Hiskey, D.E. Chavez, D.L. Naud, S.F. Son, H.L. Berghout, C.A. Bome, Proc. *Pyrotech. Semin.,* **2000**, *27*, 3.

[4] H. Singh, A.S. Chawla, V.K. Kapoor, D. Paul, R. Malhotra, *Prog. Med. Chem.,* **1980**, *17*, 151.

[5] V.A. Ostrovskii, R.E. Trifonov, E.A. Popova, *Russ. Chem. Bull., Int.Ed.,* **2012,** *61*, 768.

[6] W. Ouellette, S. Jones, J. Zubieta, *CrystEngComm*, **2011**, *13*, 457.

[7] J. Roh, K. Vávrov, A. Hrabálek, *Eur. J. Org. Chem.,* **2012**, *31,* 6101.

[8] Q. Xu and J. Xu, *Acta Cryst.,* **2011**, *E67*, o43

[9] Y. Zhang and X. Chen, *Acta Cryst.,* **2010**, *E66*, o3297

[10] W. Zheng and X. Chen, *Acta Cryst.,* **2011**, *E67*, o53

[11] A.T.M. Serajuddin*, Adv. Drug Deliver. Rev.*, **2007**, *59*, 603.

[12] J. F. Remenar, J. M. MacPhee, B.K. Larson, V. A. Tyagi, J. H. Ho, D. A. McIlroy, M. B. Hickey, P. B. Shaw, O. Almarsoon, *Org. Process Res. Dev.*, **2003**, *7*, 990.

[13] R.K. Verbeeck, I. Kanfer, R.B. Walker, *Eur. J. Pharm. Sci.,* **2006**, *28,* 1.

[14] S. P. Delaney, E. M. Witko, T.M. Smith, T.M. Korter, *J. Phys. Chem. A*, **2012**, *116*, 8051.

[15] S. P. Delaney, D.Pan, M. Galella, S.X. Yin, T.M. Korter, *Cryst. Growth Des.*, **2012**, *12*, 5017.

[16] M.D. King, W.D.Buchanan, T.M. Korter, *J. Pharm. Sci.,* **2011**, *100*, 1116**.**

[17] K. Siegrist, C.R. Bucher, I. Mandelbaum, A R. Hight Walker, R. Balu, S.K. Gregurick, D.F. Plusquellic, *J. Am. Chem. Soc.*, **2006**, *128*, 5764.

[18] R. Li, J.A. Zeitler, D. Tomerini, E.P.J. Parrott, L.F. Gladden, G.M. Day, *Phys. Chem. Chem. Phys.*, **2010**, *12*, 5329.

[19] K.C. Oppenheim, T.M. Korter, J.S. Melinger, D. Grischowsky, *J. Phys. Chem. A.,* **2010**, *114,* 12513.

[20] R. Dovesi, F.F. Fava, C. Roettia, V.R. Saunders, *Faraday Discuss.,* **1997**, *106*, 173.

[21] I. Moreira, R. Dovesi, C. Roetti, V.R. Saunders, R. Orlando, *Physical Review B.,* **2000**, *62*, 7816.

[22] M. Catti and G. Sandrone, *Faraday Discuss.,* **1997**, *106*, 189.

[23] S. Pellizzeri, T.M. Korter, J. Zubieta, *J. Mol. Struct.,* **2011,** *1003*, 21

[24] R. Dovesi, M. Causà, R. Orlando, C. Roetti, V.R. Saunders, *J. Chem. Phys.,* **1990,** *92*, 7402.

[25] P.M. Hakey, D.G. Allis, M.R. Hudson,W. Ouellette, T.M. Korter, *ChemPhysChem,* **2009**, *10*, 2434.

[26] J. Wilkinson, C.T. Konek, J.S. Moran, E.M. Witko, T.M. Korter, *Chem. Phys. Lett.,* **2009**, *478,*172.

[27] H. Detert and D. Schollmeier, *Synthesis,* **1999**, 999.

[28] APEX II, Data Collection Software, version 2011.8-0; Bruker AXS Inc.: Madison, WI, **2005-2011**.

[29] SAINT Plus, Date Reduction Software, version, 6.45A; Bruker AXS Inc.: Madison, WI, **1997-2002**.

[30] Sheldrick, G. M. SADABS; University of Göttingen: Göttingen, Germany, **1996**.

[31] SHELXTL PC, version 6.12; Bruker AXS Inc.: Madison, WI, **2002**.

[32] A. Nahata, A.S. Weling, T.F. Heinz, *Appl. Phys. Lett.,* **1996**, *69*, 2321.

[33] A. Rice, Y. Jin, X.F. Ma, X.C. Zhang, D. Bliss, J. Larkin, M. Alexander, *Appl. Phys. Lett.,* **1994**, *64*, 1324.

[34] Q. Wu, M. Litz, X.C. Zhang, *Appl. Phys. Lett.,* **1996**, *68*, 2924.

[35] P.M Hakey, D.G. Allis, W. Ouellette,T.M. Korter, *J. Phys. Chem. A,* **2009**, *113*, 5119.

[36] P.M Hakey, M.R. Hudson, D.G. Allis, W. Ouellette,T.M. Korter, *J. Phys. Chem. A,* **2009**, *113*, 13013.

[37] J.R. Holden and C.W. Dickinson, *J. Phys. Chem.,* **1975**, *79*, 249.

[38] T.M Lowry and F.C. Hemmings, *J. Soc. Chem. Ind., London,* **1920**, *39*, 101.

[39] R. Dovesi, R. Orlando, B. Civalleri, R. Roetti, V.R. Saunders, C.M. Zicovich-Wilson, *Z. Kristallogr.,* **2005**, *220*, 571.

[40] R Dovesi, V. R. Saunders, R. Roetti, R. Orlando, C.M. Zicovich-Wilson, F. Pascale, B. Civalleri, K. Doll, N. M. Harrison, I. J. Bush, P. D'Arco, M. Llunell, CRYSTAL09 User's Manual. University of Torino: Torino, 2009.

[41] A. D. Becke, *J. Chem. Phys.*, **1993**, *98*, 5648.

[42] M. F. Peintinger, D. V. Oliveira, T. Bredow, *J. Comput. Chem.,* **2013**, *34*,451.

[43] F. Pascale, C.M. Zicovich-Wilson, F.L. Gejo, B. Civalleri, R. Orlando, R. Dovesi, *J. Comput. Chem..,* **2004**, *25,* 888.

# Chapter 5

# A Solid-State Density Functional Theory Investigation of the Effect of Metal Substitution (Metal = Mn, Cd, Co) on the Terahertz Spectra of Isomorphous Molecular Metal 5-(4-pyridyl)tetrazolato Complexes

The material contained within this chapter is published in *Journal of Molecular Structure* (Pellizzeri, S.; Witko, E. M.; Korter, T.M.; Zubieta, J. *J. Mol. Struct.* **2013**, *1048*, 214-222). This article has been reproduced with permission from Elsevier.

## 5.1 Introduction

Tetrazole as a functional group has found many uses in fields as diverse as coordination chemistry, where it is used as a ligand due to its multiple binding modes to metal centers,[1] medical chemistry, where it finds a role as a surrogate for a carboxylic acid group,[2] and material science as a special explosive.[3,4] Tetrazoles can easily be substituted to increase its ability to coordinate to multiple metal centers so as to form more complex material. One such derivative is 5-(4-pyridyl)tetrazole, which has found extensive use as a templating ligand in building multi-dimensional metal–organic frameworks.[5] It has been previously shown that this ligand can bind through the pyridyl group to form many isostructural compounds with various transition metals of the form $[M(C_6H_4N_5)_2(H_2O)_4]\cdot 2H_2O$ (M = Mn,Cd, Co, Zn, Cu).[6–9] The title compounds (M = Mn, Cd, Co) are isomorphous with the same space group and almost identical unit cells, illustrated in **Figure 5.1** (Mn-4PT, Cd-4PT) and **Figure 5.2** (Co-4PT).

The only significant difference between these three molecular complexes is the central metal atom. This difference should give rise to interesting vibrational information related to the effects of the metal atom. However, due to extensive similarities in structure, the near-IR spectra are almost identical with only minor variation.[6] Therefore, to determine the effects of metal center substitution we were motivated to examine the lower energy vibrational bands that can be observed using terahertz (THz) spectroscopy.

Terahertz spectroscopy has been previously used to investigate molecular crystals to study the terahertz absorption caused by the lattice vibrations unique to three-dimensional ordered solids.[10–12] Unlike near-IR vibrational spectroscopy, there are no characteristic group frequencies in the THz region; therefore, the task to determine what vibrations lead to these absorptions has fallen on computational approaches.[13–15] Since these molecular clusters are

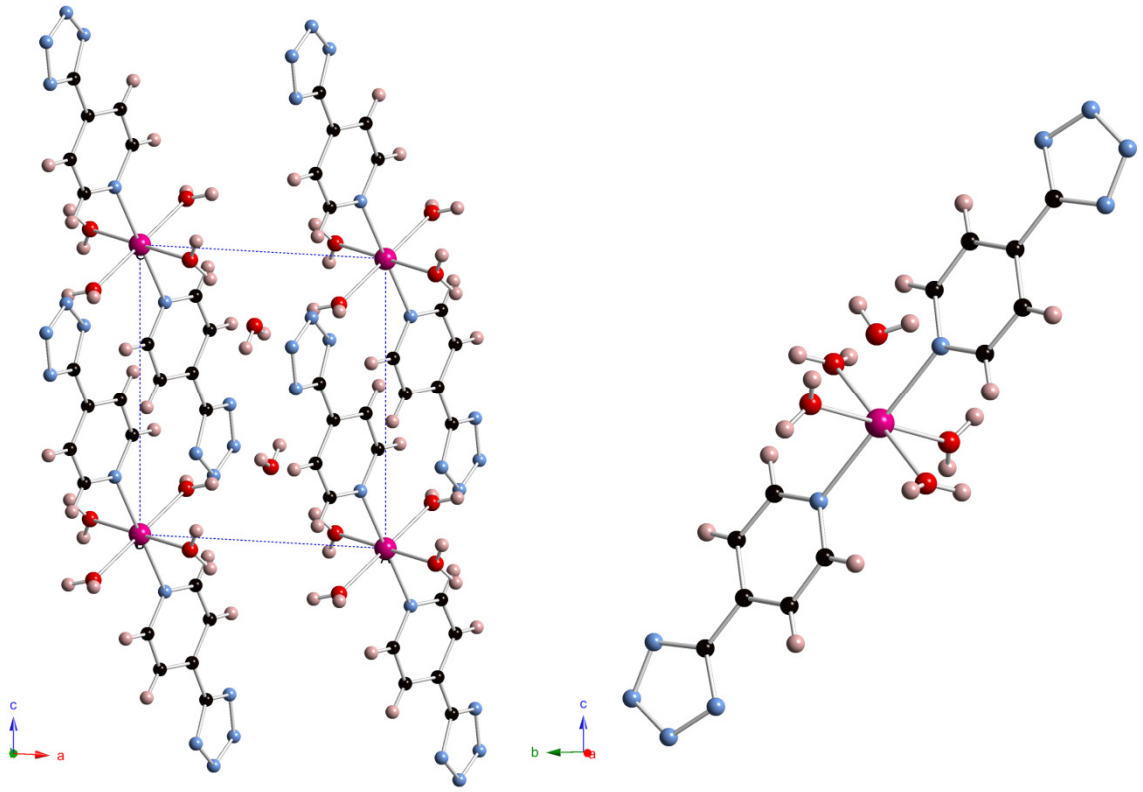


**Figure 5.1** Ball and Stick representation of the packing structure and single molecular unit of $[M(C_6H_4N_5)_2(H_2O)_4]\cdot 2H_2O$ (M = Mn, Cd). (manganese/cadmium is shown in purple, carbon is shown in black, nitrogen is show in light blue and oxygen is shown in red)

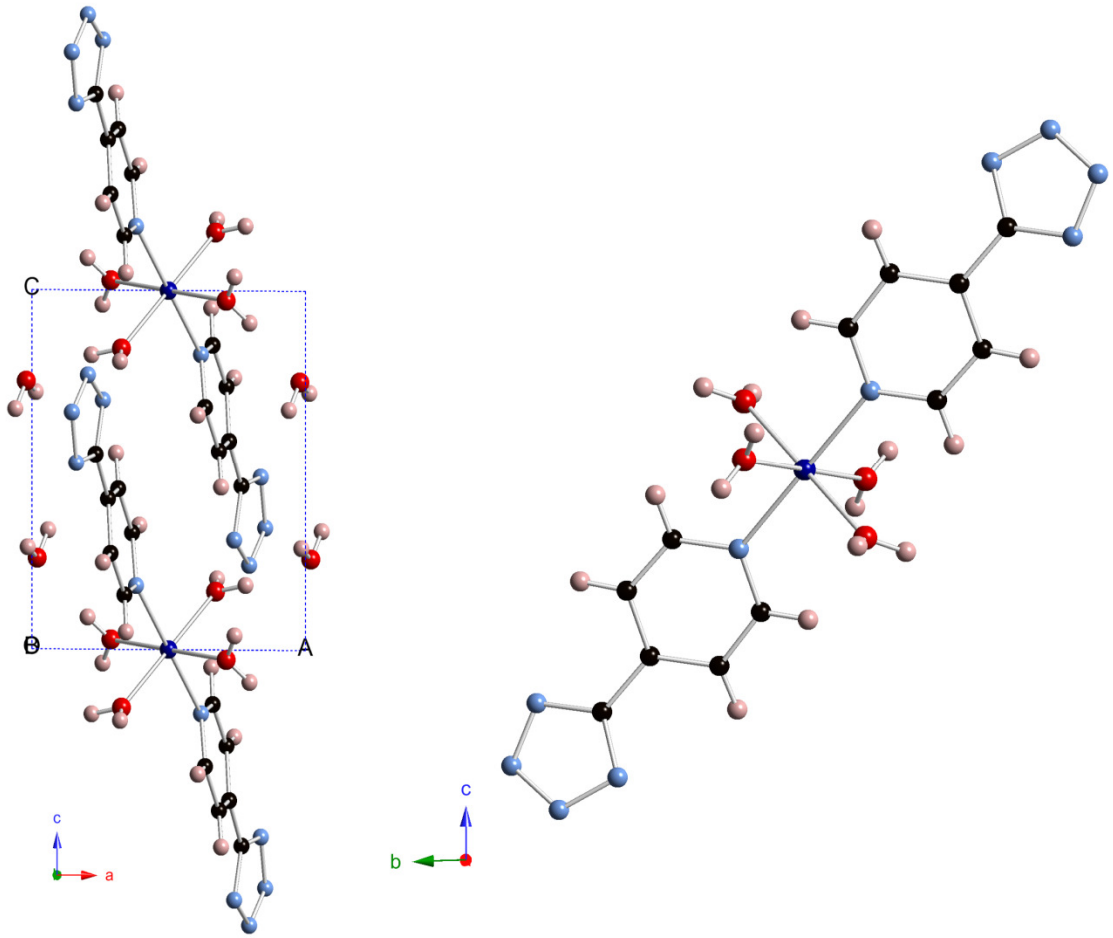


**Figure 5.2** Ball and Stick representation of the packing structure and single molecular unit of $[Co(C_6H_4N_5)_2(H_2O)_4]\cdot 2H_2O$ (Co-4PT). (cobalt is shown in dark blue, carbon is shown in black, nitrogen is show in light blue and oxygen is shown in red)

stabilized through strong hydrogen bonding contacts between the coordinated water on the transition metal and the water of crystallization, and additionally from the coordinated water to the tetrazolate ring on adjacent clusters, the vibrational modes are influenced by these interactions across unit cells. Therefore, in order to accurately predict these vibrational modes, the computational approach implemented must be able to reproduce the intermolecular forces that are unique to these ordered substances. An approach that has been shown to produce quality simulations of THz spectra is solid-state density functional theory (DFT).

The solid-state DFT approach that was used in this study is implemented in CRYSTAL09. The CRYSTAL program has been previously used to simulate many inorganic systems to determine their structural, electronic, magnetic and vibrational properties,[16–19] as well as the vibrational spectra of organic systems.[20–22] CRYSTAL09 utilizes periodic boundary conditions, which are required to accurately simulate vibrational motions that are perturbed by crystal packing forces, and perhaps equally important, to couple external lattice motions to the internal ‘‘molecular’’ motions of the asymmetric repeat unit. In this study, CRYSTAL09 was used to replicate the geometric parameters of the metal 5-(4-pyridyl)tetrazolato complexes as well as to determine the vibrationally active modes in the THz region and to evaluate the normal modes that are the result of these absorptions. Any differences that are observed in the terahertz spectra can be almost directly related to the metal center and rather than to symmetry or packing differences.

## 5.2 Experimental and theoretical methods

### *5.2.1 Experimental*

#### *5.2.1.1 Synthesis of Metal 5-(4-pyridyl)tetrazolato Complexes*

Manganese(II) sulfate tetrahydrate (98%, Aldrich), cobalt(II) chloride hexahydrate (98%, Aldrich), cadmium(II) nitrate tetrahydrate (98%, Aldrich), 4-pyridinenitrile (98% Aldrich), sodium azide (99%, Alfa Aesar), and methanol (99.8%, Aldrich) were purchased from their respective vendors and used without further purification. 5-(4-Pyridyl)tetrazole was prepared using previously published methods.[23] Water was distilled above 3.0 MΩ in-house using a Barnstead Model 525 Biopure Distilled Water Center.

All metal 5-(4-pyridyl)tetrazolato complexes were synthesized following literature procedures[6,7] with minor variations. In the synthesis of $[Mn(C_6H_4N_5)_2(H_2O)_4]\cdot 2H_2O$ (Mn-4PT) the $Mn(NO_3)_2\cdot 4H_2O$ was replaced with $Mn(SO_4)\cdot 4H_2O$. The $[Co(C_6H_4N_5)_2(H_2O)_4]\cdot 2H_2O$ (Co-4PT) procedure was performed with no modification to the literature synthesis. Lastly, in the $[Cd(C_6H_4N_5)_2(H_2O)_4]\cdot 2H_2O$ (Cd-4PT) preparation, the $Cd(SO_4)\cdot 8H_2O$ was replaced with $Cd(NO_3)_2\cdot 4H_2O$. All metal 5-(4-pyridyl)tetrazolato complexes were confirmed using single-crystal X-ray diffraction.

#### *5.2.1.2 X-ray Crystallography*

Crystallographic data for all compounds was collected on a Bruker KAPPA APEX DUO diffractometer using Mo Ka radiation (k = 0.71073 Å) containing a APEX II CCD system.[24] All data collections were taken at low temperature (90 K). The data were corrected for Lorentz and polarization[25] effects, and adsorption corrections were made using SADABS.[26] Structures were

solved by direct methods. Refinements for each structure were carried out using the SHELXTL[27] crystallographic software. Following assignment of all non-hydrogen atoms, the models were refined against $F^2$ first using isotropic and then using anisotropic thermal displacement parameters. The hydrogen atoms were introduced in calculated positions and then refined isotropically. Neutral atom scattering coefficients along with anomalous dispersion corrections were taken from the International Tables, Vol. C.

#### *5.2.1.3 Time-domain Terahertz Spectroscopy*

The experimental terahertz spectra of the compounds were acquired using a pulsed time-domain THz spectrometer based on an amplified femtosecond Ti:Sapphire laser system operating in the near-infrared region. For the generation and detection of THz radiation, the instrument utilized optical rectification[28,29] and free space electro-optic sampling,[28,30] respectively. A detailed description of the spectrometer along with the experimental setup has been provided elsewhere.[21,31,32]

The metal 5-(4-pyridyl)tetrazolato complexes were used without further purification and were mixed with a spectroscopic grade powdered polytetrafluoroethylene (PTFE) matrix. Polytetrafluoro ethylene is mostly transparent in the THz region, and its usage in dilution of the metal 5-(4-pyridyl)tetrazolato samples ensures that the concentration of the sample pellet is within the optimal absorption range. The sample and the matrix were then mechanically pulverized using a stainless-steel ball mill (Dentsply Rinn 172 3110-3A), the length of the pulverization being dependent on the hardness of the sample. This allowed for a homogeneous distribution of the sample through the matrix, reduced the particle size, and thus minimized radiation scattering.[33,34] The mixture was then pressed into a pellet at 2000 psi using a hydraulic press (ICL E-Z Press 12). The resulting sample pellet had a total mass of approximately 0.55 g,

thickness of ~2.0 mm, diameter of 13.0 mm. The final sample pellets contained 1.62% w/w Cd-4PT, 1.35% w/w Co-4PT, and 0.74% w/w Mn-4PT. The blank (reference) pellet was prepared with pure PTFE in a similar manner.

The sample and blank pellets were both held under vacuum in a variable-temperature cryostat and held at temperatures of 293 K (room temperature) and 78 K (liquid-nitrogen temperature). Each individual spectrum of the sample (or the blank pellet) consisted of an average of 36 THz-waveform scans over a time window of ~30 ps. These waveforms were then symmetrically zero-padded to a total of 6000 data points, and subsequently were Fourier-transformed (utilizing a Hanning window function) into the frequency-domain. Elimination of any THz absorption by the PTFE matrix was accomplished by taking a ratio of the transformed spectrum of a PTFE blank versus the transformed spectrum of a sample pellet. To improve the final signal-to-noise ratio, four blank/sample sets were collected and averaged, yielding the THz spectra ultimately reported here in. The THz absorption spectra cover a range of 10–100 $cm^{-1}$ with a spectral resolution of approximately 1.0 $cm^{-1}$.

### *5.2.2 Theoretical methodology of CRYSTAL09*

Geometry optimizations, harmonic frequencies, and intensity calculations were performed using the CRYSTAL09 program.[35,36] Due to the different possible spin states for manganese and cobalt, all the calculations were performed using an unrestricted spin B3LYP[37] hybrid density functional. This functional was also used for the cadmium complex which has no unpaired spins. The basis set chosen for manganese, cobalt, and cadmium were Mn_86-411d41G,[38] Co_86-411d41G,[39] and the Cd_dou[40] basis set, respectively. The Pople basis set 6-31G(d,p)[41] adapted from the 6-31G(d,p) basis set obtained from the EMSL Basis Set Exchange,[42,43] was used for the remaining atoms.

The positions of the atoms contained within the unit cell were optimized within the constraints of the lattice parameters and space group symmetry. From the optimized structures, the bond lengths and bond angles were determined and compared with the experimental crystallographic results. After optimizing the structures, harmonic-limit normal-mode analyses on the organometallic complexes were conducted. Frequencies were determined by a mass-weighted numerical evaluation of the Hessian matrix[44] and intensities were calculated through the Berry phase approach.[36]

Several of the convergence parameters were changed to optimize the accuracy and computational time of the calculations. The convergence criteria were modified to set the root mean square of the maximum gradient (TOLDEG) and the maximum displacement (TOLDEX) to be 0.00001 and 0.00004 Å, respectively. To improve the numerical accuracy of the calculations the truncation criteria for bielectronic integrals (TOLINTEG) was set to 8 8 8 8 16 and the DFT integration was set to XLGRID (75,974). (See Refs.[35,36] for details). Total energy convergence (TOLDEE) was set to DE < 1 x $10^{-8}$ Hartree for the geometry optimizations and DE < 1 x $10^{-11}$ Hartree for frequency analyses. To induce the calculations to converge in a timely fashion, a modified Broyden[45] scheme, following the method proposed by Johnson,[46] was applied. The parameters used by Albaese and co-workers[47] were applied. As a result, after 10 SCF iterations for each complex, with 90% of Fock/KS matrices simple mixing, the Fock/KS matrices simple mixing was reduced to 50%. The optimum sampling of reciprocal space was determined by comparing the total energy of the converged system to the k-point count using the keyword SHRINK. The optimum SHRINK values for the metal 5-(4-pyridyl)tetrazolato complexes were determined to be SHRINK = 6 6 which corresponds to 112 points in the irreducible part of the Brillouin Zone and 112 points in the Gilat Net.

## 5.3 Results and discussion

### *5.3.1 X-ray Crystallography*

In order to accurately compare the experimentally collected data to the theoretical data, it is necessary to use unit cell parameters and atomic positions from a crystal structure that has been determined near the same temperature at which the THz spectroscopy has been performed. The previously published crystal structures for Mn-4PT and Cd-4PT were determined at 90 K; however, the crystal structure for Co-4PT was determined at 294 K. Therefore, it was necessary to collect a crystal structure of Co-4PT at 90 K, to be able to more accurately represent the THz spectrum collected at 78 K. The structure was found to be isostructural with the published room temperature crystal; however, the unit cell parameters are contracted slightly as expected. Co-4PT crystallized in the P-1 space group with unit cell dimensions of $a$ = 7.112(2) Å, $b$ = 7.767(2) Å, $c$ = 8.659(3) Å, α = 91.685(6)°, β = 90.069(5)◦, and γ = 100.743(5)°.

### *5.3.2 Comparison of the calculated and experimental structures*

The calculated and experimental bond lengths, bond angles, and the root-mean-squared deviation (RMSD) values are shown in **Tables 5.1–5.3** (see **Figure 5.3** for the labeling scheme) for each of the metal 5-(4-pyridyl)tetrazolato complexes, and the results are visualized in **Figure. 5.4.** The calculated bond lengths were very well modeled with RMSDs of 8.76 x $10^{-3}$, 11.14 x $10^{-3}$ and 23.07 x $10^{-3}$ for the Mn-4PT, Co-4PT, and Cd-4PT complexes, respectively. The manganese and cobalt structures were modeled with a higher level of precision than the cadmium, which produced an RMSD twice that obtained for the smaller transition metals. The major deviations were found to be for the cadmium–nitrogen and cadmium–oxygen bond lengths

**Table 5.1** Interatomic bond lengths (Å), angles (°), and RMSD values for Mn-4PT. See **Figure 5.3** for atomic labels. Experimental parameters are from Ref. [6].

| Bond, Å | Experimental | Theoretical |
|---|---|---|
| **Mn1-N1** | 2.3013 | 2.2844 |
| **Mn1-O2** | 2.1643 | 2.1593 |
| **Mn1-O3** | 2.1627 | 2.1768 |
| **C1-N1** | 1.3470 | 1.3460 |
| **C1-C2** | 1.3748 | 1.3870 |
| **C2-C3** | 1.3896 | 1.4004 |
| **C3-C4** | 1.3906 | 1.3989 |
| **C3-C6** | 1.4630 | 1.4650 |
| **C4-C5** | 1.3825 | 1.3890 |
| **C5-N1** | 1.3368 | 1.3446 |
| **C6-N2** | 1.3368 | 1.3423 |
| **C6-N5** | 1.3424 | 1.3445 |
| **N2-N3** | 1.3390 | 1.3315 |
| **N3-N4** | 1.3198 | 1.3169 |
| **N4-N5** | 1.3443 | 1.3341 |
| | **RMSD** | **0.00876** |

| Angle,˚ | Experimental | Theoretical |
|---|---|---|
| **O3-Mn1-O3'** | 180.000 | 180.000 |
| **O3-Mn1-O2** | 91.017 | 91.492 |
| **O3-Mn1-O2'** | 88.983 | 88.508 |
| **O2-Mn1-O2'** | 180.000 | 180.000 |
| **O3-Mn1-N1** | 88.877 | 88.844 |
| **O3-Mn1-N1'** | 91.123 | 91.156 |
| **O2-Mn1-N1** | 92.672 | 92.289 |
| **O2-Mn1-N1'** | 87.328 | 87.711 |
| **N1-Mn1-N1'** | 180.000 | 180.000 |
| **C1-N1-C5** | 116.545 | 117.236 |
| **C1-N1-Mn1** | 120.112 | 119.762 |
| **C5-N1-Mn1** | 123.284 | 122.882 |
| **N1-C1-C2** | 123.514 | 123.361 |
| **C1-C2-C3** | 119.589 | 119.248 |
| **C2-C3-C4** | 117.366 | 117.545 |
| **C2-C3-C6** | 121.233 | 120.602 |
| **C4-C3-C6** | 121.395 | 121.844 |
| **C3-C4-C5** | 119.199 | 119.197 |
| **N1-C5-C4** | 123.774 | 123.391 |
| **N2-C6-N5** | 111.306 | 110.509 |
| **N2-C6-C3** | 124.502 | 124.820 |
| **N5-C6-C3** | 124.162 | 124.649 |
| **C6-N2-N3** | 104.975 | 105.090 |
| **N2-N3-N4** | 109.690 | 109.908 |
| **N3-N4-N5** | 109.157 | 109.140 |
| **C6-N5-N4** | 104.870 | 105.352 |
| **C2-C3-C6-N2** | 165.940 | 166.158 |
| **C2-C3-C6-N5** | -11.926 | -11.954 |
| **C4-C3-C6-N2** | -13.147 | -12.725 |
| **C4-C3-C6-N5** | 168.987 | 169.163 |
| | **RMSD** | **0.3629** |

**Table 5.2** Interatomic bond lengths (Å), angles (°), and RMSD values for Co-4PT. See **Figure 5.3** for atomic labels. Experimental parameters are from 90K crystallographic data.

| Bond, Å | Experimental | Theoretical |
|---|---|---|
| **Co1-N1** | 2.1367 | 2.1314 |
| **Co1-O2** | 2.0737 | 2.1060 |
| **Co1-O3** | 2.1141 | 2.1120 |
| **C1-N1** | 1.3399 | 1.3448 |
| **C1-C2** | 1.3764 | 1.3876 |
| **C2-C3** | 1.3915 | 1.4003 |
| **C3-C4** | 1.3921 | 1.3996 |
| **C3-C6** | 1.4686 | 1.4664 |
| **C4-C5** | 1.3717 | 1.3865 |
| **C5-N1** | 1.3435 | 1.3444 |
| **C6-N2** | 1.3398 | 1.3452 |
| **C6-N5** | 1.3407 | 1.3430 |
| **N2-N3** | 1.3413 | 1.3349 |
| **N3-N4** | 1.3144 | 1.3155 |
| **N4-N5** | 1.3454 | 1.3312 |
| | **RMSD** | **0.01114** |

| Angle,˚ | Experimental | Theoretical |
|---|---|---|
| **O2-Co1-O2'** | 180.000 | 180.000 |
| **O2-Co1-O3** | 90.045 | 90.642 |
| **O2-Co1-O3'** | 89.955 | 89.358 |
| **O3-Co1-O3'** | 180.000 | 180.000 |
| **O2-Co1-N1** | 90.132 | 90.377 |
| **O2-Co1-N1'** | 89.868 | 89.663 |
| **O3-Co1-N1** | 87.151 | 87.159 |
| **O3-Co1-N1'** | 92.849 | 92.841 |
| **N1-Co1-N1'** | 180.000 | 180.000 |
| **C1-N1-C5** | 116.684 | 117.322 |
| **C1-N1-Co1** | 122.040 | 121.594 |
| **C5-N1-Co1** | 120.796 | 120.533 |
| **N1-C1-C2** | 123.729 | 123.300 |
| **C1-C2-C3** | 119.200 | 119.254 |
| **C2-C3-C4** | 117.294 | 117.436 |
| **C2-C3-C6** | 122.207 | 121.981 |
| **C4-C3-C6** | 120.493 | 120.582 |
| **C3-C4-C5** | 119.590 | 119.315 |
| **N1-C5-C4** | 123.446 | 123.319 |
| **N2-C6-N5** | 111.620 | 110.441 |
| **N2-C6-C3** | 125.296 | 125.950 |
| **N5-C6-C3** | 123.072 | 123.600 |
| **C6-N2-N3** | 104.868 | 105.327 |
| **N2-N3-N4** | 109.295 | 109.173 |
| **N3-N4-N5** | 109.974 | 109.939 |
| **C6-N5-N4** | 104.241 | 105.120 |
| **C2-C3-C6-N2** | -14.188 | -14.611 |
| **C2-C3-C6-N5** | 167.132 | 166.614 |
| **C4-C3-C6-N2** | 164.917 | 164.968 |
| **C4-C3-C6-N5** | -13.764 | -13.807 |
| | **RMSD** | **0.4241** |

**Table 5.3** Interatomic bond lengths (Å), angles (°), and RMSD values for Cd-4PT. See **Figure 5.3** for atomic labels. Experimental parameters are from Ref. [6].

| Bond, Å | Experimental | Theoretical |
|---|---|---|
| **Cd1-N1** | 2.3295 | 2.3858 |
| **Cd1-O2** | 2.2826 | 2.3256 |
| **Cd1-O3** | 2.2900 | 2.3348 |
| **C1-N1** | 1.3465 | 1.3440 |
| **C1-C2** | 1.3755 | 1.3867 |
| **C2-C3** | 1.3939 | 1.4014 |
| **C3-C4** | 1.3829 | 1.3989 |
| **C3-C6** | 1.4658 | 1.4641 |
| **C4-C5** | 1.3744 | 1.3880 |
| **C5-N1** | 1.3452 | 1.3417 |
| **C6-N2** | 1.3418 | 1.3421 |
| **C6-N5** | 1.3329 | 1.3440 |
| **N2-N3** | 1.3365 | 1.3308 |
| **N3-N4** | 1.3186 | 1.3168 |
| **N4-N5** | 1.3455 | 1.3330 |
| | **RMSD** | **0.02307** |

| Angle, ˚ | Experimental | Theoretical |
|---|---|---|
| **O3-Cd1-O3'** | 180.000 | 180.000 |
| **O3-Cd1-O2** | 92.215 | 96.227 |
| **O3-Cd1-O2'** | 87.785 | 83.773 |
| **O2-Cd1-O2'** | 180.000 | 180.000 |
| **O3-Cd1-N1** | 89.226 | 89.296 |
| **O3-Cd1-N1'** | 90.774 | 90.704 |
| **O2-Cd1-N1** | 93.222 | 93.409 |
| **O2-Cd1-N1'** | 86.778 | 86.591 |
| **N1-Cd1-N1'** | 180.000 | 180.000 |
| **C1-N1-C5** | 116.648 | 118.208 |
| **C1-N1-Cd1** | 120.575 | 120.176 |
| **C5-N1-Cd1** | 122.692 | 121.466 |
| **N1-C1-C2** | 123.290 | 122.856 |
| **C1-C2-C3** | 119.444 | 119.035 |
| **C2-C3-C4** | 117.506 | 117.931 |
| **C2-C3-C6** | 120.809 | 120.610 |
| **C4-C3-C6** | 121.677 | 121.452 |
| **C3-C4-C5** | 119.571 | 119.101 |
| **N1-C5-C4** | 123.527 | 122.845 |
| **N2-C6-N5** | 111.597 | 110.516 |
| **N2-C6-C3** | 123.971 | 124.742 |
| **N5-C6-C3** | 124.407 | 124.725 |
| **C6-N2-N3** | 104.484 | 105.064 |
| **N2-N3-N4** | 110.041 | 109.913 |
| **N3-N4-N5** | 108.884 | 109.146 |
| **C6-N5-N4** | 104.992 | 105.360 |
| **C2-C3-C6-N2** | 166.216 | 166.332 |
| **C2-C3-C6-N5** | -11.830 | -12.020 |
| **C4-C3-C6-N2** | -12.739 | -12.654 |
| **C4-C3-C6-N5** | 169.214 | 168.994 |
| | **RMSD** | **1.1577** |

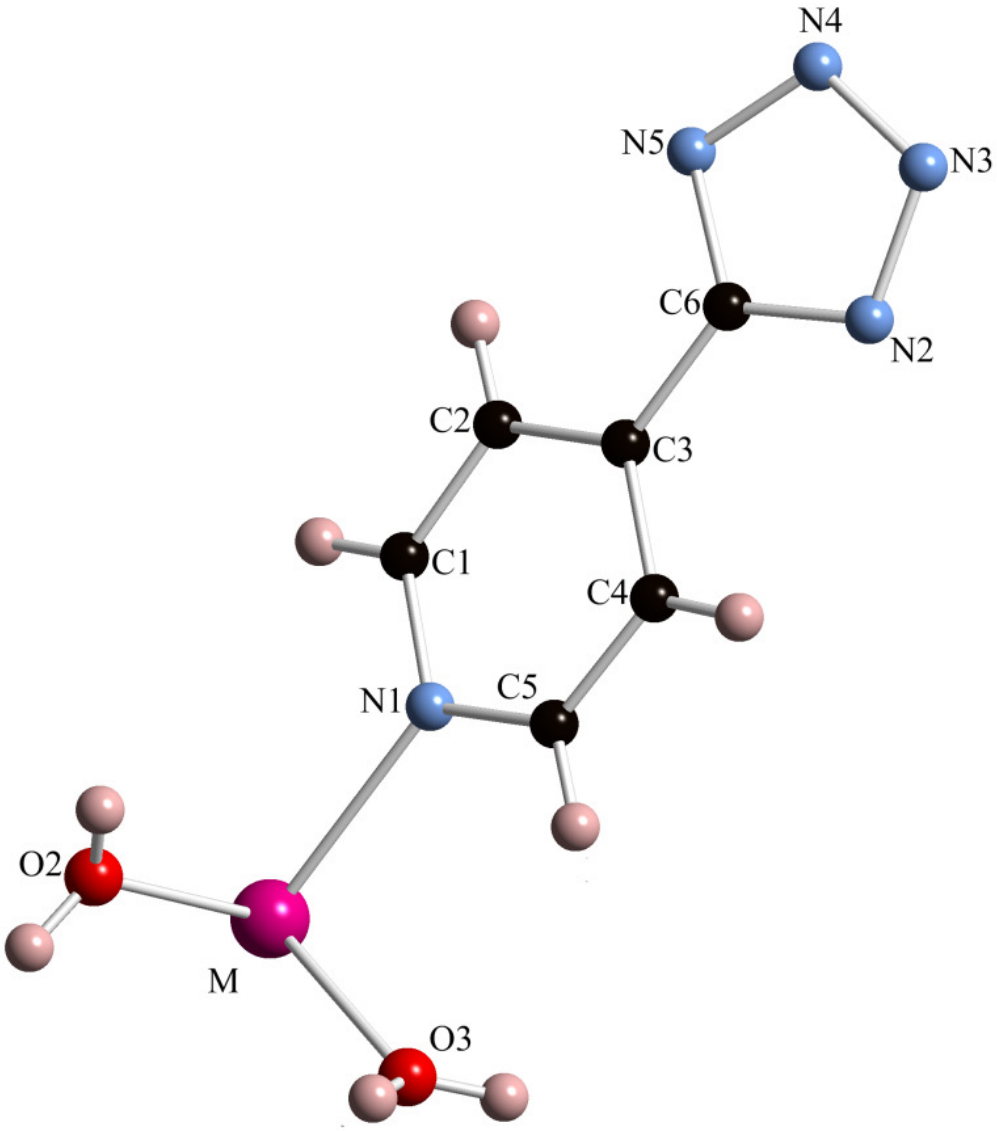


**Figure 5.3** The atom labeling for $[M(C_6H_4N_5)_2(H_2O)_4]\cdot 2H_2O$ (M = Mn, Co, Cd ).

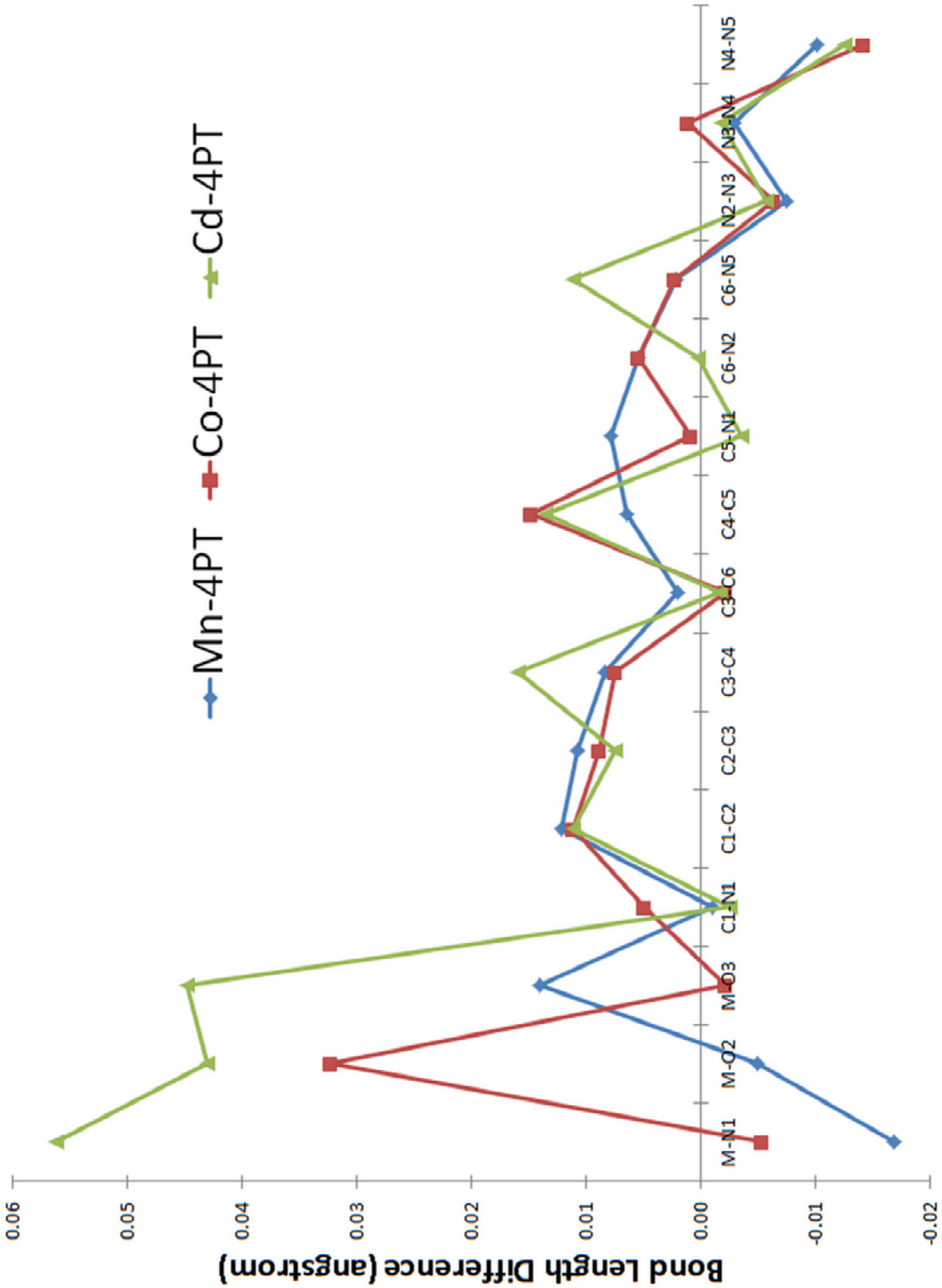


**Figure 5.4** Calculated bond-length differences for Mn-4PT, Co-4PT, and Cd-4PT.

which were overestimated by on average ~0.05 Å. However this difference should have no major consequences on the simulation of the frequency modes.

The angles were also modeled with a fair degree of accuracy, as shown by the low RMSDs. The calculated RMSDs for the Mn-4PT, Co-4PT, and Cd-4PT complexes were 0.3629, 0.4241 and 1.1577 respectively. The manganese and cobalt structures once again provided RMSD values of about half that found for the cadmium simulation. It is important to note that four torsion angles are included, because in these systems the tetrazolate ring is canted by ~13°, which occurs when the pyridyl nitrogen donor is bound to the metal. This is not observed to the same extent (~2°) in the free ligand, as shown in the previously published crystal structure.[48] The solid state DFT method used was able to accurately model this torsion angle, which is significant, because it shows that the pyridyl ring and the tetrazolate ring can move independently. Therefore, they are not locked in a planar conformation by delocalization of the pi bonds over the entire molecule.

Due to the different possible spin state arrangement of the *d* electrons of the manganese(II), which is $d^5$, and cobalt(II), which is $d^7$, an unrestricted spin calculation was employed. This was necessary because complexes could be in either a high or low spin arrangement, which would drastically change the metal bond distances. As expected from the nature of the coordination spheres of the metals, both Mn-4PT and Co-4PT converged in a high spin state, and the strong correlation between the crystallographic and theoretical bond distances of the metal–nitrogen bonds confirms the high spin assignment.

### *5.3.3 Comparison of theoretical and experimental vibrational frequencies*

The experimental and calculated terahertz spectra are shown in **Figure 5.5** and summarized in **Table 5.4** for each metal 5-(4-pyridyl)tetrazolato complex. Empirical analyses of the major vibrational modes observed using J-ICE[49] are summarized in **Table 5.5**. Overall, the modeling of the terahertz spectra show a fair degree of accuracy, exhibiting a similar number of peaks as well as a majority of the intensities with the same order of magnitude, excluding the cobalt complex. Based on the RMSD values, given in **Table 5.4**, the simulation for Cd-4PT is better than that for the Mn-4PT and the Co-4PT complexes. It is interesting to note that the order of the RMSD values for the vibrational correlation is not the same as the order for the bond length and angle correlations. This discrepancy shows that there is not always a direct correlation between the accuracy in the bond lengths and the accuracy of the frequencies.

The Mn-4PT spectrum at 78 K shows four peaks and the 298 K spectrum shows only two. It can be assumed that at the higher temperature the peaks at 83.33 $cm^{-1}$ and 96.66 $cm^{-1}$ in the low temperature spectrum are within the bandwidth of the high temperature peak at 87.77 $cm^{-1}$. The simulated spectrum shows a good correlation with the two major peaks of the experimental spectrum but at a slightly higher frequency. However, the two smaller peaks at ca. 83.17 and 96.49 $cm^{-1}$ were not found in the calculated spectra. The Co-4PT spectrum at 78 K shows three peaks and the 298 K spectrum shows only two. The simulated spectrum can be correlated with the major peaks of the experimental spectrum but at a higher frequency. The Cd-4PT spectra at 78 K and 298 K both show three peaks. The simulated spectrum shows a good correlation with all the peaks appearing at slightly higher frequencies than the experimental spectrum. It can be assumed that the combination of peaks at 86.60 $cm^{-1}$ and 91.58 $cm^{-1}$ in the

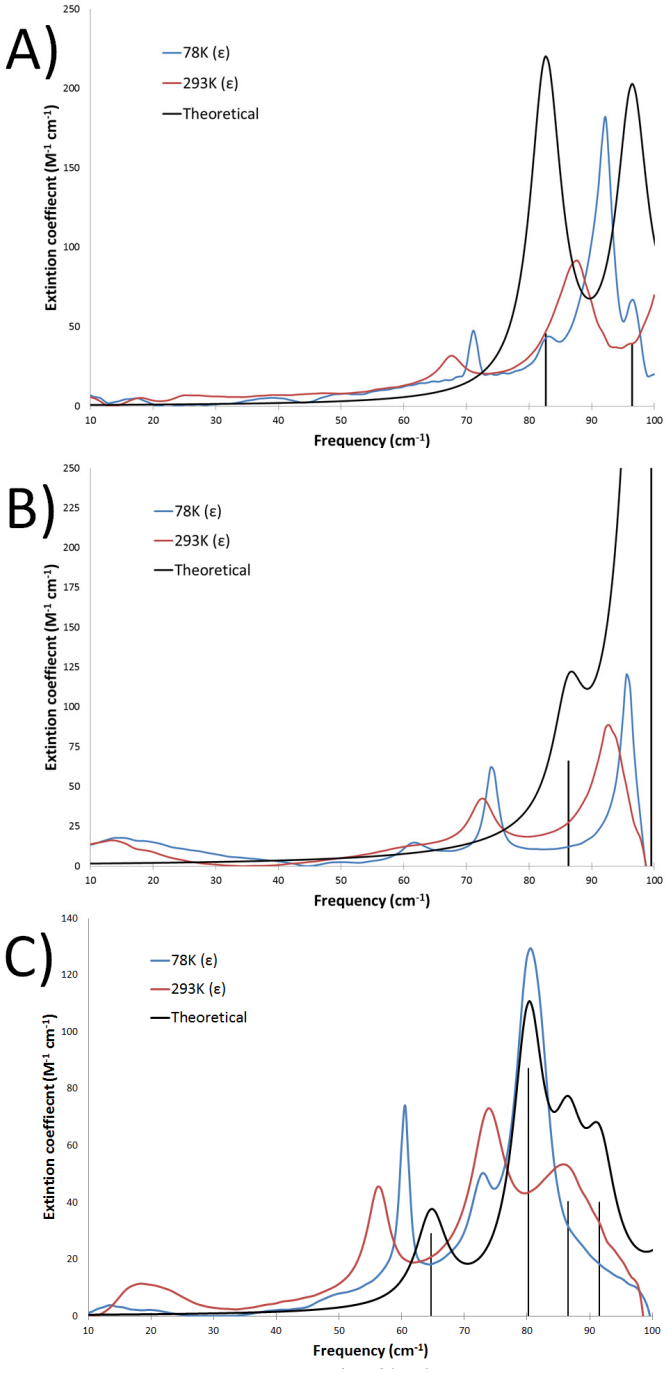


**Figure 5.5** The experimental and theoretical traces for the terahertz spectra of A) Mn-4PT, B) Co-4PT, and C) Cd-4PT. An empirical 3.0 $cm^{-1}$ full-width-half-maximum Lorentzian line shape has been applied to the theoretical data to aid in comparison. The 99.50 $cm^{-1}$ peak in the Co-4PT spectra was cut off to aid in visualization, the intensity peaks at ~850 $M^{-1}$ $cm^{-3}$

**Table 5.4** Frequency positions ($cm^{-1}$) and RMSD for the experimental and theoretical terahertz spectra of the metal 5-(4-pyridyl)tetrazolato complexes. The blanks are peaks that have no obvious correlation between experiment and theory. Visual inspection was used to correlate experimental and theoretical vibrational modes. Mode descriptions are described in **Table 5.5**.

| Mn-4PT | | | | |
|---|---|---|---|---|
| **Mode** | **Exp. (78K)** | **Exp. (293K)** | **Theory** | **Intensity** |
| a | 71.13 | 67.65 | 82.68 | 45.37 |
| --- | 83.17 | --- | --- | --- |
| b | 92.15 | 87.60 | 96.46 | 39.25 |
| --- | 96.49 | --- | --- | --- |
| | | **RMSD** | 6.161 | |

| Co-4PT | | | | |
|---|---|---|---|---|
| **Mode** | **Exp. (78K)** | **Exp. (293K)** | **Theory** | **Intensity** |
| --- | 61.72 | --- | --- | --- |
| a | 74.07 | 72.55 | 86.33 | 15.88 |
| b | 95.72 | 92.59 | 99.50 | 176.32 |
| | | **RMSD** | 6.417 | |

| Cd-4PT | | | | |
|---|---|---|---|---|
| **Mode** | **Exp. (78K)** | **Exp. (293K)** | **Theory** | **Intensity** |
| a | 60.50 | 56.32 | 64.74 | 6.99 |
| b | 73.00 | 73.92 | 80.26 | 21.01 |
| b+c | 80.56 | 85.82 | 86.60 | 9.73 |
| c | | | 91.58 | 9.67 |
| | | **RMSD** | 3.735 | |

**Table 5.5**. Empirical normal mode analysis of the metal 5-(4-pyridyl)tetrazolato complexes.

| Mode | Description |
|---|---|
| a | Ligand scissoring along the *a* axis |
| b | Ligand wagging along the *bc* plane |
| c | Pyridyl ring rotation in the *ab* plane |

theoretical spectrum comprises the peaks at either 80.56 $cm^{-1}$ or 85.82 $cm^{-1}$ in the low or high temperature spectra, respectively.

When comparing the normal modes of the three metal 5-(4-pyridyl)tetrazolato complexes, a total of three different types of modes are observed in each case. All three complexes share the same two low energy scissoring vibrations (**Figure 5.6A**) and a wagging of the 5-(4-pyridyl)tetrazolato ligands (**Figure 5.6B**) with respect to each other along different axes. The cadmium complex shows a new type of vibration within the measured range corresponding to pyridyl ring rotation that does not involve motion of either the metal center or the tetrazolate ring (**Figure 5.6C**). This motion is not found in the measured range (10–100 $cm^{-1}$) for the manganese or cobalt complexes. However they are predicted to be at 112.35 $cm^{-1}$ and 107.12 $cm^{-1}$ for the Mn-4PT and Co-4PT complexes, respectively.

Two trends are found when comparing the vibrational modes for all three complexes. The first trend is illustrated with the location of pyridyl ring rotation, which shows the typical response due to increasing the mass of the complex, which causes the vibrations shift to lower frequencies. This observation implies that this motion is at a higher frequency for the manganese complex and at a much lower frequency for the cadmium complex. The second trend is related to the ligand scissoring and wagging motions, where once again there is a significant effect due to increasing the mass of the complex, with the consequence that these frequencies are shifted to their lowest values in the cadmium complex. However, for the manganese and cobalt complexes, this trend is reversed, indicating that the heavier cobalt complex exhibits a higher frequency than the lighter manganese complex. This observation suggests that the bond strength of the cobalt–nitrogen bond is greater than that of the manganese–nitrogen bond, and the experimental bond lengths support this inference with the cobalt–nitrogen bond distance being much shorter at

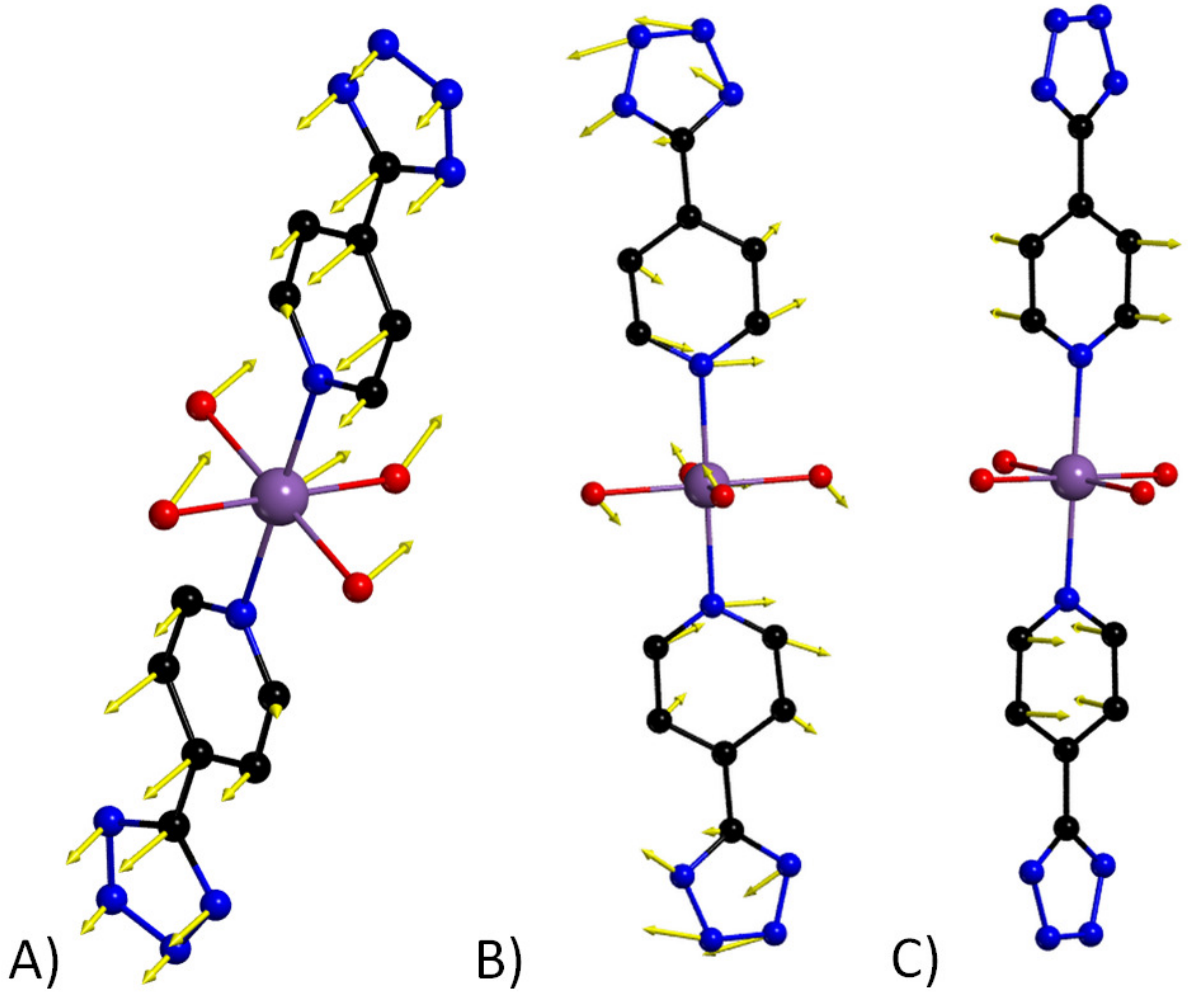


**Figure 5.6** Visualization of vibrational normal modes A) ligand scissoring along the *a* axis, B) ligand wagging along the *bc* plane, and C) pyridyl ring rotation in the *ab* plane. Arrows denote the direction of molecular motion.

2.1367 Å than that of the manganese–nitrogen bond of 2.3013 Å. Furthermore, the metal–nitrogen bond is the significant determinant because there is no major experimentally observed deviation in the metal–oxygen bond lengths.

## 5.4 Conclusions

The solid-state simulation of the geometric and vibrational properties of three metal 5-(4-pyridyl)tetrazolato complexes was performed to determine the effect of the size and mass of the metal center on the vibrational frequencies in the low energy THz region. Comparing the spectra of these compounds has shown that while the three are isomorphous and are nearly identical in the near-IR, there are large differences in the terahertz region. These differences in the THz region are likely caused by the different metal centers.

Solid-state DFT using CRYSTAL09 was found to replicate the complex interactions that are occurring in these hybrid metal–organic materials. Due to the possibility of different spin states for the manganese(II), which is $d^5$, and cobalt(II), which is $d^7$, an unrestricted spin calculation was performed. Both the Mn-4PT and Co-4PT complexes converged in a high spin state, and the strong correlation between the crystallographic and theoretical bond distances of the metal–nitrogen bond suggests that these complexes are in fact high spin, as expected form the nature of the coordination spheres. The ability to correctly assign the spin state led to strong correlations for the structures of the manganese and cobalt complexes. However the less accurate simulation for the cadmium complex provided the closest correlation with the experimental terahertz spectrum.

Three unique vibrational modes were found, and two trends were discovered when comparing these vibrational modes across all three complexes. The first trend is related to the frequency of pyridyl ring rotation, which shows the common trend of the vibrations shifting to

lower frequencies as the mass of the complex increases. The second trend emerges in comparing the ligand scissoring and wagging motions, where once again there is a significant effect of increased the mass of the complex resulting in lower frequencies. However, this trend is reversed for the manganese and cobalt complexes where the significantly stronger cobalt–nitrogen bond outweighs the effect of the increasing mass. Consequently, the effects of the metal center in the low energy lattice and molecular motions found in the terahertz region are sensitive to differences in not only the mass but also on the bond strength, when the metal plays a role in the normal mode. These effects may not be observable in the higher energy regions of the infrared spectrum.

## 5.5 Supporting Information

The supporting information consists of an ORTEP view of the asymmetric unit of Co-4PT, showing the partial atom-labeling schemes and 50% thermal ellipsoids (**Figure C-1**)

Additional material available from the Cambridge Crystallographic Data Centre, CCDC No. CCDC 924460, comprises the final atomic coordinates for all atoms, thermal parameters, and a complete listing of bond distances and angles. Copies of this information may be obtained free of charge on application to The Director, 12 Union Road, Cambridge, CB2 2EZ, UK, fax: +44 1223336 033, e-mail: data_request@ccdc.cam.ac.uk or http://www.ccdc.cam.ac.uk. Supplementary data associated with this article can be found, in the with this article can be found, in the online version, at http://dx.doi.org/10.1016/j.molstruc.2013.05.055.

## 5.6 Acknowledgments

This work was supported in part by a grant from National Science Foundation (CHE0907787). Funding for this work was also provided by a grant from the National Science Foundation CAREER Program (CHE-0847405).

## 5.7 References

[1] R.N. Butler, in: A.R. Katrizky, C.W. Rees, E.F.V. Scriven (Eds.) Comprehensive Heterocyclic Chemistry, vol. 4, Pergamon, Oxford, UK, **1996**.

[2] H. Singh, A.S. Chawla, V.K. Kapoor, D. Paul, R. Malhotra, *Prog. Med. Chem.*, **1980**, *17*, 151.

[3] V.A. Ostrovskii, M.S. Pevzner, T.P. Kofmna, M.B. Shcherbinin, I.V. Tselinskii, *Targets Heterocycl. Syst.*, **1999,** *3*, 467.

[4] M. Hiskey, D.E. Chavez, D.L. Naud, S.F. Son, H.L. Berghout, C.A. Bome, Proc. *Pyrotech. Semin.*, **2000**, *27*, 3.

[5] W. Ouellette, S. Jones, J. Zubieta, *CrystEngComm*, **2011**, *13*, 457.

[6] F.A. Mautner, C. Gspan, K. Gatterer, M.A.S. Goher, M.A.M. Abu-Youssef, E. Bucher, W. Sittee, *Polyhedron*, **2004**, *23*, 1217.

[7] W.F. Zhu and X.F. Zhou, *Acta Cryst*, **2008**, *E64,* m1478.

[8] J.M. Seco, M. de Araújo Farias, N.M. Bachs, A.B. Caballero, A. Salinas-Castillo, A. Rodríguez-Diéguez, *Inorg. Chim. Acta*, **2010**, *363*, 3194.

[9] J.W. Wang, J.X Guo, F. Fu, D.S. Li, J.J. Wang, M.L. Zhang, *Z. Kristallogr.*, **2007**, *222*, 55.

[10] M.C. Beard, G.M. Turner, C.A. Schmuttenmaer, *J. Phys. Chem. B*, **2002**, *106*, 7146.

[11] D.F. Plusquellic, T.M. Korter, G.T. Fraser, R.J. Lavrich, E.C. Benck, C.R. Bucher, A.R. Hight Walker, J.L. Domenech, *Int. J. High Speed Electron. Syst.*, **2003**, *13*, 1287.

[12] P. F. Taday, *Philos. Trans. R. Soc. London, Ser. A*, **2004**, *362*, 351.

[13] K. Siegrist, C.R. Bucher, I. Mandelbaum, A R. Hight Walker, R. Balu, S.K. Gregurick, D.F. Plusquellic, *J. Am. Chem. Soc.*, **2006**, *128*, 5764.

[14] R. Li, J.A. Zeitler, D. Tomerini, E.P.J. Parrott, L.F. Gladden, G.M. Day, *Phys. Chem. Chem. Phys.*, **2010**, *12*, 5329.

[15] K.C. Oppenheim, T.M. Korter, J.S. Melinger, D. Grischowsky, *J. Phys. Chem. A.*, **2010**, *114,* 12513.

[16] R. Dovesi, F.F. Fava, C. Roettia, V.R. Saunders, *Faraday Discuss.*, **1997**, *106*, 173.

[17] I. Moreira, R. Dovesi, C. Roetti, V.R. Saunders, R. Orlando, *Phys. Rev. B.*, **2000**, *62*, 7816.

[18] M. Catti and G. Sandrone, *Faraday Discuss.*, **1997,** *106*, 189.

[19] S. Pellizzeri, T.M. Korter, J. Zubieta, *J. Mol. Struct.*, **2011,** *1003*, 21

[20] R. Dovesi, M. Causà, R. Orlando, C. Roetti, V.R. Saunders. *J. Chem. Phys.*, **1990,** *92*, 7402.

[21] P.M. Hakey, D.G. Allis, M.R. Hudson,W. Ouellette, T.M. Korter, *ChemPhysChem*, **2009**, *10*, 2434.

[22] J. Wilkinson, C.T. Konek, J.S. Moran, E.M. Witko, T.M. Korter, *Chem. Phys. Lett.*, **2009,** *478,*172.

[23] H. Detert, D. Schollmeier, *Synthesis*, **1999**, 999.

[24] APEX II, Data Collection Software, version 2011.8-0; Bruker AXS Inc.: Madison, WI, **2005-2011**.

[25] SAINT Plus, Date Reduction Software, version, 6.45A; Bruker AXS Inc.: Madison, WI, **1997-2002**.

[26] Sheldrick, G. M. SADABS; University of Göttingen: Göttingen, Germany, **1996**.

[27] SHELXTL PC, version 6.12; Bruker AXS Inc.: Madison, WI, **2002**.

[28] A. Nahata, A.S. Weling, T.F. Heinz, *Appl. Phys. Lett.*, **1996**, *69*, 2321.

[29] A. Rice, Y. Jin, X.F. Ma, X.C. Zhang,D. Bliss, J. Larkin, M. Alexander, *Appl. Phys. Lett.*, **1994**, *64*, 1324.

[30] Q. Wu, M. Litz, X.C. Zhang, *Appl. Phys. Lett.*, **1996**, *68*, 2924.

[31] P.M Hakey, D.G. Allis, W. Ouellette,T.M. Korter, *J. Phys. Chem. A*, **2009**, *113*, 5119.

[32] P.M Hakey, M.R. Hudson, D.G. Allis, W. Ouellette,T.M. Korter, *J. Phys. Chem. A*, **2009**, *113*, 13013.

[33] J.R. Holden and C.W. Dickinson, *J. Phys. Chem.*, **1975**, *79*, 249.

[34] T.M Lowry and F.C. Hemmings, *J. Soc. Chem. Ind., London*, **1920**, *39*, 101.

[35] R. Dovesi, R. Orlando, B. Civalleri, R. Roetti, V.R. Saunders, C.M. Zicovich-Wilson, *Z. Kristallogr.*, **2005**, *220*, 571.

[36] R Dovesi, V. R. Saunders, R. Roetti, R. Orlando, C.M. Zicovich-Wilson, F. Pascale, B. Civalleri, K. Doll, N. M. Harrison, I. J. Bush, P. D'Arco, M. Llunell, CRYSTAL09 User's Manual. University of Torino: Torino, 2009.

[37] A. D. Becke, *J. Chem. Phys.*, **1993**, *98*, 5648.

[38] M.D. Towler, N.L. Allan, N.M. Harrison, V.R. Saunders, W.C. Mackrodt, E. AprÃ , *Phys. Rev. B*, **1994**, *50*, 5041.

[39] R. Dovesi, F. Freyria Fava, C. Roetti , V.R. Saunders, *Faraday Discuss.*, **1997**, 106, 173.

[40] Y. Dou, R.G. Egdell, D.S.L. Law, N.M Harrison, B.G. Searle, *J. Phys. Cond. Matter*, **1998**, *10*, 8447.

[41] P.C. Hariharan and J.A. Pople, *Theoret. Chimica Acta*, **1973**, *28,* 213.

[42] D. Feller, *J. Comp. Chem.*, **1996,** *17*, 1571.

[43] K. L. Schuchardt, B. T. Didier, T. Elsethagen, L. Sun, V. Gurumoorthi, J. Chase, J. Li, T. L. Windus. Basis Set Exchange: A Community Database for Computational Sciences.

[44] F. Pascale, C.M. Zicovich-Wilson, F.L. Gejo, B. Civalleri, R. Orlando, R. Dovesi, *J. Comput. Chem.*, **2004**, *25,* 888.

[45] C. G. Broyden, *Math. Comput.*, **1965**, 19, 577.

[46] D. D. Johnson, *Phys. Rev B.*, **1988**, *38*, 12807.

[47] E. Albanese, B. Civalleri, M. Ferrabone, S. Galli, A. Maspero, C.Pettinari, *J. Mater. Chem.*, **2012,** *22*, 22592.

[48] Q. Xu and J. Xu, *Acta Cryst.*, **2011**, *E67*, o43.

[49] J-ICE: a new Jmol interface for handling and visualizing Crystallographic and Electronics properties. P. Canepa, R.M. Hanson, P. Ugliengo, M. Alfredsson, *J. Appl. Cryst*., **2011**, 44.

# Chapter 6

# Crystal Structure and Terahertz Spectroscopy of α,α,α′,α′-Tetrabromo-*p*-xylene Modeled using Solid-State Density Functional Theory

## 6.1 Introduction

α,α,α′,α′-Tetrabromo-*p*-xylene (TBX) has been primarily used in recent years as a starting material in the electrochemical synthesis of poly(*p*-phenylenevinylene) (PPV).[1-5] This provides an alternative to the traditional synthesis of PPV[6,7] which leaves traces of unreacted starting material that hinders the properties of the resulting polymer. The electrochemical method of the PPV synthesis using TBX does not have this drawback. TBX has also been used more recently as a starting material in conjunction with 3,5-dimethylpyrazole to produce complex bitopic ligands.[8] Despite its uses in chemical applications, the crystal structure of TBX has not yet been reported. While the structure might not have any significant effect on its current uses, the conformation of the freely rotating -$CHBr_2$ substituent could be quite interesting, in particular how this substituent might affect the packing of the molecules in three dimensional space. Therefore, we have crystallized TBX, determined its structure and discovered that the nature of the packing within the molecular crystal is primarily held through electrostatic interactions, shown in **Figure 6.1**.

Most molecular crystals exhibit lattice vibrations which are the consequence of intermolecular interactions.[9] For the majority of molecular crystals these vibrations are found in the terahertz (THz) region (3-333$cm^{-1}$) consisting of intermolecular contributions from translations and rotations which involve weaker electrostatic and dispersive forces. To measure these vibrational motions, THz spectroscopy was then utilized to measure the absorption caused by these lattice vibrations which are unique to three-dimensional solids.[10-12] Since the field of interpreting the nature of THz vibrations is still relatively young, this system which is not affected by strong interactions, such as hydrogen bonding between unit cells, should result in a clearer interpretation of the vibrational modes.

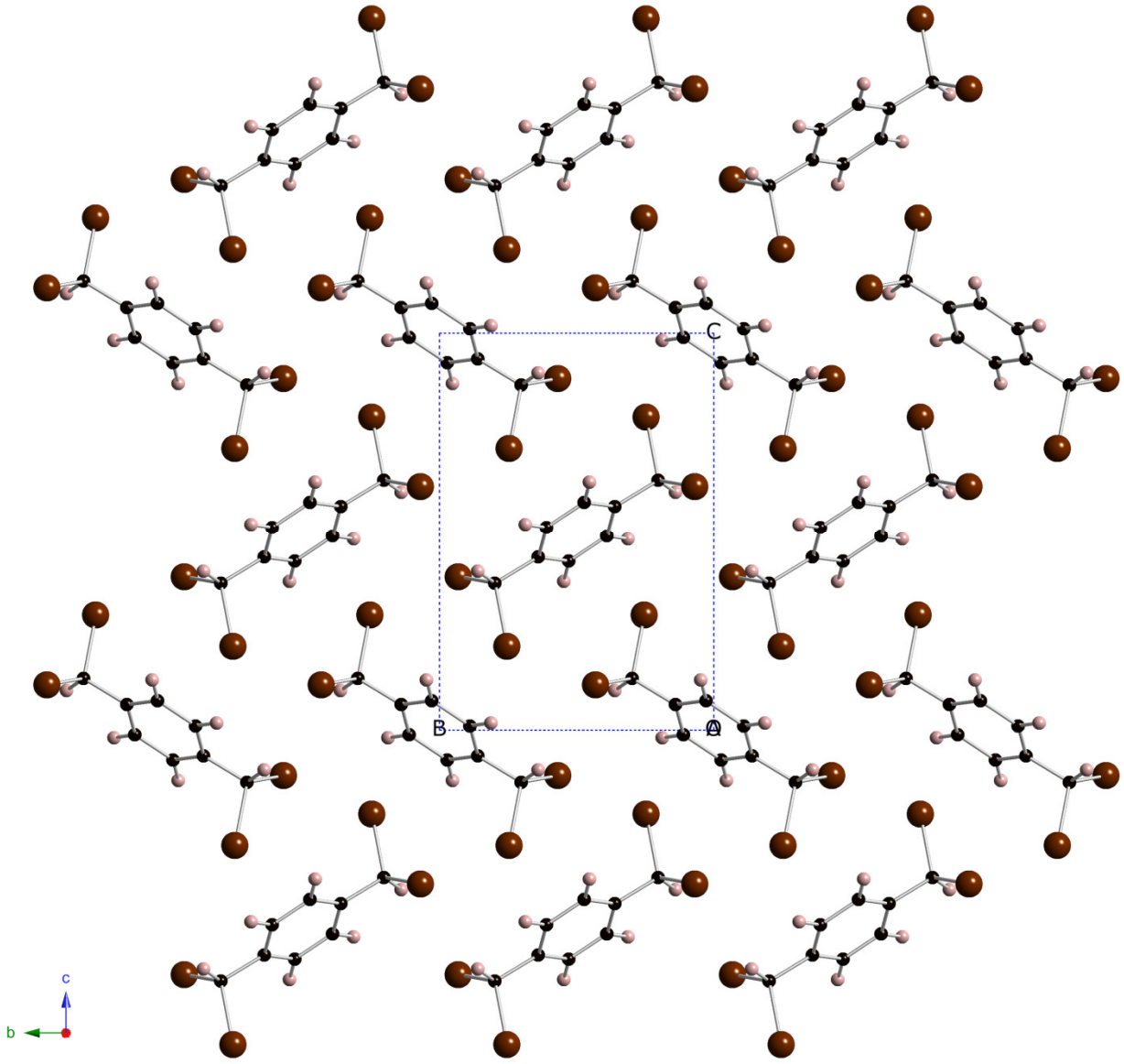


**Figure 6.1** Ball and Stick representation of the molecular packing of α,α,α′,α′-tetrabromo-*p*-xylene (TBX). (Bromine is shown in dark red, carbon is shown in black and hydrogen is shown in pink)

To determine the nature of these vibrations in the THz region the use of computational approaches was necessary due to the absence of characteristic group frequencies, unlike near-IR vibrational spectroscopy.[13-15] Since this system is held together primarily through electrostatic interactions across unit cells, accurate prediction of the vibrational modes requires a computational approach that reproduces the intermolecular forces that are unique to this substance. An approach that has been shown to produce quality simulations of THz spectra is solid-state density functional theory (DFT).

The solid-state DFT approach that was used in this study is implemented in CRYSTAL09, which has been used with great success to simulate many organic systems in order to determine their structural and vibrational properties.[16-18] CRYSTAL09 utilizes periodic boundary conditions, which are required to accurately simulate vibrational motions that are perturbed by crystal packing forces, and perhaps equally important, to couple external lattice motions to the internal "molecular" motions of the asymmetric repeat unit. Therefore, CRYSTAL09 was used to replicate the geometric parameters of TBX as well as to determine the vibrationally active modes in the THz region and to evaluate the normal modes that are the result of these absorptions.

## 6.2 Experimental and Theoretical Methods

### *6.2.1 Experimental*

#### *6.2.1.1 Recrystallization of α,α,α′,α′-Tetrabromo-p-xylene.*

α,α,α′,α′-Tetrabromo-*p*-xylene (98%) was purchased from VWR and recrystallized from acetone to yield colorless needles that were suitable for X-Ray diffraction. IR (KBr pellet, $cm^{-1}$):

3007(w), 2372(w), 2344(w), 1913(w), 1417(s), 1306(w), 1233(m), 1151(m), 1111(m), 1015(w), 841(m), 780(s), 651(s), 635(s).

#### *6.2.1.2 X-Ray Crystallography*

Crystallographic data for the compound was collected on a Bruker KAPPA APEX DUO diffractometer using Mo-$K_\alpha$ radiation ($\lambda$ = 0.71073Å) containing an APEX II CCD system[19] at low temperature (90K). The data was corrected for Lorentz and polarization[20] effects, and adsorption corrections were made using *SADABS*.[21] The structure was solved by direct methods. Refinement was carried out using the SHELXTL[22] crystallographic software. Following assignment of all non-hydrogen atoms, the models were refined against $F^2$ first using isotropic and then using anisotropic thermal displacement parameters. The hydrogen atoms were introduced in calculated positions and then refined isotropically. Neutral atom scattering coefficients along with anomalous dispersion corrections were taken from the *International Tables*, Vol. C.

### *6.2.2 Time-domain Terahertz Spectroscopy*

The experimental terahertz spectrum of the compound was acquired using a pulsed time-domain THz spectrometer based on an amplified femtosecond Ti:Sapphire laser system operating in the near-infrared region. For the generation and detection of THz radiation, the instrument utilized optical rectification[23,24] and free space electro-optic sampling,[23,25] respectively. A detailed description of the spectrometer along with the experimental setup has been provided elsewhere.[17,26,27]

TBX was used without further purification and was mixed with a spectroscopic grade powdered polytetrafluoroethylene (PTFE) matrix. The sample and the matrix were then

mechanically pulverized using a stainless-steel ball mill (Dentsply Rinn 3110-3A), allowing a homogeneous distribution of the sample through the matrix, thereby reducing the particle size, and minimizing radiation scattering.[27,28] The mixture was then pressed into a pellet at 2000 psi using a hydraulic press (ICL E-Z Press 12). The resulting sample pellet had a total mass of 0.56657 g, thickness of 2.01 mm, diameter of 13.0 mm, containing 13.63% w/w TBX. The blank (reference) pellet was prepared with pure PTFE in a similar manner.

The sample and blank pellets were both held under vacuum in a variable-temperature cryostat and held at temperatures of 293 K (room temperature) and 78 K (liquid-nitrogen temperature).

Each individual spectrum of the sample (or the blank pellet) consisted of an average of 36 THz-waveform scans over a time window of ~30 ps. These waveforms were then symmetrically zero-padded to a total of 6000 data points, and subsequently were Fourier-transformed (utilizing a Hanning window function) into the frequency-domain. Elimination of any THz absorption by the PTFE matrix was accomplished by taking a ratio of the transformed spectrum of a PTFE blank versus the transformed spectrum of a sample pellet. To improve the final signal-to-noise ratio, four blank/sample sets were collected and averaged, over a range of 10 to 100 $cm^{-1}$ with a spectral resolution of approximately 1.0 $cm^{-1}$, yielding the THz spectrum reported here.

### *6.2.3 Theoretical Methodology of CRYSTAL09*

Geometry optimizations, harmonic frequencies, and intensity calculations were performed using the CRYSTAL09 program.[29,30] All calculations were performed using a spin restricted B3LYP[31] hybrid density functional. The basis set chosen for all the atoms was a Gaussian type triple valence basis set with polarization (pob_TZVP).[32]

The positions of the atoms contained within the unit cell were optimized within the constraints of the literature lattice parameters and space group symmetry. From the optimized structures, the bond lengths and bond angles were determined and compared with the experimental crystallographic results. After optimizing the structures, harmonic-limit normal-mode analyses on the organometallic complexes were conducted. Frequencies were determined by a mass-weighted numerical evaluation of the Hessian matrix[33] and intensities were calculated through the Berry phase approach.[30]

Several of the convergence parameters were changed to optimize the accuracy and computational time of the calculations. The convergence criteria were modified to set the root mean square of the maximum gradient (TOLDEG) and the maximum displacement (TOLDEX) to be $1 \times 10^{-5}$ and $4 \times 10^{-5}$ angstroms, respectively. To improve the numerical accuracy of the calculations the truncation criteria for bielectronic integrals (TOLINTEG) was set to 8 8 8 8 16 and the DFT integration was set to XLGRID (75,974). (See Ref. [29,30] for details). Total energy convergence (TOLDEE) was set to $\Delta E < 1 \times 10^{-8}$ Hartree for the geometry optimization and $\Delta E < 1 \times 10^{-11}$ Hartree for frequency analysis.

To assist in a timely convergence, the "Fock/KS matrix mixing" (FMIXING) was increased from the default value of zero to 50 for all systems. The eigenvalue level shifter was also activated with the level shifter set to a value that corresponds to a shift of 0.5 Hartree, and the state was locked, confining it to an insulating state. Determination of the optimum sampling of reciprocal space was determined by comparing the total energy of the converged system to the k-point count using the keyword SHRINK. The optimum SHRINK value was determined to be SHRINK = 6 6 which corresponds to 80 points in the irreducible part of the Brillouin Zone and 80 points in the Gilat Net.

## 6.3 Results and Discussion

### *6.3.1 X-Ray Crystallography*

The molecular structure of TBX crystallizes in the monoclinic space group $P2_1/n$. Crystallographic details for TBX are provided in **Table 6.1**. Packing of the structure in the *bc* plane displays a zig-zag pattern up the *c* crystallographic axis as previously shown in **Figure 6.1**. This packing arrangement allows the molecules to be close-packed with one another with the shortest interatomic distance between two bromide atoms of two adjacent TBX molecules being 3.835(8)Å. In addition to the close packing of neighboring molecules, the bromide on a neighboring molecule is situated perpendicular to the plane of the benzene ring. This arrangement is favorable due to the apparent electron withdrawing effect of the $–CHBr_2$ substituent on the benzene ring creating a slight positive charge on the carbon atoms of the benzene ring, leading to a favorable interaction with the slightly negative bromide atom. A graphical representation of the Mulliken population analysis for TBX is provided in **Figure 6.2**. Images of the crystal structures were generated using CrystalMaker®.[34] An ORTEP plot of the structure is displayed in **Figure D-2**.

### *6.3.2 Comparison of the Calculated and Experimental Structures*

The calculated and experimental bond lengths, bond angles, and the root-mean-squared deviation (RMSD) values are shown in **Table 6.2** (see **Figure 6.3** for the labeling scheme), and the results are visualized in **Figure 6.3**. The theoretical strategy used was able to model the bond

**Table 6.1** Summary of crystallographic data for α,α,α′,α′-tetrabromo-*p*-xylene.

| | α,α,α′,α′-Tetrabromo-*p*-xylene |
|---|---|
| Empirical Formula | C8 H6 Br4 |
| Formula Weight | 421.77 |
| Crystal System | Monoclinic |
| Space Group | $P2_1/n$ |
| *a (Å)* | 5.409(3) |
| *b (Å)* | 8.193(4) |
| *c (Å)* | 12.002(6) |
| *α (°)* | 90 |
| *β(°)* | 98.289(11) |
| *γ(°)* | 90 |
| $V(Å^3)$ | 526.4(4) |
| *Z* | 2 |
| $D_{calc}(g\ cm^{-3})$ | 2.661 |
| $\mu\ (mm^{-1})$ | 15.235 |
| *T (K)* | 90 |
| Wavelength | 0.71073 |
| $R_1$[a] | 0.0284 |
| $wR_2$[b] | 0.0743 |

[a] $R1 = \Sigma|F_o| - |F_c|/\Sigma|F_o|$. [b] $wR2 = \{\Sigma[w(F_o^2 - F_c^2)^2]/\Sigma[w(F_o^2)^2]\}^{1/2}$

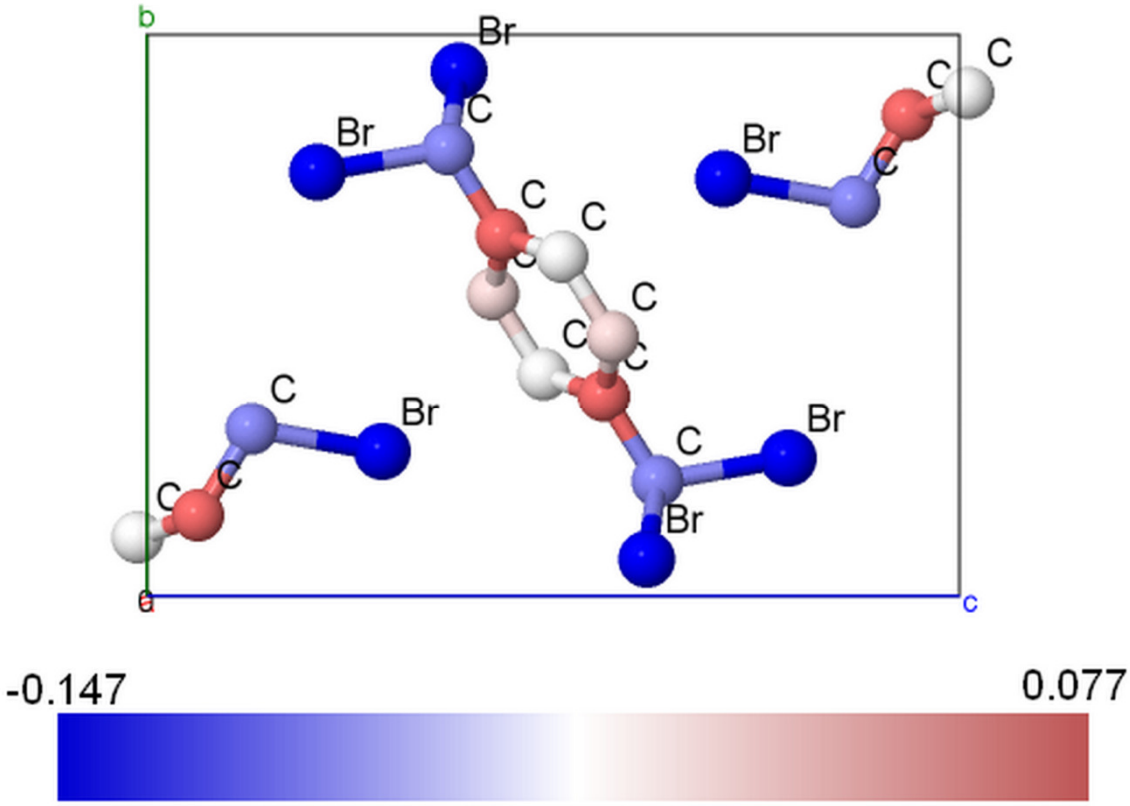


**Figure 6.2** Graphical representation of the Mulliken population analysis of α,α,α′,α′-Tetrabromo-*p*-xylene.

**Table 6.2** Interatomic bond lengths (Å), angles (°), and RMSD values for α,α,α′,α′-tetrabromo-*p*-xylene. See **Figure 6.3** for atomic labels. Experimental parameters are from 90 K crystallographic data.

| Bond, Å | Experimental | Theoretical |
|---|---|---|
| **Br1-C1** | 1.9513 | 1.9806 |
| **Br2-C1** | 1.9514 | 1.9799 |
| **C1-C2** | 1.5191 | 1.4857 |
| **C2-C3** | 1.3803 | 1.3931 |
| **C2-C4** | 1.3738 | 1.3898 |
| **C3-C4** | 1.3611 | 1.3807 |
| **C1-H1** | 0.9994 | 1.0804 |
| **C3-H3** | 0.9499 | 1.0811 |
| **C4-H4** | 0.9495 | 1.0815 |
| | **RMSD** | **0.02446** |

| Angle, ° | Experimental | Theoretical |
|---|---|---|
| **Br1-C1-C2** | 111.028 | 112.701 |
| **Br2-C1-C2** | 110.820 | 112.464 |
| **Br1-C1-Br2** | 109.822 | 109.730 |
| **C1-C2-C3** | 115.020 | 118.187 |
| **C1-C2-C4** | 125.703 | 122.209 |
| **C3-C2-C4** | 119.276 | 119.598 |
| **C2-C3-C4** | 120.531 | 120.355 |
| **C2-C4-C3** | 120.192 | 120.046 |
| | **RMSD** | **1.8676** |

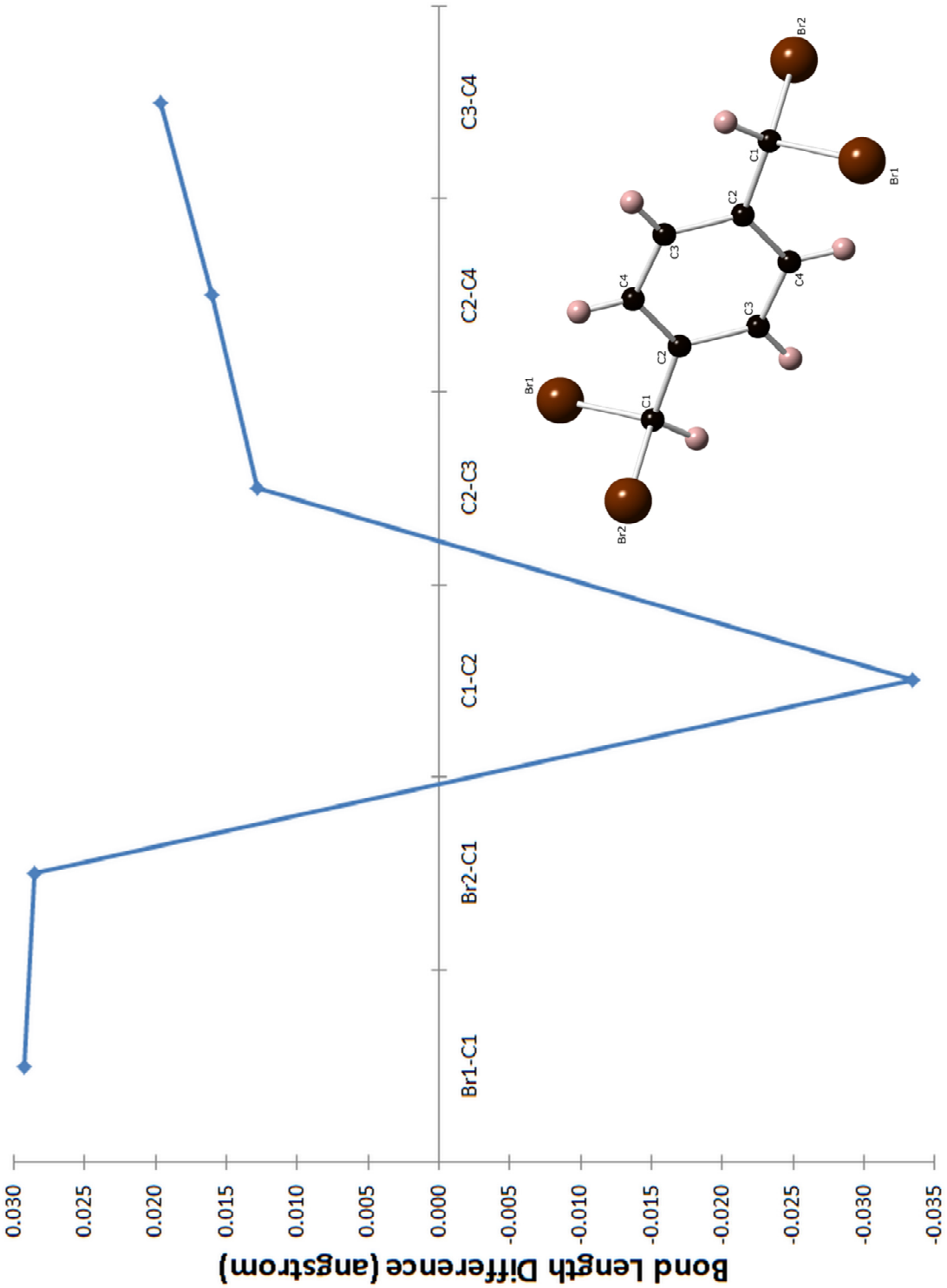


**Figure 6.3** Calculated bond-length differences for α,α,α′,α′-tetrabromo-*p*-xylene (TBX). The inset figure shows the atom labeling for TBX.

lengths with a very reasonable amount of accuracy, replicating each of the bonds within ±0.035Å and producing a RMSD of 0.02446. In addition to the bond lengths, the angles were also modeled with a high level of accuracy, producing no large deviations from the experimentally derived structure. The packing arrangement remains consistent in the optimized structure with the shortest interatomic distance between two bromide atoms of two adjacent TBX molecules being 3.891Å, which is only an overestimation of 1.46%. The strong correlation between the optimized structure and the experimentally determined structure suggests that the structure is at a potential energy minimum, which is necessary for an accurate simulation of the vibrational frequencies.

### *6.3.3 Comparison of Theoretical and Experimental Vibrational Frequencies*

The experimental and calculated terahertz spectra are shown in **Figure 6.4** and are summarized in **Table 6.3**. Empirical analysis of the vibrational modes observed using J-ICE[35] are shown in **Table 6.4**. Although there is a combination of intramolecular and intermolecular motions, only the major motion is listed. Overall, the fit to the theoretically determined terahertz spectrum produces a close match to the experimentally determined spectrum. In addition, the intensities of the theoretically determined spectrum are reasonably similar to the experimental terahertz spectrum.

The spectrum at 78K displays three peaks. However, the bands at 35.69 $cm^{-1}$ and 49.10 $cm^{-1}$ both show a shoulder, whose frequencies were determined using a Lorentzian multi-peak fitting function and are included in **Table 6.3**, a graphical representation of the fitting is available in the supplementary materials (**Figure D-3).** The 298K spectrum in comparison only displays two peaks with no discernible shoulders. This difference in the quantity of the observed peaks can be likely attributed to the broadening of the peaks observed in the 78K spectra due to the

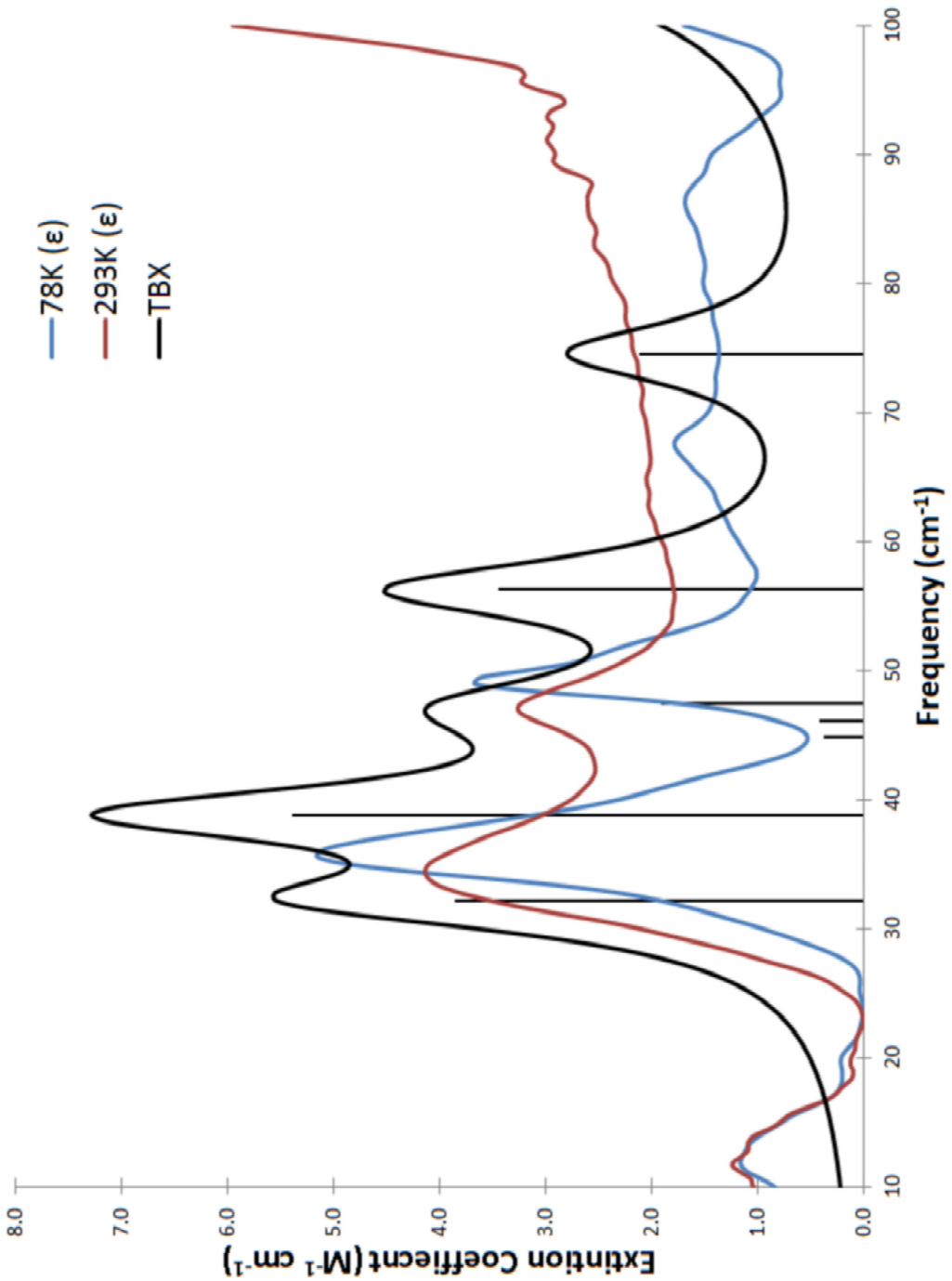


**Figure 6.4** The experimental and theoretical traces for the terahertz spectrum of α,α,α′,α′-tetrabromo-*p*-xylene (TBX). An empirical 3.0 $cm^{-1}$ full-width-half-maximum Lorentzian line shape has been applied to the theoretical data to aid in comparison.

**Table 6.3** Frequency positions ($cm^{-1}$) and RMSDs for the experimental and theoretical terahertz spectra of α,α,α′,α′-tetrabromo-*p*-xylene. The blanks are peaks that have no obvious correlation between the room temperature and cryogenic experimental spectra. When multiple peaks corresponded to only one peak in the experimental spectra, the weighted average was used in calculating the RMSD. Mode descriptions are described in **Table 6.4**.

| Mode | Exp. (78K) | Exp. (293K) | Theoretical | Intensity |
|---|---|---|---|---|
| a | 35.44 | 34.39 | 32.11 | 0.93 |
| b | 37.28 | | 38.81 | 1.3 |
| c | | | 44.88 | 0.09 |
| d | 48.97 | 47.01 | 46.10 | 0.1 |
| e | | | 47.43 | 0.46 |
| f | 51.52 | | 56.26 | 0.83 |
| g | 67.52 | --- | 74.56 | 0.51 |
| | | **RMSD** | 4.242 | |

**Table 6.4** Empirical normal mode analysis of the halide salts of α,α,α′,α′-tetrabromo-p-xylene.

| Mode | Description |
|---|---|
| a | Translation along c |
| b | Translation along b |
| c | Translation along a |
| d | Molecular scissoring in the ac plane |
| e | Molecular scissoring in the bc plane |
| f | Molecular scissoring in the ab plane |
| g | Molecular rocking in the ac plane |

increase in the number of populated vibrational states due to the increase in thermal energy, resulting in the decrease of the observable peaks in the 298K spectrum.

The theoretically determined frequencies show an excellent correlation with the experimentally determined spectrum determined at 78K, producing an RMSD of 4.232. It was found that two peaks in the experimental spectrum were comprised of two peaks in the theoretically determined spectrum. These included the experimental peak at 40.51 $cm^{-1}$, which is a combination of the peaks found at 38.81 $cm^{-1}$ and 44.88 $cm^{-1}$, where the former was the major component. It was also determined that the peak at 49.10 $cm^{-1}$ was comprised of the peaks at 46.10 $cm^{-1}$ and 47.43 $cm^{-1}$ where the latter was the major component.

The empirical visualization of the modes showed that there were three major motion types as illustrated in **Figure 6.5**. The first type (**Figure 6.5A**) corresponds to the lowest energy modes a-c, which involves translations along the primary axes of the unit cell. The second type (**Figure 6.5B**) corresponds to modes d-f, which involves molecular scissoring in various crystallographic planes. Lastly, type C (**Figure 6.5C**) corresponds to mode g, which involves molecular rocking in the ac plane. With the exception of the last mode, the two major features in the experimentally determined spectrum located at 35.69$cm^{-1}$ and 49.10 $cm^{-1}$ and their corresponding shoulders are the combination of all the possible perturbations of either translational or scissoring motions available.

## 6.4 Conclusions

The crystal structure of α,α,α′,α′-tetrabromo-p-xylene was determined using single crystal x-ray diffraction. In addition, the solid-state simulation of the geometric and vibrational properties were performed using the CRYSTAL code. The crystal structure revealed that α,α,α′,α′-tetrabromo-*p*-xylene crystallizes as a molecular crystal and is primarily held together through

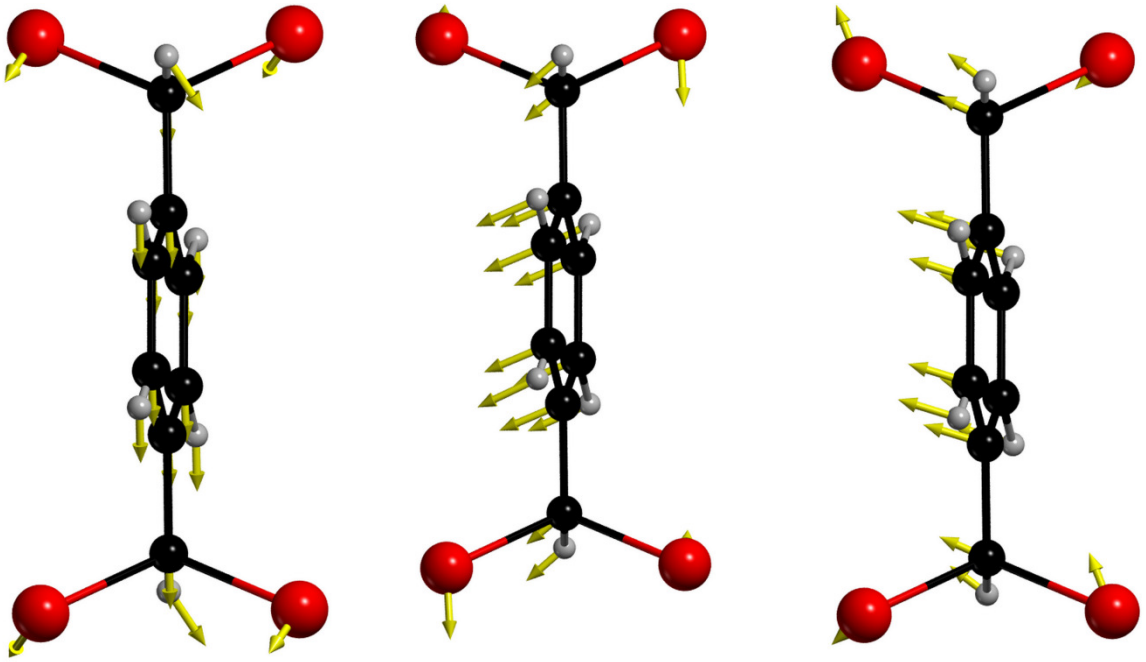


**Figure 6.5** Visualization of vibrational normal modes. Type A corresponds to modes a-c, which involve translations along the primary axes. Type B corresponds to modes d-f, which involves molecular scissoring in various planes. Type c corresponds to mode g, which involves molecular rocking in the ac plane. Arrows denote the direction of molecular motion. (Bromine is shown in red, carbon is shown in black and hydrogen is shown in grey.)

electrostatic forces. Due to the nature of the packing, the complex made a prime candidate for characterization by terahertz spectroscopy due to its ability to probe lattice vibrations unique to molecular crystals.

Examining the Mulliken population analysis of TBX suggests that the $–CHBR_2$ substitution on the benzene rings results in an electron withdrawing effect creating a slightly positive charge on the ring. This small positive charge results in a favorable electrostatic interaction between the bromide and benzene rings of neighboring molecules. This interaction is most likely the attributing factor for the orientation of the molecules in three-dimensional space.

The strong correlation of the optimized structure with the experimental structure resulted in a strong correlation of the measured and predicted terahertz spectra. The lack of strong interactions across unit cells led to a simplified interpretation of the vibrational motions, resulting in the determination of the translations along all the principle axes as well as all the variations of whole molecule scissoring and wagging along the crystallographic planes. Therefore, when a molecular crystal is held together primarily through weaker interactions, such as dispersion and electrostatic interactions, the resulting terahertz spectra will not be complicated by complex interactions across unit cells.

## 6.5 Supporting Information

The supporting information consists of the near-Infrared vibration spectrum of TBX shown from 4000-400 $cm^{-1}$ (**Figure D-1**). The supporting information also contains an ORTEP view of the asymmetric unit of α,α,α′,α′-tetrabromo-*p*-xylene, showing the partial atom-labeling schemes and 50% thermal ellipsoids (**Figure D-2**). Lastly, a graphical representation of the peak fitting procedure is illustrated in **Figure D-3**.

Additional material is available from the Cambridge Crystallographic Data Centre, CCDC No. 947074, comprises the final atomic coordinates for all atoms, thermal parameters, and a complete listing of bond distances and angles. Copies of this information may be obtained free of charge on application to The Director, 12 Union Road, Cambridge, CB2 2EZ, UK, fax: +44 1223 336 033, e-mail: data_request@ccdc.cam.ac.uk or http://www.ccdc.cam.ac.uk.

## 6.6 Acknowledgment

This work was supported in part by a grant from the National Science Foundation (CHE0907787). Funding for this work was also provided by a grant from the National Science Foundation CAREER Program (CHE-0847405).

## 6.7 References

[1] H. Nishihara, M. Tateishi, K. Aramaki, T. Ohsawa, O. Kimura, *Chem. Lett.*, **1987**, *3*, 539.

[2] P. Damlin, C. Kvarnström, A. Ivaska, *Electrochim. Acta*, **1999**, *44*,1919.

[3] T. Kim, S. Park, *Electrochim. Acta,* **2005**, *50*, 1461.

[4] N. M. Alpatova, G. P. Girina, *Russ. J. Electrochem.*, **2006**, *42*, 670.

[5] G. P. Girina, N. M. Alpatova, L. G. Feoktistov, *Russ. J. Electrochem.*, **2006**, *42*, 102.

[6] J.H. Burroughs, D. D. Bradley, A. R. Brown, R. N.Marks, K. Mackay, R. H. Friend, P. L. Burn, A. B. Holmes, *Nature (London),* **1990**, *347*, 539.

[7] P. Denton, A. Sarker, P. M. Lahti, R. O. Garay, F. E. Karasz, *J. Polym. Sci., Part A: Polym. Chem.*, **1992**, *30*, 2233.

[8] A. S. Potapov, E. A. Nudnova, G. A. Domina, L. N. Kirpotina, M.T. Quinn, A. I. Khlebnikov, I. A. Schepetkin, *Dalton Trans.*, **2009**, *23*, 4488.

[9] M.C. Beard, G.M. Turner, C.A. Schmuttenmaer, *J. Phys. Chem. B*, **2002**, *106*, 7146.

[10] S. P. Delaney, E. M. Witko, T.M. Smith, T.M. Korter, *J. Phys. Chem. A*, **2012**, *116*, 8051.

[11] S. P. Delaney, D.Pan, M. Galella, S.X. Yin, T.M. Korter, *Cryst. Growth Des.*, **2012**, *12*, 5017.

[12] M.D. King, W.D.Buchanan, T.M. Korter, *J. Pharm. Sci.*, **2011**, *100*, 1116.

[13] K. Siegrist, C.R. Bucher, I. Mandelbaum, A R. Hight Walker, R. Balu, S.K. Gregurick, D.F. Plusquellic, *J. Am. Chem. Soc.*, **2006**, *128*, 5764.

[14] R. Li, J.A. Zeitler, D. Tomerini, E.P.J. Parrott, L.F. Gladden, G.M. Day, *Phys. Chem. Chem. Phys.*, **2010**, *12*, 5329.

[15] K.C. Oppenheim, T.M. Korter, J.S. Melinger, D. Grischowsky, *J. Phys. Chem. A.,* **2010**, *114,* 12513.

[16] R. Dovesi, M. Causà, R. Orlando, C. Roetti, V.R. Saunders, *J. Chem. Phys.,* **1990**, *92*, 7402.

[17] P.M. Hakey, D.G. Allis, M.R. Hudson,W. Ouellette, T.M. Korter, *ChemPhysChem,* **2009**, *10*, 2434.

[18] J. Wilkinson, C.T. Konek, J.S. Moran, E.M. Witko, T.M. Korter, *Chem. Phys. Lett.,* **2009**, *478,*172.

[19] APEX II, Data Collection Software, version 2011.8-0; Bruker AXS Inc.: Madison, WI, **2005-2011**.

[20] SAINT Plus, Date Reduction Software, version, 6.45A; Bruker AXS Inc.: Madison, WI, **1997-2002**.

[21] Sheldrick, G. M. SADABS; University of Göttingen: Göttingen, Germany, **1996**.

[22] SHELXTL PC, version 6.12; Bruker AXS Inc.: Madison, WI, **2002**.

[23] A. Nahata, A.S. Weling, T.F. Heinz, *Appl. Phys. Lett.,* **1996**, *69*, 2321.

[24] A. Rice, Y. Jin, X.F. Ma, X.C. Zhang,D. Bliss, J. Larkin, M. Alexander, *Appl. Phys. Lett.,* **1994**, *64*, 1324.

[25] Q. Wu, M. Litz, X.C. Zhang, *Appl. Phys. Lett.,* **1996**, *68*, 2924.

[26] P.M Hakey, M.R. Hudson, D.G. Allis, W. Ouellette,T.M. Korter, *J. Phys. Chem. A,* **2009**, *113*, 13013.

[27] J.R. Holden, C.W. Dickinson, *J. Phys. Chem.,* **1975**, *79*, 249.

[28] T.M Lowry,F.C. Hemmings, *J. Soc. Chem. Ind., London,* **1920**, *39*, 101.

[29] R. Dovesi, R. Orlando, B. Civalleri, R. Roetti, V.R. Saunders, C.M. Zicovich-Wilson, *Z. Kristallogr.,* **2005**, *220*, 571.

[30] R Dovesi, V. R. Saunders, R. Roetti, R. Orlando, C.M. Zicovich-Wilson, F. Pascale, B. Civalleri, K. Doll, N. M. Harrison, I. J. Bush, P. D'Arco, M. Llunell, CRYSTAL09 User's Manual. University of Torino: Torino, **2009**.

[31] A. D. Becke, *J. Chem. Phys.*, **1993**, *98*, 5648.

[32] M. F. Peintinger, D. V. Oliveira, T. Bredow, *J. Comput. Chem.,* **2013**, *34*,451.

[33] F. Pascale, C.M. Zicovich-Wilson, F.L. Gejo, B. Civalleri, R. Orlando, R. Dovesi, *Journal of Computational Chemistry,* **2004**, *25,* 888.

[34] CrystalMaker® : a crystal and molecular structures program. CrystalMaker Software Ltd., Oxford, England (www.crystalmaker.com).

[35] P. Canepa, R.M. Hanson, P. Ugliengo, M. Alfredsson, *J. Appl. Cryst*., **2011**, *44*, 225-229.

# Chapter 7

# Conclusions

## 7.1 Conclusions

The work presented here has made a contribution to the field of interpretation of the THz spectroscopy of a variety of substances. These substances included organic, inorganic, and hybrid organometallic materials. The field of interpreting the THz spectra of molecular solids is still quite young; therefore, much work must be done to better understand the origins of the absorption in the THz region. By sampling examples of three major types of substances, this task has been accomplished to some degree. In addition to sampling different types of structures, multiple configurations of the same compound were tested. By investigating these polymorphs, the changes exhibited can be directly linked to differences in structure and packing and not inherent to composition. Nevertheless, in a couple of cases pseudo-polymorphs were investigated where the structures could be considered identical, although small composition differences were present. Changes in these systems can be directly related to composition. However, not all the substances tested displayed absorption in the THz region.

The purely inorganic set of polymorphs of $VOPO_4$ did not have absorptions in the THz region due to the modes not being IR active in this region. Therefore, near-IR spectroscopy was utilized in its place to investigate the three polymorphs tested. In this study, the choice of basis set for the oxygen atoms was also studied. At the time of publication, this investigation showed that standard Pople basis sets do not always transfer well to periodic systems. The basis set that was found to be the most consistent within all the phases was one that was optimized for the use in periodic systems and specifically for use in CRYSTAL. This discovery lead to the use of mostly periodically optimized basis sets for future work as seen in the studies presented in Chapters 3, 5, and 6. While no insight into peak assignments in the THz region was done in this study, it was postulated that the similarity in the structure and spectra of the $\alpha_1$ and $\beta$ phases,

could give reason for the conversation of the $\alpha_1$ phase to the β phase. In addition, reasoning for why the $\alpha_2$ phase, which is only different from the $\alpha_1$ phase by the location of the vanadium atom inside the octahedral polyhedron, will not convert to the β phase is reported.

Another system that was investigated was α,α,α′,α′-tetrabromo-*p*-xylene which is an organic species that is mostly used as a precursor in the synthesis of poly(*p*-phenylenevinylene). This system is unique in relation to most molecular crystals, because this species is not held together through strong hydrogen bonding or ion-dipole type interactions. This system is held together through electrostatic interactions between neighboring molecules consisting of dipole-dipole interactions between the bromines and the π orbitals from the aromatic rings. In addition to the THz investigation, the crystal structure for the compound was also determined, as it was previously unknown. This system produced a THz spectrum that could almost be considered a prototypical spectrum due to the clear assignment of each experimental peak. Each peak of the THz spectrum was composed of each possible iteration of the low energy translational motions, and the higher energy molecular deformations in the form of a scissoring motion was obtained and assigned.

The last set of systems was the most extensively studied in this work. This set of systems allowed the investigation of a whole series of compounds based on three types of polymorphs each centered on the same compound, the 5-monosubsituted tetrazole, 5-(4-pyridyl)tetrazole. The three sets included two polymorphic forms based purely on packing, a set of isomorphic hydrohalide salts and lastly a set of isomorphous transition metal complexes containing 5-(4-pyridyl)tetrazole as the coordinating ligand.

The first set of 5-(4-pyridyl)tetrazole species is polymorphic in the traditional sense, because it only varies in the packing of the hydrogen-bonded chains in three-dimensional space.

This difference is subtle as the previously known form contains chains running parallel with each other, while in the newly discovered form the chains are running antiparallel. In addition to recording the THZ spectra, the energy of formation was determined, and it was found that the energy difference between the polymorphs was minimal. Additional work was conducted and it was found that the known phase is more stable at lower temperatures while the newly discovered phase was more stable at higher temperatures. The THz spectra showed a small 2 $cm^{-1}$ shift in the frequency between the two phases. Therefore, when there are no large differences in crystallinity the shift in frequency is not large. However, this small difference can be attributed to the polymorphic forms and not experimental error because this same shift is also seen in the computational model.

The next set of compounds containing 5-(4-pyridyl)tetrazole can be considered pseudo-polymorphic since both are hydrohalide salts of 5-(4-pyridyl)tetrazole. The hydrohalide salts have nearly identical structures with the bromine salt having a slightly expanded unit cell due to the increased size of the anion. This study examined what effect the halide would have on the THz spectra. It was found that the mass of the halide atom had an overall effect similar to that exhibited in the infrared region of the EM spectrum. The increased mass of the bromide results in a red shift in the frequency positions. Therefore, extending these findings to similar compounds, a similar shift in the THz spectra should be observed proportional to the mass difference when there is only a mass difference and no packing or conformational differences.

The last sets of compounds were based on transition metal complexes containing 5-(4-pyridyl)tetrazole. Three isomorphous complexes of the form $[M(C_6H_4N_5)_2(H_2O)_4]\cdot 2H_2O$ (M = Mn, Cd, Co) were tested to study what effect the mass and size of the transition metal has on the THz spectra of these compounds. This set of systems led to a new issue that was not seen in any

of the other systems tested in this work. In the previous work there was no ambiguity in the arrangement of the electrons in the orbitals of the atoms; however, the inclusion of transition metals with unfilled *d* orbitals led to an issue with the accuracy of the simulations. These systems could not be treated like the others, and it was not until the electrons spins were allowed to fluctuate that a solution could be found. The other issue was that the spin states of these complexes were not known. Through the course of the investigation, it was found that both the manganese and cobalt complexes were in fact high spin, which required special treatment of these atoms in the simulations. The cadmium had no such issues due to it having a filled *d* orbital. Once this issue with spin was taken into account, the simulation produced very good agreements with the experimentally obtained crystal structure and THz spectra. A clear trend was found that was indeed mass dependent, comparable to that seen in the investigation of the hydrohalide salts of 5-(4-pyridyl)tetrazole. However, the size of the transition metal also played an important role when the normal modes involved motions associated with the metal.

In this instance, the bond strength of the metal with the ligand was more important than the mass. Due to the smaller size of the cobalt, the bond strength between the metal and the nitrogen was increased and produced a shift opposite to what would be expected based purely on mass, compared to the manganese complex, which has a larger ionic radius. To reiterate, this effect was only seen when observing motions directly linked to the metal center; otherwise, standard mass related shifts were seen. This system presented a unique set of complexes that are not commonly investigated in the study of molecular crystals. The addition of transition metals with unfilled *d* orbitals added complications to an otherwise simple system. However, a set of conditions were developed which could be applied to similar systems in the future. This could

potentially be very useful in the investigation of the large number of molecular solids found in the field of hybrid metal-organic chemistry.

The research that was conducted spanned a wide range of issues. Some of these included fundamental methodologies in the classification and interpretation of a set of compounds that is rarely investigated due to their inherent complexity. In addition, all the sets of polymorphs tested only had minor structural or compositional changes. When there were compositional differences, a large change was found in the spectra, which is ideal for distinguishing halides or transition metals using THZ spectroscopy, especially if the system is not previously known. However, when there is only a small rearrangement in space the effect is much more subtle. Nevertheless, THz spectroscopy was able to distinguish the systems and the computational methods produced assignments that agreed with those experimentally observed.

In addition to the collection and interpretation of THz spectra, this work also illustrated the use of a computational method that is suitable for the study or a wide range of crystalline solids. The methods applied in CRYSTAL09 have proven to be a valuable tool in the interpretation of the absorption in THz active compounds. Along with it use to predict vibrational spectra, CRYSTAL09 can also be used to predict more complicated systems and predict other useful properties such as magnetism and surface absorption which could be applied to other work that is being conducted in the Zubieta research group.

## APPENDIX A. Chapter 3 Supporting Information

**Contents:**

**Figure A-1** ORTEP view of the building unit of α form of 5-(4-pyridyl)tetrazole, showing the partial atom-labeling scheme and 50% thermal ellipsoids.

**Figure A-2** ORTEP view of the building unit of β form of 5-(4-pyridyl)tetrazole, showing the partial atom-labeling scheme and 50% thermal ellipsoids.

**Figure A-3** The room temperature (298K) experimental and theoretical traces for the terahertz spectra of the A) α and B) β forms of 5-(4-pyridyl)tetrazole shown from 10-95 $cm^{-1}$. An empirical 3.0 $cm^{-1}$ and 6.0 $cm^{-1}$ full-width-half-maximum Lorentzian line shape has been applied to the theoretical data of the α and β forms of 5-(4-pyridyl)tetrazole, respectively, to aid in comparison.

**Figure A-4** Normalized near-infrared vibration spectra of the α and β forms of 5-(4-pyridyl)tetrazole shown from 4000-400 $cm^{-1}$

.

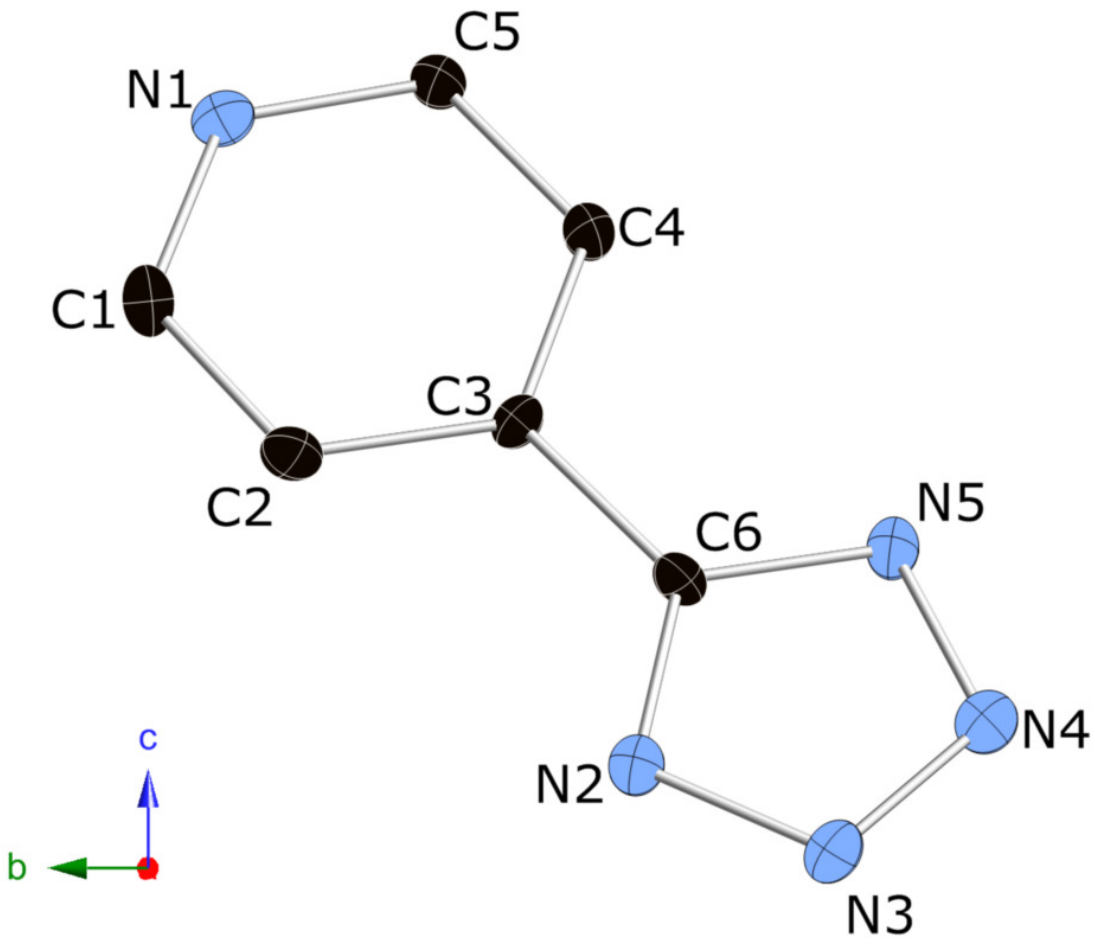


**Figure A-1** ORTEP view of the building unit of α form of 5-(4-pyridyl)tetrazole, showing the partial atom-labeling scheme and 50% thermal ellipsoids.

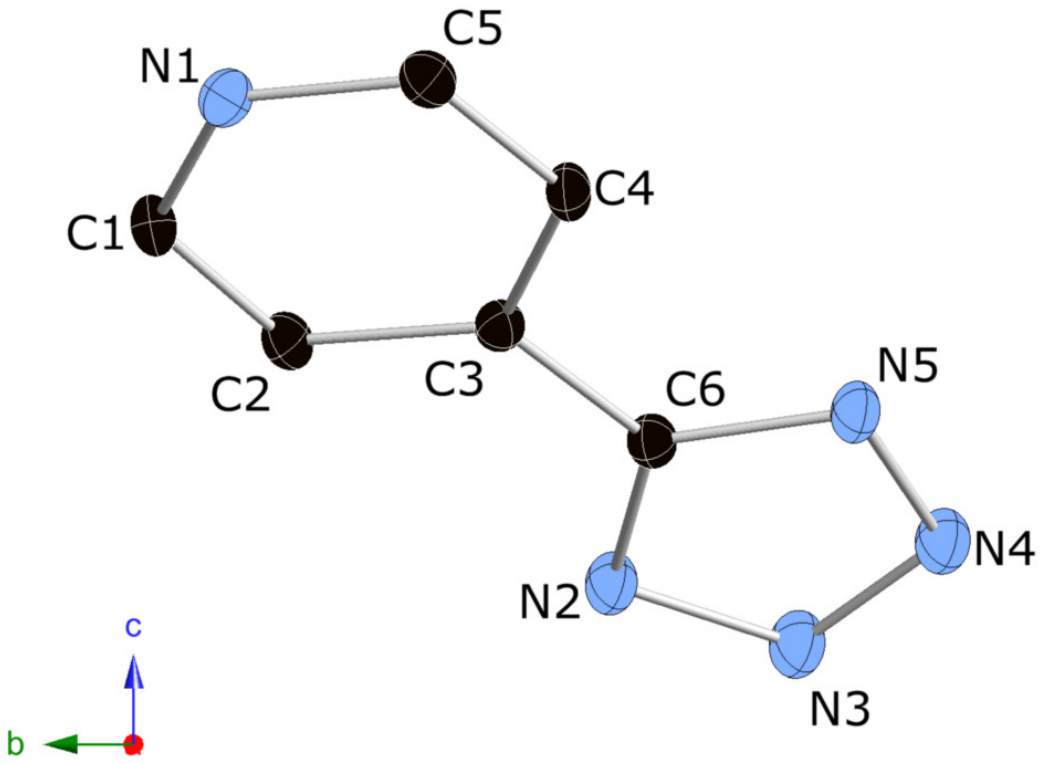


**Figure A-2** ORTEP view of the building unit of β form of 5-(4-pyridyl)tetrazole, showing the partial atom-labeling scheme and 50% thermal ellipsoids.

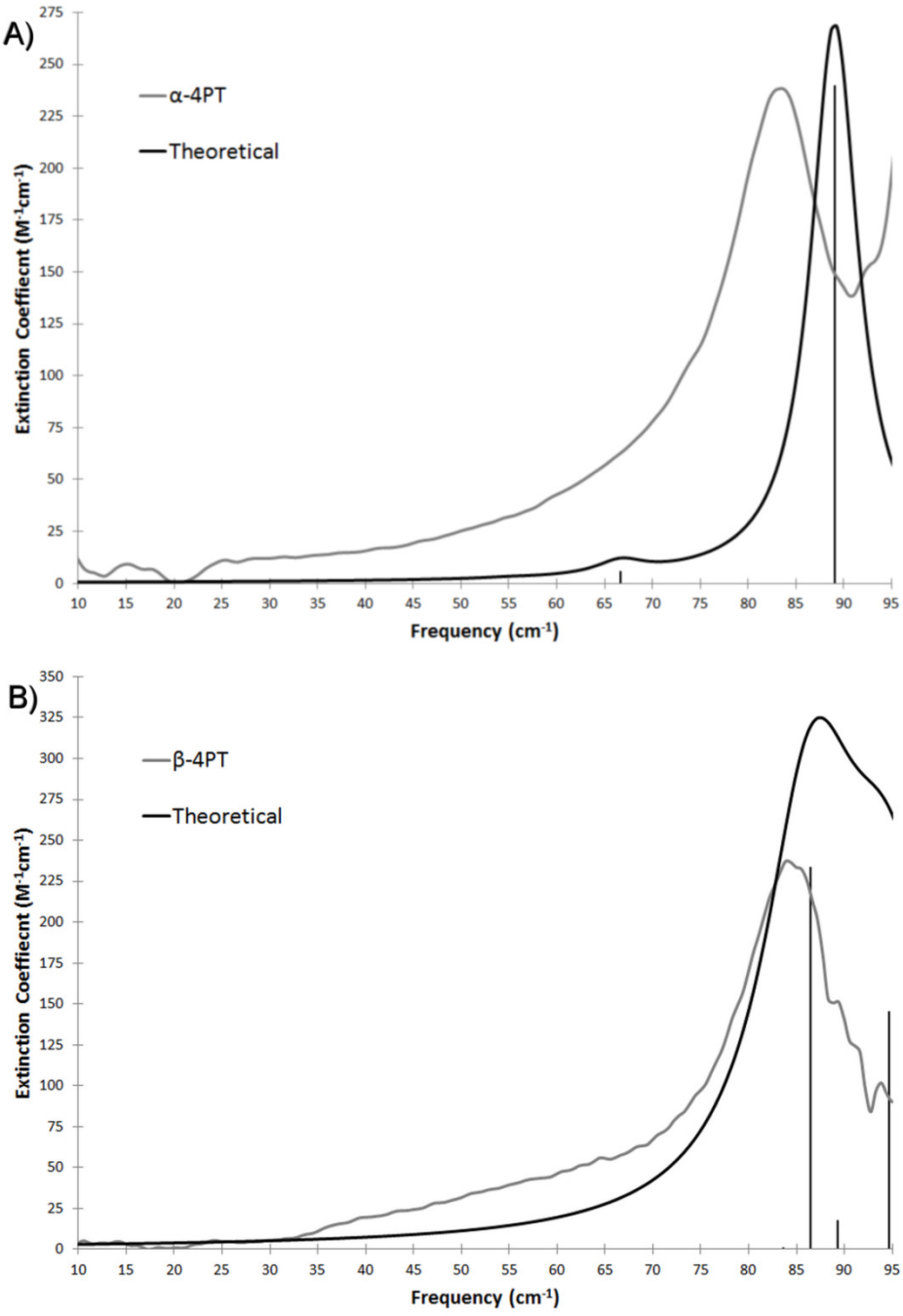


**Figure A-3** The room temperature (298K) experimental and theoretical traces for the terahertz spectra of the A) α and B) β forms of 5-(4-pyridyl)tetrazole shown from 10-95 $cm^{-1}$. An empirical 3.0 $cm^{-1}$ and 6.0 $cm^{-1}$ full-width-half-maximum Lorentzian line shape has been applied to the theoretical data of the α and β forms of 5-(4-pyridyl)tetrazole, respectively, to aid in comparison.

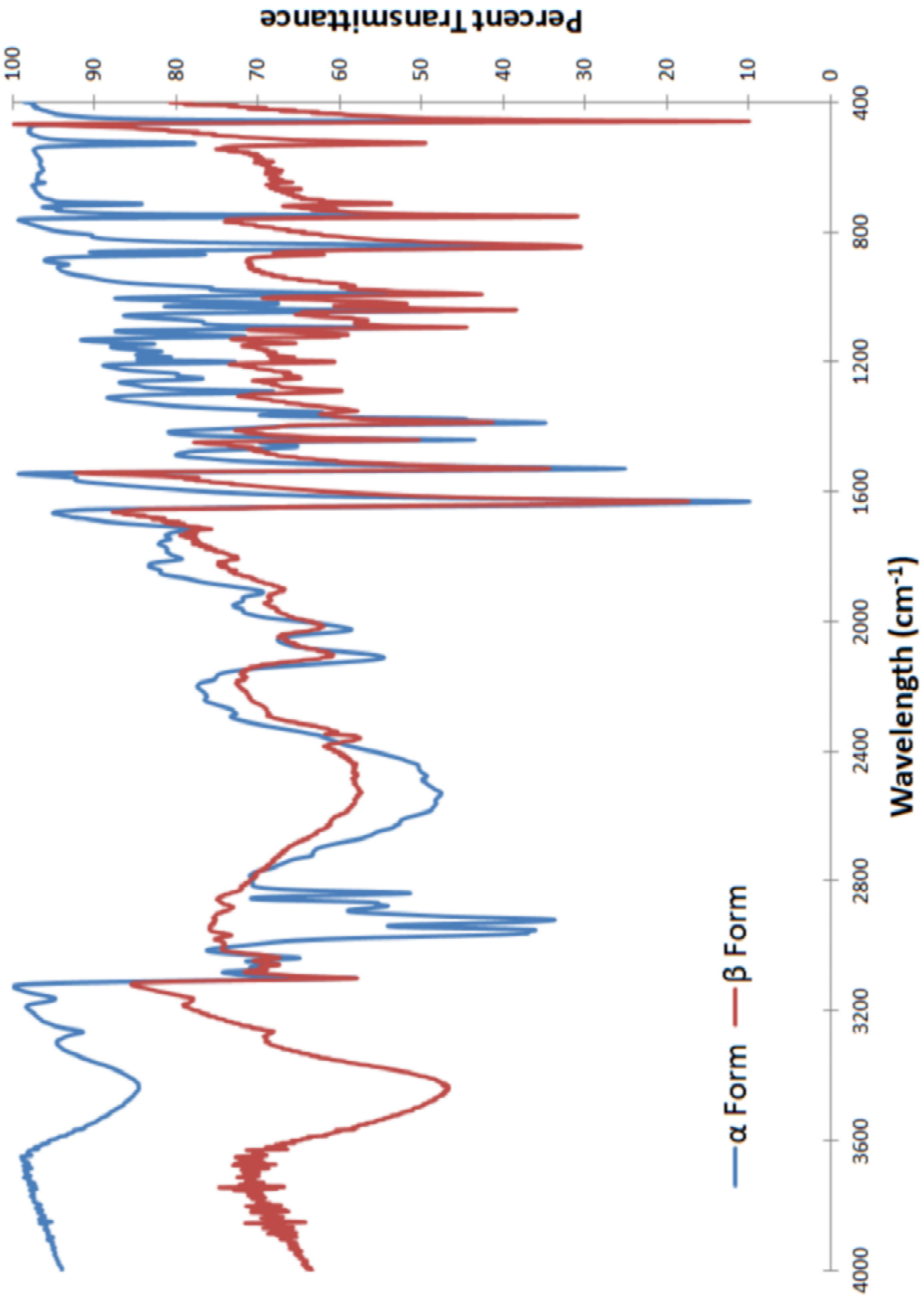


**Figure A-4** Normalized near-infrared vibration spectra of the α and β forms of 5-(4-pyridyl)tetrazole shown from 4000-400 $cm^{-1}$

## APPENDIX B. Chapter 4 Supporting Information

**Contents:**


**Figure B-1** Near-Infrared vibration spectral overlay of 4-PT·HCl and 4-PT·HBr shown from 4000-400 $cm^{-1}$

**Figure B-2** The experimental and theoretical traces for the terahertz spectra of 4-(1H-Tetrazol-5-yl)pyridinium chloride (4-PT·HCl). The frequency positions have been reduced to be 90% of the original value. An empirical 3.0 $cm^{-1}$ full-width-half-maximum Lorentzian line shape has been applied to the theoretical data to aid in comparison.

**Figure B-3** ORTEP view of the building unit of 4PT·HCl, showing the partial atom-labeling scheme and 50% thermal ellipsoids.

**Figure B-4** ORTEP view of the building unit of 4PT·HBr, showing the partial atom-labeling scheme and 50% thermal ellipsoids.

**Table B-1** Frequency positions ($cm^{-1}$) and RMSD for the experimental and theoretical terahertz spectra of 4PT · HCl. The frequency positions have been reduced to be 90% of the original value. The blanks are peaks that have no obvious correlation between the room temperature and cryogenic experimental spectra. When multiple peaks corresponded to only one peak in the experimental spectra, the weighted average was used in calculating the RMSD. Mode descriptions are described in **Table 4.5**.

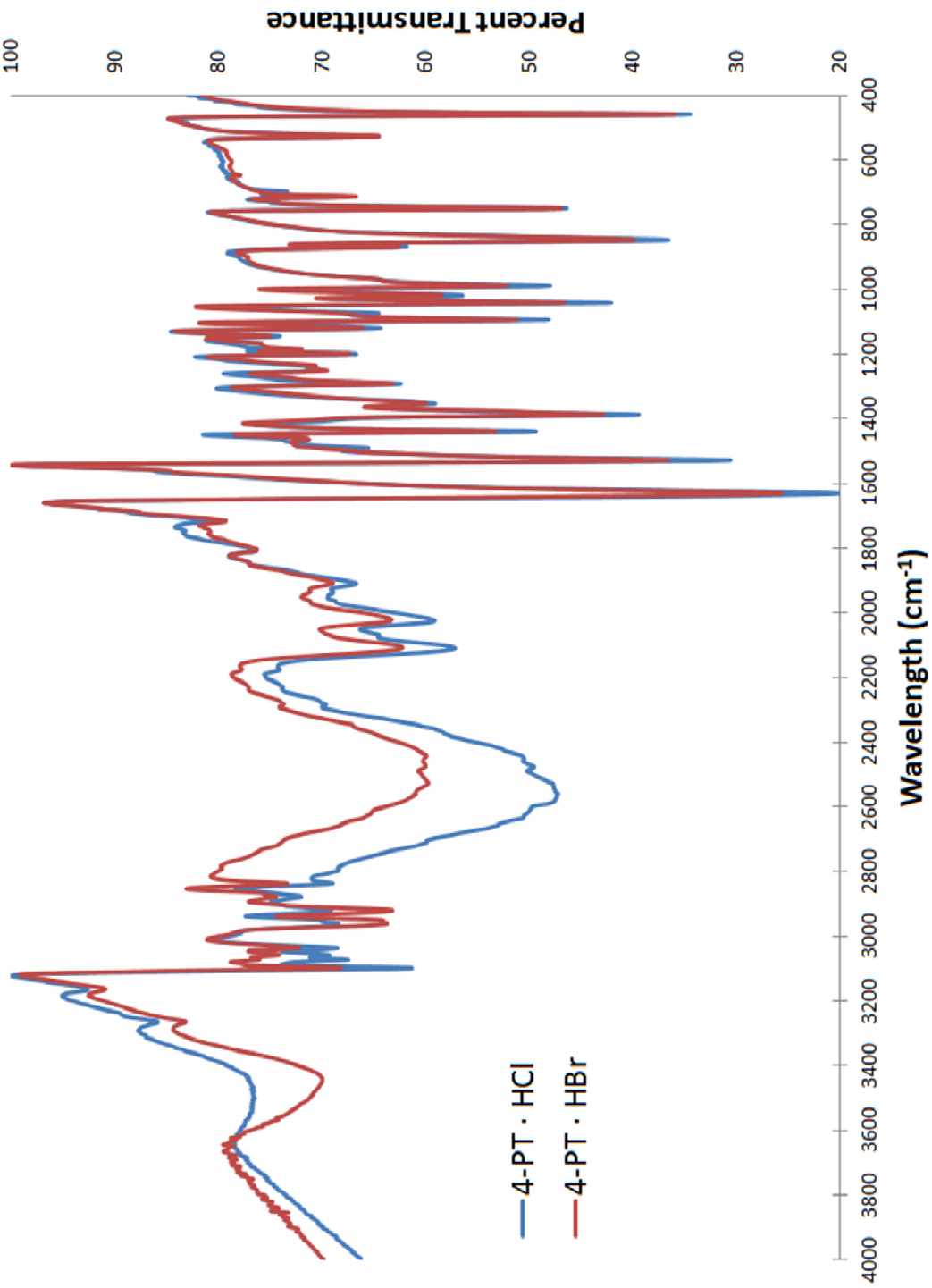


**Figure B-1** Near-Infrared vibration spectra of 4-PT·HCl and 4-PT·HBr shown from 4000-400 $cm^{-1}$

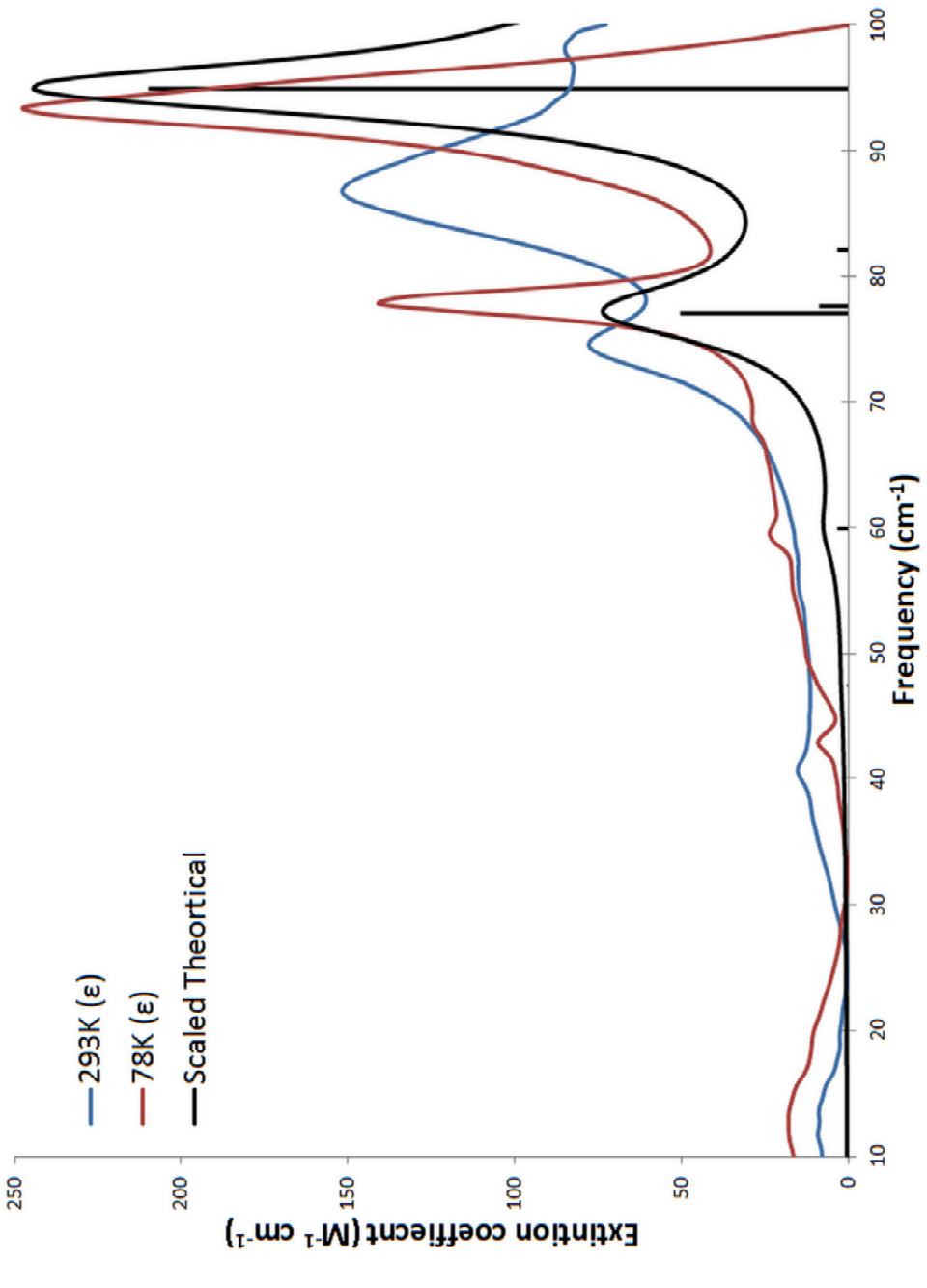


**Figure B-2** The experimental and theoretical traces for the terahertz spectra of 4-(1H-Tetrazol-5-yl)pyridinium chloride (4-PT·HCl). The frequency positions have been reduced to be 90% of the original value. An empirical 3.0 $cm^{-1}$ full-width-half-maximum Lorentzian line shape has been applied to the theoretical data to aid in comparison.

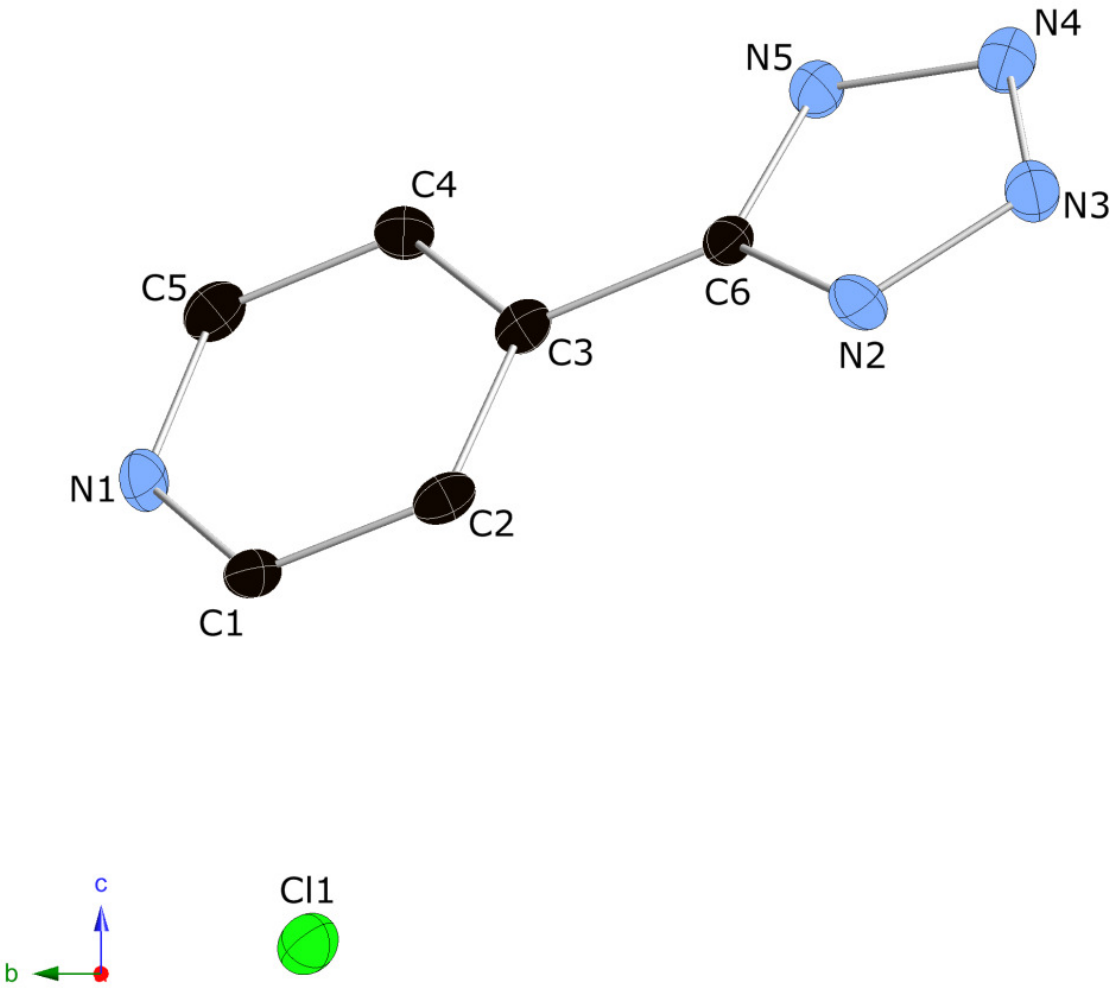


**Figure B-3** ORTEP view of 4PT·HCl, showing the atom-labeling scheme and 50% thermal ellipsoids.

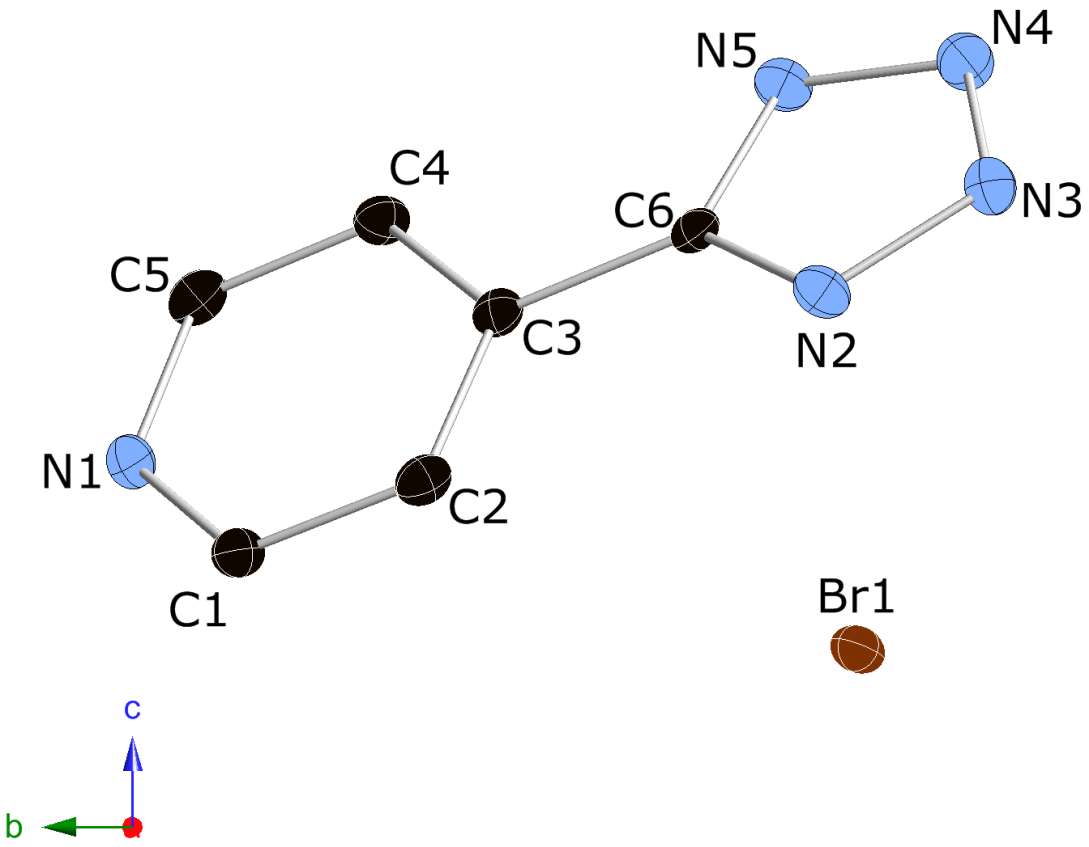


**Figure B-4** ORTEP view of 4PT · HBr, showing the atom-labeling scheme and 50% thermal ellipsoids.

**Table B-1** Frequency positions ($cm^{-1}$) and RMSD for the experimental and theoretical terahertz spectra of 4PT·HCl. The frequency positions have been reduced to be 90% of the original value. The blanks are peaks that have no obvious correlation between the room temperature and cryogenic experimental spectra. When multiple peaks corresponded to only one peak in the experimental spectra, the weighted average was used in calculating the RMSD. Mode descriptions are described in **Table 4.5**.

| Mode | Exp. (78K) | Exp. (293K) | Theoretical | Intensity (ε) |
|---|---|---|---|---|
| a | 42.89 | 40.65 | 47.44 | 0.07 |
| b | 59.46 | 56.21 | 59.87 | 0.79 |
| c | 68.59 | --- | 64.78 | 0.03 |
| d | 77.89 | 74.54 | 77.04 | 12.15 |
| e | | | 77.66 | 2.14 |
| f | 93.27 | 86.72 | 82.03 | 0.81 |
| g | | | 94.95 | 50.63 |
| h | --- | 98.07 | 100.28 | 8.75 |
| | | **RMSD** | 2.761 | |

## APPENDIX C. Chapter 5 Supporting Information

**Contents:**

**Figure C-1** ORTEP view of compound Co-4PT, showing the atom-labeling scheme and 50% thermal ellipsoids.

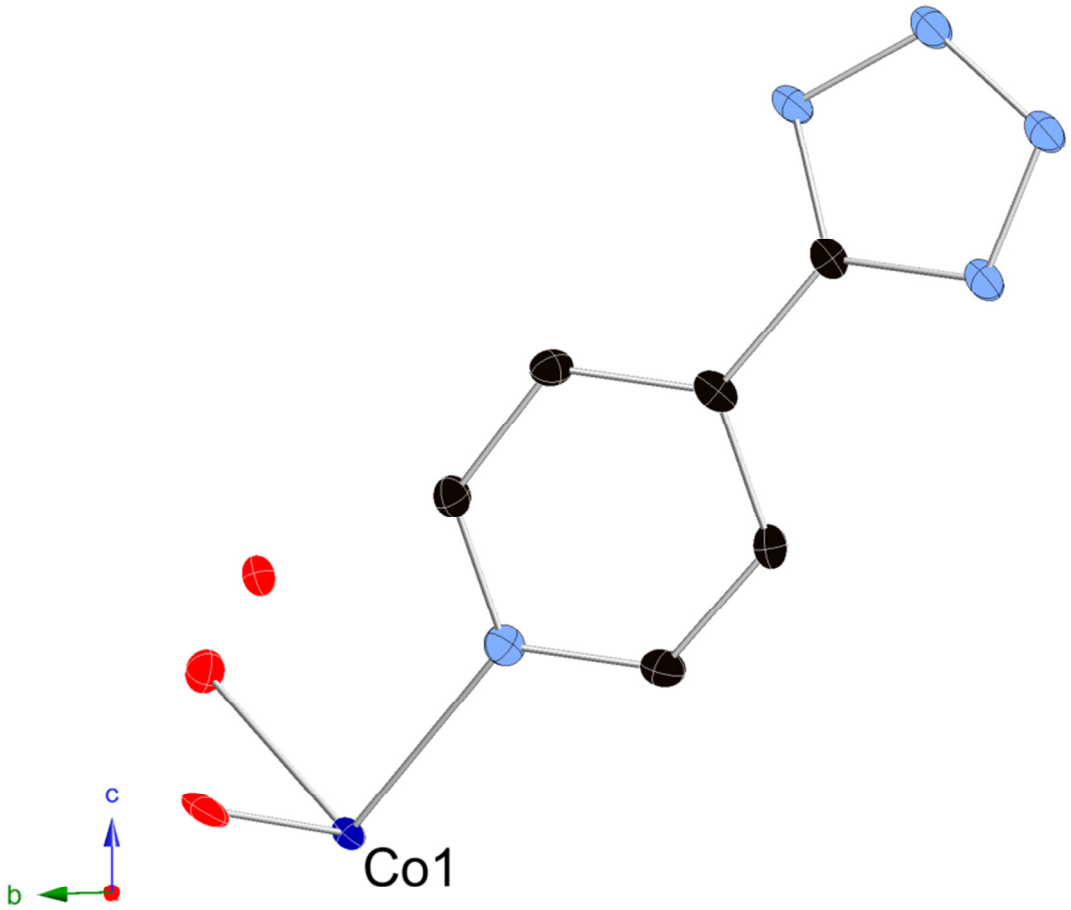


**Figure C-1** ORTEP view of compound Co-4PT, showing the atom-labeling scheme and 50% thermal ellipsoids.

## APPENDIX D. Chapter 6 Supporting Information

**Contents:**

**Figure D-1** Infrared spectrum for the compound of this study.

**Figure D-2** ORTEP view of the building unit of the compound of this study, showing the partial atom-labeling schemes and 50% thermal ellipsoids.

**Figure D-3** Decomposition of the peaks based on the Lorentzian multi-peak fitting of the spectral features displaying maximums at A) ~36 $cm^{-1}$ and B) ~49 $cm^{-1}$.

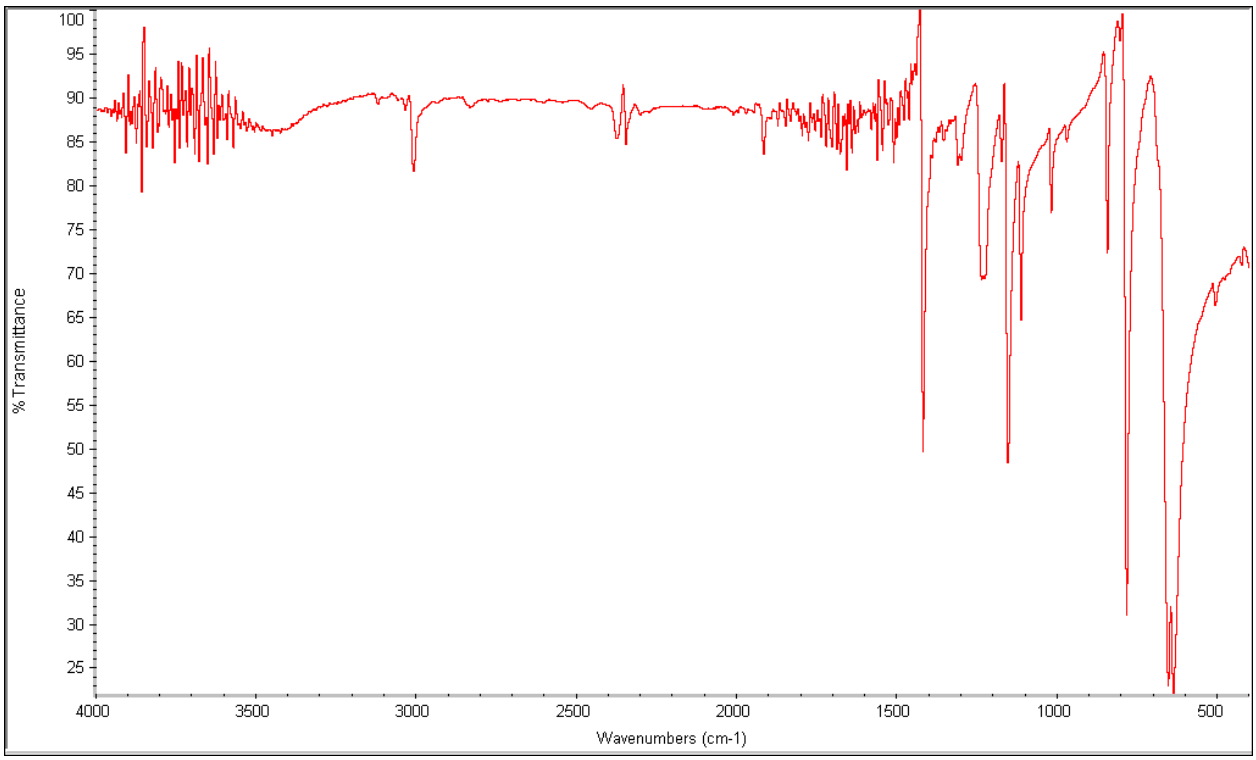


**Figure D-1** Infrared spectra for α,α,α′,α′-Tetrabromo-*p*-xylene.

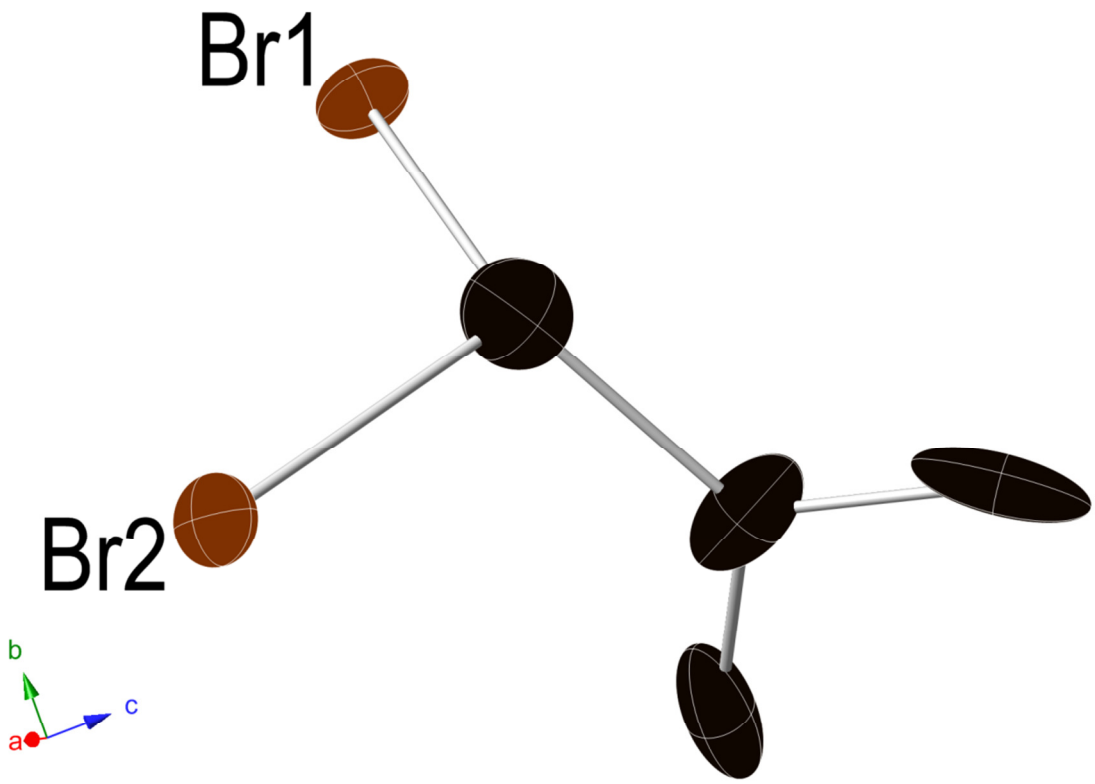


**Figure D-2** ORTEP view of compound α,α,α′,α′-Tetrabromo-*p*-xylene, showing the atom-labeling scheme and 50% thermal ellipsoids.

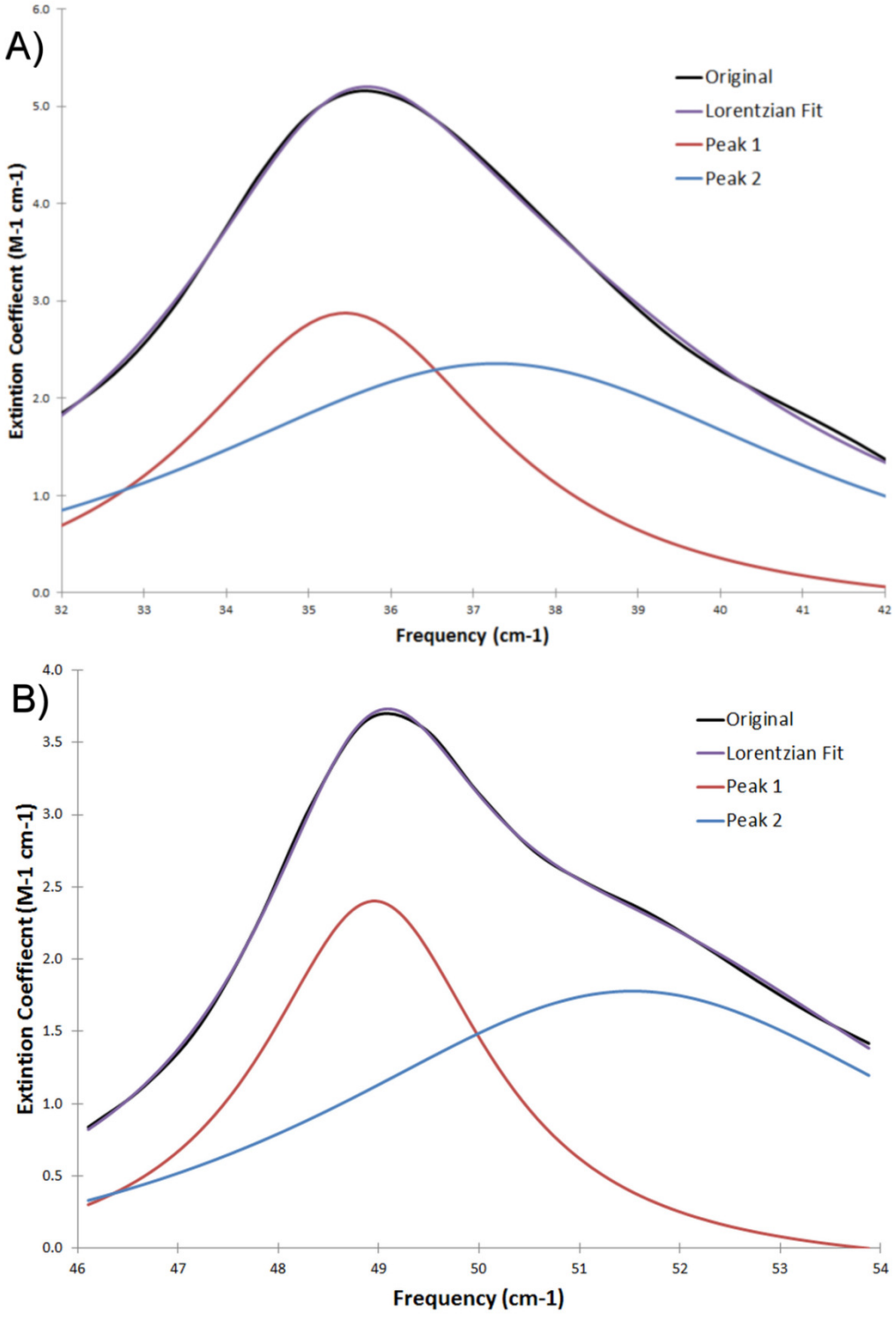


**Figure D-3** Decomposition of the peaks based on the Lorentzian multi-peak fitting of the spectral features displaying maximums at A) ~36 $cm^{-1}$ and B) ~49$cm^{-1}$.

# VITA

# Steven L. Pellizzeri

68A Hunter Street
Glens Falls, NY 12801
(315) 416-0889
slpelliz@syr.edu


## Education

PhD. Chemistry, Syracuse University, Syracuse, New York, December 2013
Dissertation title: The Solid State Simulation of the Structure and Vibrational Modes of Organic, Hybrid organometallic and Inorganic species using the CRYSTAL09 code.
Advisor: Professor Jon A. Zubieta

M.Phil. Chemistry, Syracuse University, Syracuse, New York, Spring 2010
Advisor: Professor Jon A. Zubieta

B.S. Polymer Chemistry with High Honors, Rochester Institute of Technology, Rochester, NY, May 2007
Undergraduate Research: Physical and Electronic Interactions Between a Straight Chain Conjugated Polymer and Single Wall Carbon Nanotubes, Probed By Fluorescence Spectroscopy.
Advisor: Professor Christopher Collison

## Relevant Work Experience

Fall 2008-May 2013 Graduate Teaching Assistant**,** Syracuse University, Syracuse, NY

- General Chemistry Recitation (2 semesters)
- General Chemistry for Engineers Lab (1 semester)
- Honors General Chemistry Lab (1 semester)
- Organic Chemistry Lab (3 semesters)
- Physical-Analytical Chemistry Lab (1 semester)

Fall 2012 Head TA, General Chemistry for Engineers Lab, Syracuse University, Syracuse, NY

- Helped with course development for this new course and preformed some administrative tasks.
- Tested labs for potential issues and made corrections prior to student participation.

Fall 2005-Spring 2007 Undergraduate Research Experience, Rochester Institute of Technology, Rochester, NY

- Conducted independent research under advisor Dr. Christopher Collison.
- Researched organic photovoltaics in the goal of creating a better organic solar cell using MEH-PPV.

Fall 2005 Course Developer, Rochester Institute of Technology, Rochester, NY

- Worked with professors in the development of a new computer course for chemistry majors.

Fall 2004-Spring 2005 Teaching Assistant, Rochester Institute of Technology, Rochester, NY

- General Chemistry Lecture for Chemistry Majors (2 quarters)
- Quantitative Analysis Lab for Chemistry Majors (1 quarter)

## Awards and Scholarships

- Teaching Assistantship, Syracuse University Chemistry Department, Fall 2008- May 2013
- Research Assistantship, Syracuse University Chemistry Department, Fall 2010
- Distinguished Research Scholar, Rochester Institute of Technology, Spring 2007
- Pasto Undergraduate Co-Op Fellowship, Rochester Institute of Technology, Winter 2006
- Summer Undergraduate Research Grant, Rochester Institute of Technology, Summer 2006
- Undergraduate Polymer Chemistry Award, Rochester Institute of Technology, Spring 2006
- Rochester Institute of Technology Presidential Scholarship, Rochester Institute of Technology, Fall 2003
- Memberships: American Chemical Society

## Training

- Refinement of Solvent Disorder with SHELXL, Non-Merohedral Twinning, Workshops by Peter Mueller, Syracuse, NY, 2012
- Crystallography software: SMART, APEX II, Platon, Cell Now, Crystalmaker
- Computational software: CRYSTAL, Gaussian

## Peer-Reviewed Publications (11 total)

**Pellizzeri, Steven**; Smith, Tiffany M.; Delaney, Sean P.; Korter, , Timothy M.; Zubieta, Jon. *Crystal Structure and Terahertz Spectroscopy of α,α,α′,α′-tetrabromo-p-xylene Modeled using Solid-State Density Functional Theory*, Journal of Molecular Structure, **2013**, In Press.

**Pellizzeri, Steven**; Delaney, Sean P.; Korter, Timothy M.; Zubieta, Jon. *Using Solid-state Density Functional Theory and Terahertz Spectroscopy to Spectroscopically Distinguish the Various Hydrohalide Salts of 5-(4-pyridyl)tetrazole*, Journal of Molecular Structure, *1050*, **2013**, 27-34.

**Pellizzeri, Steven**; Witko, Ewelina M.; Korter, Timothy M.; Zubieta, Jon. *A Solid-State Density Functional Theory Investigation of the Effect of Metal Substitution (Metal = Mn, Cd, Co) on the Terahertz Spectra of Isomorphous Molecular Metal 5-(4-pyridyl)tetrazolato Complexes*, Journal of Molecular Structure, *1048*, **2013**, 214-222.

Jones, Stephanie; Vargas, Jose M.; **Pellizzeri, Steven**; O'Connor, Charles J.; Zubieta, Jon. *Solid state coordination chemistry: Structural consequences of varying diphosphonate tether length and fluoride incorporation in the copper–bisterpy/oxomolybdenum/organodiphosphonate system (bisterpy = 2,2':4',4":2",2"'-quarterpyridyl-6',6"-di-2-pyridine)*,Inorganica Chimica Acta., *395*, **2013**, 44-57.

Darling, Kari; Ouellette, Wayne; **Pellizzeri, Steven**; Smith, Tiffany; Vargas, Jose; Tomaszfski, Steven; O'Connor, Charles J.; Zubieta, Jon. *One- and two-dimensional coordination polymers of substituted tetrazoles with cadmium(II)*, Inorganica Chimica Acta., *392*, **2013**, 417-427.

Bartholomae, Mark; Chueng, Hoi; **Pellizzeri, Steven**; Ellis-Guardiola, Kenneth; Jones, Stephanie; Zubieta, Jon. *Novel building units in the construction of materials of the oxomolybdate-organodiphosphonate/copper(II)-dipodal-organonitrogen ligand system: Structural influences of dipodal ligand tether length and flexibility*, Inorganica Chimica Acta., *389*, **2012**, 90-98.

Darling, Kari; Burkholder, Eric M.; **Pellizzeri, Steven**; Nanao, Max; Zubieta, Jon. *A bimetallic oxide network constructed from oxomolybdoarsonate clusters and copper(II)-tetrapyridylpyrazine building blocks*, Inorganic Chemistry Communications, *14*, **2011**, 1745-1748.

**Pellizzeri, Steven**; Korter, Timothy M.; Zubieta, Jon. *A solid-state density functional theory investigation of the structure and vibrational modes of vanadium phosphate polymorphs*, Journal of Molecular Structure, *1003*, **2011**, 21-30.

Collison, Christopher J.; Spencer, Susan; Preske, Amanda; Palumbo, Chad; Helenic, Alysha; Bailey, Rebecca; **Pellizzeri, Steven**. *A New Model for Quantifying the Extent of Interaction between Soluble Polyphenylene-Vinylenes and Single-Walled Carbon Nanotubes in Solvent Dispersions*, Journal of Physical Chemistry B., *114*, **2010**, 11002-11009.

Collison, Christopher J.; **Pellizzeri, Steven**; Coombs, Sidney G.; Colleton, April; O'Donnell, Marc J. *Fluorescence quenching of conjugated polymers by single-walled carbon nanotubes to investigate energy transfer in complexes formed in composite solutions*, PMSE Preprints, *101*, **2009**, 1651-1652.

Collison, Christopher J.; **Pellizzeri, Steven**; Ambrosio, Filip. *Spectroscopic Evidence for Interaction of Poly[2-methoxy-5-(2'-ethylhexyloxy)-1,4-phenylenevinylene] Conformers and Single-Walled Carbon Nanotubes in Solvent Dispersions*, Journal of Physical Chemistry B., *113*, **2009**, 5809-5815

*Note: 1 paper also in progress.

## Presentations

1. *Solid State investigation of polymorphs and halide salts of 5-(4-pyridyl)tetrazole*

St. Lawrence University, Canton, NY.
**Steven Pellizzeri**, Timothy Korter, Jon Zubieta, April 2013, oral presentation (invited seminar).

2. *Solid-state simulation of the vibrational modes and intensities of simple vanadium phosphates*

240th ACS National Meeting, Boston, Massachusetts.
**Steven Pellizzeri**, Timothy Korter, Jon Zubieta, August 2010, poster presentation.

3. *Characterization of the mixing between MEH-PPV and single wall carbon nanotubes using fluorescence spectroscopy*

RIT Undergraduate Symposium 2006, Rochester, New York.
**Steven Pellizzeri**, Christopher Collison, August 2007, oral presentation.

4. *Characterization of the mixing between MEH-PPV and single wall carbon nanotubes using fluorescence spectroscopy*

RIT Undergraduate Symposium 2006, Rochester, New York.
**Steven Pellizzeri**, Christopher Collison, August 2007, poster presentation.

5. *Characterization of the mixing between MEH-PPV and single wall carbon nanotubes using fluorescence spectroscopy*

34th Northeast regional Meeting of the American Chemical Society, Binghamton, New York.
**Steven Pellizzeri**, Christopher Collison, October 2006, poster presentation.

6. *Physical and electronic interactions between a straight chain conjugated polymer and single wall carbon nanotubes, probed by fluorescence spectroscopy*

232nd ACS National Meeting, San Francisco, California.
**Steven Pellizzeri**, Christopher Collison, April Colleton, September 2006, poster presentation.